I. CEDAR -- AN APPROACH TO THE COMPUTER AUTOMATION OF SHORT-PERIOD LOCAL SEISMIC NETWORKS

II. SEISMOTECTONICS OF THE IMPERIAL VALLEY OF SOUTHERN CALIFORNIA

Thesis by

Carl Edward Johnson

In Partial Fulfillment of the Requirements

for the Degree of

Doctor of Philosophy

California Institute of Technology

Pasadena, California

1979

(Submitted May 2, 1979)

Dedicated to the Nancy

of

seemingly infinite patience

ACKNOWLEDGEMENTS

I would like to express my heartfelt thanks and appreciation to Clarence Allen and David Harkrider for their enthusiastic support of the effort that went into the preparation of this thesis. Their reading and criticism of handwritten drafts contributed to an earlier completion of this work than might otherwise have been the case. I would like to particularly thank Bernard Minster for reviewing the rough draft of much of this thesis as well as for many fruitful discussions during which many of the ideas presented here were solidified.

My interest in seismology emerged during a rather confused time in my life as a direct result of my association with Frank Press and Shawn Biehler while at M.I.T. At this time my relationship with Joe Andrews, Frank Richter, and Al Smith provided considerable direction to my later interests.

I have found the Seismological Laboratory at Caltech to be a particularly stimulating environment in which to develop my research interests. The importance of the freedom to follow one's own interests and to make one's own mistakes is an opportunity whose importance should not be overlooked. I have particularly enjoyed my association with Don Anderson whose support of my research interests, despite their occasional undirectability, is deeply appreciated. In general, I have found my experience with the Seismological Laboratory, its faculty, students, and staff to be a highly rewarding one. My relationship with Robert Hart and Sue Raikes has provided a perspective that was particularly valuable.

During the early stages of the development of the CEDAR system

discussions with Ken Anderson and Robert Geller were of inestimable value. The automation of the Southern California network would not have been conceivable without the warm support and encouragement of James Whitcomb. Conversations with Ken Anderson were of considerable value with respect to overall systems design. I would like to particularly thank Anne Blanchard, Kate Hutton, Shirley Fischer, Karen Richter and Doug Given for making things work despite early bugs in the CEDAR system as well as generally dealing with those difficulties that arose while I was inextricably involved with the preparation of this thesis. The development of the catalog manipulation and graphical software was strongly influenced by my association with Vlady Keilis-Borok during the summer of 1978 when he visited the lab as a Distinguished Fairchild Scholar.

David Hadley was extremely instrumental in the development of my initial interest in earthquake swarms in the Imperial Valley and seismicity studies more generally. This work has also been considerably benefitted by discussions with Dave Hill, Gary Fuis, Robert Sharp, and Karen McNally. Karen Ward provided data for the first few years of the operation of the Imperial Valley network.

Much of the research and most of the drafting was carried out using the Seismological Laboratory's Prime 500 computer. It is extremely unlikely that this thesis would have appeared in its present form were it not for the existence of this facility. I would like to thank Lazlo Lenches for his efforts with respect to many of the figures and whose professionalism I admire. The typing was accomplished by Janet Boike whose experience has caused a considerable

amount of order and style to emerge from confusion.

Finally, I would like to particularly acknowledge the patience and dedication of my wife, Nancy, for the many sacrifices required during the completion of this thesis.

The initial development of the CEDAR system was supported by NASA/JPL contract No. 49-681-02081-0-8260, Nuclear Regulatory Commission contract No. AT(49-24) - 0195. Subsequent development and implementation of the CEDAR system was supported in part under U. S. Geological Survey contracts No. 14-08-0001-16629 and No. 14-08-0001-17642. General support for the organization and analysis of seismicity data was provided by the U. S. Geological Survey under contract No. 14-08-0001-16719. Considerable support for both parts of this thesis was provided by the Caltech Earthquake Research Affiliates. This research was partially supported by the Advanced Research Projects Agency of the Department of Defense and was monitored by the Air Force Office of Scientific Research under contract No. F49620-77-C-0022.

ABSTRACT

A real-time detection and recording system (CEDAR) is developed as a means of automating the acquisition and processing of data from short-period local networks. This system has been used for the past two years for the analysis of data from 150 stations in Southern California with an annual workload of about 7500 local events. Two minicomputers are used with one dedicated to the real-time detection and digital recording of local earthquakes while the other is used for timing, location, and data archiving based on interactive graphical techniques. The use of this system has substantially reduced the effort required for the routine analysis of local data. The discussion is kept at a general level so as to be useful to those setting up similar systems with somewhat different requirements. In support of the CEDAR system a magnitude scale, M_{CA}, is developed that is particularly adapted to the needs of local digital seismic networks. The supporting algorithm is based on median absolute amplitudes of any on-scale portion of the post-S seismic coda. The use of a power law coda shape function in the form $a(t) = a_o t^{-q}$ makes the proposed method directly commensurable with the already widely used and highly successful duration method. The M_{CA} magnitude scale is predicated on the same short-term averages used by the event detection algorithm on the real-time system, permitting a direct stochastic analysis of the spatial magnitude thresholds of a particular configuration of the detection logic. Such an *a priori* evaluation of detection capability is necessary since detection failure results in considerable extraneous effort. The use of these techniques has permitted the compilation of

a local earthquake catalog and attendant phase data base that are substantially more uniform and accurate than what is generally obtained using manual methods.

The nature of earthquake swarms in the Imperial Valley is investigated with the goal of placing specific constraints on the physical mechanisms governing their behavior. Within the Imperial Valley most earthquakes occur as swarms concentrated within a narrow, sharply bounded, spindle-shaped zone joining the northern terminus of the Imperial Fault with the southern end of the San Andreas Fault. Although over the past five years the seismicity within this zone, designated the Brawley Seismic Zone, is surprisingly uniform, on time scales of a few weeks activity is highly clustered in both space and time. Seismicity is not confined to a few "hot spots", as might be expected, but rather seems to move around, seldom if ever reactivating the site of a previous swarm. Seven sequences of swarms are analyzed in detail using a master event approach in order to provide some insight into supporting tectonic structures. It is generally observed that swarm sequences comprise discrete bursts of activity, each of which appears to "illuminate" a single planar fracture transverse to the major tectonic elements in the Imperial Valley such as the Imperial Fault and the Brawley Fault. Development of activity during a sequence of swarms generally begins with high clustered activity followed by continuous, progressive involvement of the transverse structures, and progressive but discontinuous development in the form of spatially and temporally isolated clusters along the major fault elements. Observed migration rates

range from .5 km/hr to .5 km/day. The consistency observed with respect to the pattern of development of independent sequences strongly suggests that a deterministic, physical model can be obtained. One possible model is suggested that relates the swarms on transverse structures with propagating, episodic creep on the major transforms. In this model both the creep rate and the triggering of earthquake swarms is governed by perturbations of pore-pressure in a fluid-infiltrated elastic matrix.

TABLE OF CONTENTS

GENERAL INTRODUCTION

This thesis has been organized into two parts as if unrelated and therefore distinct. The first part addresses the problems of acquiring data from a dense, short-period seismic network and extracting information from it in a moderately efficient manner. At the level of individual samples it is clear that the information content is exceedingly low; one can throw away almost all incoming data and lose nothing of scientific value. The primary consideration in the development of an efficient means of dealing with the massive quantity of "data" generated by modern, dense networks is to discard all that is nonessential as quickly and as effectively as possible; one needs to become a clever dustman. Although significant progress has already been made, much work remains before the true value of dense networks with respect to understanding the physics of earthquakes can be realized.

Chapter 1 describes the history, underlying philosophy and design criteria of the CEDAR (Caltech Earthquake Detection and Recording) system as it has evolved since June 1976. This system is responsible for the digitization of telemetered seismic signals in real-time while eliminating all data immediately for those intervals deemed uninteresting (i.e., lacking earthquakes of sufficiently large magnitude). This definition is undoubtedly too restrictive for some purposes, but some sacrifices must be made, I think, in order to avoid complete paralysis. Consonant with the aforementioned philosophy it is requisite to reduce the data stream as quickly as is reasonably possible in order to avoid rendering later stages of processing

ineffective. The discussion avoids the details of a specific implementation as much as possible and is hopefully geared toward being useful to those setting up systems based on a somewhat different approach.

The second chapter continues the effort of making the reduction of network data as efficient as possible by means of an automated magnitude estimation procedure appropriate for digital data streams. This approach is predicated on developing a systematics describing the "shape" of the post-S coda that can be inverted to obtain a magnitude estimate from median rectified coda amplitudes. The method is sufficiently general so that any available segment of coda can be utilized regardless of beginning and ending times. The current implementation utilizes consecutive 5.12 s coda segments for this purpose. This algorithm turns out to be a direct extension of the already widely used duration method. During the course of its development considerable insight was obtained, not entirely unintentionally, regarding properties of the seismic coda as well as site and propagation effects for local earthquakes. The approach, I have taken is an empirical one and does not depend on any particular preconceptions regarding coda development.

Chapter 3 describes preliminary efforts to ascertain what data are being discarded in real-time. The approach taken is to try to evaluate the detection capability of the CEDAR system in terms of magnitude threhold contours. The method developed is specific to the CEDAR system event detector and is predicated on the propagation and coda systematics developed in Chapter 2.

The second part of this thesis deals with the application of the tools assembled in the first to the furthering of the understanding of earthquake swarms in the Imperial Valley. The desire to pursue this line of research was a primary factor in motivating the development of efficient techniques for the processing of dense network data.

Chapter 4 is essentially historical and sets the stage for a more detailed discussion of earthquake swarms in Chapter 5. Both the development of Imperial Valley seismicity since the 1940 El Centro earthquake and the general relationship of the Imperial Valley to the tectonics of the Gulf of California and the San Andreas Fault system are discussed.

Chapter 5 is an in-depth analysis of Imperial Valley swarms directed toward developing some understanding of the physical processes that govern them. The bulk of Chapter 5 describes the detailed observations and analysis of seven sequences that occurred during the past five years. A tripartite model is then suggested which appears to be capable of explaining many of these observations as well as the longer term changes in Imperial Valley seismicity discussed in Chapter 4.

Chronologically the order in which this research was conducted was quite different from the order of presentation in this thesis. The first work completed was the analysis of the 1975 Brawley swarm in Chapter 5 using manual methods of timing and data preparation. The inconvenience of this procedure motivated the development of a more practical approach of getting accurate data to the analysis stage in a timely fashion as discussed in Chapters 1, 2, and 3.

This in turn facilitated the completion of the research presented in Chapters 4 and 5.

One reason for investing a considerable amount of effort in extracting information from small earthquakes is predicated on the belief that information can be obtained that is not available with a higher magnitude threshold. Specifically, ten years of data at a magnitude of 3.0 threshold may not answer the same questions as one year at a magnitude 2.0 threshold even though the number of events is the same in each case. This is essentially a refutation of a notion firmly imbedded in the foundation of many seismicity studies that earthquake phenomena, particularly statistical properties, are scale invariant with respect to magnitude. This precept of self-similarity, although convenient for predicting such things as recurrence intervals, appears to be demonstrably false. At the upper magnitude range one is frequently confronted by such apparent paradoxes as regions in which the recurrence time for great earthquakes cannot be reconciled with depressed seismicity of smaller events by any reasonable choice of "b" value. At the small magnitude end of the scale, the results of Chapter 5 hopefully demonstrate that inferences based on the analysis of small events could not be obtained from a study restricted only to the largest earthquakes regardless of how long such a study was conducted. It is in this light that I regard the partition between the development of tools and their research application, as reflected in the structure of this thesis, as being artificial. If we are to push our inquiry into the domain of diminishing magnitude, then it is simply an attendant necessity to develop the techniques necessary to do so.

PART I

C E D A R -- AN APPROACH TO THE COMPUTER AUTOMATION OF SHORT PERIOD LOCAL SEISMIC NETWORKS

CHAPTER 1

THE IMPLEMENTATION AND OPERATION OF A LOCAL DIGITAL SEISMIC NETWORK IN SOUTHERN CALIFORNIA

INTRODUCTION

The last ten years have seen something of a revolution in network and array seismology with advances in electronics spurring a transition from analog methods of data handling to digital approaches. Teleseismic arrays operating at lower frequencies and hence with less demanding sampling rate requirements were the first to take advantage of the advances in digital technology. In the last four or five years digital approaches, such as those developed by Stewart et al. (1971), Stevenson (1976), Stewart (1977), Stevenson et al. (1978) and Allen (1978) have emerged for the processing of data from local short period networks and portable arrays. In this paper we would like to apply this technological resource to the automation of network processing in Southern California through the development of the CEDAR (Caltech Earthquake Detection and Recording) system.

The CEDAR system is a collection of real-time and off-line computer equipment and software intended to facilitate a substantial increase in the efficiency of the routine processing of data from the short-period regional network in Southern California. Its principal objective is to provide researchers in a timely manner with better, more accurate, and more complete data than was possible with previous approaches. These data take the form of precisely timed arrivals of P and S phases for earthquakes and quarry blasts occurring in Southern California, a library of high quality digital records for local and regional events and teleseismic body phases, and a complete and objective catalog of accurately located local earthquakes. The local earthquake catalog is now growing at a rate of 7,000 events per year while the seismogram

library contains in excess of 500,000 digitized records. Among the advantages realized by the CEDAR system over previous methods are more accurate picking of relative arrival times, much more efficient processing of the data, the ability to record first motions for nearby events, and a greater dynamic range permitting precise timing in the codas of preceding events.

The need for an automated approach is demonstrated by the histogram of the number of located events each year shown in Figure 1. It is apparent that this number has increased by nearly an order of magnitude over the last ten years, principally as a result of the increased station density in Southern California. One need only consider that the number of timed phases, and hence overall workload, increases by roughly the square of the number of located events to appreciate the situation that motivated the development of the CEDAR system.

The implementation of the CEDAR system was begun in July, 1976. In one month the real-time system was operational and by the end of three months an off-line processor was sufficiently developed to allow the initiation of timing in parallel with the develocorder routine. After a three-month trial period the Caltech part of the develocorder routine was abandoned, although film recording continued, and all timing was accomplished, using the interactive graphics software developed for the off-line computer discussed below. Until June, 1977 the use of the off-line computer was limited to event timing. Phase cards were punched and the remaining tasks of routine location and catalog preparation were carried out using previous methods. Over

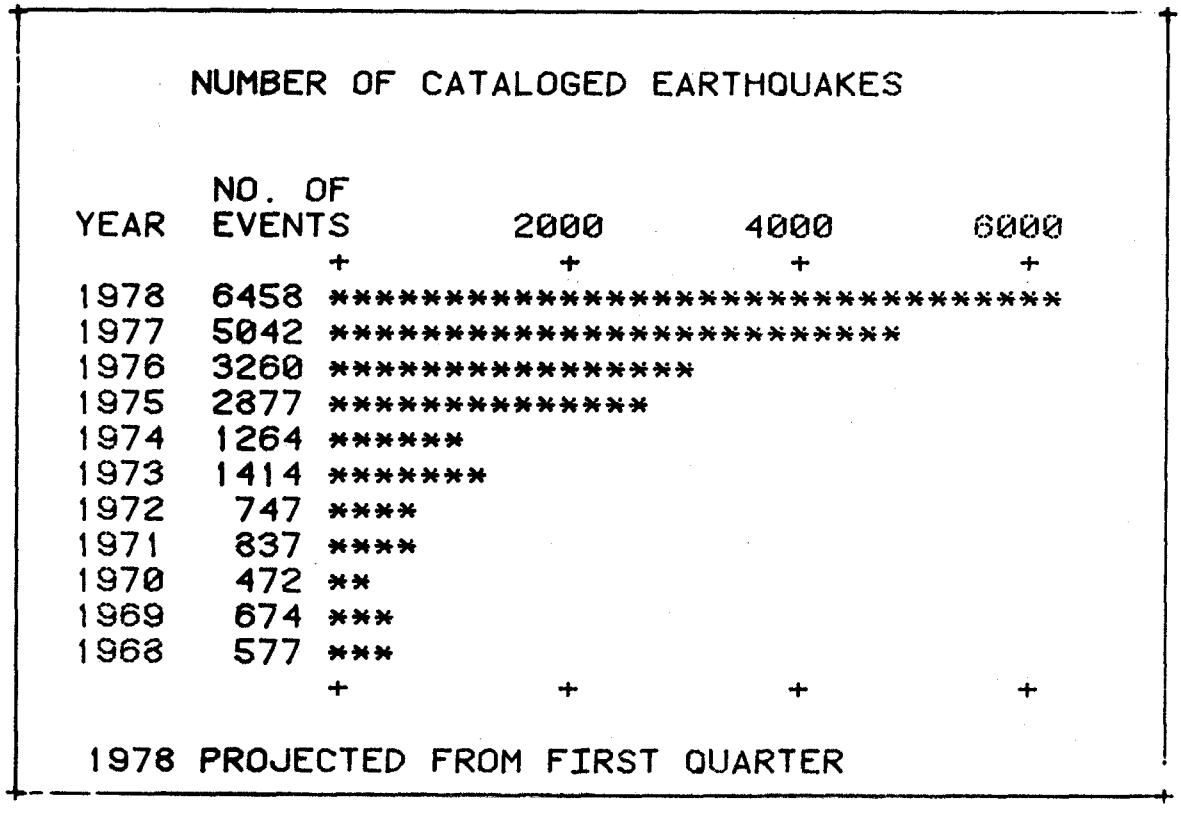

Figure 1. Number of events located and catalogued each year.

the next twelve months computer based procedures slowly replaced their counterparts in the preceding manual routine. This imposed a structure on the automated processing that might well have been different had a totally independent development effort been possible.

In the following discussion the emphasis will be on describing what the CEDAR system is in a functional sense. It is hoped that the information presented will be of some help to others embarking on similar programs.

SOUTHERN CALIFORNIA ARRAY FOR RESEARCH ON LOCAL EARTHQUAKES AND TELESEISMS -SCARLET-

More than 140 seismographic stations, spanning 600 km east to west and 500 km north to south and crossing diverse seismotectonic provinces, comprise the short period regional seismic network in Southern California (Figure 2).

A majority of the U.S.G.S. installed seismometers are high-gain short period (Mark L-4) moving coil, vertical instruments designed to record impulsive first arrivals of small to moderate earthquakes within several hundred kms. The system response for these instruments is sharply peaked at about 14 Hz. A few (24) vertical short period instruments, mostly C.I.T. stations equipped with Benioff seismometers, are ideally suited to record multiple phases of local and regional events out to distances of more than a thousand km. Their system response is peaked at 1-5 Hz. Two of these and three of the short period sites are equipped for the recording three components (one vertical and two horizontal). The analog signals from these sites

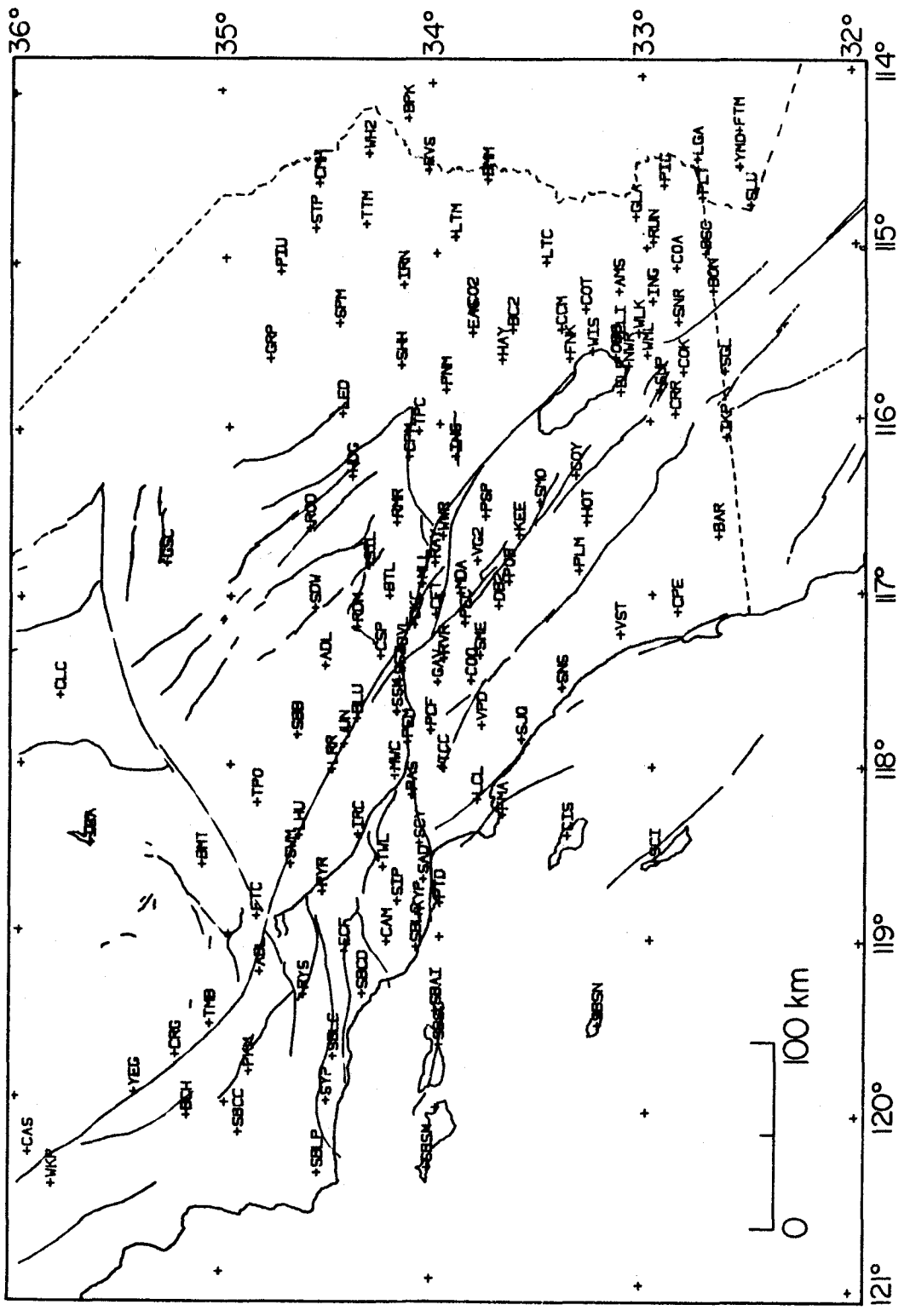

Figure 2. Permanent stations of the Southern California (SCARLET)

are telemetered to Caltech using frequency multiplexed telemetry over leased telephone lines. The multiplexed signals are recorded on multi-channel analog magnetic tape in addition to being fed to a bank of discriminators where the signals from each station are isolated and recorded in the traditional manner on either a develocorder or helecorder. In addition, the isolated signals are fed to a multi-channel A/D converter for digitization, detection, and subsequent analysis.

COMPUTER EQUIPMENT

In this section we discuss the computer equipment currently supporting the CEDAR system. This should not be taken as an endorsement of a particular computer or computer vendor. Generally speaking, the CEDAR system could be implemented on any 16 bit minicomputer with hardware fixed point addition and subtraction, DMA control of disc, tape, and the A/D converter, and a real-time clock capable of generating processor interrupts. The speed of the central processor dictates the number of stations that can be carried on-line.

The configuration of the on-line computer (System A) is shown in Figure 3. The CPU is a Data General 820 with 32K words of core memory. This amount of memory is demanded by the use of five 4,000 word buffers by the event detection algorithm (Appendix I). Smaller networks might require less core. The A/D unit is a DATEL 256 with a maximum sampling capability of about 60 KHz. We are currently running 160 channels with bipolar single ended inputs. The maximum signal range is ±5 volts. The event detector could be more easily

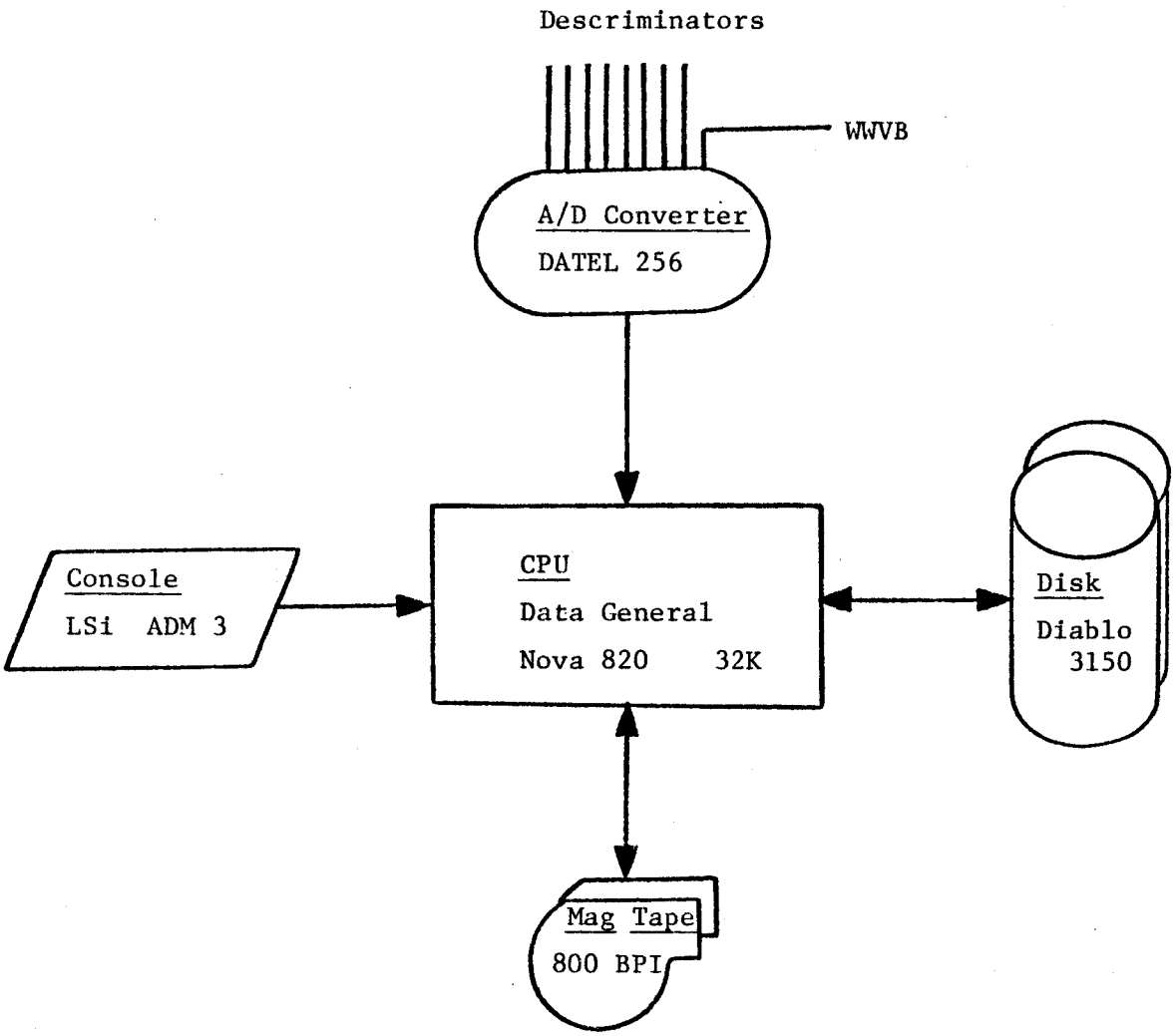

Figure 3. Block diagram showing the relationship between major components of System A.

implemented and would be considerably more efficient if monopolar inputs had been used instead. The disc is a 3.5 megabyte removable cartridge system with moving heads. It is used both as a program storage device as well as a pre-event memory buffer. A solid state memory device or bulk memory should be more reliable, although since the application is dedicated we have had little trouble. The console device is a low priced alphanumeric CRT. Although it is easy to imagine a more versatile role, its sole purpose at present is to start and stop the real-time system every few months for preventive maintenance. Digital data for triggered events is stored on 2,400 foot nine-track magnetic tape at 800 BPI. Two tape drives are required, which are used alternately, so that data can be written on one while a new tape is being mounted on the other. Use of more than two drives or a higher bit density would be advantageous.

The off-line computer configuration (system B) is shown in Figure 4. Since it is occasionally required to assume the real-time tasks, system B requires all of the hardware and capabilities discussed above. The A/D converter on system B is also desirable for development and testing of real-time software. If a multi-task operating system were available it should not be difficult to run a second real-time operation, such as a teleseismic monitor, in addition to routine processing tasks.

A matrix line printer (Versatec D1200A) is used for earthquake location listings and program development in addition to plotting seismograms for event identification during the pre-event analysis stage of routine processing discussed below. We are currently using

OFF-LINE SYSTEM

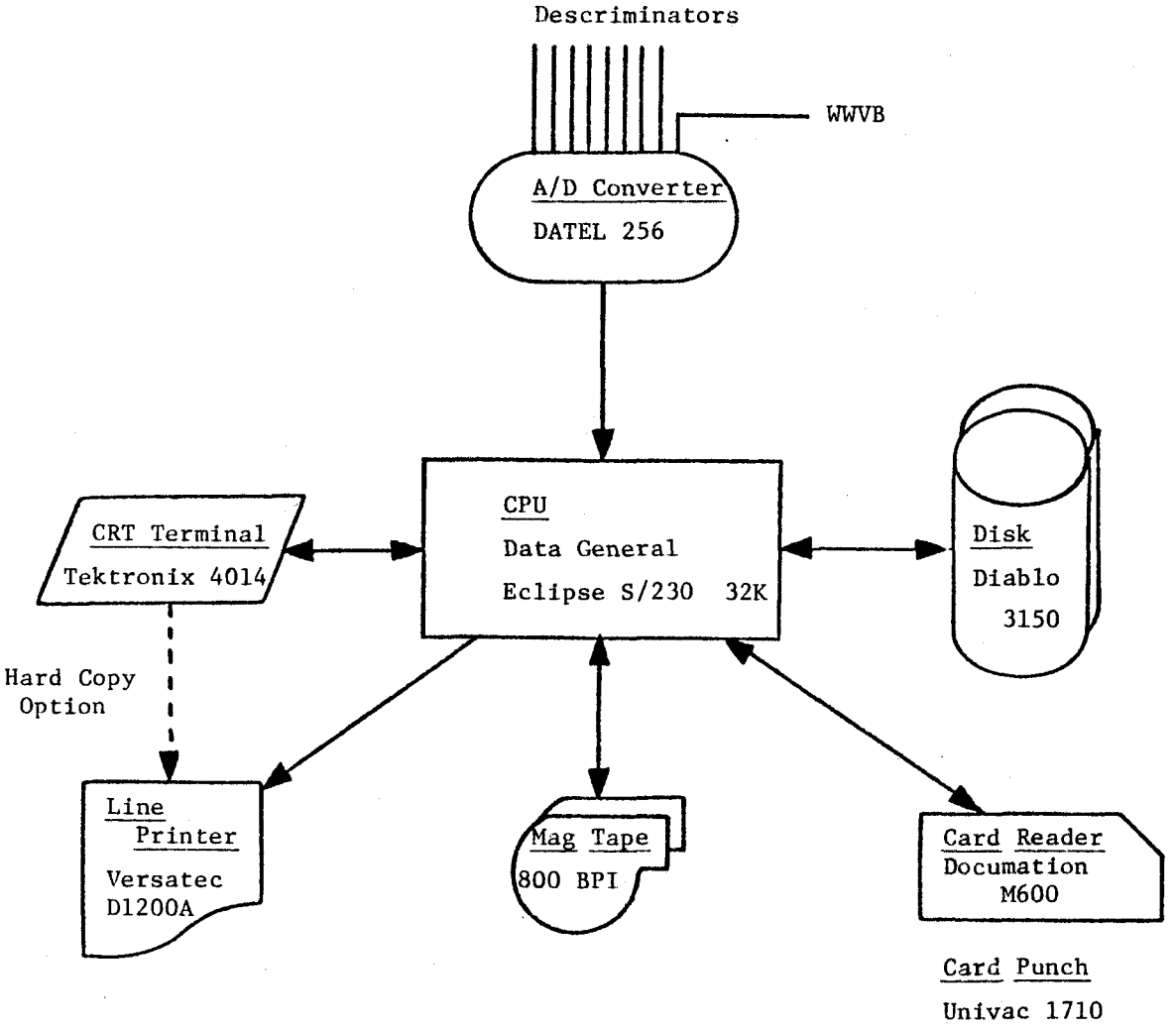

Figure 4. Block diagram showing the relationship between major components of System B.

a Tektronix 4014 with enhanced interactive graphics capability for event timing. The resolution represented by 4096 addressible rasters horizontally appears to be a minimum requirement for accurate timing. The 4014 is a storage tube device with limited refresh capability and an adjustable cross-hair cursor used for arrival time picking.

ROUTINE PROCESSING BEFORE 'CEDAR'

Routine processing is defined, for our purposes, as the collection of activities that accepts as input a set of short period seismograms or seismic signals and has as its principal product an ordered set of earthquake hypocenters called a catalog. In this section we will be discussing the procedures that were employed subsequent to the installation of develocorders and the concomitant increase in the number of stations being recorded. Before the development of the CEDAR system routine processing was based on manual methods with the principal data source being the ubiquitous develocorder. Signals from 130 short period, vertical seismometers were recorded on a bank of nine develocorders generating about 3 km of 35 mm film each week. A team of research assistants scanned these films each day while compiling a list of events for possible timing at a later stage. Once all nine films were previewed in this manner the lists were combined and the films remounted for timing of events with more than three impulsive arrivals. Timing consisted of aligning a taut wire hair-line with the WWVB radio code recorded at the top and bottom of the film, measuring the relative times on the viewer screen with a ruler, and then entering the arrival times, qualities, and

durations on a set of forms for later keypunching. The data from various analysts was combined with data read from the fourteen helecorders and nine outside stations for hypocenter calculation on the main campus computer. The resulting locations were reviewed, timing errors were corrected by remounting the develocorder films a third time, and the phase card deck was corrected and rerun. Eventually event summary cards emerged from this process, which were then assembled into a catalog after the calculation of local magnitudes. Although this approach is suitable for small networks, it does not scale well as the number of stations increases.

CEDAR SYSTEM ROUTINE -- AN OVERVIEW

It has been a fundamental goal in setting up automated routine processing procedures to seek an optimal partition between those functions best suited to machines and those that find their best expression in the human condition. Machines, it is felt, are very good at keeping track of things, manipulating data, and presenting data to a human analyst for consideration. The human being, on the other hand, is an incredibly efficient pattern recognizer and synthesizer of experience. The failure to make this partition correctly will result in either substantial inefficiency as a result of continual manual correction of machine inadequacies or a system that is so complex as to defy understanding.

Routine processing under the CEDAR system is divided into four stages. These are data acquisition, pre-timing analysis, timing and preliminary analysis, and retiming and final analysis. Table 1

TABLE 1

PROCESS STAGE	INPUT	
1. Acquisition (1 Month)	1. Analog Seismic Signals 2. Analog WWVB 3. Network Configuration File	1. Digital Event Tape
2. Identification (2 weeks)	1. Digital Event Tape	1. Plot of triggered stations 2. Decoded WWVB File
3. Timing and Preliminary Analysis (2 months)	1. Digital Event Tape 2. Decoded WWVB File 3. Station Change File 4. Station data (latitude, longitude, delays)	1. Archival Event Tape 2. Preliminary Event Summary Tape (PEST) 3. Preliminary Location Listings 4. Preliminary Event Summary Cards
4. Final Analysis (12 months)	1. Preliminary Event Summary Tape 2. Timing and Amplitudes from non-digitized stations 3. Rereads 4. Station data	1. Final Event Summary Tape 2. Final Location Listings 3. Final Event Summary Cards

summarizes this process.

Data acquisition is an unattended process running on the off-line computer. Incoming data are first digitized and then analyzed by an event detection algorithm. Data are saved on magnetic tape in digital form for all stations whenever an event is detected anywhere in the network. This stage is roughly analogous to the first pass through of the develocorder films discussed above in that subsequent consideration is confined to that portion of the data stream that has been deemed seismic. The remaining three stages make use of the off-line computer. The second stage, pretiming analysis, is also unattended. During this stage radio time is decoded and plots are made of all triggered stations for the purpose of separating seismic events from false triggers. In the third stage an analyst times all relevant arrivals and subsequently runs a program that calculates preliminary locations. Obvious blunders can be corrected at this time. The products of stage 3 are an Archive Digital Event Tape (ADET) which is similar in format to the raw digital event tape with false triggers and non-recording stations deleted, a Preliminary Event Summary Tape (PEST) containing all event timing data, and a preliminary catalog. This catalog can generally be kept current to within two to three days to support the timely analysis of current seismicity. The fourth stage is delayed by several weeks until seismograms from the sparse array of Wood-Anderson torsion seismometers become available. During this stage any necessary retiming is combined with data for stations that are not recorded on-line. Final locations are run with a consistant set of assumptions; magnitudes are calculated

automatically from Wood-Anderson readings and coda amplitudes, quarry blasts are flagged, and a final catalog is produced. In the next four sections the stages of routine processing are discussed in detail.

STAGE 1 - DATA ACQUISITION

The heart of the CEDAR system is the seismic event detector running in real-time. It must be conservative since any events that it lets pass are essentially gone forever. On the other hand, if it is too conservative it will flood later stages of processing with false triggers generating considerable inefficiency. It is necessary to strike a balance between these two extremes. Techniques for fine tuning the response of the event detector are discussed in Chapter 3. There are two levels of analysis in the detection algorithm. The first is concerned with the circumstances causing a single station to enter a triggered state; the second involves the spatial distribution of simultaneously triggered stations that can cause a network trigger and subsequent dump of all data for all stations to digital magnetic tape.

The basic approach to single station detection is an extension of the method of comparing a short term and a long term average (e.g., Ambuter and Solomon, 1974). Five functions of the incoming seismic data control the trigger condition of a single station. They are

$$\overline{S}_i = 1/256 \sum_{j=0}^{255} S_{i+j} \qquad (1)$$

$$\overline{\overline{S}}_i = 1/8\ \overline{S}_i + 7/8\ \overline{\overline{S}}_{i-334} \qquad (2)$$

$$\bar{r}_i = 1/256 \sum_{j=0}^{255} |S_{i+j} - \bar{\bar{S}}_{i-334}| \qquad (3)$$

$$\bar{\bar{r}}_i = 1/8\ \bar{r}_i + 7/8\ \bar{\bar{r}}_{i-334} \qquad (4)$$

and

$$\varepsilon_i = \bar{r}_i - 3/2\ \bar{\bar{r}}_{i-334} - |\bar{\bar{S}}_{i-334} - \bar{S}_i| - 8 \qquad (5)$$

where S_i is the i^{th} digitized sample. The values of these functions can be interpreted as a short term average, a long term average, a short term rectified average, a long term rectified average, and an instantaneous trigger condition respectively. A station is said to be in a triggered state if "ε" has been positive within the preceding 30 seconds. With our current sampling rate of 50 Hz, $\bar{S}_i$ and $\bar{r}_i$ represent 5.12 second averages. The corresponding long term averages are calculated recursively with an exponential time constant of just over 45 seconds. Without the last two terms equation (5) would simply require the short term rectified average to exceed the long term rectified average by 50 percent for a single station trigger. The third term desensitizes the triggering threshold so that one sided pulses, common on telephone line telemetry due to line switching transients and high amplitude single sample A/D glitches, do not trigger the system. Both of these problems are particularly severe since they frequently affect groups of neighboring stations simultaneously. The fourth term in equation (5) prevents quiet stations from triggering excessively. The above calculations (including triggering decisions) require 334 digitization intervals (6.68 seconds). Intervening values, though formally defined, are not calculated.

The second level of analysis reduces the number of false triggers due to spurious noise bursts by requiring a fixed number of nearby stations to be in a triggered state simultaneously. This has been implemented in Southern California by breaking the network up into 20 substantially overlapping sub-networks of between 12 and 20 stations each. Figure 5 shows the distribution of stations making up the sub-network responsible for detecting events in the zone of San Fernando aftershocks and that portion of the San Andreas fault running from Gorman to Palmdale. The magnitude thresholds shown in this figure were calculated by the methods discussed in Chapter 3. A given station generally participates as an element in several sub-networks. A particularly good station in a sparse region of the network is occasionally included in the same sub-network twice. This in effect gives it "two votes" in the detection logic. A sub-network enters a triggered state whenever a fixed number of its constituent stations are simultaneously triggered. The network as a whole enters a triggered condition and the dumping of digital data to tape occurs whenever any sub-network enters a triggered state.

The critical detection parameters and the distribution of stations among the various sub-networks is determined by a disc file (Network Configuration Deck) that is read and analyzed when the system is initiated. It is our intention to allow sufficient flexibility to accommodate the range of station density and geographical distribution for most regional short period networks. Currently, modification of the network configuration requires a temporary switchover to system B, although there are clear advantages to providing for dynamic, inter-

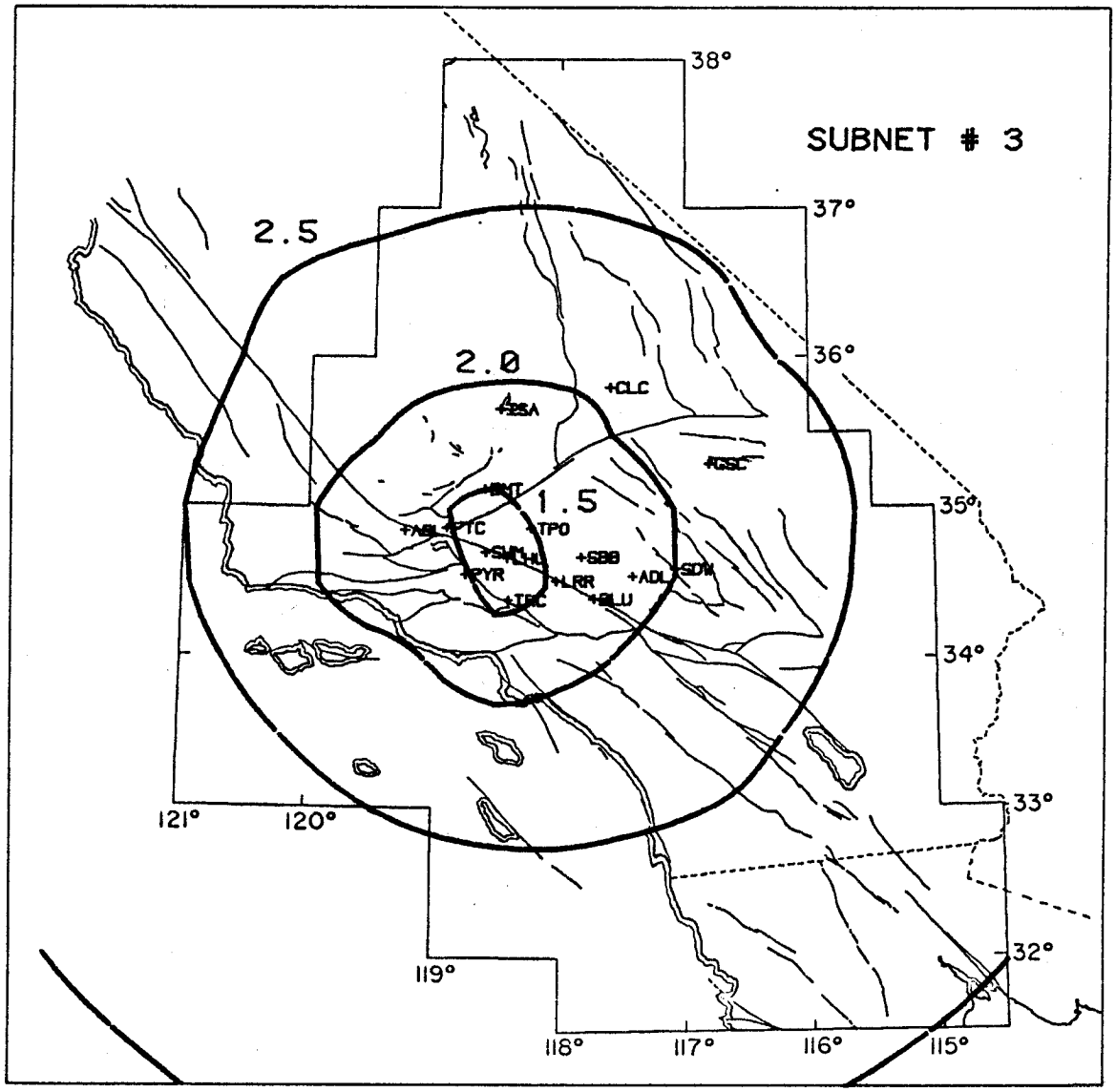

Figure 5. Station configuration comprising subnetwork No. 3 in the CEDAR system detection logic. Magnitude contours represent 90th percentile thresholds as calculated in Chapter 3.

active reconfiguration of the network detection logic.

Several blocks of data are written to the raw digital event tape ahead of the digitized seismic data. This includes a block containing a "snapshot" of the detection logic at the time the triggering decision was made and a 70 second section of digitized WWVB radio time code. In addition, each record of digitized data contains a 32 bit clock count updated from the real-time clock. This count permits the recovery of accurate absolute timing from preceding or following triggers if the digitized time code for the current trigger is undecodable.

The decision to stop dumping digital data to tape turns out to be a somewhat more difficult problem than deciding when to trigger. Currently the algorithms "detrigger" whenever a network triggered state exists for more than 30 seconds without any sub-network being in a triggered condition. It turns out that this tends to prematurely truncate the codas of large events, a problem that will certainly be mitigated in the near future. A complete, general, and essentially computer independent discussion of the implementation details of the CEDAR event detection algorithm is provided in Appendix I.

STAGE 2 - PRETIMING ANALYSIS

The function of this stage of analysis is to separate events from triggers caused by noise. Currently the detection logic is set up so that a false alarm rate of between 50 and 60 percent is realized. To accomplish this function the raw digital event tape produced in the preceding stage is read and the seismograms from all triggered stations are

graphed together on a matrix printer/plotter. An example of this output for an event occuring near the San Jacinto fault is shown in Figure 6. The "snapshot" of the detection logic preceding each event trigger is printed out in tabular form. The listing includes the short term averages, biases, noise levels, and number of unsupported triggers for all stations of the network. This information is useful in recognizing flaws in the network detection logic as well as for discovering problems with performance of individual stations. In addition the block of digitized WWVB time code is decoded and any required time interpolation is accomplished. A check is made to insure that the decoded time is correct and consistent for all events on the tape. The absolute times of the first sample of each event is saved on a disc file (P-FILE) for later combination with relative arrival times during the next processing stage.

STAGE 3 - TIMING AND PRELIMINARY ANALYSIS

Event timing represents the first point of strong interaction between man and machine. Eventually it is expected that part of this interaction can be replaced by P-picking algorithms such as those discussed by Anderson (1978) and Allen (1978). Even then the final arbiter will probably be a human analyst. For now we will use the computer to organize and present data to the analyst utilizing the simplest interactive procedure we can devise. Data are displayed on a vector CRT and the analyst picks and identifies each arriving phase using an adjustable cross-hair cursor. The machine subsequently is charged with calculating precise arrival times, storing these times

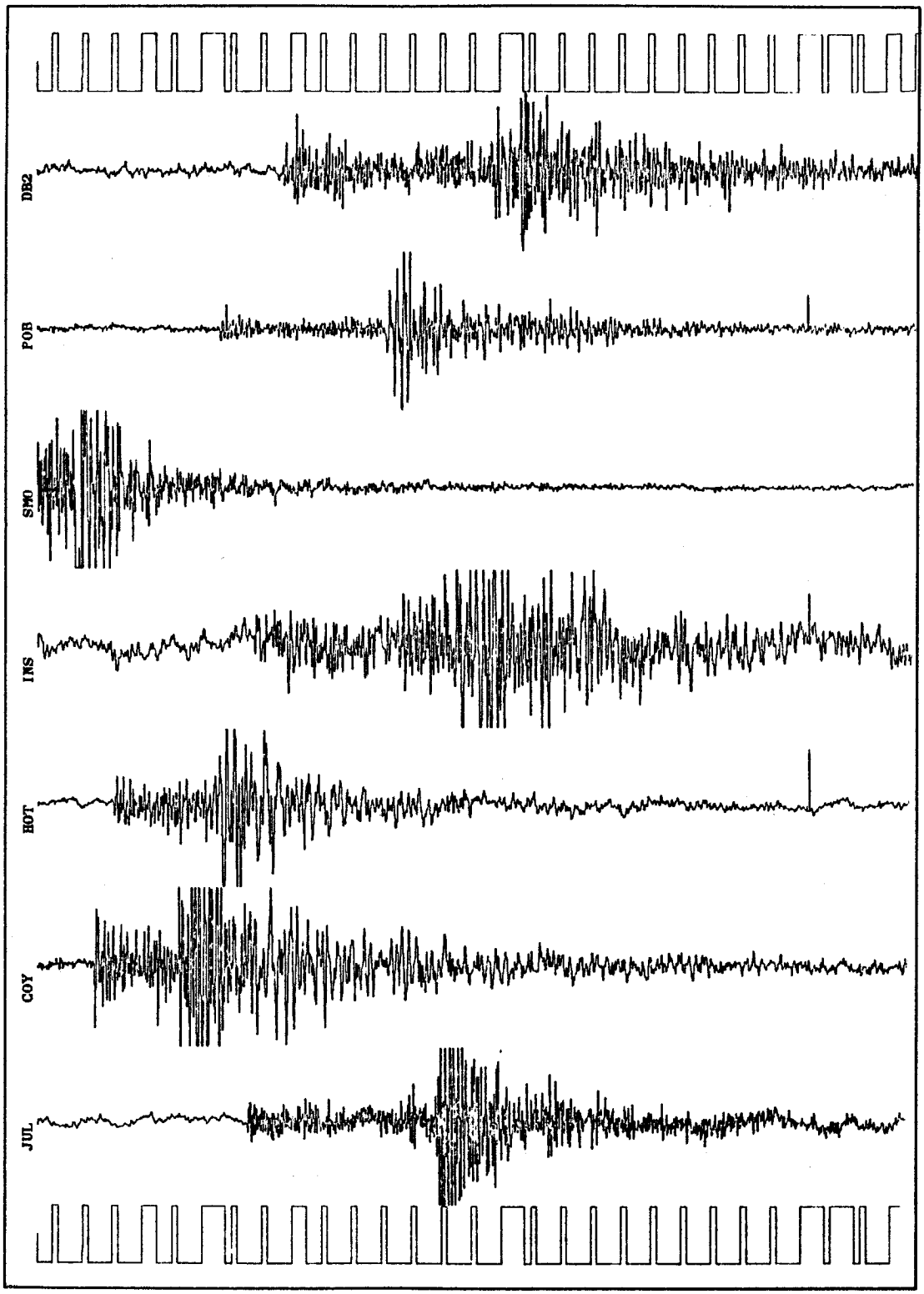

Figure 6. Typical output of the program PRESCAN.

for later location calculations and generally making sure that a particular datum once generated is preserved.

In detail, event timing is accomplished by remounting the raw digital event tape and then timing all identifiable major phases for each of the events recognized during Stage 2. For each event the timing process is organized into two passes through the stations of the network. During the first pass all stations are displayed as shown by the CRT image in Figure 7 so that the analyst can select portions of record for closer analysis. Although Figure 7 shows only ten traces, the stations are generally viewed 30 to 60 at a time at the operator's discretion. Each trace can be selected for more detailed analysis, flagged as seismic but untimeable, or ignored. In the latter case the data for the particular station are discarded at the end of Stage 3.

During the second pass stations selected as timeable are displayed singly as shown in Figure 8. The seismogram is displayed on the lower 9^{th} of the screen with a contracted time scale so that the various phases can be viewed in context. Any portion of this trace can be expanded by a factor of eight into a high resolution work space occupying the top 8/9 of the screen. Timing and phase identification is accomplished on that portion of the seismogram displayed in the work space using the cross-hair cursor. In Figure 8 both the P and S arrivals are clearly visible on the upper trace. In Figure 9 a section of WWVB ratio time code is displayed in the same manner as the seismogram in Figure 8 to illustrate the relative time scales and the timing accuracy that can be obtained. The rising edges of this code

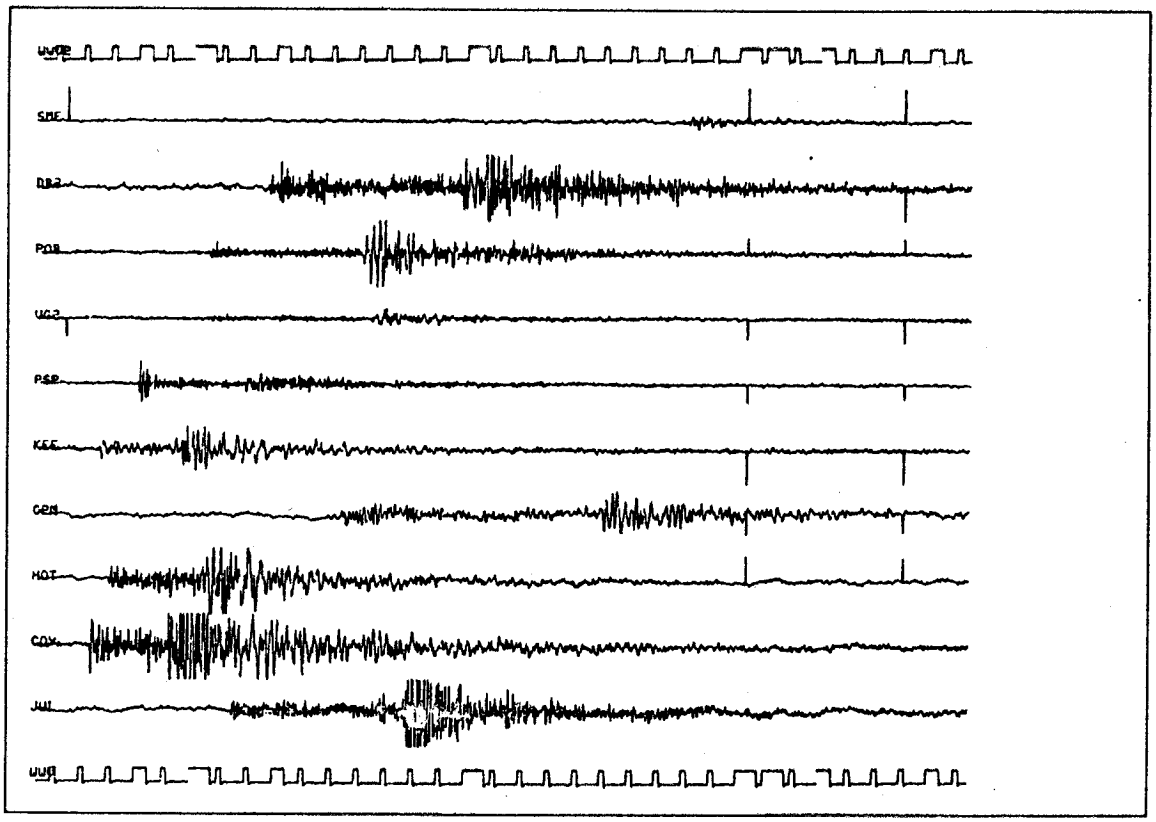

Figure 7. Typical CRT screen image from the first pass of the event timing program (SCANZ). This display is repeated until all stations have been examined. Digitized WWVB time code is shown as the top and bottom traces. Rising edges mark each second.

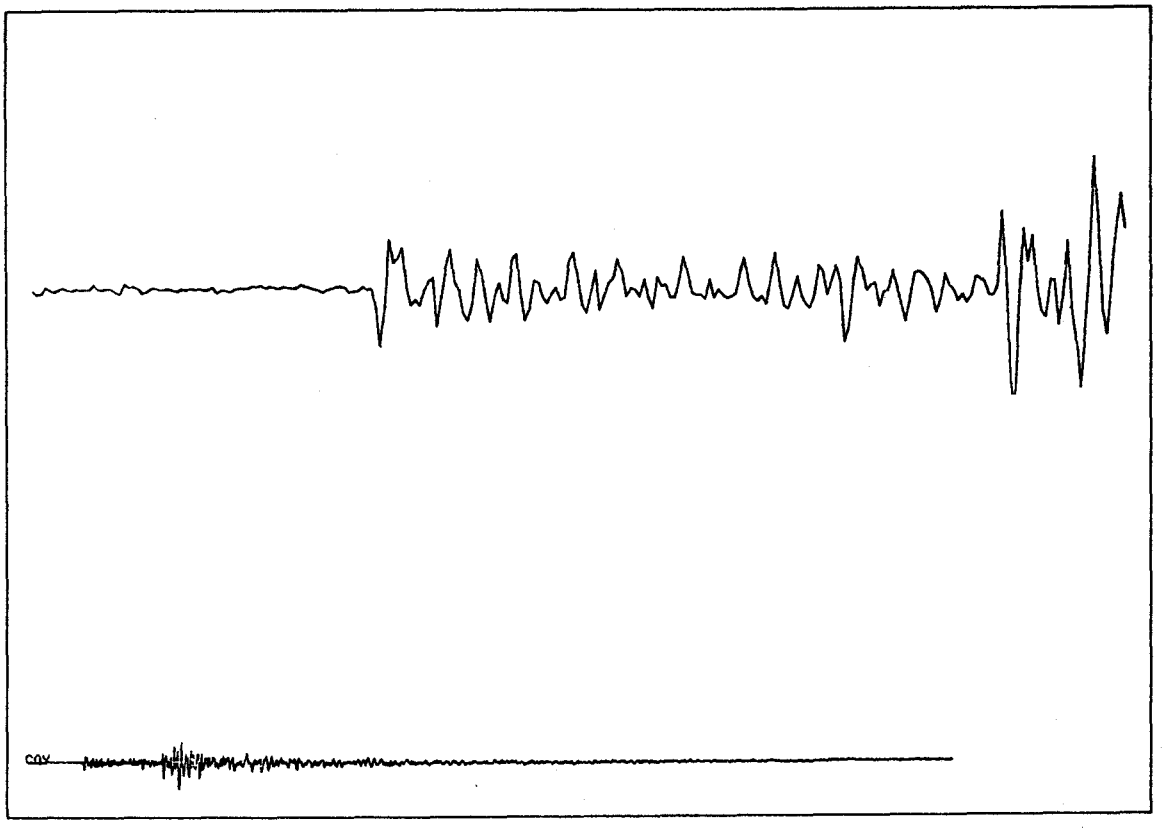

Figure 8. Typical CRT screen image from the second pass of the event timing program (SCANZ). The station, COY, shown in this example can also be seen in Figure 7.

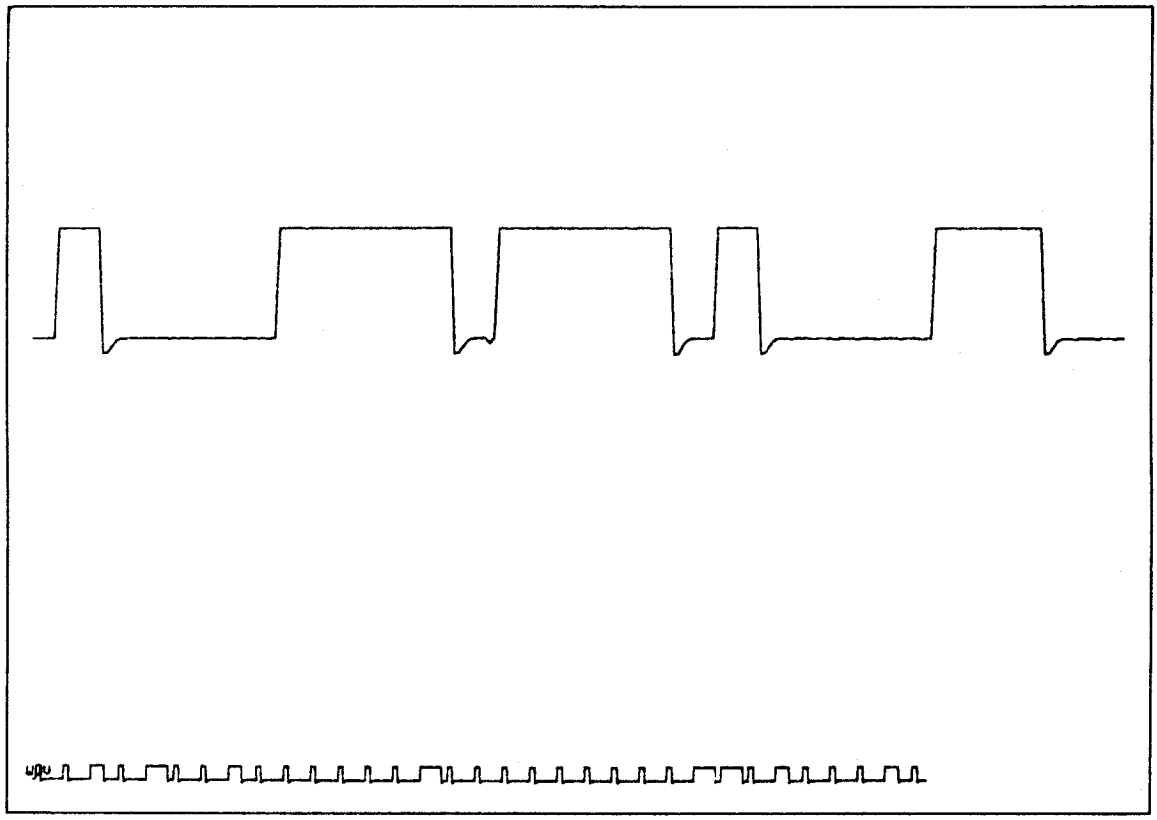

Figure 9. Typical CRT screen image from the second pass of the event timing program (SCANZ). Digitized WWVB time code is displayed in the same manner as seismic data in order to illustrate the degree of timing precision that can be obtained.

are one second apart. For impulsive arrivals timing accuracy comparable with the sampling interval of .02 seconds is routine.

Once all of the events on a tape are processed in this manner, the relative times are combined with the WWVB times calculated during Stage 2 to obtain absolute arrival times, any changes in A/D line assignment since the initialization of the on-line system are incorporated, and preliminary locations are calculated. This provides the analyst with information relevant to picking procedures at a time when memories of the stations encountered are still fresh. If necessary corrections can be entered at this time. Summary cards are then punched and incorporated into a preliminary catalog.

Stage 3 is concluded by copying all traces identified as being seismic to an Archival Digital Event Tape together with the data blocks from Stage 2 and the phase picks generated above. The Archival Digital Event Tape is in the same format as its predecessor and can be processed in the same manner starting with Stage 2. Once the integrity of the Archival Digital Event Tape is verified, the original tape is recycled. The Archival Digital Event Tape is then processed by a program that extracts the timing data and calculates coda amplitude averages to produce a Preliminary Event Summary Tape for analysis during the final stage of routine processing. At present the data on the Archival Digital Event Tape are unmodified beyond this point.

STAGE 4 - RETIMING AND FINAL ANALYSIS

The final stage is also highly interactive. The main software tool consists of a system of programs that facilitate the manipulation

of the event data base read from the Preliminary Event Summary Tape. These programs implement a simple command language that allows for the addition, modification, or deletion of arrival time data and amplitudes, the interactive location of events using a variety of velocity models and station delay assumptions including master event techniques, and the calculation of magnitude by several different methods. Events having problems with the original timing are reread and the corrected arrival times are re-entered together with times and amplitudes from photographic stations, helecorders, and adjacent networks. Most events are assigned a magnitude, M_{ca}, based on the coda averages calculated during Stage 3 using the method discussed in Chapter 2. For larger events the peak trace amplitudes obtained from Wood-Anderson torsion seismometers are used to calculate value of M_L (Richter, 1958). Summary cards produced during the calculation of final locations replace the preliminary ones in the Southern California catalog. All locations are calculated by a program based on the generalized inverse method as formalized by Wiggins (1972). Finally an updated Final Event Summary Tape (FEST) is produced and saved for later research.

SUMMARY OF EXPERIENCE

The underlying philosophy in the design of the CEDAR system was the maintenance of maximum flexibility at each stage of the development. Although the starting point (analog seismic signals) and the ultimate goals (precisely timed arrivals and an accurate and complete earthquake catalog) were well defined, we had in the beginning no overall plan

for the details of the final systems configuration. In fact, we lacked a clear understanding of how the various tasks themselves, such as timing and catalog preparation, should be organized. Each of the four stages was completed before the next was fully conceived. Ordinarily the rejection of modern principles of systems design would doom a moderately complex undertaking to failure. By carefully avoiding situations that would tend to circumscribe subsequent tasks we were able to avoid this pitfall. Considering the limited personnel available for design and implementation it is difficult to see how the problem could be approached in any other way.

One of the most serious lessons acquired during the development process was that there is a considerable gulf between implementing the parts of a system and assembling these parts into a workable whole. The basic elements of displaying seismograms, locating earthquakes, and assembling catalogs are not particularly difficult. Putting these pieces together into an efficient system that appears sensible to those who must work with it on a daily basis, some of whom may not be sophisticated with respect to the use of modern computers, is quite a different matter. The difficulty in bringing the basic elements together was grossly underestimated at the outset. It is likely that had a more precise awareness been available, the project would not have been undertaken at all.

From an operational point of view, the CEDAR system must be considered highly successful. We are currently locating ten times more events and picking nearly thirty times more arrivals than five years ago with an operational staff that has not increased in size.

In addition, considerably more attention can be devoted to analysis and understanding than was previously relegated to the routines of catalog compilation. Such a situation is not always the result of the computerization of a previously manual operation.

At present we are able to maintain an awareness of regional seismicity that is far more current than was possible in the recent past. Generally an event is timed and located within a day or two of its occurrence. This has the benefit of making routine processing far more interesting for those involved, as there is an aura of excitement about yesterday's earthquakes that dims with the passing years. A preliminary catalog can be assembled for analysis with a delay that seldom exceeds one week. While we are monitoring all manner of geophysical data for clues to the problems of earthquake prediction, the importance of a timely knowledge of variations in seismicity can hardly be exaggerated.

The daily workload, plotted in Figure 10 as the number of detected events, currently averages about 20 earthquakes each day. Occasionally the number of events approaches 1,000. At such times, represented by the peaks in Figure 10, the routine processing falls two to three weeks behind. A distinct change in number of detected events around September 1, 1977 was due to a deliberate sensitization of the detection logic. A general increase in the number of days with high seismicity (peaks in Figure 10) appears to be real. Its significance, if any, is not understood.

One concern early in the project was that a digital system with real-time event detection capability would be of marginal reliability,

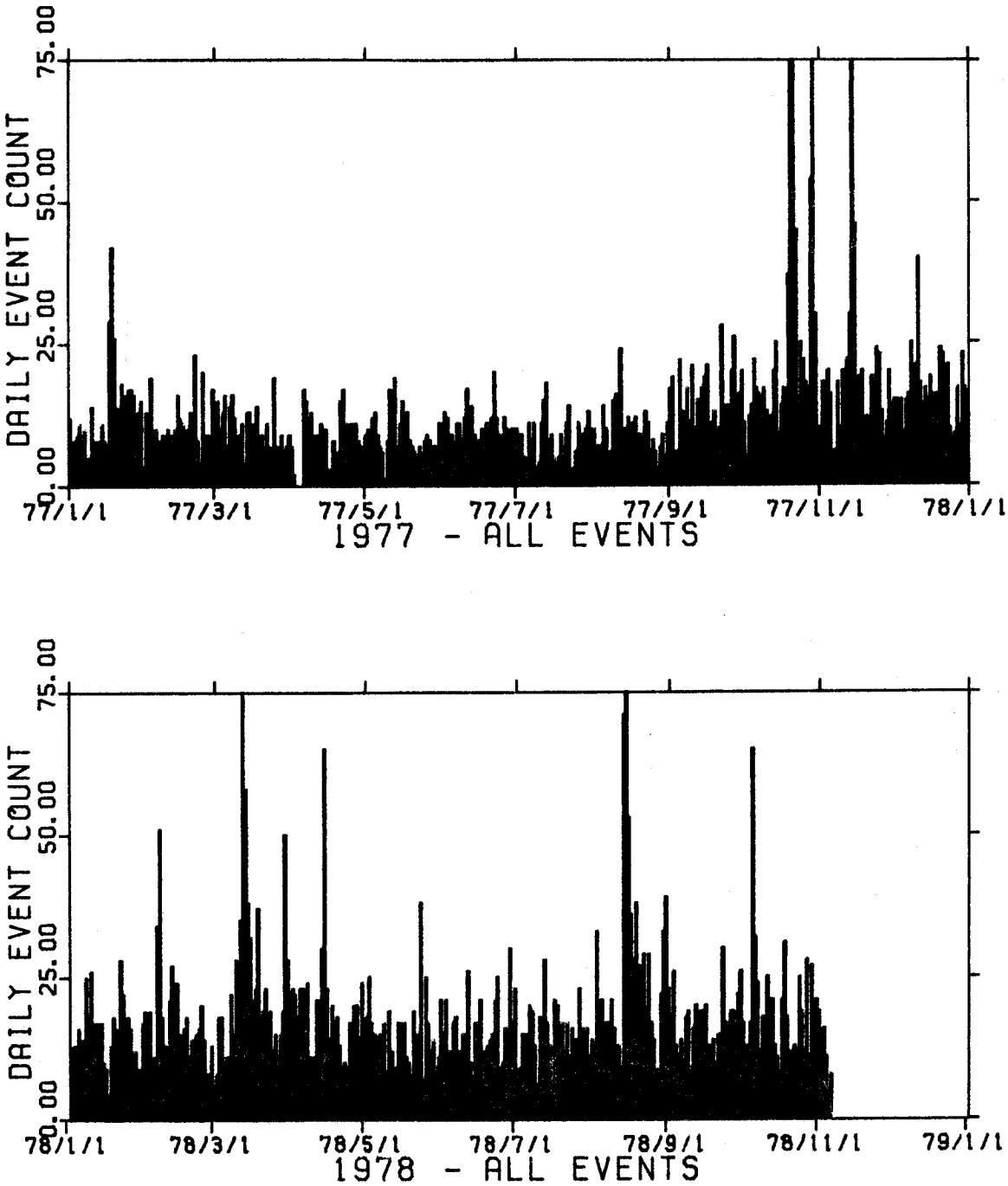

Figure 10. Histogram showing the daily number of events detected, timed, and located by the CEDAR system during 1977 and the first 10 months of 1978. The level increase in September, 1977 corresponds to a sensitization of the detection logic.

especially because of our use of a moving head disc on the on-line system. Such fears now appear groundless. At the time of this writing we have been in continuous operation 24 hours a day for more than 18 months. Occasional equipment failures have not resulted in any loss of data. During periods of scheduled preventive maintenance, network monitoring has been taken over by the off-line system. It must be considered likely that this record exceeds the long term mean time between failures.

On the whole our experience with the development of the CEDAR system and the computer automation of the Southern California network has been a positive one. Still, despite a moderate amount of success, it is clear that considerable improvement is possible.

FUTURE GOALS

As with virtually all endeavors of moderate complexity, hindsight is far sharper than foresight. In this section we discuss the ways in which the CEDAR system implementation might have been different had we known at its inception what we have learned along the way.

The areas most urgently in need of attention are those that have become "bottlenecks" for routine processing. One of these is our current use of a single task operating system on the off-line computer. This insures that nearly all of the available CPU time during the day is wasted. As a result personnel involved in routine processing must work at odd hours in order to complete all required work. Another "bottleneck" derives from the fact that we currently have less than 1 megabyte of scratch disc available on system "B". Since this is

insufficient to store the data for even a single trigger, a considerable amount of "tape jockeying" attends the timing process. In addition, the lack of disc space forced the sequentialization of the processing into a tape oriented approach. It is clear that a vertical integration of the four stages of routine processing could be affected with a considerable increase in efficiency if more disc scratch space were available. This would not only obviate the need of continually remounting the input tape, but would also reduce the time spent copying intermediate results to temporary tapes. In addition, the efficiency of the timing process could be greatly enhanced if the data were preprocessed by a picking algorithm such as the one described by Anderson (1978) or Allen (1978). The machine picks could then be presented to an analyst for review.

Several enhancements to the on-line system seem highly desirable. The addition of a crude picking algorithm on a limited number of stations would greatly increase our ability to respond to public requests for information while not substantially impacting the system throughput. A limited event location capability would be even better. Another enhancement that is nearly essential is the capability of making dynamic changes to the detection configuration interactively, such as disabling a noisy station or changing line assignments, without requiring a complete system initialization. It is hoped that at least a few of these changes can be implemented in the near future.

REFERENCES

Allen, R. V. (1978). Automatic earthquake recognition and timing from single traces, Bull. Seism. Soc. Am., 68, 1521-1532.

Ambuter, B. P. and S. C. Solomon, (1974). An event-recording system for monitoring small earthquakes, Bull. Seism. Soc. Am., 64, 1181-1188.

Anderson, K. R. (1978). Automatic processing of local earthquake data, Ph.D. Thesis, Massachusetts Institute of Technology.

Richter, C. F. (1958). Elementary Seismology, W. H. Freeman and Co., San Francisco.

Stevenson, P. R. (1976). Microearthquakes at Flathead Lake, Montana: a study using automatic earthquake processing, Bull. Seism. Soc. Am., 66, 61-80.

Stevenson, P. R., T. C. Jackson, J. L. Hobson, R. L. Haken and S. K. Fang (1978). A computer-based processing system for seismic network data (Abstract), Trans. Am. Geophys. Un., 59, 316.

Stewart, S. W. (1977). Real-time detection and location of local seismic events in Central California, Bull. Seism. Soc. Am., 67, 433-452.

Stewart, S. W., W. H. K. Lee and J. P. Eaton (1971). Location and real-time detection of microearthquakes along the San Andreas Fault system in Central California, Recent Crustal Movements, Royal Soc. New Zealand, Bull. 9, 205-209.

Wiggins, R. A. (1972). The general linear inverse problem: implication of surface waves and free oscillations for earth structure, Rev. of Geophys. and Space Phys., 10, 251-285.

APPENDIX I

CEDAR SYSTEM EVENT DETECTOR

The following discussion is primarily intended to be of use to those implementing similar software on other systems. It is assumed that the host computer will have the minimal capabilities of hardware addition and subtraction of 16 bit integers; direct memory access from external devices including disc, magnetic tape, and the A/D converter; and the generation of processor interrupts at regular intervals using a real-time clock. Beyond these requirements the following discussion is kept as machine independent as possible.

Several programming procedures are used for enhanced efficiency. All multiplication and division is done with at least one value that is an even power of the two. This reduces the processes of multiplication and division to word shifting operations. All major movement of data is between I/O devices and memory using DMA techniques with only minor movement of data occurring between internal core buffers. The basic design is such that the work load does not increase substantially when triggering commences. Consequently, if the real-time software works at all, given a particular configuration of the network detection parameters, then it can be expected to function properly when stressed by periods of relatively high seismicity. Each of the five core buffers is roughly 4,000 words in length.

The logic diagram for the CEDAR system event detector is shown in Figure I.1. Processing is distributed between two tasks running in parallel. Task "A" is the higher priority of the two and is entered every sample interval (1/50 second) as a result of system interrupts

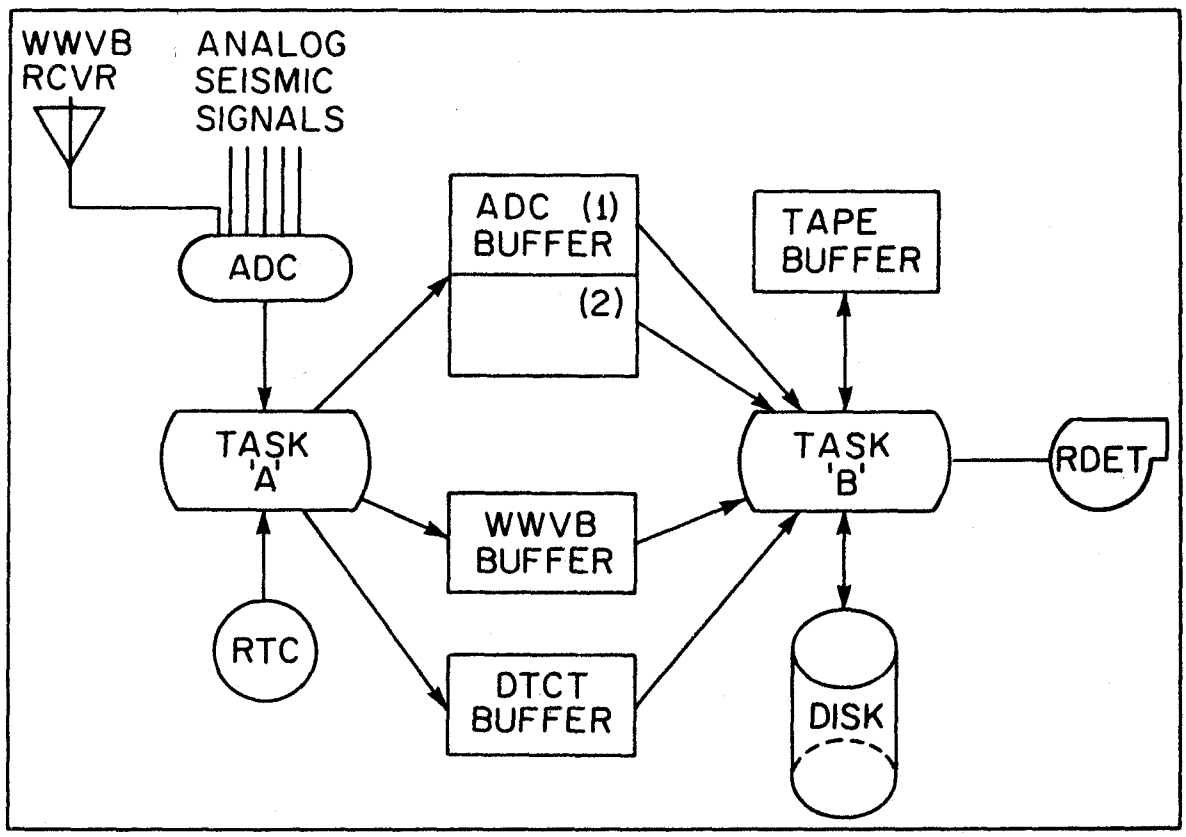

Figure I. 1. Block diagram showing relationship between major tasks and core data buffer comprising the CEDAR system event detector.

generated by a real-time clock (RTC). Its responsibilities are the initiation of a block sample by the analog to digital converter (ADC) and the analysis of the input data stream for local events. It is crucial that Task "A" never utilizes more than one sample interval for its calculations. Task "B" uses the remaining CPU resources not needed by Task "A". Its responsibilities are that of general housekeeping and the orderly transfer of data from core buffers to disc, from disc to core, and from core to magnetic tape. These transfers utilize DMA but do not generate processor interrupts. Instead the status of a particular device is polled occasionally as the various I/O operations progress in parallel. The organization of the real-time processing into two parallel tasks is similar to the system developed and described by Stewart (1977). The remaining discussion deals with the details of the implementation of these two tasks.

The processing in Task "A" can be divided into two operational phases. The first is identical for all sample intervals. It consists of initiating the next conversion by the ADC and the updating of a circular WWVB buffer with the last sample digitized from the channel carrying radio time code. This buffer allows the storage of somewhat in excess of 70 seconds of digitized time code which is adequate, when clean, to permit decoding regardless of where the minute code falls with respect to the ends of the buffer. The A/D buffer is treated as one continuous double length buffer by Task "A". Contiguous vectors of multiplexed digitized data are transferred directly into contiguous "records" by DMA. This buffer is also treated as a circular

buffer. The testing of a status flag located at the beginning of each "record" before initiating the next ADC request insures that Task "B" is keeping up with its processing load.

The second phase of Task "A" implements the event detection logic. The data obtained from the ADC operation initiated during the preceding sampling interval are analyzed at this time. The detection decision is distributed over 334 sampling intervals by a logic sequencer following the steps shown in Table I.1. The column labeled REPT gives the number of sampling intervals for which a given operation is repeated. Hence, the detection decision itself is actually encountered once every 334 intervals. This structure permits the implementation of quite involved algorithms by spreading the necessary calculations over as many sampling intervals as required. The results of all intermediate calculations are stored in the DTCT buffer which is transferred to magnetic tape ahead of the digitized seismic data to provide a "snapshot" of the detection logic at the time that detection occurred. This buffer is initialized from a Network Configuration Deck stored on disc when the real-time system is started. The only communication between Task A and Task B relating to detection is the setting and resetting of a detection status flag by Task A.

Most of the time utilized by Task B is spent monitoring the progress of Task A through the ADC buffer. Whenever processing of one of the halves of this buffer is completed, it is written to a circular buffer on disc. The length of the disc buffer determines the amount of data preceding the event that can be recovered. This buffer

TABLE 1.1

OPER	REPT	FUNCTION
RST	1	Reset the detection logic and calculate trigger thresholds for each station.
P1	256	Accumulate double word sums of the incoming signal and rectified signal for each station of the network.
CAL1	1	Calculate $\overline{S}$ and $\overline{r}$ from the preceding double sums. Update station threshholds to take into account any instantaneous change in DC bias.
P2	1	Check each station to see if $\overline{r}$ exceeds triggering thresholds.
P3	20	Count number of stations triggered in each of the 20 sub-networks. A different sub-network is analyzed during each repetition.
DON	1	Check to see if the condition requiring the initiation of detection exists.
DOFF	1	Check to see if the condition requiring the termination of detection exists.
RTN1	50	Do nothing. This is adjustable time padding that reduces the overall proportion of CPU time required by Task A.
CAL2	1	Calculate $\overline{\overline{S}}$ recursively from its old value and the new short term average, $\overline{S}$, for each station.
CAL3	1	Calculate $\overline{\overline{r}}$ recursively from its old value and the new short term average, $\overline{r}$, for each station.
CD	1	Reset the logic sequencer to the first step (RST).

is organized on the disc in a manner as to minimize head positioning time. Writing is destructive unless a triggered state exists. When a triggered state begins, several things occur before disc writing becomes non-destructive. First the DTCT buffer is copied to the Raw Digital Event Tape (RDET). This block of data is referred to as a "Detection Block". Subsequently the WWVB buffer is transferred to tape providing a "time block". Once these operations are completed, disc output becomes non-destructive and each "data block" is first transferred to the Tape Buffer in core and then to the data tape before being overwritten on disc by new data. Once established, this pattern of processing continues until the triggered condition lapses. When triggering is terminated, a check is made to determine if there is sufficient space on the current tape for another event. If not, the tape unit is placed off-line and the next event is written at the beginning of a new tape on a different tape drive.

CHAPTER 2

A ROBUST METHOD OF MAGNITUDE ESTIMATION SUITABLE FOR LOCAL DIGITAL SEISMIC NETWORKS

INTRODUCTION

An automated magnitude estimation procedure is essential for the efficient operation of a local digital seismic network. For example, in Southern California more than 90% of the earthquakes detected by the CEDAR system event detector (Chapter 1) are smaller than $M_L = 2.5$. Of these, fewer than 5% are situated such as to allow the estimation of local magnitudes, M_L, from the sparse array of 9 sites with Wood-Anderson torsion seismometers or the electronic equivalent. Consequently, one of the most time-consuming tasks in the operation of a digital network is the assignment of magnitude to small events.

The main goal of this study is to develop an efficient means of magnitude estimation for small local earthquakes. We have available the digitized records themselves, so that possible approaches to this problem are manifold. Since we are chiefly interested in small events, it seems likely that we should make use of highest amplitude portion of the record, which is generally that part immediately following the S onset. In order to achieve a smooth transition with other magnitude scales, notably local magnitude, or M_L, we are compelled to examine earthquakes large enough that the initial portion of the S coda is beyond the linear range of the instrumentation. Thus it appears that we must develop a formalism that will allow us to correct the amplitudes from one portion of the S coda to another. There is at present no physically based, simple, deterministic model that can predict the coda amplitudes from the S onset to the later

portions of the coda, although the scattering models developed by Aki (1969), Aki and Chouet (1975) and extended by Sato (1977a, 1977b, 1978) perform remarkably well for times that are long compared to the S travel time.

Our approach to the problem of developing an efficient magnitude estimation procedure can be divided into three tasks. The first task is to develop a systematic relationship that will permit the prediction of amplitudes given the magnitude, distance, and lapsed time from origin time of a particular segment of the post S coda. Presumably this relationship will involve several parameters that vary from station to station so that our second task is to develop a method for calibrating these parameters for the various stations of a seismic network. The third task is to invert the derived amplitude systematics such that a magnitude can be estimated from the coda amplitudes, distance, and relative position within the post S coda.

DATA

The digital seismograms used in this study were recorded by the CEDAR system developed at Caltech. This system, which replaces the develocorder system in function, is described in Chapter 1. In brief, analog signals from 150 stations in Southern California (Figure 1) are telemetered to Caltech using frequency multiplexed telemetry. After discrimination, each signal is digitized at 50 Hz and analyzed by a real-time event detection algorithm implemented on a NOVA 820 minicomputer. Those portions of the

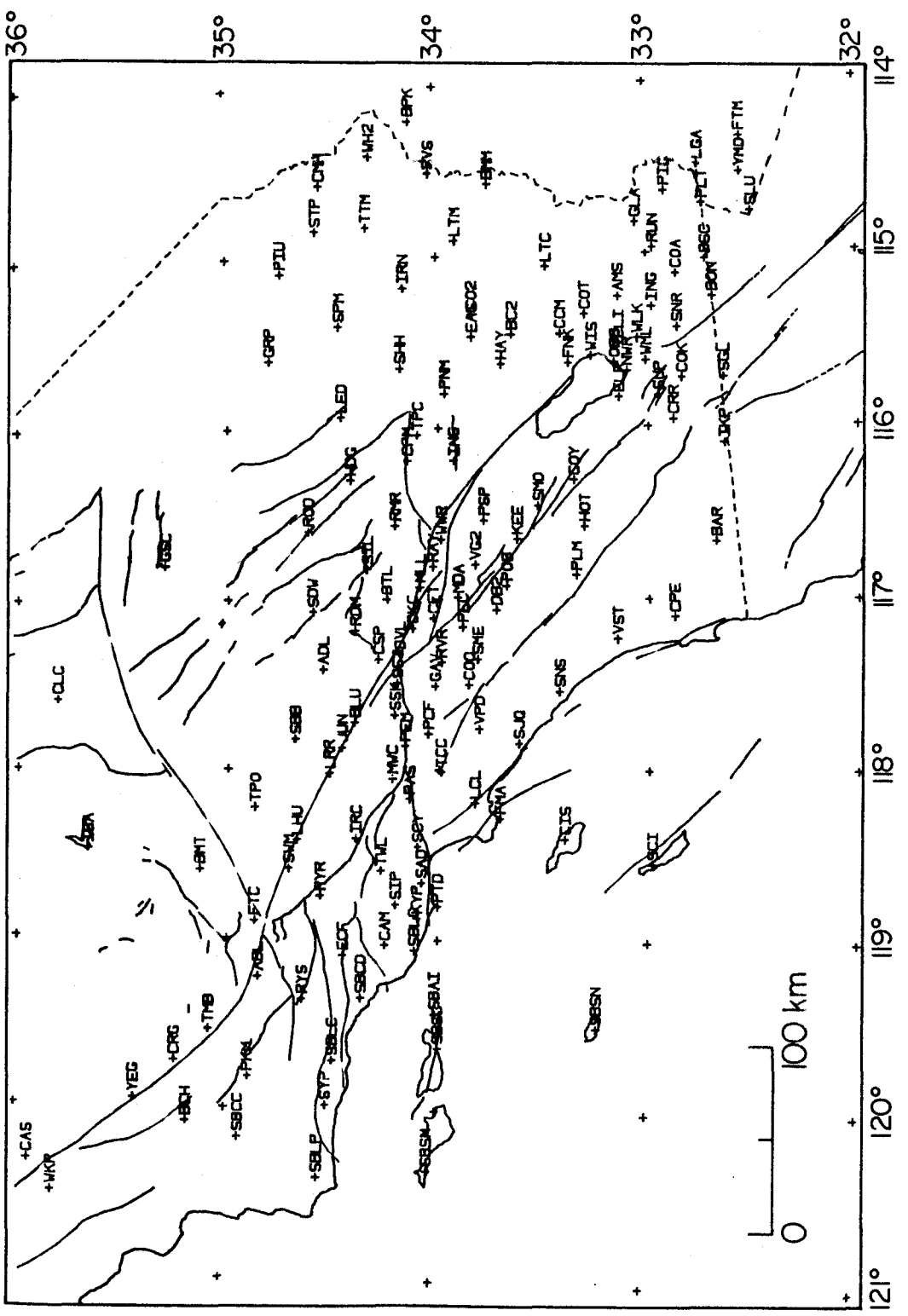

Figure 1. Permanent stations of the Southern California Seismic Network (SCARLET).

digital data stream containing an event are saved on digital magnetic tape for subsequent analysis. Recordings for earthquakes and quarry blasts are separated from false triggers and noise bursts by inspection and saved in an archival data base. Over the course of a year several hundred thousand records are incorporated into these archival files.

As a measure of amplitude of the S-wave coda we have chosen to use the parameter $\overline{r}$ as calculated by the CEDAR system real-time event detector. At a particular time, t_i, referenced to the event origin time, $\overline{r}\ (t_i)$ can be calculated from the digitized seismogram using the expression

$$\overline{r}\ (t_i) = 1/256 \sum_{j=0}^{255} |s_{i+j} - \overline{\overline{s}}| \qquad (1)$$

where $\overline{\overline{s}}$ is the long term DC bias. Since the sampling rate is 50 Hz we are in effect calculating a 5.26 second rectified average.

There are two reasons for adopting this particular definition of coda amplitude. Currently the necessary calculations are being carried out by the CEDAR system event detector in real time. Although the results of these calculations are discarded, with relatively little effort they can be preserved on the digital event tape making the subsequent magnitude estimation procedure far more efficient. Secondly, the use of $\overline{r}$ in the development of the coda amplitude systematics will eventually permit its prediction within the S-coda due to an earthquake of given magnitude and distance. This makes possible the calculation of spatial magnitude detection thresholds as discussed in Chapter 3.

A suite of 85 earthquakes with well known, consistent M_L values was selected for the investigation of the coda amplitude systematics. These events are listed in Table 1 and their epicenters are plotted in Figure 2. Events were chosen with the intention of obtaining a reasonably homogeneous geographical distribution over the Southern California network. The digitized seismograms for these events were then extracted from the CEDAR system archives and calculation of the average coda amplitudes, $\overline{r}$, was performed using equation (1). A typical seismogram recorded at the station RMR is plotted in Figure 3. The vertical bars illustrate the manner in which the post S coda has been segmented into 5.12 s sections.

THE CODA AMPLITUDE SYSTEMATICS

Initially we will assume that there exists some function $a(t,d,M_L)$ that can predict the values $\overline{r}(t_i)$ with sufficient accuracy to support the development of a magnitude estimation technique. For this purpose we will examine the family of functions described by

$$a(t,d,M_L;\ A_o,\ q,t_o,b,c) = 10^{A_o}\ 10^{cM_L}(t-t_o)^{-q}e^{-b(t-t_o)} \qquad (2)$$

where t is the lapsed time from the origin time, M_L is the local magnitude (Richter, 1935, 1958), and d is epicentral distance in kilometers. The remaining constants parameterize a family of functions that is, hopefully, sufficiently general to adequately describe the observed amplitude decay within the post S coda. A_o controls the station gain, t_o is an arbitrary translation in time, and c is a

TABLE 1

HYPOCENTRAL INFORMATION FOR THE "85 STANDARD EARTHQUAKES"
USED IN THE INITIAL NETWORK CALIBRATION

Year	Month	Day	Hour	Min.	Sec.	Latitude	Longitude	Depth	M_L	M_{CA}
1977	6	7	4	36	9.05	33 51.35	116 16.69	0.13	2.6	2.6
1977	6	7	6	41	36.55	32 20.07	115 6.56	5.00	3.0	2.9
1977	6	7	9	45	39.35	33 54.61	117 40.66	5.64	2.2	1.9
1977	6	10	12	31	31.92	34 3.81	117 49.15	3.78	2.0	2.2
1977	6	11	14	18	20.49	34 22.82	118 37.14	5.00	3.2	3.4
1977	6	11	14	53	40.04	34 22.57	118 36.57	5.94	2.8	2.7
1977	6	13	3	17	44.86	34 10.59	116 20.30	0.95	2.8	2.8
1977	6	13	3	19	36.89	33 51.95	118 38.41	5.00	2.8	2.9
1977	6	14	1	56	33.59	34 1.10	118 18.90	5.06	2.8	2.8
1977	6	14	3	54	19.82	34 12.73	117 16.73	5.31	2.4	2.6
1977	6	16	15	36	24.48	34 6.62	116 59.59	4.40	2.5	2.7
1977	6	19	13	56	11.62	35 10.90	118 35.78	8.61	2.7	2.5
1977	6	20	16	38	1.04	32 46.29	115 27.49	16.62	2.4	2.6
1977	6	21	21	54	11.92	32 49.67	118 17.50	5.00	2.9	3.1
1977	6	22	3	54	3.65	34 16.54	116 19.63	2.99	2.6	2.6
1977	6	22	22	4	8.20	32 45.31	118 19.09	4.96	3.2	3.3
1977	6	23	7	12	51.50	33 15.74	116 0.32	5.04	3.2	3.1
1977	6	26	13	40	26.64	32 19.27	115 5.21	6.54	2.7	2.8
1977	6	27	20	59	43.44	34 6.53	117 57.59	11.72	2.9	2.7
1977	6	29	13	58	25.35	33 34.89	117 37.03	5.00	2.5	2.6
1977	6	30	1	7	29.43	34 13.41	117 26.63	8.69	2.4	2.2
1977	6	30	2	48	21.00	33 35.23	117 36.99	5.00	2.2	2.2
1977	7	2	1	22	37.68	33 37.68	116 42.80	12.60	2.9	3.0
1977	7	3	20	51	28.00	35 5.01	119 1.86	5.00	2.6	2.6
1977	7	6	2	18	9.95	35 15.76	118 34.08	5.89	2.6	2.5
1977	7	7	14	21	2.28	35 39.50	120 33.56	5.00	3.2	2.9
1977	7	8	9	49	48.00	35 59.06	120 16.50	4.92	3.2	3.1
1977	7	8	17	1	2.10	35 49.28	117 49.67	5.12	2.4	2.5

TABLE 1 (continued)

Year	Month	Day	Hour	Min.	Sec.	Latitude	Longitude	Depth	M_L	M_{CA}
1977	7	8	17	38	24.77	35 58.89	117 50.13	5.19	2.7	2.7
1977	7	9	30	22	41.79	33 27.41	118 1.89	5.07	2.4	2.5
1977	7	11	6	13	46.34	35 43.50	116 27.60	5.04	3.7	3.5
1977	7	11	11	42	8.75	35 51.66	116 31.51	3.38	3.4	3.3
1977	7	12	15	0	10.13	35 15.66	118 33.69	5.47	2.8	2.7
1977	7	12	18	55	12.06	33 22.63	118 25.98	5.00	2.9	2.9
1977	7	13	8	12	48.55	33 59.93	116 49.83	10.45	3.0	2.9
1977	7	16	5	1	6.91	33 40.40	116 48.17	5.02	2.9	2.8
1977	7	20	22	17	34.88	34 0.02	116 49.62	10.41	2.8	2.8
1977	7	21	18	4	30.68	34 9.31	116 42.96	1.99	2.6	2.7
1977	7	21	18	4	110.94	34 21.76	117 4.44	5.75		1.8
1977	7	22	5	11	3.24	36 20.58	117 1.02	5.00	3.0	2.7
1977	7	26	21	42	18.54	35 50.53	120 12.53	5.00	3.7	3.6
1977	7	28	6	15	29.53	34 16.14	120 37.93	5.21	3.5	3.3
1977	7	30	10	25	3.24	32 52.00	115 46.61	16.31	3.2	2.9
1977	8	3	0	47	15.24	34 35.82	120 37.32	4.97	3.4	3.3
1977	8	3	1	2	47.91	32 54.18	115 32.02	16.02	2.5	2.7
1977	8	3	22	8	33.73	33 49.64	118 8.35	10.86	2.5	2.8
1977	8	5	0	47	43.36	33 20.95	116 15.49	5.03	3.0	2.7
1977	8	6	12	22	52.35	33 21.14	116 22.17	13.22	2.9	2.6
1977	8	8	6	36	15.36	33 56.72	116 44.43	6.20	2.5	2.6
1977	8	8	22	26	9.67	33 17.88	115 41.91	4.41	2.8	2.9
1977	8	9	21	14	10.08	34 14.43	117 4.83	1.45	2.4	2.7
1977	8	11	9	27	25.18	34 25.75	117 1.31	4.99	2.6	2.8
1977	8	12	0	58	30.25	33 45.60	116 10.92	5.00	3.0	3.1
1977	8	12	2	19	26.08	34 22.78	118 27.52	9.50	4.5	4.5
1977	8	12	2	51	40.67	34 22.63	118 28.20	11.37	3.0	2.7
1977	8	12	4	41	38.60	34 22.87	118 26.95	5.00	3.1	3.2
1977	8	12	7	17	51.71	35 35.50	118 23.01	5.00	2.6	2.3
1977	8	13	11	31	9.01	32 40.19	116 5.69	13.74	3.1	3.1
1977	8	14	1	4	6.54	33 45.69	116 10.82	6.44	2.8	2.8

TABLE 1 (concluded)

Year	Month	Day	Hour	Min.	Sec.	Latitude	Longitude	Depth	M_L	M_{CA}
1977	8	14	22	25	25.12	34 24.58	116 56.04	2.61	2.5	2.4
1977	8	15	2	5	41.21	35 45.89	118. 1.72	5.76	2.9	2.8
1977	8	15	22	14	13.80	34 14.59	117 4.86	4.06	2.6	2.7
1977	8	16	14	41	38.85	35 41.54	118 38.84	5.00	3.2	3.1
1977	8	17	3	21	41.58	35 8.16	118 57.73	5.02	3.5	3.5
1977	8	18	1	55	26.39	32 50.65	115 24.52	4.51	2.7	3.1
1977	8	21	6	22	28.55	34 49.50	117 28.46	7.45	2.8	2.6
1977	8	24	8	2	39.42	34 25.09	116 40.90	4.04	2.6	2.6
1977	8	24	15	26	10.84	34 6.88	117 18.46	15.39	2.4	2.2
1977	8	25	18	51	3.92	34 28.29	118 41.41	5.63	2.5	2.5
1977	8	26	18	11	53.60	34 28.11	118 41.38	5.48	2.3	2.2
1977	8	29	14	30	45.14	33 49.57	117 50.30	5.57	2.3	2.6
1977	9	3	21	46	56.24	35 25.57	119 21.20	6.08	2.8	2.7
1977	9	4	2	21	31.61	34 14.79	117 28.33	10.97	2.4	2.2
1977	9	6	5	8	40.51	34 27.95	117 57.93	7.25	2.8	2.7
1977	9	6	22	13	4.17	34 25.34	118 24.93	9.73	2.6	2.4
1977	9	7	7	21	16.01	34 23.77	116 47.94	5.95	2.4	2.4
1977	9	8	0	42	16.89	34 9.23	116 43.13	1.71	2.9	2.9
1977	9	9	1	14	8.98	35 8.11	118 40.53	5.85	2.7	2.3
1977	9	10	18	44	54.00	34 2.95	118 59.37	9.54	2.5	2.5
1977	9	10	20	21	36.09	34 2.66	118 59.42	5.10	2.5	2.4
1977	9	12	6	17	42.56	34 13.06	116 58.96	5.00	3.3	3.2
1977	9	12	12	14	2.28	34 53.17	116 41.97	4.99	3.0	3.1
1977	9	12	13	59	22.28	35 37.52	117 31.49	4.28	2.8	3.0
1977	9	14	21	35	23.28	33 52.92	117 48.69	2.15	2.9	2.8
1977	9	15	2	22	5.12	33 50.02	117 6.47	14.93	2.4	2.1

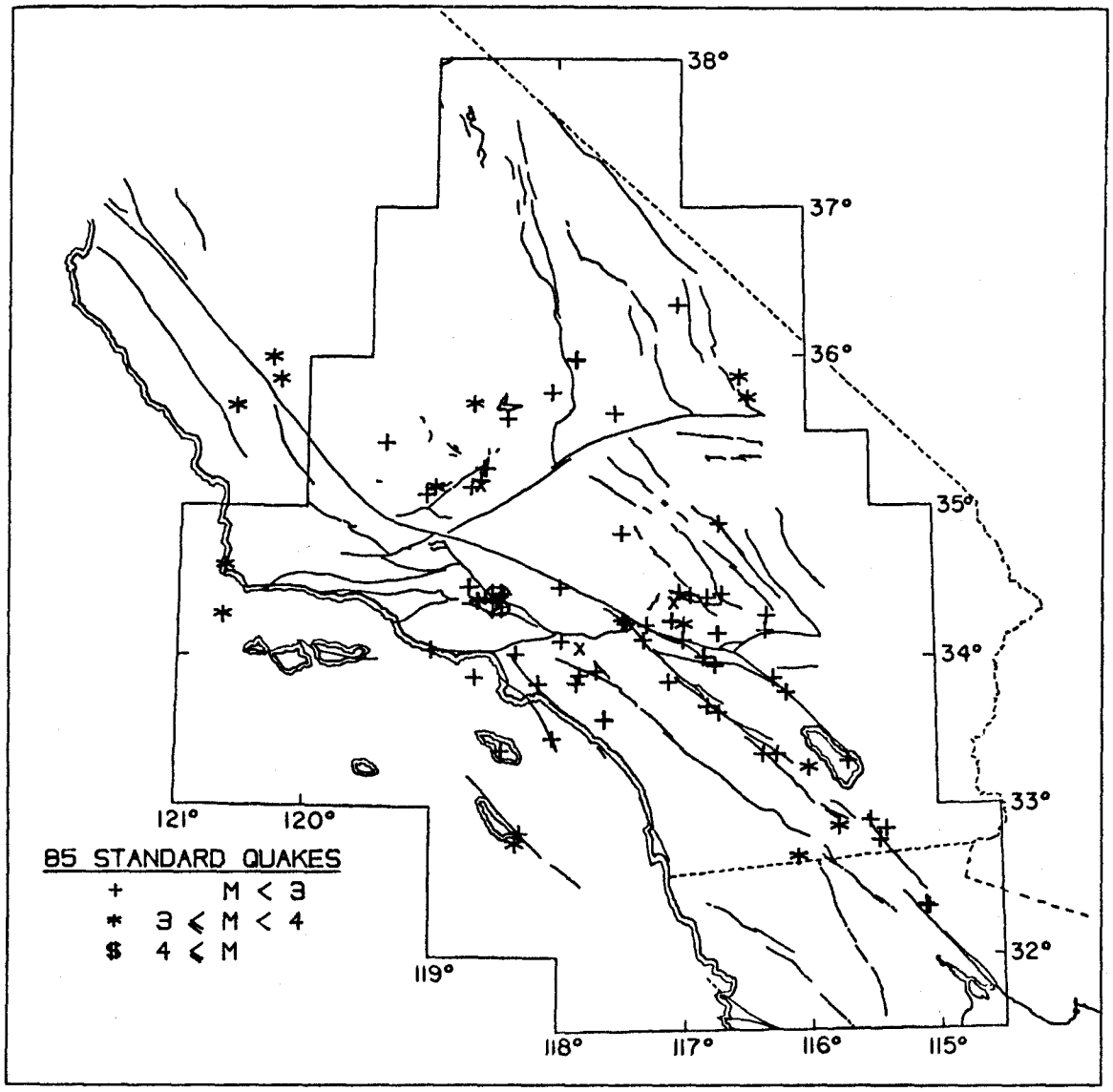

Figure 2. Epicentral distribution of the "85 standard earthquakes" used for the calibration of the coda amplitude magnitude scale M_{ca}.

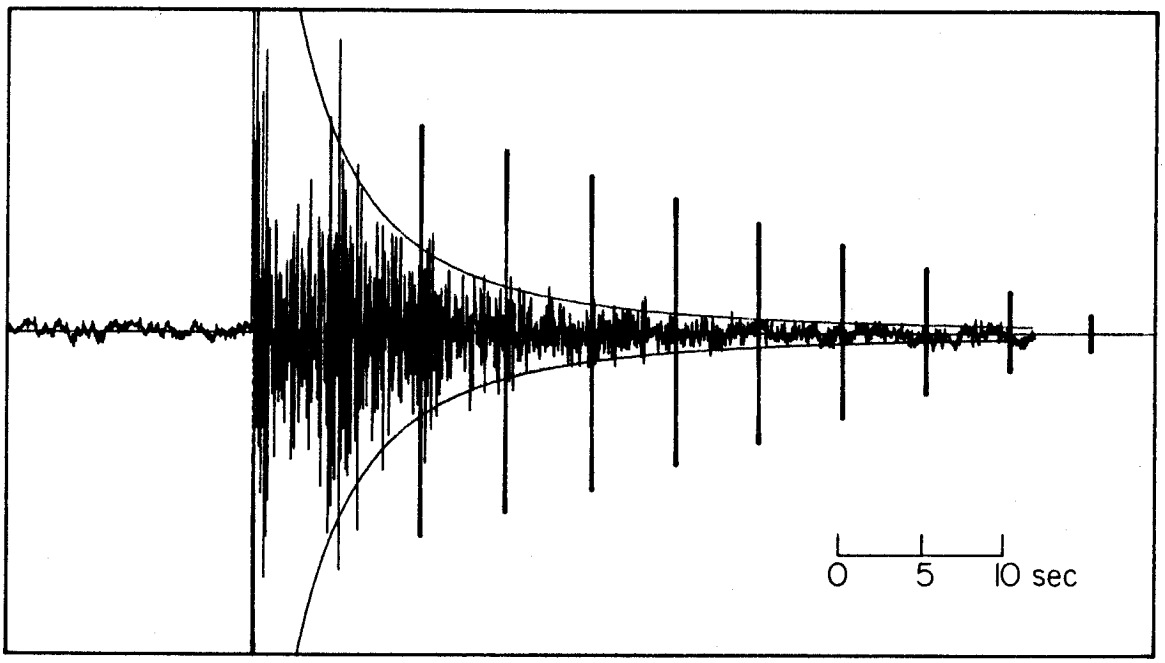

Figure 3. Typical record from the station RMB for a magnitude 2.2 earthquake at a distance of 34.7 km. A quasi-independent magnitude estimate is obtained from each of the 5.12 second coda segments delimited by vertical bars.

constant of proportionality relating magnitude and the logarithm of amplitude. If our data set were restricted to a narrow frequency band, which it is not, then q could be interpreted as the effect of geometric spreading, and b provides for dissipation whether related to Q or energy loss due to scattering. In this paper we will use upper case to denote base 10 logarithms. The distance dependence is not carried explicitly on the right hand side of equation (2) but is allowed for by possible distance dependent variation of any of the parameters q , b, or t_o. In the following discussion the parametric notation on the left hand side will be dropped.

Equation (2) is sufficiently general that it includes many of the coda amplitude functions that have previously been proposed. For example, if we take $t_o = 2.56$ we recover the form developed by Aki and Chouet (1975) and by Chouet and others (1978). If, on the other hand, we allow $t_o = t_p + 2.56$, where t_p is the P wave travel time, and $b = 0$, we include the functional form advanced by Hermann (1975), who demonstrated that this was the coda amplitude function implicitly built into the method of duration magnitude as developed and applied so successfully by such workers as Lee et al. (1972), Crosson (1972), Real and Teng (1973), and by Bakun and Lindh (1977). Note that in this case t_o is distance dependent. Equation (2) does not encompass explicitly the form used by Suteau and Whitcomb (1979) in their development of a coda amplitude magnitude scale. However, they have demonstrated a numerical equivalence to the duration magnitude method over a limited magnitude range.

It was anticipated that the number of free parameters

(currently in excess of 5) can be reduced through simplification so that no more than 2 or possibly 3 site-dependent parameters must be calculated for each station of the network. This simplification process was begun by considering the observed post S coda amplitudes at individual stations. Although the analysis was carried out for many stations of the Southern California network we will illustrate the development process using a single station, RMR. In Figure 4 we show the amplitudes calculated from equation (1) for those of the 85 "standard quakes" recorded by RMR.

Figure 5 shows the same suite of observed coda amplitudes plotted logarithmically on both axes ($\tau \equiv t-t_p$). It appears that a family of straight lines might describe the logarithms of the coda amplitudes to within about .1 magnitude units.

Similar results are obtained for other stations of the network but with slopes varying from site to site. The choice of $t_o = t_p$ was based on the observation that if t_o differed significantly from this value, the family of curves plotted as in Figure 5 would still be roughly straight, but with slopes varying with distance to about 300 km. The analysis contained in the remainder of this paper was conducted first with $t_o = 0$, and then repeated with the more appropriate value when it was discovered that the problem of distance dependence could be minimized by the above choice of t_o. Thus we were led to a formalization that is entirely compatible with the already widely used and highly successful method of duration magnitude. Further, it appears that the success of the duration magnitude method itself is due in large part to the rather fortunate, though necessary,

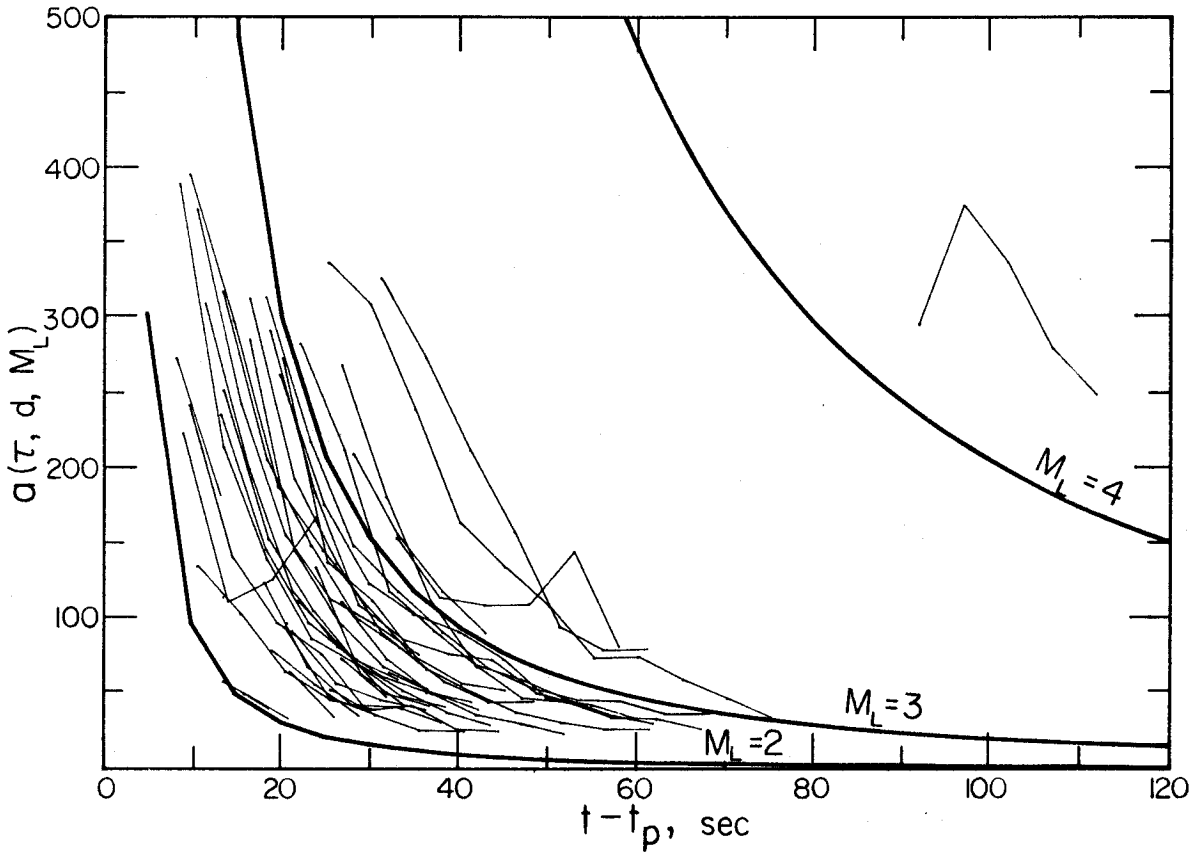

Figure 4. Five second average coda amplitudes calculated from equation (1) for those of the "85 standard earthquakes" recorded at the station RMR. Heavier curves show theoretical amplitude average based on equation (1).

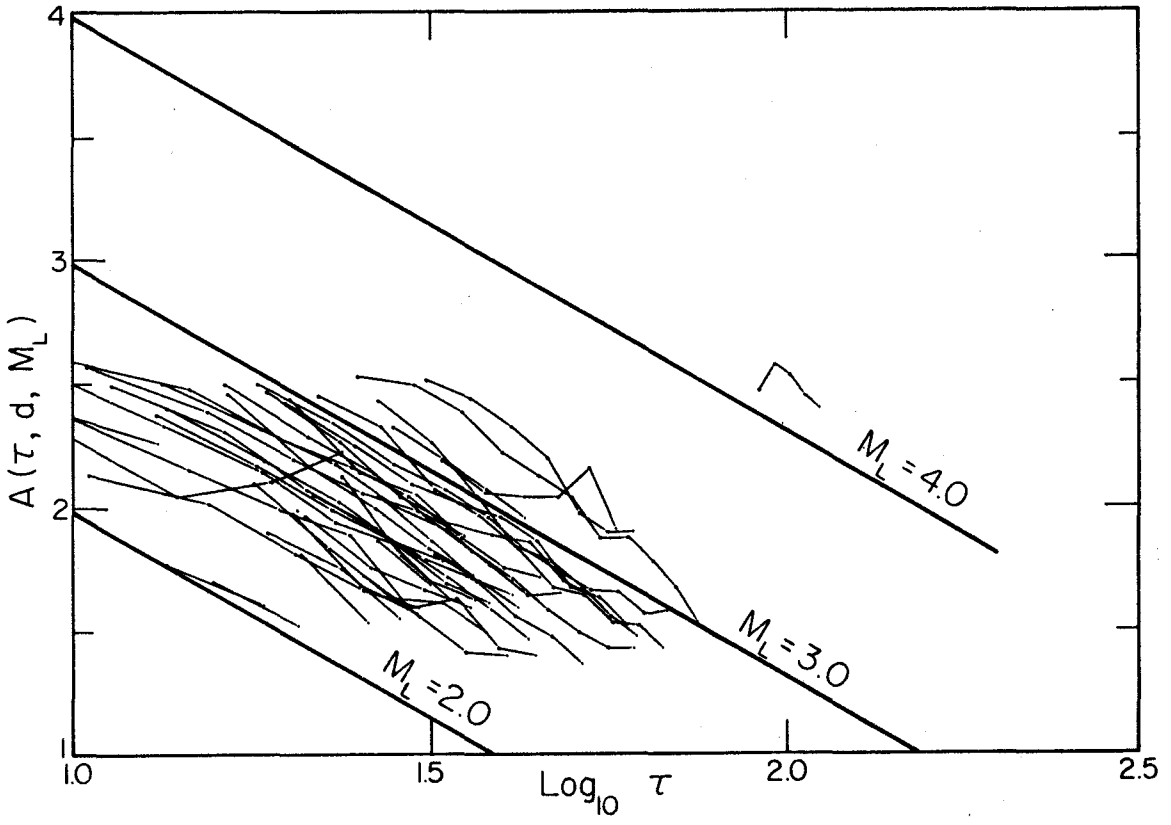

Figure 5. Logarithm of five second average coda amplitudes from equation (1) for those of the "85 standard earthquakes" recorded at the station RMR plotted as a function of the logarithm of time measured from the P-wave onset. Heavier curves show theoretical values based on equation (7).

choice of measuring duration from the P onset. Taking the logarithm of both sides of equation (2) we get

$$A(t,d,M_L) = A_o + cM_L - q \log_{10}(t-t_p) - b(t-t_p) \log_{10}e. \qquad (3)$$

From the results shown in Figure 5 we take b = 0 giving

$$A(t,d,M_L) = A_o + cM_L - q \log_{10}(t-t_p) \qquad (4)$$

which describes a family of straight lines offset from each other by a linear function of magnitude. The median slope, q , of these lines can be calculated as the weighted median of the slopes obtained by fitting a straight line to each of the decay functions in Figure 5 individually. This is done using the L_1 norm (least absolute values) discussed fully by Claerbout and Muir (1973), and by Claerbout (1976). The choice of this norm was required by the presence of large "blunders" in the amplitude data which would have led to erratic results had the method of least squares been used instead.

In taking b = 0 it is not our intention to imply that the effect of dissipation is negligible, but rather that with the available data the value of b cannot be resolved. In other words, the choice of b = 0 can be fully compensated by small adjustments to the other free parameters.

At this point it is convenient to make a small notation change replacing t with $\tau = t-t_p$ so that equation (4) becomes

$$A(\tau,d,M_L) = A_o + cM_L - q \log_{10} \tau \qquad (5)$$

with the distance dependence now expressed through the definition of τ.

Since we have already determined the value of q, we can extrapolate each of the observed codas to a common value of t where the coefficient, c, can be examined explicitly. For this purpose we have extrapolated each amplitude function to a point 1 second past the P onset. The fact that the S-wave has not yet arrived for epicentral distances greater than about 8 km should not be considered a problem. Thus we can write equation (5) as

$$A(1,d,M_L) = A_o + cM_L \quad . \tag{6}$$

This expression indicates that the parameter, c, can be examined if the extrapolated coda amplitudes are plotted against M_L as shown in Figure 6. Solid circles represent codas with more than 5 consecutive segments and are generally more reliable. A line with slope c = 1 appears to provide an adequate fit to these data.

The final form of the magnitude-coda amplitude systematics can be written as

$$A(\tau,d,M_L) = A_o + M_L - q \log_{10} \tau. \tag{7}$$

The gain constant, A_o, can be evaluated as the median of the values $\overline{r}(\tau) - M_L + q \log_{10}\tau$ taken over all coda segments available for a particular station from the data set of 85 "standard quakes".

As a final check to insure that we have not neglected any significant distance dependent trends we have plotted the median residuals for each event as a function of distance in Figure 7.

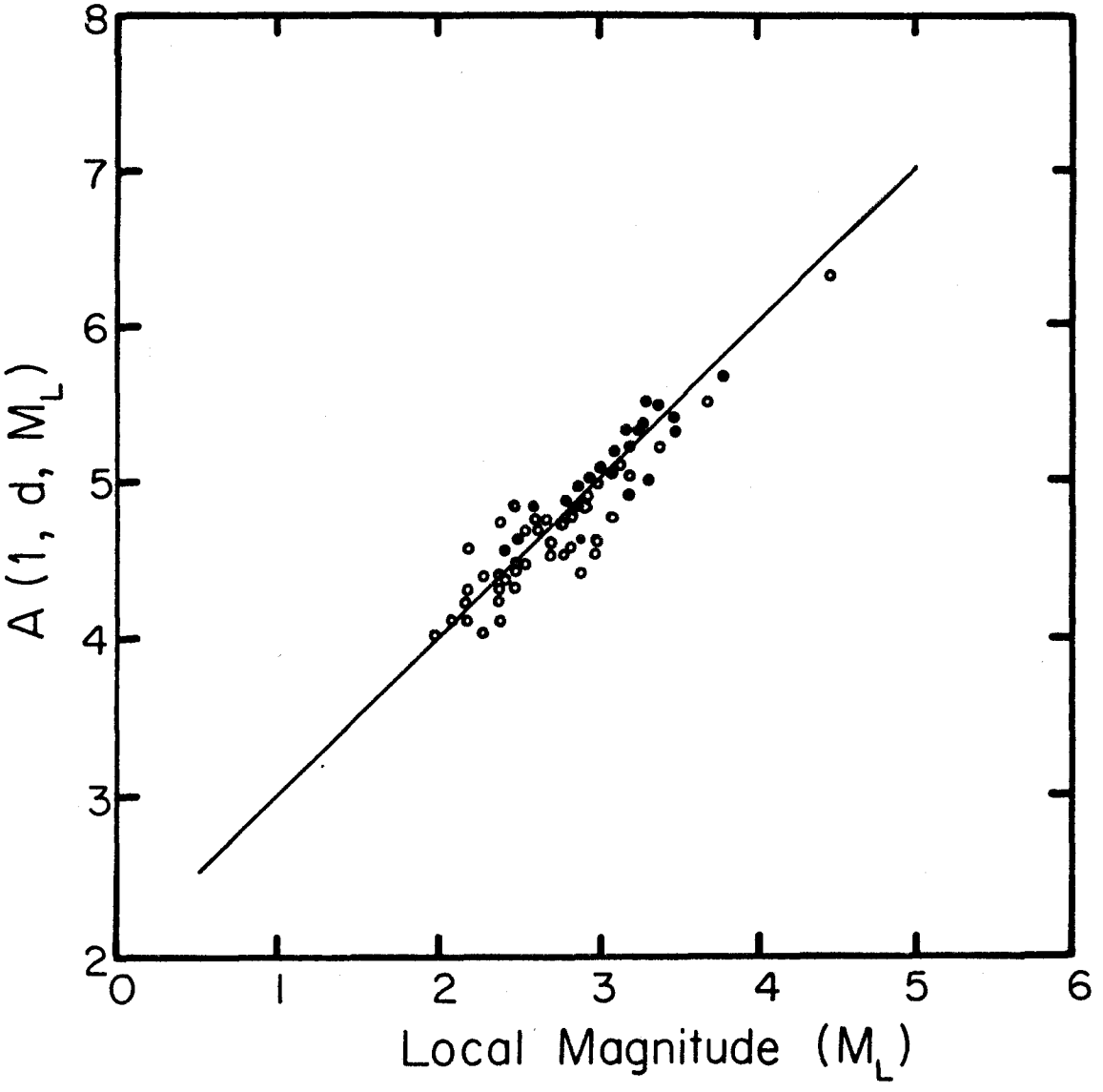

Figure 6. Relationship between local magnitude and the logarithm of average coda amplitude correct to 1 s after the P onset using equation (5) for those of the "85 standard earthquakes" recorded at the station RMR. For this calculation A_0 can be arbitrarily set to zero with no loss of generality. Filled circles denote events with more than five consecutive coda segments sufficiently above the ambient noise level. A solid line of unit slope is shown for reference purposes.

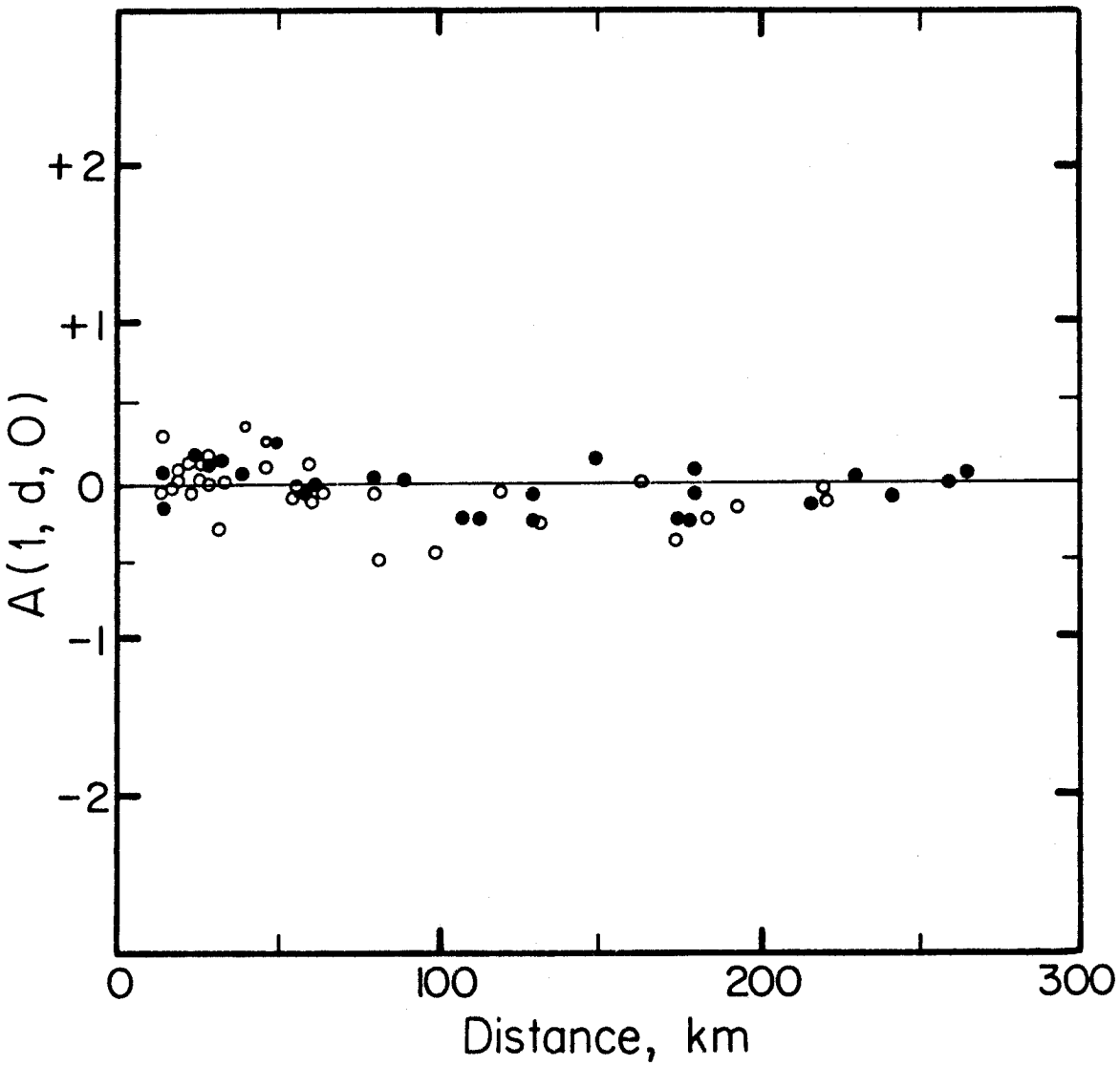

Figure 7. Remaining unexplained residuals for the logarithm of average coda amplitude adjusted to 1 second after the P onset and corrected to a local magnitude of 0.0 using equation (7) for those of the "85 standard earthquakes" recorded at the station RMR. Filled circles denote events having more than five consecutive segments sufficiently above the ambient noise level.

In preparing this plot each coda is corrected to the amplitudes predicted for an $M_L = 0$ event using equation (7). The solid circles again represent events with more than 5 useable coda segments. The horizontal line represents a reference magnitude 0 event. The scatter about this line is about what would be expected from the intrinsic errors of about .2 in M_L. It appears that for distances less than 300 km the functional form given in equation (7) is an adequate representation of the averaged coda amplitudes. This form involves two parameters that must be obtained for each station. Once these constants are known, an estimate of the magnitude, M_{ca}, can be obtained for any 5.12 s segment of the post S coda using the relation

$$M_{ca} = \overline{R}(\tau) - A_o + q \log_{10} \tau \qquad (8)$$

where $\overline{R}(\tau) = \log_{10} \overline{r}(\tau)$ can be calculated using equation (1).

Equation (8) shows that A_o can be thought of as the average amplitude that would be obtained for the coda segment beginning one second after the P onset for an earthquake of $M_L = 0$.

Implications Regarding Earthquake Magnitude and Moment

The result, $c = 1$, for the constant relating magnitude and the logarithm of amplitude was unexpected. A number of studies have addressed the relationship between magnitude and amplitude through an examination of the magnitude moment relation, $\log_{10} M_o = c_1 + c_2 M_L$. Since M_L is based on maximum peak amplitudes, it would be expected to be more related to the higher frequency end of the source spectrum

as compared to source moment. Based on the observation that the source spectrum corner frequency decreases with increasing magnitude, it seems reasonable to expect that the constant c_2 should exceed 1. If the source spectrum were not a function of magnitude or whenever the corner frequency exceeds the instrumentation pass band, then c_2 should be precisely unity.

Values determined for the constant, c_2, have generally ranged between 1.4 and 1.7 for moderate local events (e.g., Wyss and Brune, 1968; Hanks and Wyss, 1972; Thatcher and Hanks, 1973). Based on a study of 13 central California earthquakes ranging in magnitude from 2.4 to 5.1 Johnson and McEvilly (1974) obtained a value of 1.2. Recently Bakun and Lindh (1977) have reported a value of 1.2 for earthquakes less than M_L = 1.5 in the Oroville area with a pronounced break in slope to higher values above 1.5. They suggested that this change in slope, which is also observed when duration is plotted against M_L (e.g., Real and Teng, 1973; Hermann, 1975; Bakun and Lindh, 1977) might be due to the interaction of the source spectrum corner frequency, f_o, with the upper end of their instrumentation pass band. However, the corner frequency-magnitude systematics reported by Johnson and McEvilly (1974) project corner frequencies well within the pass band of the instrumentation being used by Bakun and Lindh (1977).

An alternative explanation for these phenomenon can be derived from a consideration of the modification of the scaling laws appropriate to small earthquakes as presented by Chouet *et al.* (1978). They concluded that for California earthquakes with magnitudes less than

M_L = 2.1 the source spectrum obtained by means of their coda excitation method becomes constant in the frequency range 1.5 to 24 Hz. This conclusion was based on the observation that for small earthquakes the slope of the spectral amplitudes at 1.5 Hz against those at 24 Hz becomes unity.

In a similar vein, Figure 6 demonstrates that peak amplitude (M_L) is proportional to a 5 second average amplitude with a coefficient of 2, and thus corroborates the conclusions of Chouet *et al.* (1978).

A similar phenomenon was observed by Suteau and Whitcomb (1979) during the development of a coda magnitude scale, M_c, based on the scattering model proposed by Aki (1969) and by Aki and Chouet (1975). They suggested that a discrepancy in slope between M_c and M_L could be resolved either by adjusting the constant magnitude-moment relation to a value closer to 1, or by reducing the effective Q. They appear to prefer the latter explanation while not ruling out the former. Their warning against extrapolation of the duration magnitude scale to small magnitudes appears to be soundly based and is supported by the results of the current study. If, in fact, the constant "c_2" in the moment magnitude relationship approaches 1, then as a consequence microearthquake studies using duration magnitude might be expected to encounter anomalously low "b" values as an artifact of the magnitude calculation procedure. In addition, if this observation is correct, then any theoretically based magnitude determination method must explicitly take into account the change in scaling laws for small magnitudes if it is to be strictly valid over the magnitude range 0 to 5 . Since for our

purposes we are attempting to develop a simple scheme that is applicable to the great number of small events detected by the CEDAR system we have chosen not to incorporate this complication at present, deferring any necessary adjustments until such time as a large number of events with M_L greater than 3 and magnitudes determined by various methods can support a more complete analysis. Until then it appears from the above analysis that a simple extrapolation of our results to magnitudes much greater than 3 should result in an increasing underestimation with respect to the corresponding M_L.

NETWORK CALIBRATION

The task at hand is to calculate values for the site parameters "A_o" and "q" for each of the 121 stations in the Southern California network listed in Table 2. Initially each trace contained in the standard data set was divided into a sequence of 5.12 second averages using equation (1). Most of these averages are not relevant to our purpose, for example, because they include data before the onset of S, so that it is necessary to establish a set of selection criteria to determine which coda segments are to be included in the calibration calculations or in the magnitude estimation procedure discussed in a later section. The criteria used in this study were as follows:

1) The first sample of a coda segment must follow the calculated arrival time of S.
2) The amplitude of the segment must be less than some fixed

TABLE 2. CURRENT MCA CALIBRATION PARAMETERS AND STATION INFORMATION FOR THE SOUTHERN CALIFORNIA NETWORK (SCARLET).

STA	LATITUDE	LONGITUDE	Q	A0	EPS90	EPS50	B0	B1	SITE
ABL	34 51.05	119 13.25	1.98	1.75	15	10	-0.74	1.98	B
ADL	34 33.38	117 25.02	1.23	0.26	39	31	1.22	1.23	Q
BAR	32 40.80	116 40.30	1.78	1.16	18	13	-0.06	1.78	B
BCH	35 11.10	120 5.05	2.09	2.07	17	12	-0.99	2.09	B
BC2	33 39.42	115 27.67	1.56	1.29	8	4	-0.67	1.56	B
BLU	34 24.40	117 43.61	1.94	1.94	34	26	-0.53	1.94	B
BMT	35 8.15	118 35.81	1.93	1.53	33	25	-0.12	1.93	B
BON	32 41.67	115 16.11	0.89	0.58	32	24	0.80	0.89	Q
BTL	34 15.43	117 0.29	1.32	0.88	27	20	0.44	1.32	B
CAM	34 15.27	119 2.00	1.51	1.19	34	26	0.22	1.51	Q
CFT	34 2.11	117 6.66	1.81	1.15	10	6	-0.38	1.81	Q*
CH2	33 17.77	115 20.17	1.36	1.39	18	13	-0.29	1.36	
CIS	33 24.40	118 24.20	2.19	1.67	20	14	-0.52	2.19	B
CKC	34 8.18	117 10.48	1.70	0.96	5	2	-0.67	1.70	Q*
CLC	35 49.00	117 35.80	1.82	1.63	18	13	-0.53	1.82	B
CLI	33 8.45	115 31.64	0.61	0.00	95	78	1.88	0.61	Q
CMH	34 33.18	114 34.32	1.21	0.26	18	13	0.84	1.21	
COA	32 51.81	115 7.36	0.73	0.27	24	18	0.97	0.73	Q
COK	32 50.95	115 43.61	0.66	-0.02	24	18	1.27	0.66	Q
COQ	33 51.63	117 30.58	1.68	0.86	18	13	0.24	1.68	B
COY	33 21.84	116 18.63	1.97	1.78	12	8	-0.91	1.97	B
CO2	33 50.83	115 20.68	1.81	1.95	18	13	-0.85	1.81	B
CPE	32 52.80	117 6.00	1.75	0.65	5	2	-0.36	1.75	T
CPM	34 9.24	116 11.80	1.89	1.61	16	11	-0.58	1.89	B
CRG	35 14.53	119 43.40	2.05	2.11	25	19	-0.84	2.05	T
CRR	32 53.18	115 58.10	1.40	1.30	34	26	0.11	1.40	Q*
CSP	34 17.87	117 21.33	1.85	1.36	12	8	-0.48	1.85	B
DB2	33 44.10	117 3.72	2.24	2.48	8	4	-1.86	2.24	B
DHS	33 55.58	116 23.13	1.70	1.70	35	27	-0.27	1.70	
DHSE	33 55.58	116 23.13	1.70	1.70	41	32	-0.19	1.70	
DHSN	33 55.58	116 23.13	1.70	1.70	41	32	-0.19	1.70	
ECF	34 27.48	119 5.44	1.57	1.56	49	39	0.03	1.57	T
ELR	33 8.84	115 49.95	0.78	0.10	25	19	1.17	0.78	Q
FMA	33 42.75	118 17.12	0.31	-0.93	16	11	1.97	0.31	T
FNK	33 22.98	115 38.26	1.14	0.41	12	8	0.46	1.14	Q*
FTC	34 52.25	118 53.51	1.97	1.30	8	4	-0.68	1.97	B
GAV	34 1.35	117 30.74	1.98	1.55	12	8	-0.67	1.98	Q*
GLA	33 3.10	114 49.60	1.56	1.38	5	2	-1.08	1.56	B
GRP	34 48.26	115 36.27	1.54	0.59	29	22	0.75	1.54	B
GSC	35 18.10	116 48.30	1.62	1.27	6	3	-0.87	1.62	B
HDG	34 25.73	116 18.30	1.65	1.56	39	31	-0.08	1.65	B
HOT	33 18.84	116 34.89	1.96	1.53	8	4	-0.91	1.96	B
IKP	32 38.93	116 6.48	1.54	0.38	5	2	-0.09	1.54	B
ING	32 59.30	115 18.61	0.79	-0.52	13	9	1.46	0.79	Q
INS	33 56.14	116 11.66	1.73	1.76	23	17	-0.53	1.73	B
IRC	34 23.40	118 24.00	2.18	2.00	11	7	-1.16	2.18	Q*
IRN	34 9.60	115 11.04	1.58	1.44	10	6	-0.67	1.58	B

TABLE 2. (CONTINUED)

STA	LATITUDE	LONGITUDE	Q	A0	EPS90	EPS50	B0	B1	SITE
ISA	35 39.80	118 28.40	2.08	1.47	5	2	-1.18	2.08	B
JNH	34 26.85	117 57.27	1.50	1.10	48	38	0.48	1.50	
JUL	33 2.90	116 36.77	1.80	1.20	21	15	-0.01	1.80	
KEE	33 38.30	116 39.19	1.56	1.17	46	36	0.38	1.56	B
KYP	34 6.11	118 52.77	1.51	0.94	5	2	-0.65	1.51	T
LCL	33 50.00	118 11.55	1.50	0.36	15	10	0.65	1.50	Q
LED	34 26.06	115 56.19	2.01	1.95	10	6	-1.18	2.01	T
LHU	34 40.30	118 24.70	1.74	1.38	17	12	-0.30	1.74	B
LJO	34 35.46	117 50.88	1.44	0.84	18	13	0.26	1.44	B
LJOE	34 35.46	117 50.88	1.44	0.84	25	18	0.42	1.44	B
LJON	34 35.46	117 50.88	1.44	0.84	25	18	0.42	1.44	B
LRR	34 31.56	118 1.66	1.45	1.10	43	34	0.43	1.45	B
LTC	33 29.34	115 4.20	1.56	1.29	11	7	-0.45	1.56	B
LTM	33 54.90	114 55.10	1.90	1.60	21	15	-0.41	1.90	B
MDA	33 54.78	116 59.97	1.78	0.78	34	26	0.63	1.78	T
MLL	34 5.48	116 56.18	1.86	0.79	46	36	0.76	1.86	B
MOV	34 9.35	116 30.10	1.70	1.70	35	27	-0.27	1.70	B
MWC	34 13.40	118 3.50	1.83	1.20	5	2	-0.91	1.83	B
NW2	33 5.43	115 41.54	0.94	0.05	18	13	1.05	0.94	Q
OBB	33 10.04	115 38.20	0.82	0.03	17	12	1.05	0.82	Q
PAS	34 8.95	118 10.29	1.36	0.26	4	1	-0.33	1.36	C
PCF	34 3.19	117 47.44	2.11	1.35	45	36	0.20	2.11	T
PEC	33 53.51	117 9.60	1.72	1.66	7	4	-1.10	1.72	B
PEM	34 10.04	117 52.18	1.93	1.69	7	4	-1.13	1.93	B
PKM	34 53.75	119 49.13	1.96	1.63	6	3	-1.23	1.96	T
PLM	33 21.20	116 51.70	1.69	1.15	5	2	-0.86	1.69	B
PLT	32 43.87	114 43.76	1.31	0.96	30	23	0.39	1.31	B
PNM	33 58.64	115 48.05	1.89	1.58	3	0	-2.11	1.89	B
POB	33 41.20	116 55.40	1.73	1.34	35	27	0.09	1.73	B
PSP	33 47.63	116 32.93	1.58	0.97	13	9	-0.04	1.58	B
PTD	34 0.25	118 48.38	1.55	0.93	31	24	0.44	1.55	T
PYR	34 34.08	118 44.50	1.85	1.72	6	3	-1.32	1.85	B
RAY	34 2.18	116 48.67	1.78	1.43	14	9	-0.47	1.78	B
RDM	34 24.00	117 11.10	1.76	1.40	19	14	-0.27	1.76	B
RMR	34 12.77	116 34.52	1.67	1.64	37	29	-0.18	1.67	B
ROD	34 37.78	116 36.29	1.84	2.00	21	15	-0.82	1.84	B
RUN	32 58.33	114 58.63	1.16	0.71	93	76	1.17	1.16	Q
RVM	34 10.81	114 12.02	1.98	1.91	18	13	-0.81	1.98	
RVR	33 59.60	117 22.50	1.31	0.10	5	2	0.19	1.31	B
RVS	34 2.08	114 31.08	2.18	2.36	10	6	-1.59	2.18	T
RYS	34 38.60	119 21.10	1.73	1.52	11	7	-0.68	1.73	T
SAD	34 4.86	118 39.90	1.57	1.24	13	9	-0.31	1.57	T
SBAI	34 0.80	119 26.23	1.20	0.22	19	14	0.92	1.20	T
SBB	34 41.30	117 49.50	1.59	1.19	9	5	-0.47	1.59	B
SBCC	34 56.38	120 10.32	2.18	1.71	5	2	-1.42	2.18	T
SBCD	34 22.12	119 20.63	1.78	1.24	18	13	-0.14	1.78	T
SBLC	34 29.79	119 42.81	1.63	0.90	7	4	-0.34	1.63	T
SBLG	34 6.87	119 3.85	1.43	0.70	13	9	0.23	1.43	T

TABLE 2. (CONTINUED)

STA	LATITUDE	LONGITUDE	Q	A0	EPS90	EPS50	B0	B1	SITE
SBLP	34 33.57	120 24.02	1.24	0.42	14	9	0.54	1.24	T
SBSC	33 59.68	119 37.99	2.73	2.80	19	14	-1.67	2.73	T
SBSM	34 2.24	120 21.01	2.16	2.18	34	26	-0.77	2.16	Q
SBSN	33 14.68	119 30.38	1.42	0.40	8	4	0.23	1.42	T
SCI	32 58.80	118 32.80	1.62	1.35	8	4	-0.73	1.62	T
SCY	34 6.37	118 27.25	1.57	1.02	5	2	-0.73	1.57	T
SDW	34 36.55	117 4.45	1.58	0.75	18	13	0.35	1.58	B
SGL	32 38.95	115 43.52	1.47	1.20	19	14	-0.07	1.47	Q*
SHH	34 11.26	115 39.27	1.87	2.05	14	9	-1.09	1.87	B
SIL	34 20.87	116 49.60	1.80	1.50	16	11	-0.47	1.80	B
SIP	34 12.24	118 47.94	1.92	1.94	21	15	-0.76	1.92	T
SME	33 49.36	117 21.32	1.86	1.68	4	1	-1.75	1.86	B
SMO	33 32.15	116 27.70	1.74	1.30	9	5	-0.58	1.74	B
SNS	33 25.90	117 32.90	1.96	1.31	12	8	-0.44	1.96	T
SNR	32 51.71	115 26.21	1.03	-0.09	19	14	1.23	1.03	Q
SNRE	32 51.71	115 26.21	1.03	-0.09	26	19	1.38	1.03	Q
SNRN	32 51.71	115 26.21	1.03	-0.09	26	19	1.38	1.03	Q
SPM	34 28.32	115 24.16	1.82	1.65	18	13	-0.55	1.82	B
SSK	34 12.97	117 41.32	1.94	1.67	26	19	-0.39	1.94	B
SUP	32 57.31	115 49.43	1.55	1.41	24	18	-0.17	1.55	B
SWM	34 43.00	118 35.00	1.74	1.74	16	11	-0.71	1.74	B
SYP	34 31.63	119 58.67	1.80	1.47	12	8	-0.59	1.80	T
TCC	33 59.67	118 0.77	1.50	0.72	22	16	0.48	1.50	T
TMB	35 5.24	119 32.08	2.34	2.24	13	9	-1.31	2.34	T
TPC	34 6.35	116 2.92	1.20	0.45	5	2	-0.16	1.20	B
TPO	34 52.73	118 13.66	1.79	1.70	10	6	-0.93	1.79	B
TTM	34 20.12	114 49.65	2.22	2.20	18	13	-1.10	2.22	
TWL	34 16.70	118 35.67	0.97	-0.06	56	45	1.71	0.97	B
VG2	33 49.91	116 48.55	2.15	1.57	32	24	-0.19	2.15	B
VPD	33 48.90	117 45.70	1.42	1.11	23	17	0.12	1.42	T
VST	33 9.40	117 13.90	1.30	0.67	10	6	0.10	1.30	B
WIS	33 16.56	115 35.58	0.94	-0.29	22	16	1.50	0.94	Q
WLK	33 3.08	115 29.44	0.92	0.05	40	31	1.44	0.92	Q
WML	33 0.91	115 37.35	0.41	-0.50	51	41	2.11	0.41	Q
WWR	33 59.51	116 39.36	1.77	0.70	13	9	0.23	1.77	B
YEG	35 26.18	119 57.56	1.93	1.75	18	13	-0.65	1.93	T

value to insure that clipping in the telemetry system is unlikely.

3) The last sample in the segment must precede the calculated P onset time of any later event.

4) The calculated average must exceed the pre-event ambient noise level by an amount that insures an adequate signal to noise ratio.

5) The segment must not follow a segment that has failed criterion (4).

This last condition prevents portions of the S coda reactivated by a noise burst from generating spurious large magnitude estimates. In this study we enforce the fourth criterion by requiring that a particular segment average must exceed 1.5 times the noise level. Applying these selection criteria to the 85 "standard quakes" resulted in 14,455 discrete coda segment averages.

In the calibration procedure currently in use for the Southern California network every acceptable segment average contributes an equation of the form

$$A_o - q \log_{10} \tau = \overline{R}(\tau) - M_{CA}. \tag{9}$$

Each station of the network can be considered independently. As discussed above we apply the method of least absolute values minimizing

$$\sum_k |\overline{R}(\tau_k) - M_{ca} - A_o + q \log_{10} \tau_k| \tag{10}$$

for each event recorded at a particular station, where k indexes

the set of "acceptable" coda segments. Thus each trace yields an estimate of the two parameters, A_o and q, which can be plotted in the form of a scatter plot as illustrated in Figure 8a for the station RMR. Small filled circles denote more reliable values obtained from traces with more than 5 acceptable segments. The station calibration represented by the large cross in Figure 8a is defined as the median of the marginal distributions of the two calibration constants considered independently. These values are listed in Table 2 and are plotted in Figure 10 to illustrate the range of variation within the Southern California network.

The linear trend of the points plotted in Figure 8a reveals a substantial trade-off or coupling between the two site parameters A_o and q. In order to illustrate the nature of this trade-off we have selected 5 representative points (Figure 8b) and plotted their corresponding amplitude functions in Figure 9 using the expression

$$a(\tau,d,M_L) = 10^{Mca+A_o}\ \tau^{-q} \qquad (11)$$

A typical seismogram from the same station for a magnitude 2.2 event at an epicentral distance of 34.7 km is plotted for comparison. If a more distant event had been shown instead, the P-wave arrival would be plotted in the same place since the amplitude function is referenced to the P onset. However, the S wave would arrive farther to the right and would appear to decay more slowly. Evidently it is the more distant events that contribute the greatest scatter away from the median values in Figure 8a. Fortunately the structure of the forward problem (magnitude estimation) is such that the effect of

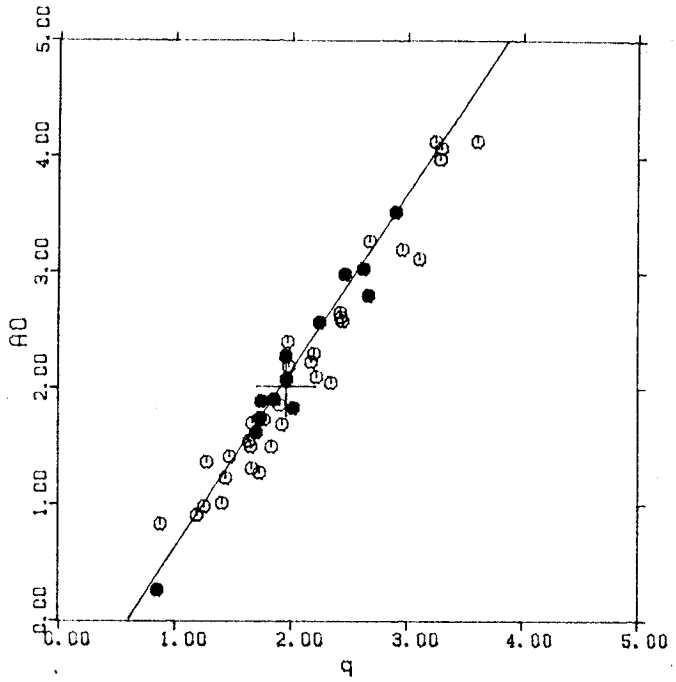

Figure 8a. Distribution of site calibration parameters determined from individual seismograms at the station RMR. Filled circles denote records from which six or more consecutive coda segments were obtained. The light cross represents the median station calibration.

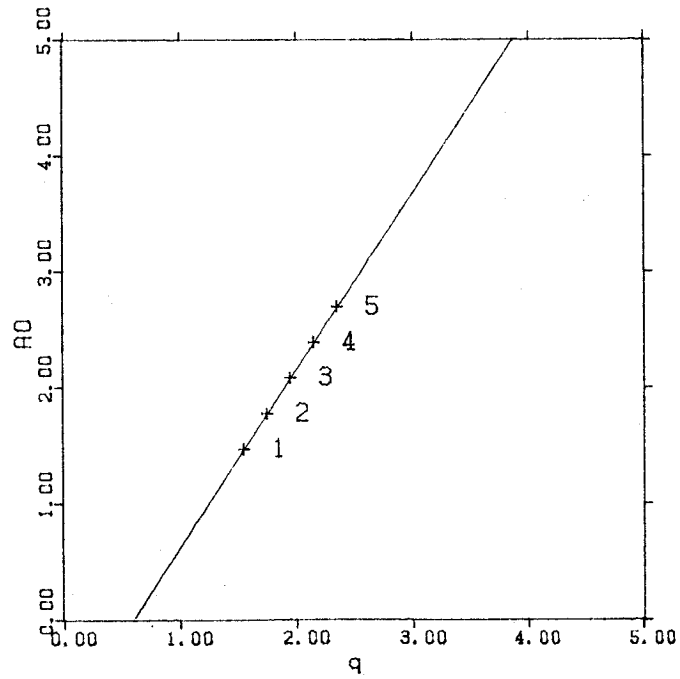

Figure 8b. Selection of points from the population of possible site calibration parameters for the station RMR chosen to investigate the nature of the trade-off in Figure 8a. The corresponding coda delay functions are shown in Figure 9.

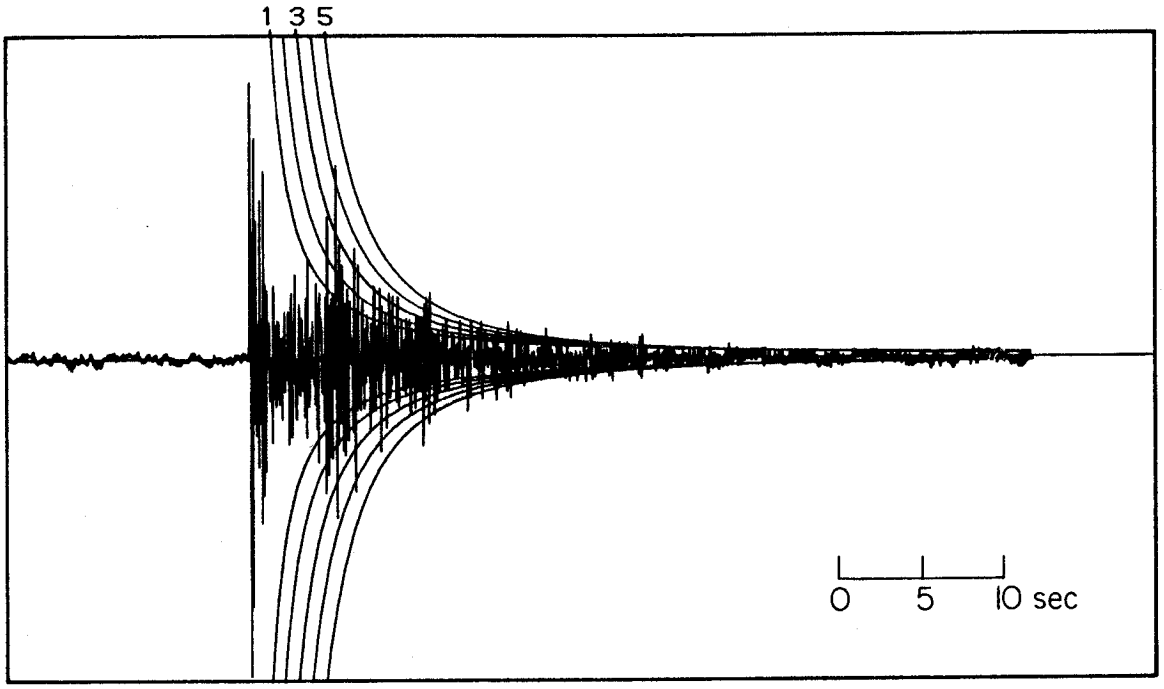

Figure 9. Typical record from the station RMR for a magnitude 2.2 earthquake at a distance of 34.7 km. The superimposed coda decay functions correspond to various points in the distribution of site parameters shown in Figure 8 in order to illustrate the nature of the intrinsic trade-off between gain, A_o, and decay rate, q.

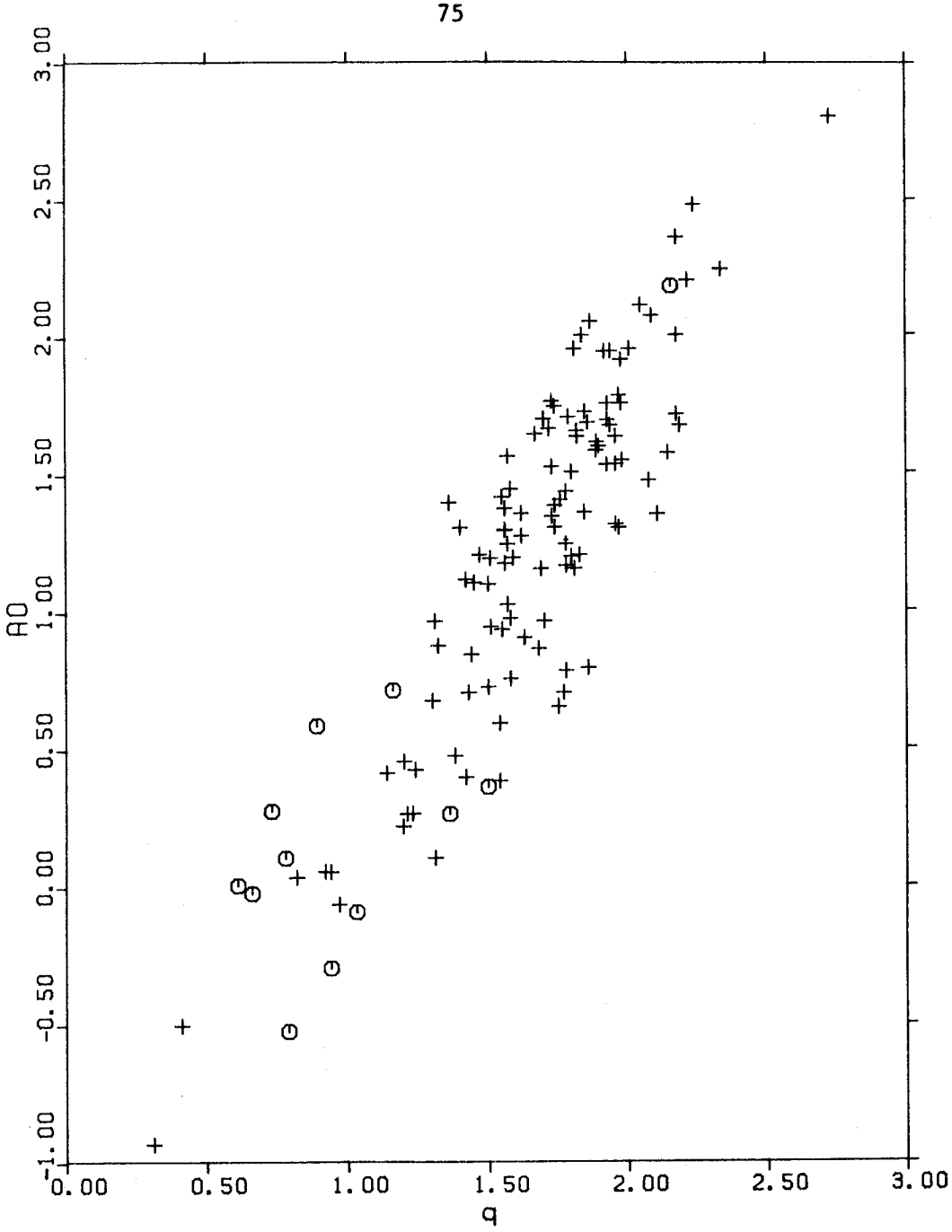

Figure 10. Distribution of M_{CA} site calibration parameters for the stations of the Southern California Network (SCARLET). The long axis of the distribution appears to be controlled by conditions local to a particular site. To illustrate this effect stations located on deep quaternary basins are represented by an open circle.

the indeterminancy in the inverse problem (calibration) is minimized. This follows from a consideration of problems with small eigenvalues as discussed by Lanczos (1961).

There is an alternative calibration procedure that offers some advantages over the one currently in use. In this approach we treat the magnitudes as unknowns as well as the site constants. This has the effect of coupling all of the equations so that we can no longer treat each station separately. Consequently, from our 85 "standard quakes" we would develop a system of 14,455 equations in 327 unknowns. Actually the generalized inverse matrix associated with this system would necessarily have at least one vanishing eigenvalue. This would require us to specify the magnitude of one of the events reducing the number of unknowns to 326. The principal advantage of this approach is that it leads to a completely internally consistent magnitude scale without introducing any assumptions or calibration problems inherent in M_L. The main reason that this method was not used here is that the analysis of a 326 x 326 matrix requires more computational resources than were available.

SITE AND PATH EFFECTS

Once the network in Southern California was calibrated a rather fascinating observation emerged relating site geology and the site parameter, q. It turned out that stations located in deep alluvial basins exhibited significantly lower values of the parameter "q" compared to values obtained from bedrock sites. In order to

investigate this phenomenon, station sites were grouped into the following four categories based on surface geology: (1) deep Quaternary basins; (2) thin Quaternary sediments, (3) Tertiary sediments; and (4) basement, including Paleozoic and Mesozoic sediments. The category assigned to each site is listed in Table 2 using the symbols Q, Q*, T, and B, respectively. Figure 11 shows the marginal distribution of q for each of the site categories. The only significantly different distribution is that obtained for deep Quaternary basins, specifically the Salton Trough and the Los Angeles Basin. This dichotomy can also be seen in Figure 10 where the basin sites are represented by open circles.

The reason for this discrepancy appears to be a path effect rather than a more local effect of the station geology. It appears that deep basins are surrounded by an "impedance barrier" associated with their margins such that seismic energy becomes trapped, reverberating within the basin until it decays. This theory finds additional support from two ancillary observations. S coda amplitudes recorded by stations within the Salton Trough for earthquakes without are smaller by about a factor of 8 than expected. This could be attributed to miscalibration or site effects were it not for the companion observation that energy is also lost for propagation paths leaving the Imperial Valley. Independent confirmation of these observations is provided by a consideration of the isoseismals of the 1948 Desert Hot Springs earthquake discussed by Richter and others (1958). They were surprised to find that reported intensities were significantly higher at San Diego than at comparable distances within

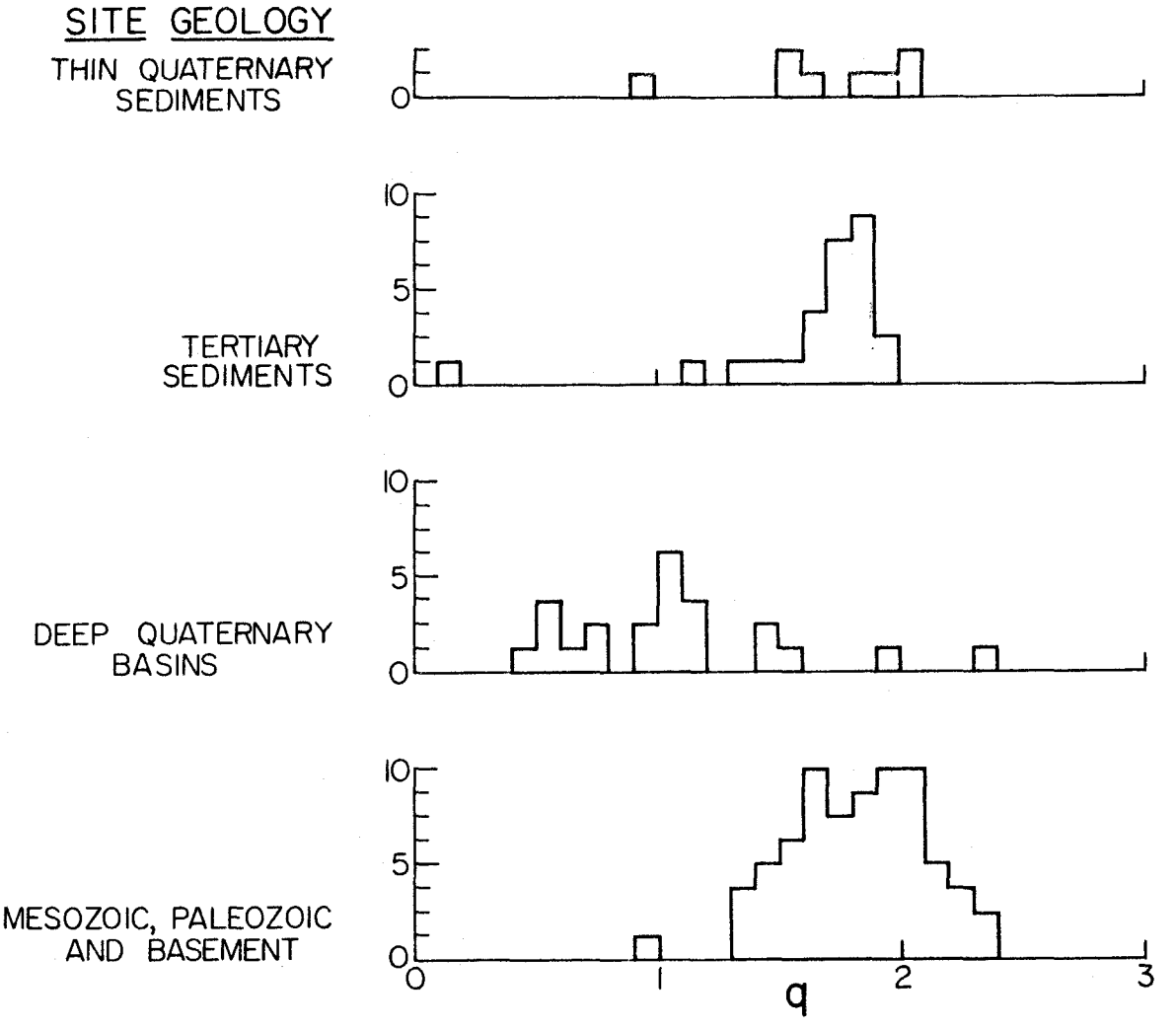

Figure 11. Set of histograms showing the effect of local site geology on the coda decay constant, q.

Imperial Valley (specifically, El Centro). From ground factor considerations (e.g., Gutenburg, 1956) one would have expected considerably greater shaking at El Centro. The explanation offered for this phenomenon was the existence of a so-called "earthquake shadow".

The existence of such large path dependent effects suggests a heretofore untapped use of short period networks with respect to strong motion prediction and microzonation studies. It is clearly not sufficient to base such studies solely on site geology. It should be possible to map the approximate locations of such "impedance barriers" using a distribution of small earthquakes within a dense network. This analysis for Southern California is the subject of a future paper.

APPLICATION TO MAGNITUDE ESTIMATION

Once the network calibration is completed, estimation of magnitude becomes simply a matter of applying equation (8) to all coda segments consistent with the five selection criteria discussed above. The median of the resulting set of magnitude estimates can then be taken as a robust estimate of the event magnitude. Such a procedure is currently being used to estimate magnitudes for the events recorded by the CEDAR system in Southern California. In addition to an overall magnitude estimate we also calculate estimates for each station independently. This allows us to quickly detect any station calibration changes that might arise as a result of vandalism or improper adjustment during site maintenance.

Two examples will be discussed to illustrate the method currently employed for processing CEDAR system data. The FORTRAN codes for the magitude estimation algorithm have been implemented on a Data General Eclipse S/230 minicomputer and on a Prime 500. In the first example (Figure 12) we estimate the M_{CA} magnitude of an M_L = 2.8 event that occurred in the Mojave Desert. The computer output is organized in columns corresponding to successive coda segments for a particular station. The rows labeled DIST, SCAL, and AZ provide the epicentral distance in kilometers, the calculated S travel time in seconds, and the station azimuth respectively. The leftmost column is the lapsed time in seconds. The numeric entries are magnitude estimates calculated from equation (8) for those coda segments that satisfied all of the five selection criteria discussed above. Segments failing criterion (1) are labeled "-", those failing criterion (2) are labeled "CLIP", and those failing criteria (4) or (5) are indicated by "+". Had any segments failed criterion (3) it would have been denoted by "MULT". The last row of each section contains the median estimates for each station. In this example the median M_{CA} assigned to this event is 2.53. The DISCREPANCY HISTOGRAM is simply a histogram of the differences between the station median estimates and the overall M_{CA} estimate. We find the consistency of the individual estimates for a particular station as well as the close agreement among the various stations extremely encouraging.

The second example concerns an earthquake with an assigned M_L

STANDARD DECK WITH DELAYS

UNCALIBRATED: WWV YMD SLU

EVENT: 83/1
HYPOCENTER: 34 49.45, 117 28.39, Z= 5.08
ORIGIN TIME: 1977/ 3/21 (233) 622 28.52 GMT

STA:	SBB	RVR	SNS	VST	LCL	SYP	SMO	RYS	BMT	BC2	LTC	ECF	CAM	WWR	IRC	MWC	PAS	TCC	VPD	PEC	TPC	CLC	SWM	PYP
DIST:	36.	93.	155.	186.	128.	232.	171.	173.	108.	226.	266.	154.	157.	119.	98.	86.	99.	105.	115.	107.	103.	111.	102.	120.
SCAL:	11.	27.	44.	53.	37.	63.	48.	49.	32.	62.	71.	44.	45.	35.	29.	25.	29.	30.	33.	31.	44.	32.	30.	35.
AZ:	295.	6.	357.	7.	329.	279.	33.	277.	252.	55.	56.	286.	294.	39.	300.	321.	320.	332.	347.	15.	98.	186.	277.	284.
11.30	2.03	-	-	-	-	-	-	-	-	-	-	-	-	-	-	-	-	-	-	-	-	-	-	-
16.44	2.28	-	-	-	-	-	-	-	-	-	-	-	-	-	-	-	-	-	-	-	-	-	-	-
21.58	2.51	-	-	-	-	-	-	-	-	-	-	-	-	-	-	-	-	-	-	-	-	-	-	-
26.72	2.54	-	-	-	-	-	-	-	-	-	-	-	-	-	-	2.63	-	-	-	-	-	-	-	-
31.86	2.58	+	-	-	-	-	-	-	+	-	-	-	-	-	2.54	2.49	2.64	2.44	-	2.62	-	-	2.49	-
37.00	+	+	-	-	-	-	-	-	+	-	-	-	-	+	2.49	+	+	2.42	2.74	2.42	-	2.41	2.71	2.35
42.14	+	+	-	-	+	-	-	-	+	-	-	-	-	+	2.49	+	+	+	2.54	2.40	-	2.37	2.49	2.59
47.28	+	+	2.28	-	+	-	-	-	+	-	-	2.43	2.27	+	2.49	+	+	+	2.52	2.47	2.53	+	2.52	2.51
52.42	+	+	+	-	+	-	+	2.45	+	-	-	+	2.41	+	+	+	+	+	+	2.41	2.45	+	2.43	2.48
57.56	+	+	+	+	+	-	+	+	+	-	-	+	+	+	+	+	+	+	+	+	+	+	2.46	+
62.70	+	+	+	+	+	-	+	+	+	+	-	+	+	+	+	+	+	+	+	+	+	+	2.72	+
67.84	+	+	+	+	+	+	+	+	+	+	-	+	+	+	+	+	+	+	+	+	+	+	+	+
MCAM:	2.51		2.28					2.45				2.43	2.41		2.49	2.63	2.64	2.44	2.54	2.42	2.53	2.41	2.49	2.51

STA:	ISA	GSC	LHU	COY	SAD	KYP	SIP	PSP	INS	PNM	LED	CPM	RMR	HDG	ROD	SPM	SHH	GRP	CO2	SME	GAV	SS2	PEM	SBLG
DIST:	130.	81.	88.	194.	137.	152.	140.	142.	153.	180.	146.	139.	107.	116.	82.	194.	181.	171.	224.	112.	89.	68.	81.	166.
SCAL:	38.	24.	26.	55.	40.	44.	40.	41.	44.	51.	42.	40.	31.	34.	24.	55.	51.	49.	62.	32.	26.	20.	24.	47.
AZ:	225.	131.	281.	33.	307.	302.	300.	36.	50.	58.	74.	57.	50.	67.	75.	78.	67.	89.	60.	6.	358.	358.	334.	299.
21.58	-	-	-	-	-	-	-	-	-	-	-	-	-	-	-	-	-	-	-	-	-	2.58	-	-
26.72	-	2.44	2.65	-	-	-	-	-	-	-	-	-	-	-	CLIP	-	-	-	-	-	2.48	2.52	2.65	-
31.86	-	2.45	2.65	-	-	-	-	-	-	-	-	-	2.59	-	CLIP	-	-	-	-	-	2.51	2.56	2.48	-
37.00	-	2.59	2.59	-	-	-	-	-	-	-	-	-	2.53	2.73	2.77	-	-	-	-	2.56	2.52	+	2.45	-
42.14	2.33	2.37	2.55	-	2.57	-	2.43	2.50	-	-	2.65	2.64	2.58	2.65	2.81	-	-	-	-	2.43	2.50	+	2.38	-
47.28	+	2.56	+	-	2.56	2.40	2.56	+	2.54	-	2.71	2.50	2.50	2.63	2.75	-	-	-	-	2.43	+	+	2.41	2.45
52.42	+	2.86	+	-	+	2.37	2.48	+	2.51	+	2.59	2.54	2.50	2.51	2.70	-	2.78	2.77	-	+	+	+	+	+
57.56	+	2.69	+	2.58	+	+	2.52	+	2.44	+	2.53	+	2.58	+	2.76	2.70	2.66	2.62	-	+	+	+	+	+
62.70	+	+	+	2.45	+	+	2.52	+	2.49	+	+	+	+	+	2.71	2.52	+	2.60	2.64	+	+	+	+	+
67.84	+	+	+	2.51	+	+	+	+	2.53	+	+	+	+	+	2.78	2.51	+	+	2.89	+	+	+	+	+
72.98	+	+	+	2.54	+	+	+	+	+	+	+	+	+	+	2.78	+	+	+	2.79	+	+	+	+	+
78.12	+	+	+	+	+	+	+	+	+	+	+	+	+	+	+	+	+	+	2.72	+	+	+	+	+
MCAM:	2.33	2.56	2.65	2.54	2.57	2.40	2.52	2.50	2.51		2.65	2.54	2.58	2.65	2.77	2.52	2.78	2.62	2.79	2.43	2.51	2.56	2.45	2.45

STA:	RAY	MOA	MLL	CFT	CKC	ADL	TPO	LRR	BLU	SIL	BTL	RDM	SDW
DIST:	106.	110.	95.	94.	81.	30.	69.	61.	52.	79.	76.	54.	44.
SCAL:	31.	32.	28.	27.	24.	9.	21.	18.	16.	23.	22.	16.	13.
AZ:	35.	23.	31.	21.	20.	10.	265.	303.	333.	48.	34.	29.	57.
11.30	-	-	-	-	-	2.20	-	-	-	-	-	-	-
16.44	-	-	-	-	-	2.44	-	-	CLIP	-	-	+	2.62
21.58	-	-	-	-	-	+	2.50	2.92	2.84	-	-	+	2.68
26.72	-	-	-	-	2.49	+	2.57	2.77	2.75	2.63	2.79	+	+
31.86	2.57	-	2.60	2.53	+	+	2.65	2.73	+	2.54	2.60	+	+
37.00	2.46	2.36	+	+	+	+	2.65	+	+	2.57	2.56	+	+
42.14	2.49	2.52	+	+	+	+	2.61	+	+	2.51	2.55	+	+
47.28	2.46	+	+	+	+	+	2.59	+	+	2.62	2.57	+	+
52.42	2.48	+	+	+	+	+	+	+	+	+	2.61	+	+
MCAM:	2.48	2.52	2.60	2.53	2.49	2.44	2.61	2.77	2.84	2.57	2.60		2.68

Figure 12. Typical output of the program, MCA, for an M_L = 2.8 earthquake in the central Mojave Desert.

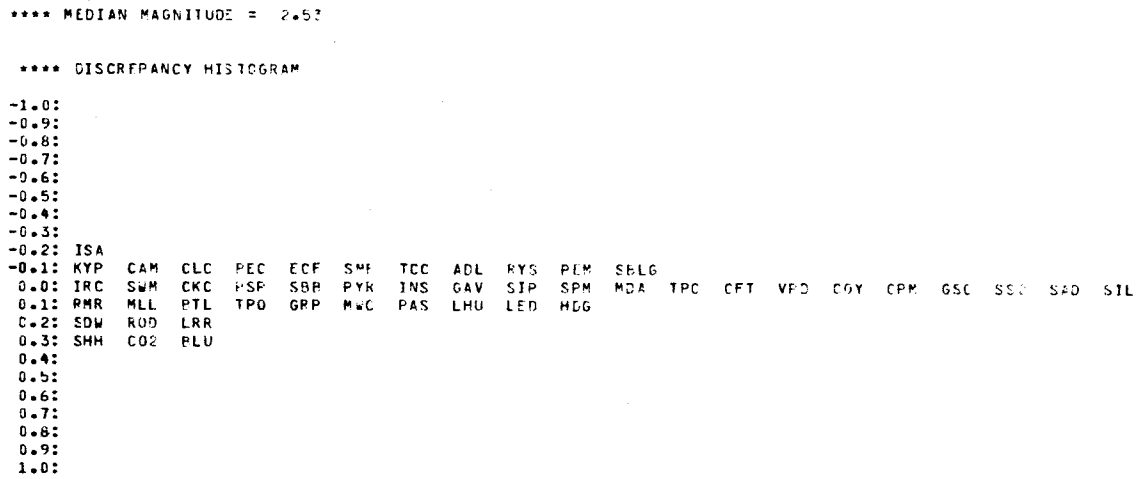

Figure 12. (continued)

of 4.5 that occurred in the aftershock zone of the 1971 San Fernando earthquake. The M_{ca} of 4.58 is in better agreement with M_L than is usually the case for an event this large. An interesting feature of this example is the bimodal nature of the DISCREPANCY HISTOGRAM shown in Figure 13. The smaller peak represents coda segments with amplitudes nearly an order of magnitude less than predicted by the coda amplitude systematics discussed above. The stations comprising this peak are, with two exceptions due to miscalibration, confined to the Imperial Valley and demonstrate quite clearly the "impedance barrier" effect discussed in the preceding section. Fortunately, path dependent problems have only a mild effect on magnitude estimation. If the Imperial Valley stations had been excluded, the result would have been to increase the M_{ca} estimate by less than .03 units of magnitude, illustrating the robust nature of the M_{ca} magnitude method.

COMPARISON WITH DURATION MAGNITUDE SCALE, M_T

The comparison of the coda amplitude magnitude scale, M_{ca}, and the duration magnitude scale, M_τ, proceeds directly from the observation that the amplitude function implicit in the definition of duration magnitude is identical in form to equation (7). It can be directly compared to the expression for duration magnitude given by Real and Teng (1973; Model I)

$$M_\tau = b_o + b_1 \log_{10} \tau_c + b_2 d \qquad (12)$$

where b_o, b_1, and b_2 are site parameters to be determined empirically

STANDARD DECK WITH DELAYS

UNCALIBRATED: SBCC SCAI

EVENT: 129/1
HYPOCENTER: 34 22.94, 118 27.41, 7= 9.15
ORIGIN TIME: 1977/ 3/12 (224) 219 26.11 .67

STA:	GLA	SNS	IKP	VST	FTM	FIC	DRC	NWP	CRR	PLT	SSK	SSY	ISC	SNS	MWC	PAS	TCC	RVR	PEC	CSP	FLM	CIS	CPK
DIST:	367.	135.	291.	177.	433.	449.	147.	294.	294.	342.	73.	170.	31.	5.	67.	41.	47.	19.	109.	131.	142.	117.	108.	204.
SCAL:	94.	38.	76.	50.	109.	99.	42.	77.	75.	99.	22.	48.	16.	3.	26.	12.	11.	18.	32.	38.	42.	31.	28.	58.
AZ:	65.	38.	48.	40.	61.	64.	60.	60.	54.	61.	75.	75.	0.	89.	120.	64.	45.	43.	66.	65.	64.	52.	3.	37.
23.85	-	-	-	-	-	-	-	-	-	-	1.65	-	-	CLIP	CLIP	CLIP	CLIP	CLIP	-	-	-	-	-	-
28.99	-	-	-	-	-	-	-	-	-	-	1.88	-	-	CLIP	CLIP	CLIP	CLIP	CLIP	-	-	-	-	-	-
34.13	-	-	-	-	-	-	-	-	-	-	1.91	-	-	CLIP	CLIP	CLIP	CLIP	CLIP	CLIP	-	CLIP	-	CLIP	-
39.27	-	2.14	-	-	-	-	-	-	-	-	2.10	-	-	CLIP	CLIP	CLIP	CLIP	CLIP	CLIP	CLIP	CLIP	-	CLIP	-
44.41	-	+	-	-	-	-	1.97	-	-	-	2.03	-	-	CLIP	CLIP	CLIP	CLIP	CLIP	CLIP	CLIP	CLIP	-	CLIP	-
49.55	-	+	-	-	-	-	2.22	-	-	-	2.32	CLIP	4.60	CLIP	CLIP	CLIP	CLIP	CLIP	CLIP	CLIP	CLIP	-	CLIP	-
54.69	-	+	-	-	2.75	-	2.44	-	-	-	2.22	CLIP	4.49	CLIP	CLIP	CLIP	CLIP	CLIP	4.31	CLIP	CLIP	CLIP	CLIP	-
59.83	-	+	-	-	2.89	-	2.51	-	-	-	2.32	4.20	4.69	CLIP	CLIP	CLIP	CLIP	CLIP	CLIP	CLIP	CLIP	CLIP	CLIP	CLIP
64.97	-	+	-	-	3.19	-	2.70	-	-	-	+	4.19	4.76	CLIP	CLIP	CLIP	CLIP	CLIP	CLIP	CLIP	CLIP	CLIP	CLIP	CLIP
70.11	-	+	-	-	3.22	-	2.90	-	-	-	+	4.28	4.64	CLIP	CLIP	CLIP	CLIP	CLIP	4.44	CLIP	CLIP	CLIP	CLIP	CLIP
75.25	-	+	-	-	3.12	-	3.02	-	CLIP	-	+	4.15	4.55	CLIP	CLIP	CLIP	CLIP	CLIP	4.46	CLIP	CLIP	CLIP	CLIP	4.55
80.39	-	+	4.21	3.31	-	-	3.12	+	CLIP	-	+	4.16	4.56	CLIP	CLIP	CLIP	CLIP	CLIP	4.36	CLIP	CLIP	CLIP	CLIP	4.52
85.53	-	+	4.27	3.26	-	-	3.11	+	CLIP	-	+	4.32	4.61	CLIP	CLIP	CLIP	CLIP	CLIP	4.28	CLIP	CLIP	CLIP	CLIP	4.64
90.67	-	+	CLIP	3.54	-	-	3.34	+	CLIP	-	+	4.22	4.71	CLIP	CLIP	CLIP	CLIP	CLIP	4.34	CLIP	CLIP	CLIP	CLIP	4.64
95.81	3.66	+	CLIP	3.33	-	-	3.42	+	CLIP	-	+	4.14	4.53	CLIP	CLIP	CLIP	CLIP	CLIP	4.14	CLIP	CLIP	CLIP	CLIP	4.53
100.95	3.81	+	4.37	3.36	-	-	3.62	+	+	-	+	4.40	4.64	CLIP	CLIP	CLIP	CLIP	CLIP	4.28	CLIP	CLIP	CLIP	CLIP	4.63
106.09	CLIP	+	4.53	3.42	-	-	3.73	+	+	CLIP	3.55	+	4.65	CLIP	CLIP	CLIP	CLIP	CLIP	4.17	CLIP	CLIP	CLIP	CLIP	4.52
111.23	CLIP	+	4.55	3.30	3.33	CLIP	+	+	+	CLIP	3.67	+	4.55	CLIP	CLIP	CLIP	CLIP	CLIP	4.53	CLIP	CLIP	CLIP	CLIP	4.52
116.37	CLIP	+	4.30	3.34	3.28	CLIP	+	+	+	CLIP	3.86	+	4.59	CLIP	CLIP	CLIP	CLIP	CLIP	4.61	CLIP	CLIP	CLIP	CLIP	4.64
121.51	CLIP	+	4.50	3.44	3.38	CLIP	+	+	+	CLIP	3.95	+	4.60	CLIP	CLIP	CLIP	CLIP	CLIP	4.56	CLIP	CLIP	CLIP	CLIP	4.68
126.65	CLIP	+	4.39	+	3.47	CLIP	+	+	+	CLIP	CLIP	+	4.60	CLIP	CLIP	CLIP	CLIP	CLIP	4.76	CLIP	CLIP	CLIP	CLIP	4.68
131.79	CLIP	+	4.39	+	3.47	CLIP	+	+	+	CLIP	CLIP	+	4.60	CLIP	CLIP	CLIP	CLIP	CLIP	4.85	CLIP	CLIP	CLIP	CLIP	4.68
136.93	CLIP	+	4.32	+	3.62	CLIP	+	+	+	CLIP	CLIP	+	4.60	CLIP	CLIP	CLIP	CLIP	CLIP	4.69	CLIP	CLIP	CLIP	CLIP	4.68
142.07	CLIP	+	4.33	+	3.56	CLIP	+	+	+	CLIP	CLIP	+	4.08	CLIP	CLIP	CLIP	CLIP	CLIP	4.61	CLIP	CLIP	CLIP	CLIP	4.67
147.21	4.24	+	4.41	+	3.79	CLIP	+	+	+	4.01	4.16	+	+	+	+	+	+	+	+	+	+	+	+	+
152.35	CLIP	+	CLIP	+	3.75	CLIP	+	+	+	CLIP	CLIP	+	+	+	+	+	+	+	+	+	+	+	+	+
MCAM:	3.81	2.14	4.37	3.31	3.47	3.73	2.90			4.01	3.86	2.10	4.00	4.60	4.83		4.79	4.61	4.45	4.22	4.46	4.52		4.61

STA:	TPC	CLC	SWM	FYR	LCL	FMA	SCI	SYC	ISA	GSC	LHU	COY	BCH	CKG	TPR	SELC	YPC	FPM	RVS	SAD	ARL	SMD	PTD	KYP
DIST:	224.	177.	39.	33.	66.	76.	156.	141.	142.	182.	32.	228.	174.	150.	126.	116.	116.	177.	365.	39.	87.	207.	53.	56.
SCAL:	61.	50.	12.	10.	19.	22.	44.	40.	40.	51.	10.	64.	49.	43.	36.	34.	33.	39.	93.	12.	26.	57.	16.	15.
AZ:	81.	154.	197.	232.	22.	12.	357.	264.	181.	124.	173.	60.	240.	231.	232.	264.	226.	246.	83.	336.	234.	62.	323.	306.
49.55	-	-	CLIP	CLIP	4.41	CLIP	CLIP	CLIP	CLIP	-	CLIP		CLIP	CLIP	CLIP	CLIP	CLIP	-		CLIP	CLIP	-	CLIP	CLIP
54.69	-	CLIP	CLIP	CLIP	4.41	4.47	CLIP	CLIP	CLIP	CLIP	CLIP	-	CLIP	CLIP	CLIP	CLIP	CLIP	-		CLIP	CLIP	-	CLIP	CLIP
59.83	-	CLIP	CLIP	CLIP	4.42	4.51	CLIP	CLIP	CLIP	CLIP	CLIP	-	CLIP	CLIP	CLIP	CLIP	CLIP	-		CLIP	CLIP	CLIP	CLIP	CLIP
64.97	CLIP	CLIP	CLIP	CLIP	4.48	4.63	CLIP	CLIF	CLIP	CLIP	CLIP	CLIP	CLIP	CLIP	CLIP	CLIP	CLIP	-		CLIP	CLIP	4.14	CLIP	CLIP
70.11	CLIP	CLIP	CLIP	CLIP	4.61	4.52	CLIP	CLIP	CLIP	CLIP	CLIP	CLIP	CLIP	CLIP	CLIP	CLIP	CLIP	-		CLIP	CLIP	4.25	CLIP	CLIP
75.25	CLIP	CLIP	CLIP	CLIP	4.62	4.60	CLIP	CLIF	CLIP	CLIP	CLIP	CLIP	CLIP	CLIP	CLIP	CLIP	CLIP	-		CLIP	CLIP	4.25	CLIP	CLIP
80.39	CLIP	CLIP	CLIP	CLIP	4.51	4.63	CLIF	CLIF	CLIP	CLIP	CLIP	CLIP	CLIP	CLIP	CLIP	CLIP	CLIP	-		CLIP	CLIP	4.35	CLIP	CLIP
85.53	CLIP	CLIP	CLIP	CLIP	4.56	4.57	CLIF	CLIF	CLIP	CLIP	CLIP	CLIP	CLIP	CLIP	CLIP	CLIP	CLIP	-		CLIP	CLIP	4.42	CLIP	CLIP
90.67	CLIP	CLIP	CLIP	CLIP	4.65	4.51	CLIF	CLIF	CLIP	CLIP	CLIP	CLIP	CLIP	CLIP	CLIP	CLIP	CLIP	-		CLIP	CLIP	4.30	CLIP	CLIP
95.81	CLIP	CLIP	CLIP	CLIP	4.63	4.49	CLIP	CLIP	CLIP	CLIP	CLIP	CLIP	CLIP	CLIP	CLIP	CLIP	CLIP	CLIP		CLIP	CLIP	4.23	CLIP	CLIP
100.95	CLIP	CLIP	CLIP	CLIP	4.58	4.52	CLIF	CLIF	CLIP	CLIP	CLIP	CLIP	CLIP	CLIP	CLIP	CLIP	CLIP	CLIP		CLIP	CLIP	4.29	CLIF	CLIP
106.09	CLIP	CLIP	CLIP	CLIP	4.55	4.50	CLIF	CLIF	CLIP	CLIP	CLIP	CLIP	CLIP	CLIP	CLIP	CLIP	CLIP	CLIP		CLIP	CLIP	4.30	CLIP	CLIP
111.23	CLIP	CLIP	CLIP	CLIP	4.55	4.56	CLIP	CLIF	CLIP	CLIP	CLIF	CLIP	CLIP	CLIP	CLIP	CLIP	CLIP	CLIP		CLIP	CLIP	4.34	4.30	CLIP
116.37	CLIP	CLIP	CLIP	CLIF	4.51	4.43	4.53	CLIP	CLIF	CLIF	CLIF	CLIP	CLIP	CLIP	CLIP	CLIP	CLIP	CLIP		CLIP	CLIP	4.26	4.10	CLIP

Figure 13. Typical output of the program, MCA, for an M_L = 4.5 aftershock of the 1971 San Fernando earthquake.

Figure 13. (continued)

```
**** MEDIAN MAGNITUDE =  4.48

     **** DISCREPANCY HISTOGRAM

 -1.0: SSK  SNS  DH2  VST  FTM
 -0.9:
 -0.8:
 -0.7: PIC  GLA
 -0.6: PLT
 -0.5: CRR
 -0.4:
 -0.3: COT  SBSN PTD  FSP  WWR  IRS  AVR
 -0.2: KEE  BC2  SMO  BLU  RMP  HPG  SME
 -0.1: SYP  SBSC POB  LRR  GAV  IKP  SHH  GRP  MDA  LTC  CFT  RTL  PWM  TMC  AVS  SELP
  0.0: SS2  TCC  CPM  SDW  PEC  BCH  CLC  COY  CIS  LCL  LHU  FTC  RAY  CKC  SIL  FSP  FMA  VCC
  0.1: SCI  CRG  YEG  LED  RDM  AEL  PCF  CPE  SAO  SELG ADL  SPM  BMT  SCY  MLL  FAS  GSC  KYS  SAM  KYP
  0.2: IRN  PKM  ISA  SBLC PEM
  0.3: MWC  PYR
  0.4: IRC
  0.5:
  0.6:
  0.7:
  0.8:
  0.9:
  1.0:
```

Figure 13. (continued)

from a suite of earthquakes with known local magnitude, M_L. Real and Teng defined the total duration, τ_c, as "the time interval between the onset of the first arrival and the point at which the earthquake signal falls and remains below the background noise level". This choice is fortunate, since normalizing the cutoff amplitude to the noise level removes the requirement of knowing the constant of proportionality relating digitizer counts and trace amplitude on a microfilm viewer. For purposes of comparison we will calculate the duration from the coda amplitude function, equation (7), at which the amplitude falls below the mean background noise level, ε_{50}. The background noise level must be calculated independently for each station of the network. As a matter of convenience values of ε_{50} were derived from previously determined values of the ninetieth percentile background noise level, ε_{90} in Table 2, by assuming that background noise sampled at random obeys a Poisson distribution. This calculation is unique since the Poisson distribution has a single controlling parameter. Values of ε_{90} had been assembled in order to calculate ninetieth percentile detection threshhold contours for the Southern California network (Chapter 3).

The method of calculation was simply to compile a set of noise samples for a particular station, sort them in ascending order, and then extract the ninetieth percentile element from this list. The noise samples used were the pre-event background noise levels, $\overline{\overline{r}}$, calculated by the real-time CEDAR system event detector. Values of both ε_{90} and ε_{50} are provided in Table 2.

τ_c can be related to ε_{50} through equation (11) to give

$$M_{ca} = \log_{10} \epsilon_{50} - A_o + q \log_{10} \tau_c \qquad (13)$$

This can be directly equivalenced to equation (12) if one makes the associations $b_o = \log_{10} \epsilon_{50} - A_o$, $b_1 = q$, and $b_2 = 0$. Setting the distance term to zero is justifiable since it is of little consequence for distances as great as 200 km. Had the distance term been ignored in the original study by Real and Teng (1973) the effect on the coefficients b_o and b_1 would certainly have been mild. Seven of the stations calibrated by Real and Teng (1973) were also calibrated in the current study. This allows a direct numerical comparison by calculating the site parameters b_o and b_1 in terms of the coda amplitude site parameters A_o and q for the common stations. The results of this comparison are given in Table 3.

The agreement between these two studies is remarkable and clearly demonstrates that the variation of site parameters from station to station is both real and apparently temporally stable.

Using the formulae developed above it appears feasible to extend Real and Teng's (1973) result to the rest of the Southern California network, thus allowing the calculation of duration magnitudes from develocorder films for periods prior to the development of the digital CEDAR system. This should be of particular interest to those conducting local and microearthquake studies in Southern California since the importance of having each station individually calibrated increases with decreasing magnitude. Values of b_o and b_1 of equation (12) have been calculated for all stations in the Southern California network and their values have been included in Table 2.

TABLE 3

COMPARISON OF THE DURATION MAGNITUDE PARAMETERS, b_0 AND b_1 AS APPLIED IN THE FORMULA

$$M_T = b_0 + b_1 \text{Log}_{10} T$$

OF REAL AND TENG (1973) WITH SIMILAR VALUES DERIVED FROM THE M_{CA} CALIBRATION PARAMETERS (TABLE 3)

	Real and Teng (1973)		Derived from M_{CA} Parameters	
STA	b_0	b_1	b_0	b_1
SYP	- .68	1.75	- .59	1.80
PAS	.03	1.48	- .33	1.36
MWC	- .31	1.67	- .91	1.83
GSC	- .81	1.74	- .87	1.62
ISA	-1.36	2.01	-1.18	2.08
GLA	- .78	1.73	-1.08	1.56
PLM	- .90	1.78	- .86	1.69

COMPARISON WITH RICHTER MAGNITUDE, M_L

The comparison with local Richter magnitude is somewhat less direct than is the case for duration magnitude. In Figure 14 coda amplitude magnitudes are compared to the corresponding Richter magnitudes for the 85 standard earthquakes. The solid line represents equality between the two magnitude scales. A scatter of one or two tenths in M_L could account for much of the scatter shown in Figure 14, especially since fluctuations in M_L enter the problem when comparing the two scales as well as in the calibration process. The slight trend toward underestimation of events greater than magnitude 3 is evident in Figure 14. The application of the coda magnitude method to earthquakes recorded in the first four months of 1977 confirms this trend (L.K. Hutton, personal communication).

Another way of comparing these two magnitude scales is by calculating the explicit distance dependence of the coda amplitude scale. This can be directly compared with the Richter magnitude distance correction which can be simply interpreted as the logarithm of the maximum peak to peak amplitude of a $M_L = 0$ earthquake at the specified distance.

The coda segment that begins with the arrival of S is expected to have the largest average amplitude. The largest peak to peak amplitude used for calculation of M_L is also generally found within this time interval. The distance dependence of the average amplitude of the coda segment beginning with the S arrival can be examined by setting τ to τ_s in equation (7) and calculating

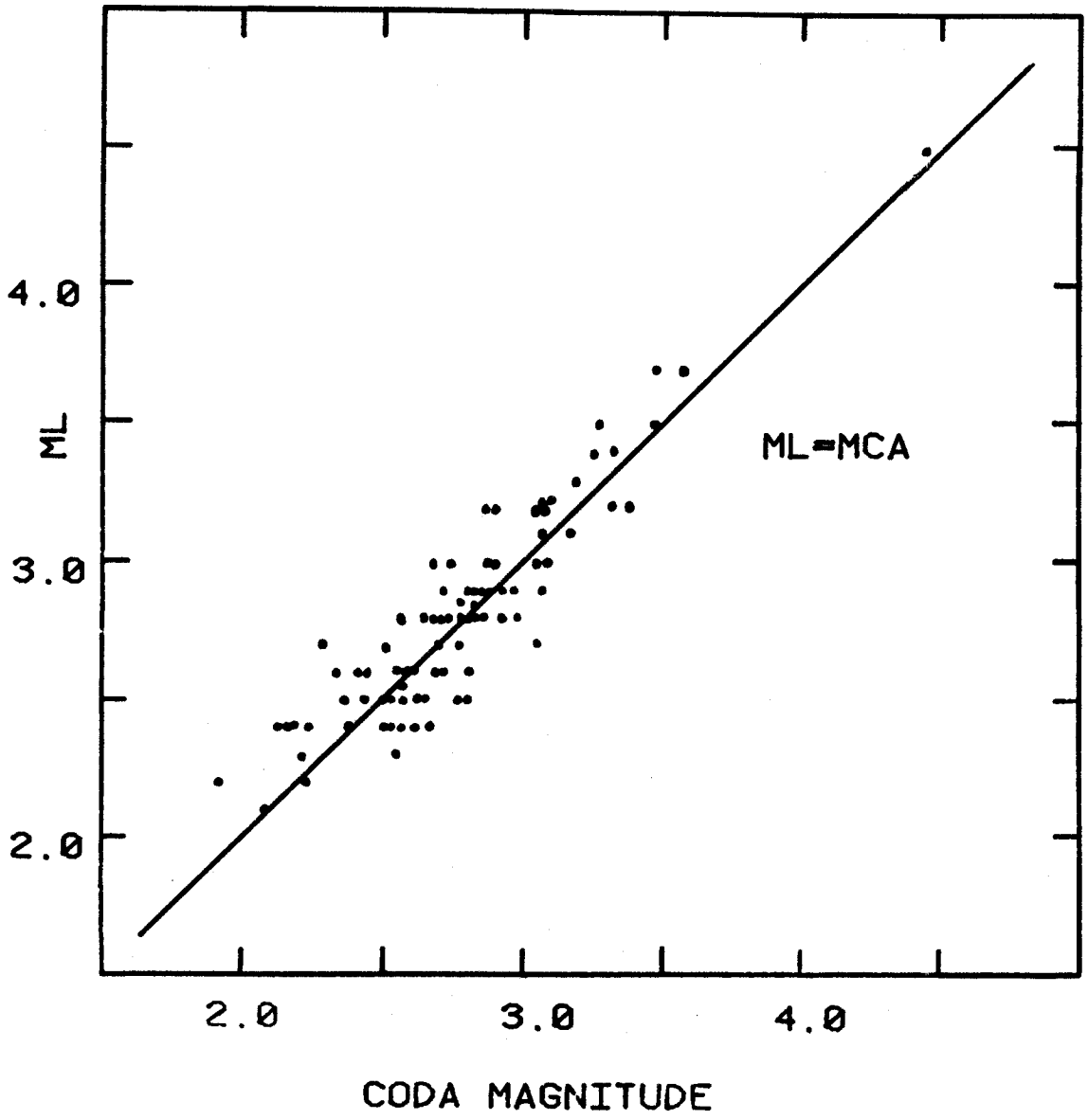

Figure 14. Comparison of local magnitude, M_L, and coda amplitude magnitude, M_{CA}, for the set of "85 standard earthquakes". The line of slope 1 represents equality between the two magnitude scales.

$$a(\tau_s,d,M_L) \cong a(d/8,d,M_L) = 10^{A_o+M_L}(d/8)^{-q} \qquad (14)$$

This calculation is illustrated schematically in Figure 15.

The comparison between the Richter magnitude distance correction and the assumptions underlying the coda amplitude scale is made explicitly in Figure 16. The open circles are the Richter magnitude distance corrections to peak amplitudes measured on a Wood-Anderson torsion seismogram in milimeters (Richter, 1958; Table 22-1). They can be interpreted as the base 10 logarithms of the peak amplitudes of a $M_L = 0$ earthquake at the indicated distances. The corresponding values for the maximum average amplitude calculated from equation (14) is shown as a solid curve. A value of 1.8 was used for "q" which represents a median of the value obtained for bedrock sites as shown in Figure 10. The constant of proportionality was selected so as to provide agreement at a distance of 100 km. The similarity between these two curves is striking with the differences less than .1 magnitude units for most of the distance range of 20 to 300 km.

CONCLUSIONS

A systematic examination of the decay characteristics of the post S coda has revealed that an adequate description is provided by a simple geometric decay law. This decay law turned out to be an implicit assumption of the duration magnitude method establishing a close parallelism between the duration magnitude scale and the coda amplitude scale, M_{ca}, developed in this paper. Techniques were

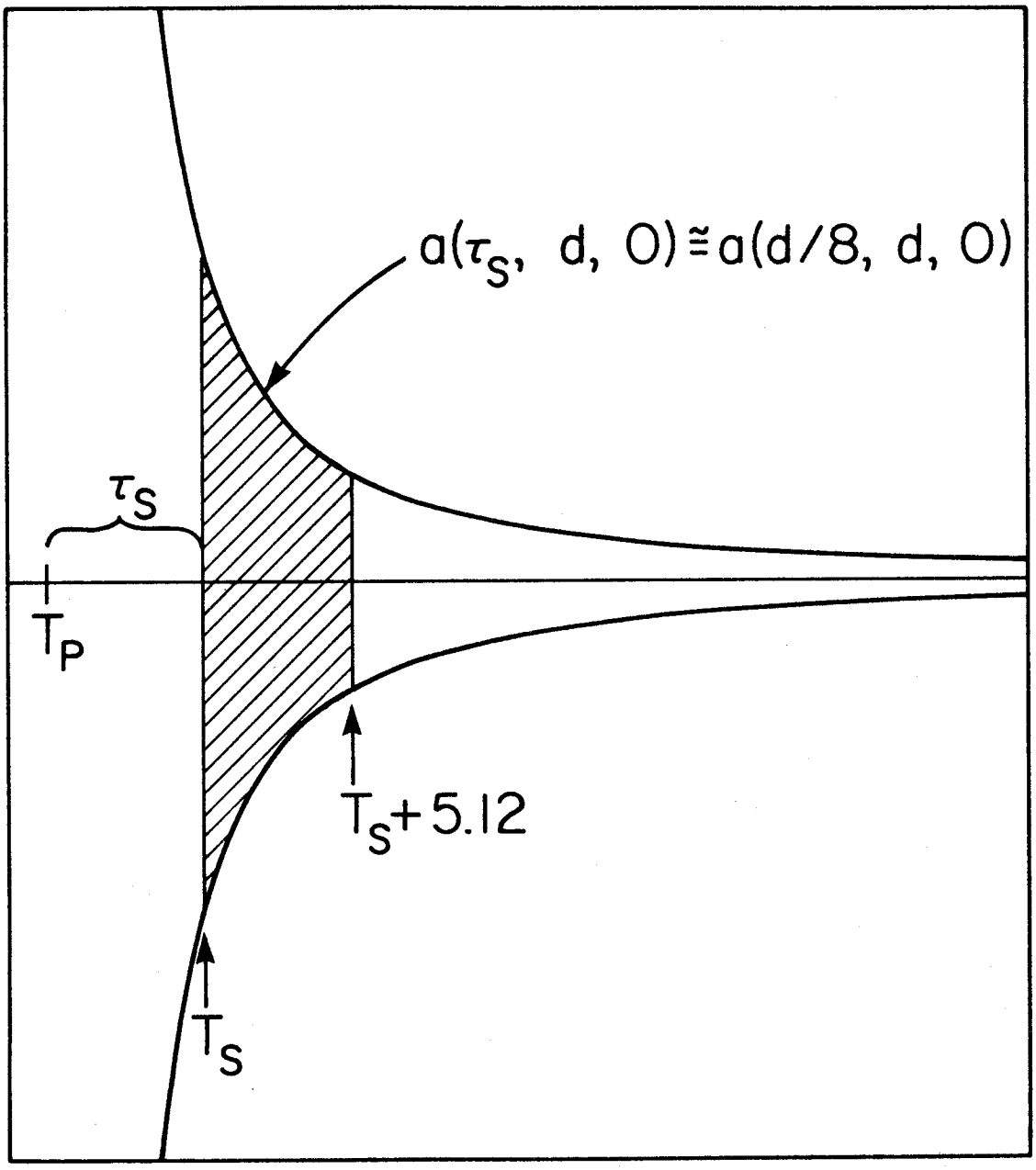

Figure 15. Schematic diagram illustrating approach used in calculating the peak average coda amplitude for direct comparison with the local magnitude distance correction in Figure 16.

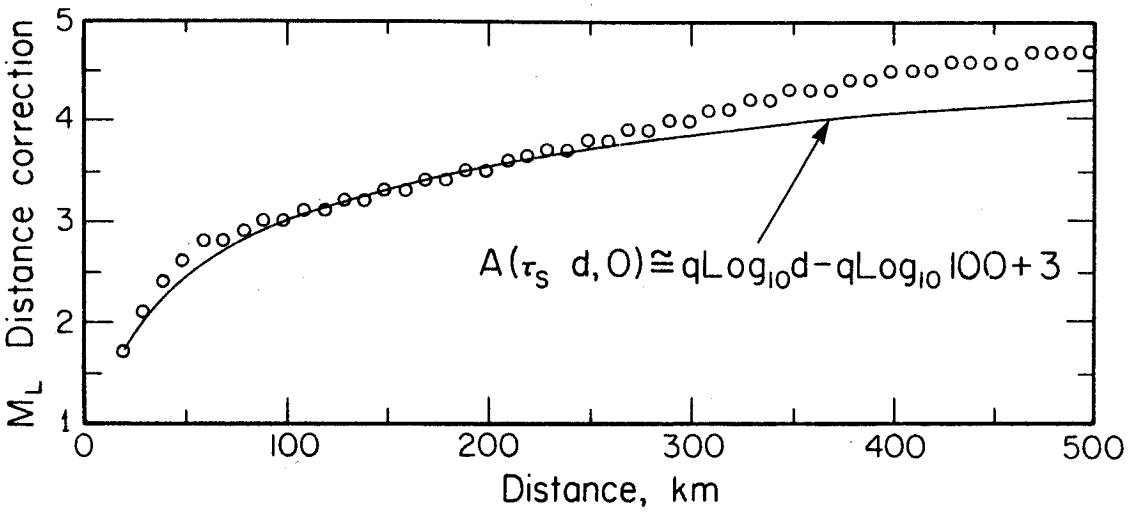

Figure 16. Comparison between the local magnitude, M_L, distance correction (open circles) and the largest average coda amplitude (solid line). The coda amplitude curve has been adjusted by a fixed gain in order to force agreement at a distance of 100 km.

developed for calibrating the two site dependent constants, A_o and q, for a particular station as well as for generating a magnitude estimate from a suite of digitized short-period seismograms. It was argued that as a result of changes in the scaling laws for small earthquakes, a tendency toward underestimation for events larger than about M_L = 3.0 might be encountered. During the calibration path dependent phenomenon were discovered which appear to have considerable bearing on discussions of micronization and strong motion prediction.

REFERENCES

Aki, K. (1969). Analysis of the seismic coda of local earthquakes as scattered waves, J. Geophys. Res., 74, 615-631.

Aki, K. and B. Chouet (1975). Origin of coda waves: source, attenuation and scattering effects, J. Geophys. Res., 80, 3322-3342.

Bakun, W. H. and A. G. Lindh (1977). Local magnitudes, seismic moments, and coda durations for earthquakes near Oroville, California, Bull. Seism. Soc. Am., 67, 615-629.

Chouet, B., K. Aki and M. Tsujiura (1978). Regional variation of the scaling law of earthquake source spectra, Bull. Seism. Soc. Am., 68, 49-79.

Claerbout, J. F. (1976). Fundamentals of Geophysical Data Processing With Applications to Petroleum Prospecting, McGraw-Hill Book Co., New York, St. Louis, San Francisco.

Claerbout, J. F. and F. Muir (1973). Robust modeling with erratic data, Geophysics, 38, 826-844.

Crosson, R. S. (1972). Small earthquakes, structures, and tectonics of the Puget Sound region, Bull. Seism. Soc. Am., 62, 1133-1177.

Gutenburg, B. (1956). Effects of ground on shaking in earthquakes, Trans. Am. Geophys. Un., 37, 757-760.

Hanks, T. C. and M. Wyss (1972). The use of body-wave spectra in the determination of seismic-source parameters, Bull. Seism. Soc. Am., 62, 561-589.

Hermann, R. B. (1975). The use of duration as a measure of seismic moment and magnitude, Bull. Seism. Soc. Am., 65, 899-913.

Johnson, L. R. and T. V. McEvilly (1974). Near-field observations and source parameters of central California earthquakes, Bull. Seism. Soc. Am., 64, 1855-1886.

Kanamori, H. (1972). Relation between tectonic stress, great earthquakes and earthquake swarms, Tectonophysics, 14, 1-12.

Lanczos, C. (1961). Linear Differential Operators, Van Nostrand Co., Ltd., London.

Lee, W. H. K., R. E. Bennet, and K. L. Meagher (1972). A method of estimating magnitude of local earthquakes from signal duration, U. S. Geol. Surv. Open-File Report, Washington, D.C.

Real, C. R. and T. Teng (1973). Local Richter magnitude and total signal duration in southern California, Bull. Seism. Soc. Am., 63, 1809-1827.

Richter, C. F. (1935). An instrumental earthquake magnitude scale, Bull. Seism. Soc. Am., 25, 1-31.

Richter, C. F. (1958). Elementary Seismology, W. H. Freeman and Co., San Francisco.

Richter, C. F., C. R. Allen, and J. M. Nordquist (1958). The Desert Hot Springs earthquakes and their tectonic environment, Bull. Seism. Soc. Am., 48, 315-337.

Sato, H. (1977a). Energy propagation including scattering effects -- single isotropic scattering approximation, J. Phys. Earth, 25,27-41.

Sato, H. (1977b). Single isotropic scattering model including wave conversions -- simple theoretical model of the short-period body wave propagation, J. Phys. Earth, 25, 163-176.

Sato, H. (1978). Mean free path of S-waves under the Kanto District of Japan, J. Phys. Earth, 26, 185-198.

Suteau, A. M. and J. H. Whitcomb (1979). A local earthquake coda magnitude and its relation to duration, moment M_o, and local Richter magnitude M_L (in press).

Thatcher, W. and T. C. Hanks (1973). Source parameters of southern California earthquakes, J. Geophys. Res., 78, 8547-8576.

Wyss, M. and J. N. Brune (1968). Seismic moment, stress, and source dimensions for earthquakes in the California-Nevada region, J. Geophys. Res., 73, 4681-4694.

CHAPTER 3

EVALUATION OF THE DETECTION CAPABILITY OF THE CEDAR SYSTEM EVENT DETECTION ALGORITHM

INTRODUCTION

The problems of management associated with the operation of a triggered, digital seismic network (Chapter 1) are quite different from those encountered with manual processing of film based systems. One of the most severe of these is insuring the adequacy of detection. Unlike continuously recording systems, the failure of a triggered system to detect can result in an irretrievable loss of data. Although at Caltech we are continuing to record the Southern California network (Figure 1) on Develocorder film, the cost of recovering data from this media becomes prohibitive if required frequently. To overcome this situation we need to be able to predict *a priori* the response of the network to an earthquake of given magnitude within our region of principal coverage.

At present our results are quite preliminary, and considerable work remains with respect to refinement of network calibration (as discussed in Chapter 2), understanding the statistical and time-dependent properties of background noise, and completing the development of the stochastic model controlling CEDAR system detection. The exigency of the situation demands that we develop and implement a preliminary approach to detection evaluation utilizing simplified assumptions and a less than complete analysis of controlling parameters. It is hoped that an attitude of conservatism can compensate for inadequacies in the model when applying this scheme to the problems of network tuning and adjustment of the parameters influencing detection capability.

The purpose of this chapter is to discuss current progress towards

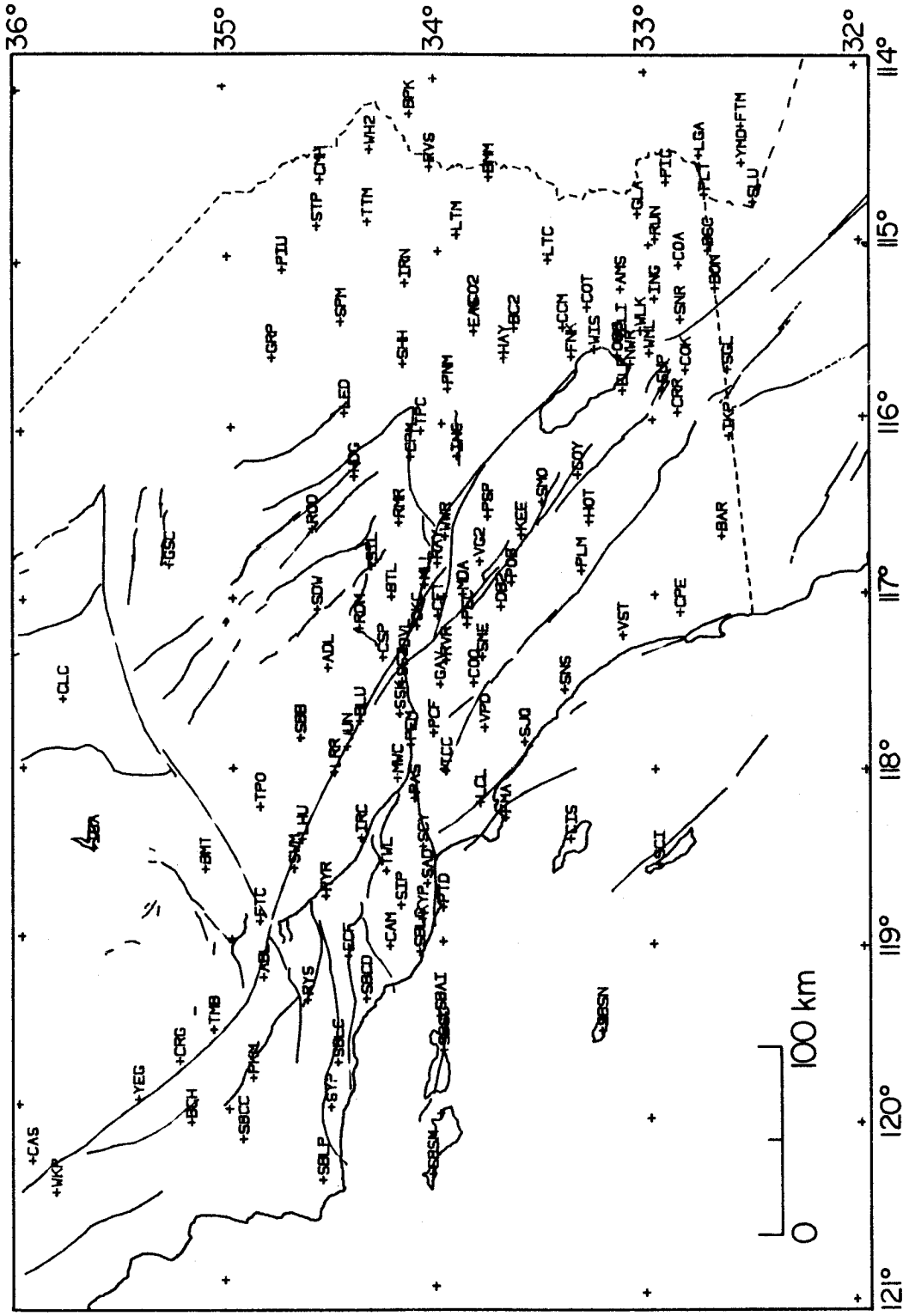

Figure 1. Permanent stations of the Southern California Seismic Network (SCARLET)

this goal. It is not our intention either to review or to contribute to the general problems of network detection evaluation or methods of network optimization in a general sense. Our interest is restricted to the problem of development of a means of predicting the performance of the CEDAR system detection algorithm as detailed in Chapter 1. Although it is anticipated that a more complete analysis will eventually emerge from these efforts, it is beyond the scope of the present discussion.

Initially detection parameters were specified in a rather ad hoc manner. The real-time system discussed in Chapter 1 was operated for nearly three months while event identification and timing relied on the scanning and analysis of Develocorder film. This learning period allowed the correction of some of the more severe gaps in coverage. Subsequent to adopting the CEDAR system as our primary routine analysis system the U.S.G.S. continued to scan and time film data for several months providing an extremely important check on the successes and failures of the detection configuration. Several additional refinements were required during this period.

While this project is born of necessity, several additional benefits accrue from its solution. The question of homogeneous coverage did not arise with the development of triggered digital systems, although it did become more acute. It has long been known that the effectiveness of available sites varies both regionally and locally. For example, stations located along coast lines suffer far greater noise problems than those located futher inland. Thus a higher station density is required to compensate for higher noise

levels in order to maintain homogeneous coverage. Previously there was no means of prescribing just what station density was required, nor was it possible to predict what the local magnitude threshold might be given a particular station distribution. The assessment of network performance requires the analysis of the capabilities of each individual site. Ineffective stations can be moved or replaced such as to optimize the distribution of available fixed resources.

INDIVIDUAL STATION ANALYSIS

The detection logic used by the CEDAR system is a straightforward application of an amplitude ratio trigger coupled with a condition for local coincidence. The amplitude ratio scheme controls the triggering of individual stations independently. The local coincidence criterion is then applied at the network level to determine what configurations of simultaneously triggered stations will precipitate a network trigger condition deflecting the incoming digitized data stream to tape. Thus we will first discuss the conditions for single station triggering and then extend the discussion to overall network response. The notation and variable names used in this chapter are consistent with those of Chapters 1 and 2.

Without loss of generality we can restrict our attention to the case of constant long term noise, $\bar{r}$, since we will only need to consider for our purposes the first several seconds of the S onset. The contribution of the P coda to $\bar{r}$ (see Chapter 1 for definition) is negligible for situations of marginal triggering. We can also assume that the signal has zero bias allowing us to express the

detection criterion at a single station for the i^{th} sample as

$$\bar{r}_i - \frac{3}{2}\bar{\bar{r}} - 8 > 0 \qquad (1)$$

The short-term rectified average, $\bar{r}_i$, is calculated using

$$\bar{r}_i = \frac{1}{256} \sum_{j=0}^{255} |s_i| \qquad (2)$$

where s_i is the i^{th} element of the digitized signal. For purposes of network coincidence analysis the triggering condition represented by relation (1) persists once met for 30 seconds.

The magnitude scale, M_{CA}, developed in Chapter 2 was intentionally predicated on coda amplitude averages calculated according to equation (2), permitting a direct analysis of the single station triggering condition represented by expression (1) in terms of magnitude and distance. The expected coda amplitude average beginning at the i^{th} sample can be written

$$r_i = 10^{A_o + M_L} (t_i - t_p)^{-q} \qquad (3)$$

where A_o and q are parameters that must be calculated for each station of the network individually, t_i is the time associated with the i^{th} digital sample, and t_p is the time of the P onset. Values for A_o and q were obtained for the entire network in Chapter 2 (Table 2). The distribution of these parameters for the Southern California network is shown in Figure 2. The open circles are associated with the anomalously slow coda decay rates for stations in deep quaternary basins.

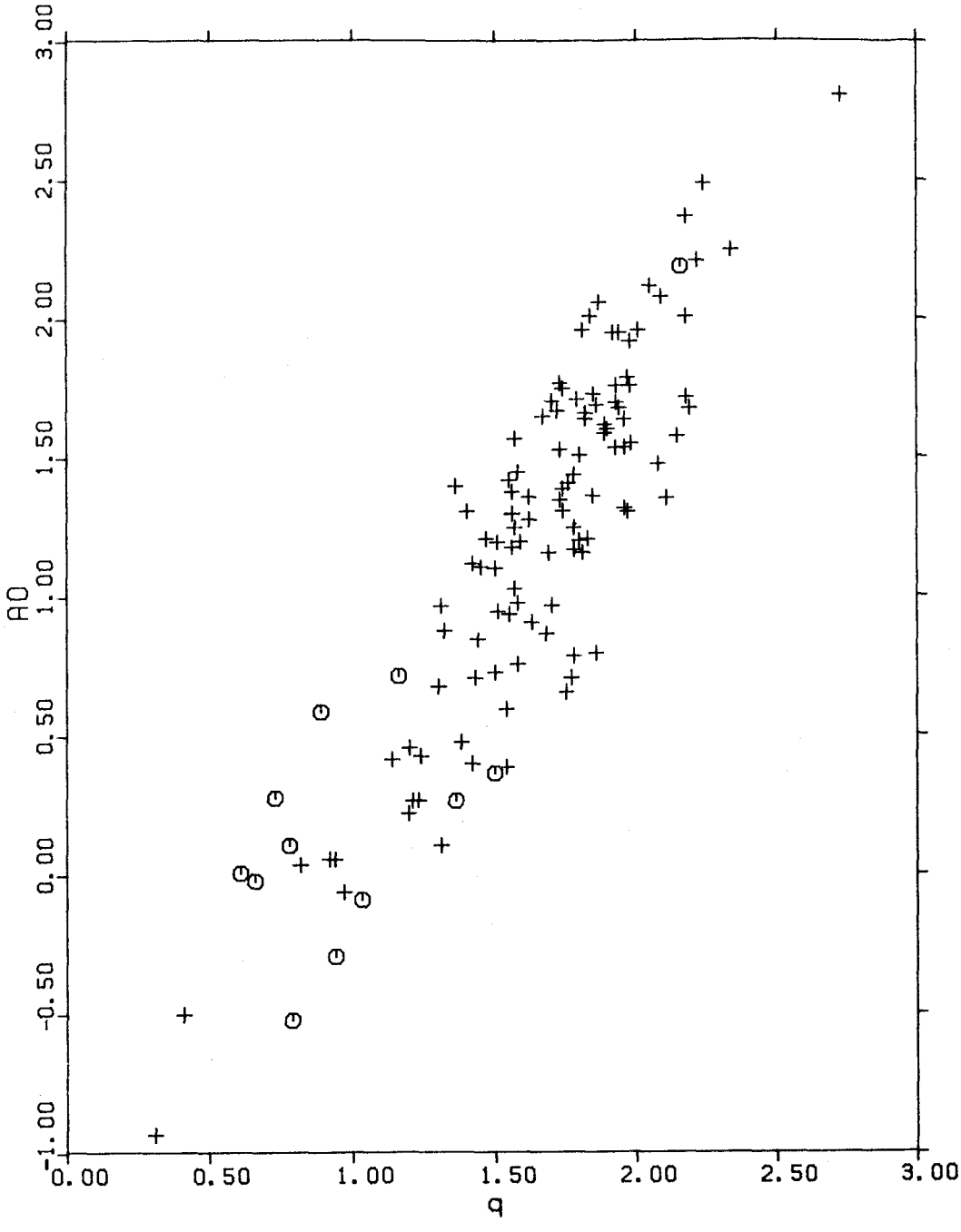

Figure 2. Distributions of M_{CA} calibration parameters for stations of the Southern California Seismic Network. Open circles denote stations situated on deep quaternary basins.

For the smallest detectable events triggering is controlled by the amplitude of the beginning of the S coda. Detection probability is maximum for intervals beginning at the S-wave onset, decreasing monotonically thereafter. Since the detection logic recycles every 6.7, seconds a conservative requirement for triggering is that expression (1) should remain positive for at least 6.7 seconds past the S-wave arrival time. Theoretically larger events will then always be detected while smaller events will be detected with a probability proportional to the fraction of 6.67 seconds that the triggering condition remains positive. This condition will be met if M_L satisfies the relation

$$10^{A_o + M_L} (t_s + 6.67 - t_p)^{-q} - \overline{\overline{r}} - 8 > 0 \qquad (4)$$

which can be related explicitly to the hypocentral distance in kilometers as

$$10^{A_o + M_L} (\frac{d}{8} + 6.67)^{-q} - \overline{\overline{r}} - 8 > 0 \qquad (5)$$

From equation (5) we can develop an explicit method of ranking the stations of the network by considering the smallest magnitude satisfying condition (4) at a specified fixed distance. In particular, we can look at the locus of station calibration parameters, A_o and q, such that the detection threshold at a given distance is some specific magnitude. To accomplish this we write equation (5) in the form

$$A_o = q \log_{10} (\frac{d}{8} + 6.7) + \log_{10} (\overline{\overline{r}} + 8) - M_L \qquad (6)$$

As an example of the application of expression (6) we have plotted the family of curves associated with detection thresholds of M_L = 0, 1, 2, and 3 at a distance of 50 km in Figure 3. Calibration parameters for the stations of the Southern California network are shown as crosses. Figure 3 shows an ideal situation in which all sites are assumed to be noise-free. A more realistic presentation is given in Figure 4 where the gain parameter, A_o, has been replaced by the quantity

$$A_o + \log_{10}(8) - \log_{10}(\epsilon_{90} + 8)$$

in order to include the effect of ambient site noise. Values of the noise estimate, ϵ_{90}, were obtained by ranking random noise samples for each station and then selecting the ninetieth percentile element from the resulting list. Provided the station calibration is sufficiently accurate, this means that we are looking at a magnitude threshold in detection at least 90% of the time. Values of ϵ_{go} for the Southern California network are provided in Table 2 of Chapter 2. The inclusion of station noise level results in a decrease in detection threshold of nearly 1 magnitude unit.

A rather interesting general observation emerges from a consideration of Figures 3 and 4. It seems that stations with a more rapid coda amplitude decay constant, q, are also the most sensitive with respect to detection capability. Such stations are generally situated on massive bedrock outcrops and are often said to be more "transparent" because of the greater simplicity of their seismograms. On the other end of the distribution one

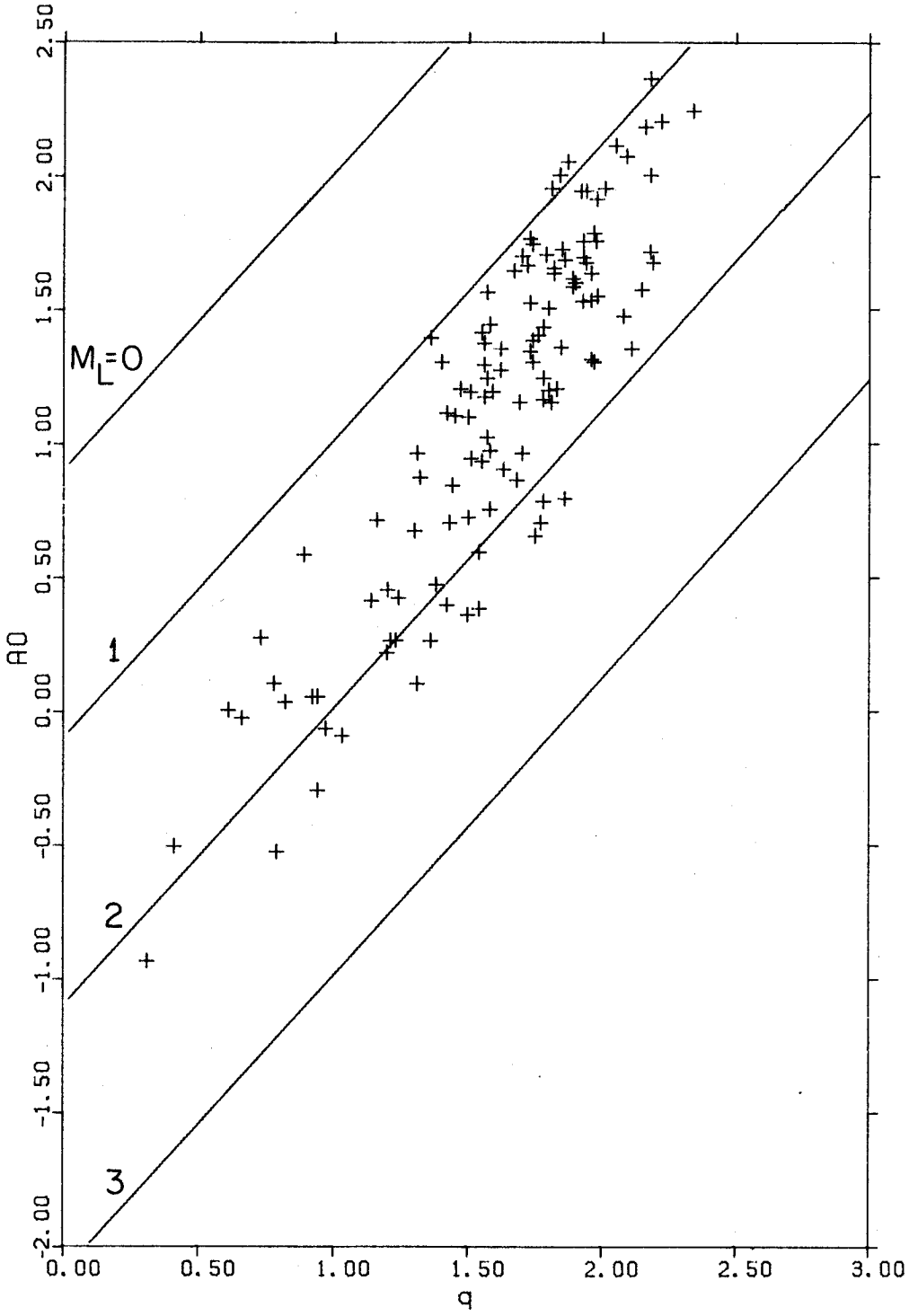

Figure 3. Theoretical noise free magnitude thresholds for the stations of the Southern California Seismic Network at a distance of 50 km. Note the tendency of sites with a high coda decay constant, q, to trend toward lower magnitude thresholds.

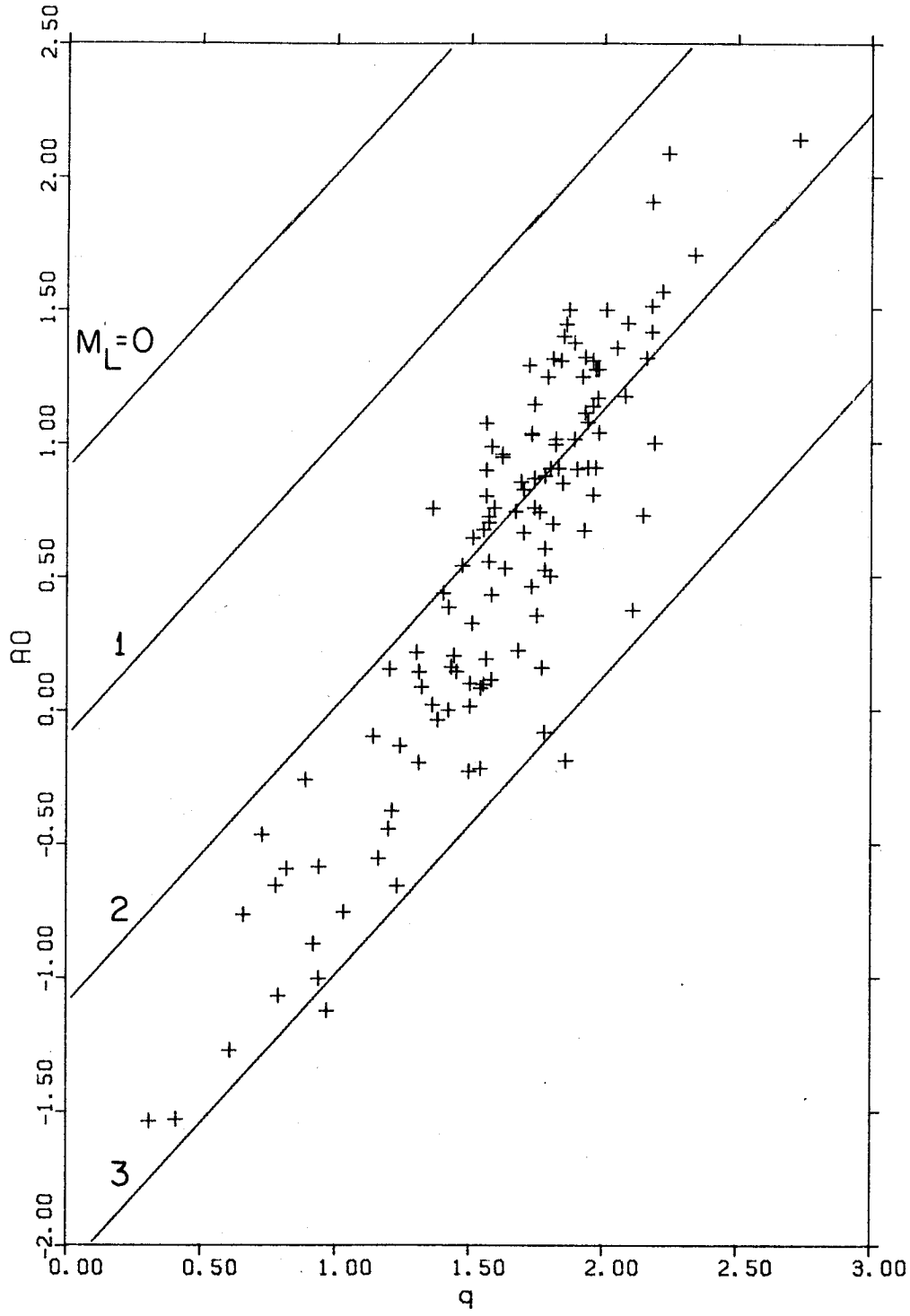

Figure 4. Theoretical 90th percentile magnitude detection thresholds for the stations of the Southern California Network calculated for a distance of 50 km. Stations have been shifted vertically by an amount determined by the ambient background noise level.

finds those sites associated with deep quaternary basins (Figure 2). Such sites manifest high noise levels, more complex waveforms suggesting substantial reverberation, and poor detection capability. Although this conclusion is consistent with "common sense" it is important to be able to quantify it in an objective manner.

The above analysis provides a means of ranking the effectiveness of various stations at a fixed distance. The station order might be quite different at other distances. To explore this possibility further we have graphed the ninetieth percentile detection magnitude as a function of distance in Figure 5 for all calibrated stations of the Southern California network. These curves represent the expression.

$$M_L = q \log_{10} \left(\frac{d}{8} + 6.7\right) + \log_{10} \left(\varepsilon_{90} + 8\right) - A_o \qquad (7)$$

At any given distance the spread in detection threshold spans about 1 magnitude unit. This suggests that apart from regional noise variations, considerable improvement in network performance may be attainable by means of a judicious relocation or replacement of an identifiable subset of the network.

The question might arise as to what proportion of the scatter in Figure 5 can be attributed to imprecision of the calibration process. This possibility is addressed in Figure 6 where we show curves similar to those in Figure 5 except that now each curve represents the results of an independent calibration for a single station (RMR). Each pair of calibration parameters, A_o and q, were obtained from a single event using only records for which at least 8 successive coda

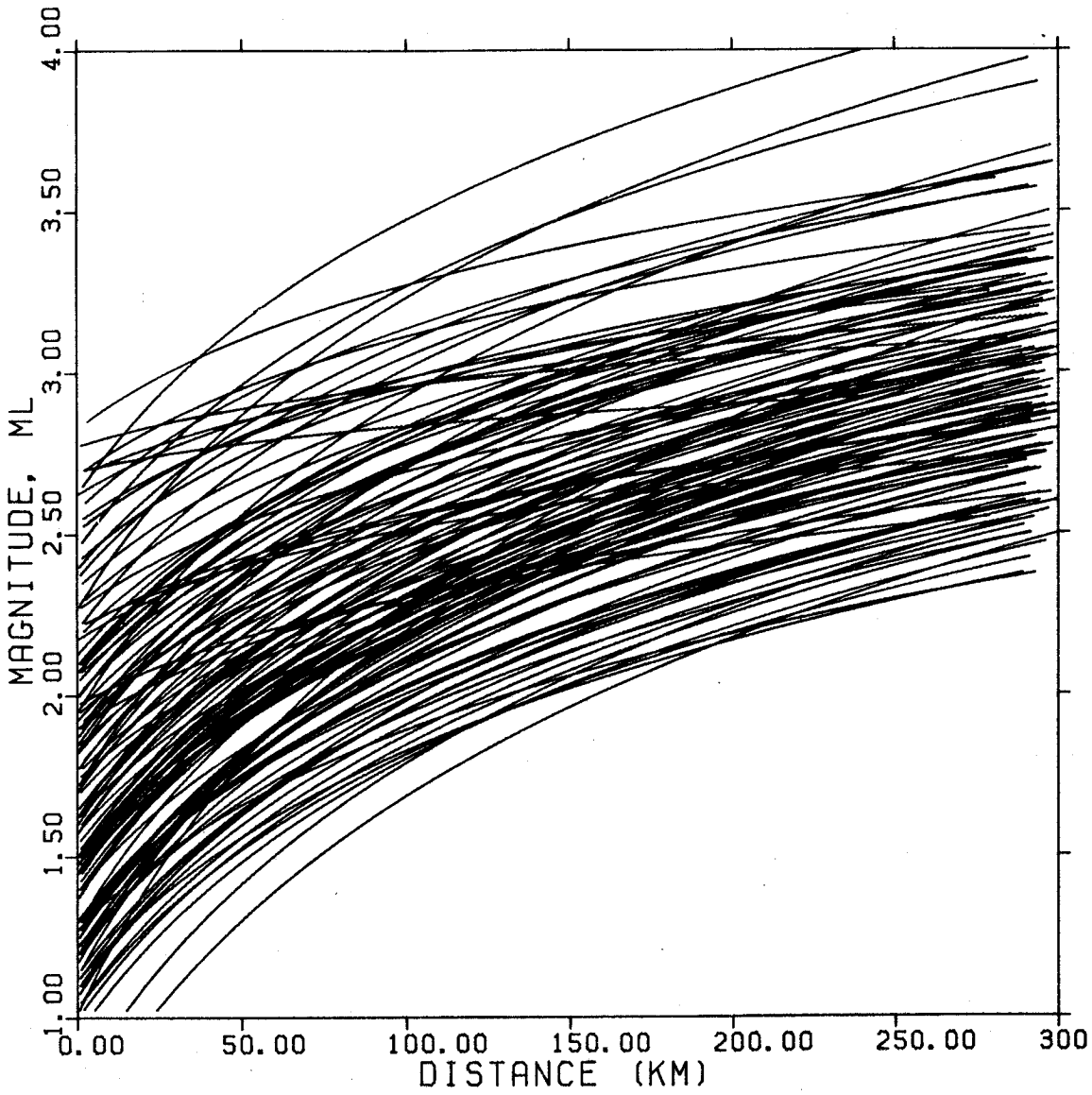

Figure 5. Theoretical 90th percentile magnitude detection thresholds plotted as a function of distance. Each curve represents the response of a single site. Detection capability for various stations spans a range of 2 magnitude units at all distances.

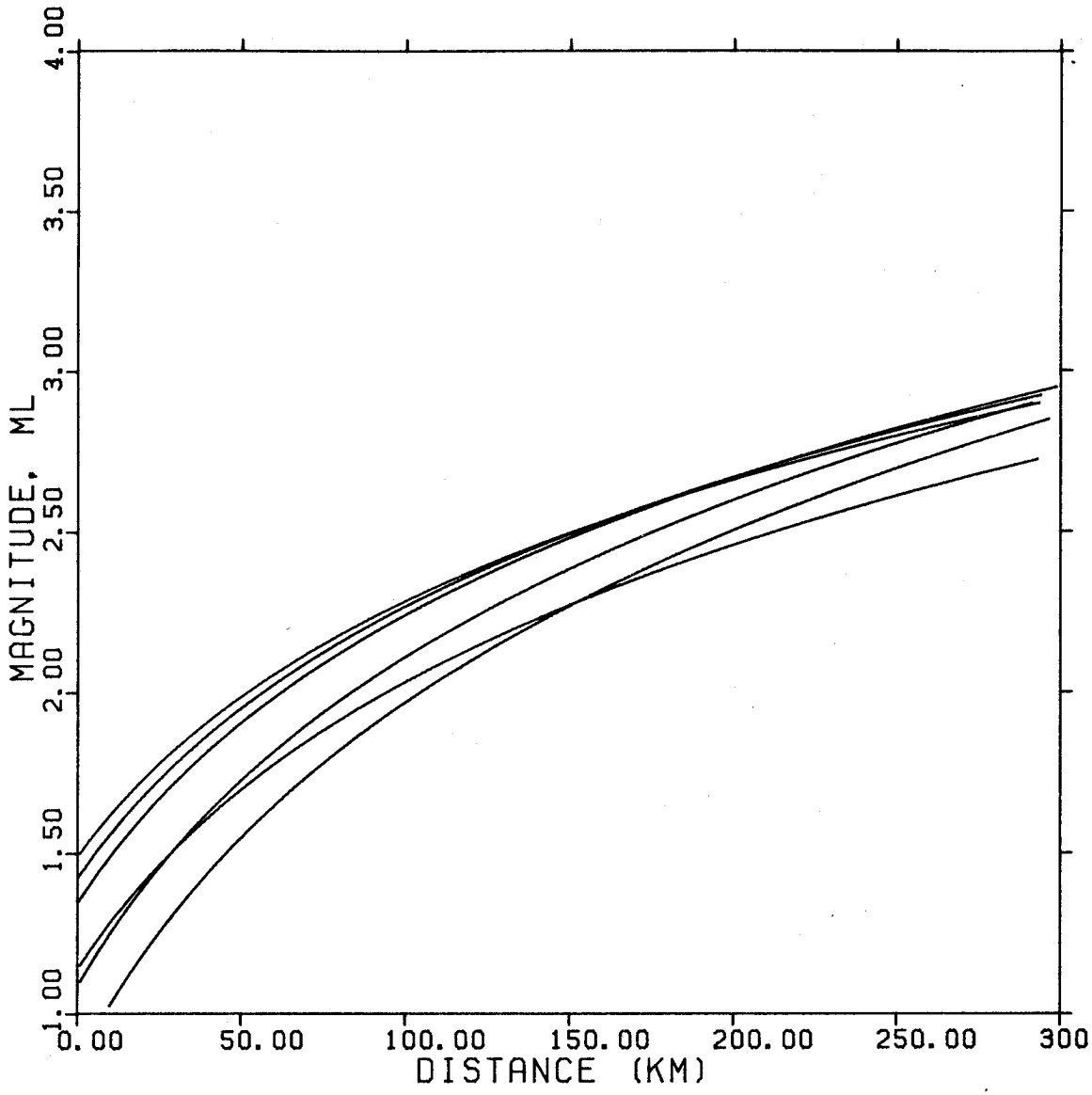

Figure 6. Several estimates of the 90th percentile magnitude detection threshold as a function of distance for the station RMR illustrating the stability inherent in the calibration procedure. Each curve is determined by a single seismogram with an independently assigned M_L. Disregarding the error in ambient noise, a standard error of about .2 magnitude units seems appropriate for well-calibrated sites.

segments (5.12 s sections) were available. Six such events for the station RMR were present in the standard data set described in Chapter 2. Such a limited data set for each independent calibration pair might be expected to introduce considerable scatter, yet Figure 6 suggests that a standard error of about .2 magnitude units at a given distance is not unreasonable for well-calibrated sites. Unfortunately, for some rather low gain stations the data were so limited that even this level of precision is unobtainable. For these stations recalibration with an expanded data set will be necessary.

NETWORK DETECTION ANALYSIS

The local coincidence criterion for network triggering is imposed by grouping the stations of the Southern California network into several overlapping subnetworks. An individual station may participate in an arbitrary number of subnetworks. Two examples from the current network configuration are shown in Figures 7 and 8. An earthquake causes a network trigger whenever at least N stations within any subnetwork are simultaneously in a triggered state. The count threshold, N, is set independently for each subnetwork. The calculation of network detection threshold contours requires first the analysis of the detection capability for each subnetwork. The network detection threshold at any given point then is simply the smallest detection threshold for any subnetwork at that point.

The spatial analysis of the detection capability for a particular subnetwork is undertaken by superimposing a 40 x 40 point rectilinear grid over Southern California. The same grid is used for all sub-

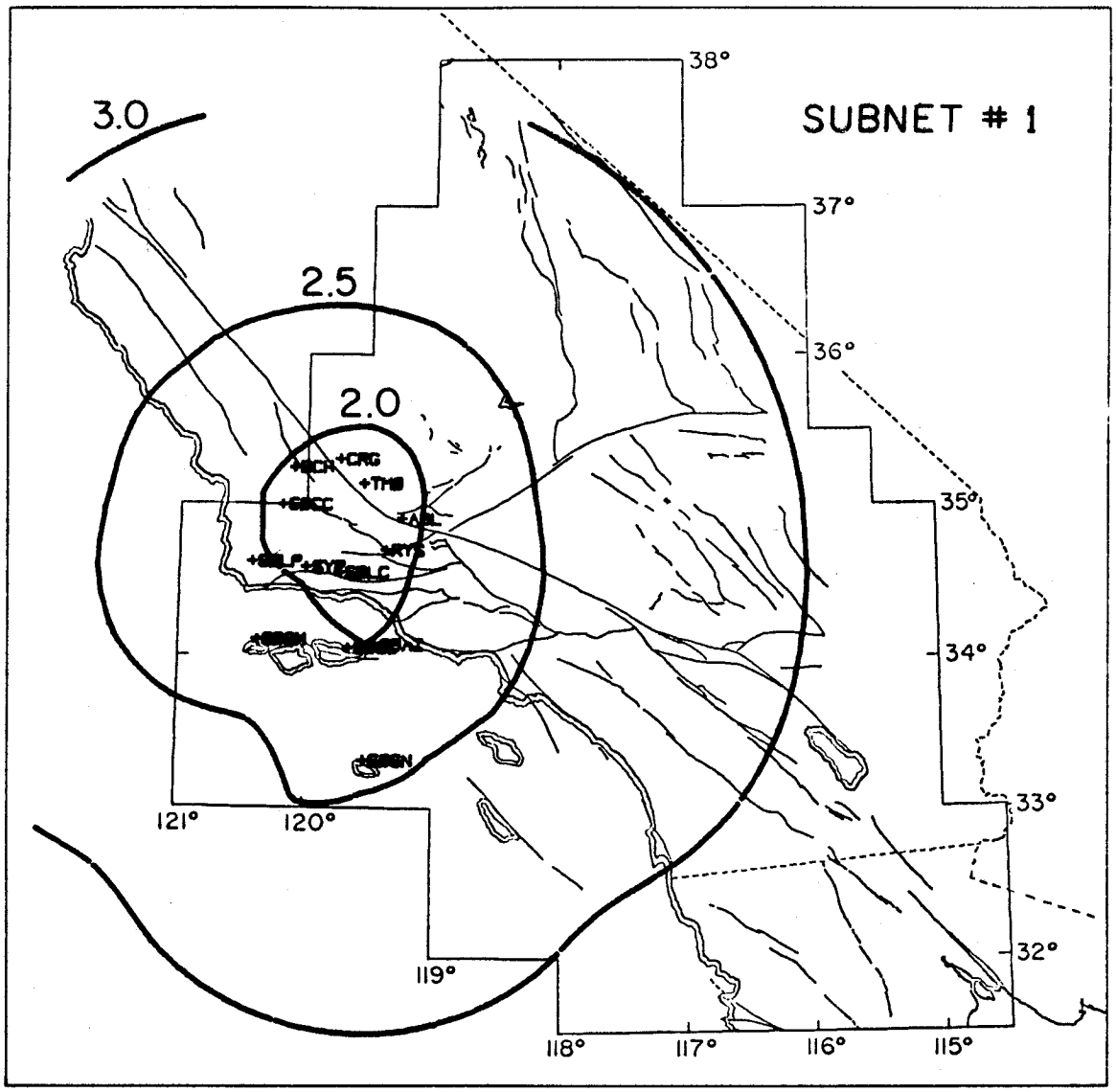

Figure 7. Ninetieth percentile magnitude detection threshold contours and station distribution for subnetwork #1 if the current CEDAR system detection configuration.

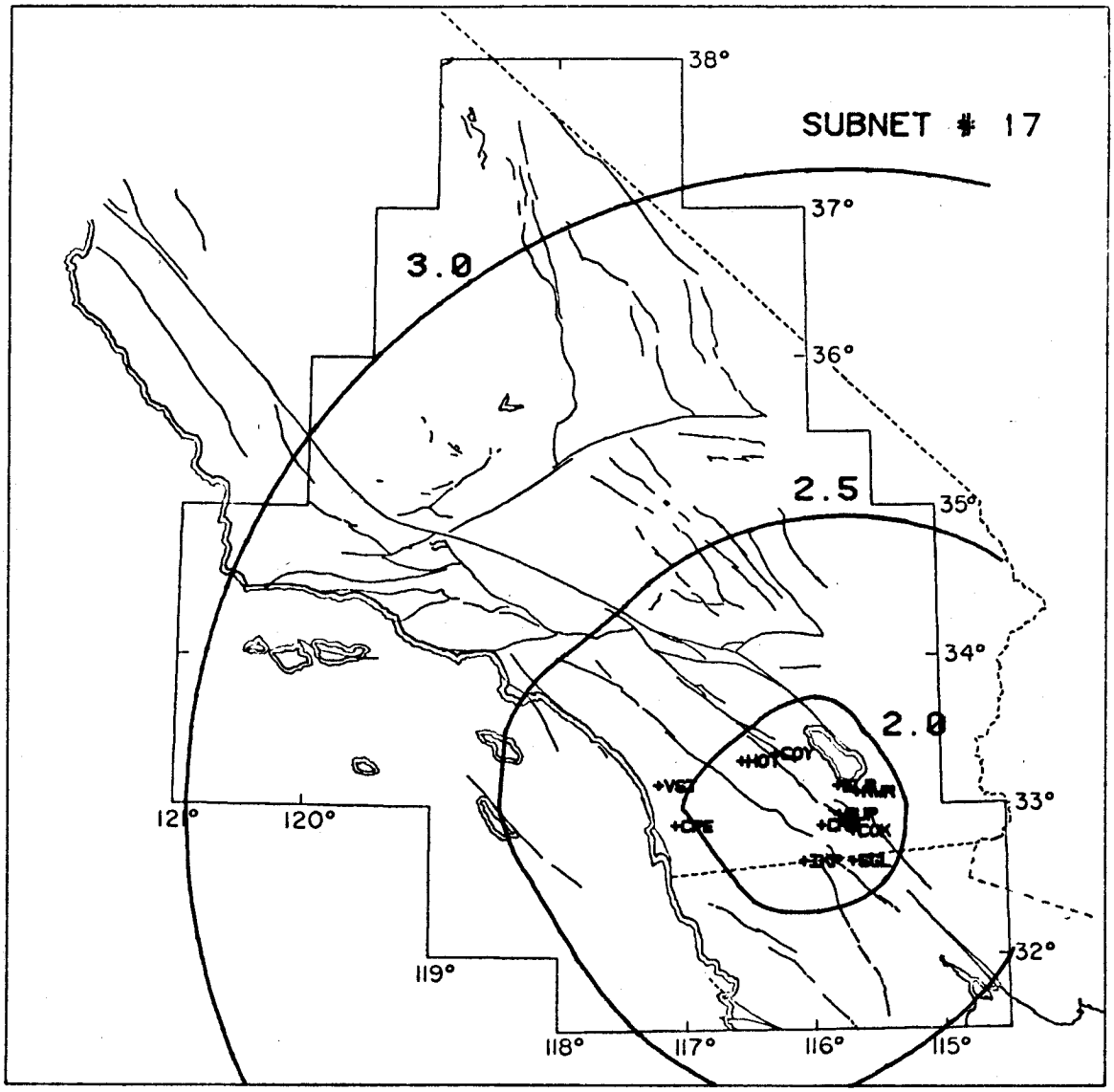

Figure 8. Ninetieth percentile magnitude detection threshold contours and station distribution for subnetwork #17 of the current CEDAR system detection configuration.

networks to simplify the subsequent calculation of network threshold contours. At each grid point a list of the detection thresholds for all stations within a particular subnetwork is compiled using expression (7). This list is then sorted into ascending order and the subnetwork detection threshold is taken to be the N^{th} entry. Once completed, the resulting distribution is contoured using standard software. Examples of the detection threshold contours for two subnetworks in the current configuration are shown in Figures 7 and 8. These curves represent the locus of points at which an earthquake of the designated magnitude will be detected at least 90% of the time.

A similar grid is used to calculate the detection thresholds for the network as a whole. Since the triggering of any single subnetwork is sufficient to cause a network trigger, the network detection threshold at a given grid point is just the smallest value associated with the corresponding grid point for any subnetwork. The resulting threshold contours for the current detection configuration for the Southern California network is shown in Figure 9.

DISCUSSION

There are several inadequacies in the above analysis that could result in excessive optimism with respect to the resulting thresholds. In the analysis of the detection capabilities of a single station all assumptions were made so as to bias the estimate of detection toward higher values. Unfortunately the estimate of subnetwork detection capability may be biased toward low detection thresholds, in violation of our precept toward conservatism. This bias arises

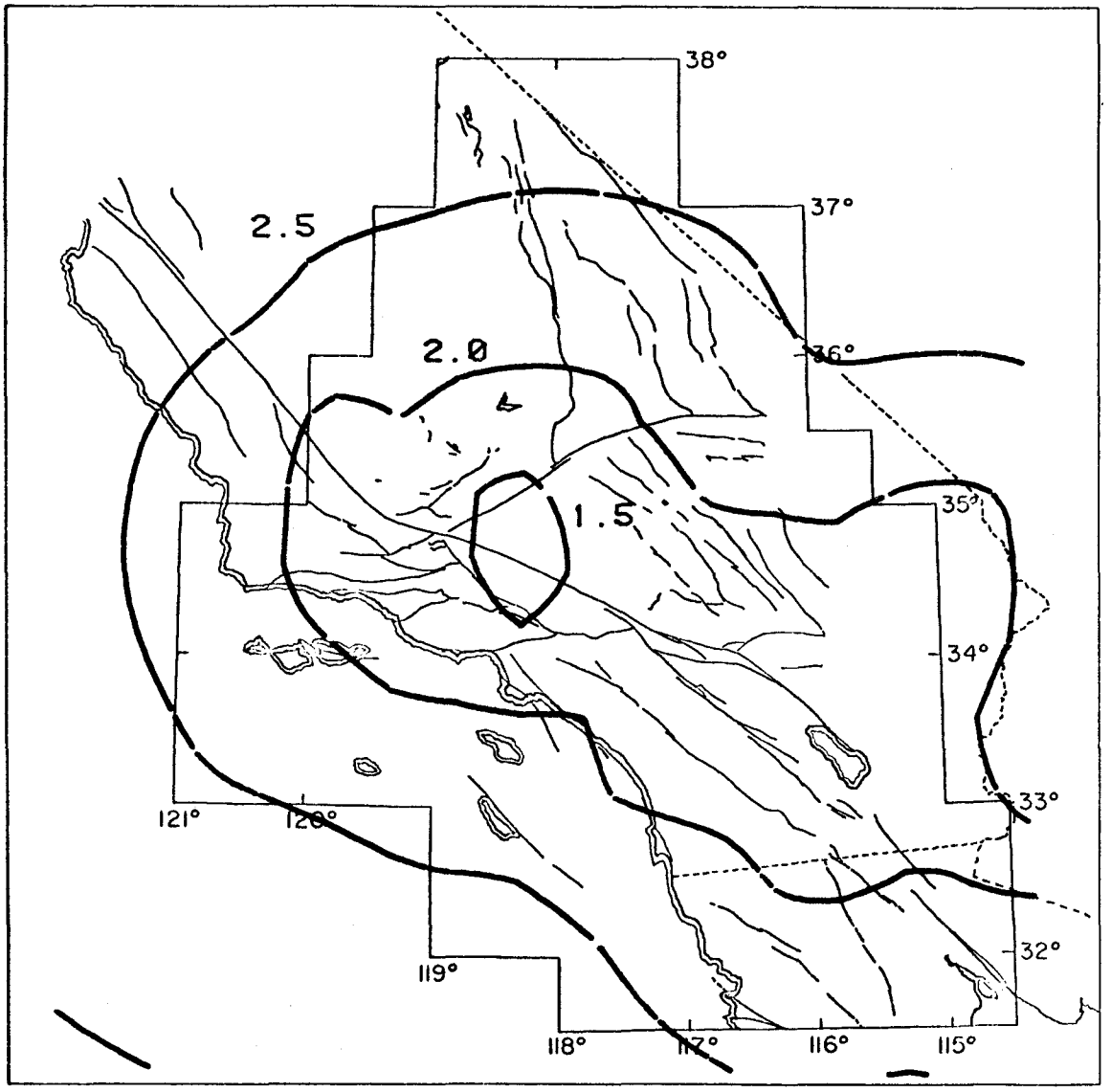

Figure 9. Ninetieth percentile magnitude detection threshold contours for the current configuration of the CEDAR system event detection logic.

essentially from two sources. The first, and by far the most significant, is that the distribution of the N^{th} entry in a sorted list of stochastic variables is strongly affected by the errors associated with the individual entries as well as by the number of entries in the list. For example, consider a subnetwork of several sensors all equidistant from a given point. Further, let all stations have the same central estimate of detection threshold at that point with identical probability distributions. Then it is clear that the estimate of subnetwork detection threshold calculated as in the previous section will decrease as the errors in the threshold estimates for individual stations increase. Thus a poorly calibrated network will appear to be more sensitive. In addition, if we increase the number of stations, assuming all are equidistant with identical detection capabilities, the estimate of detection threshold for the subnetwork will again decrease. In this case, though, a part of the improved performance is real.

These two sources of bias are somewhat mitigated if the component stations are calibrated with sufficient accuracy. The standard error of detection threshold at a given distance from a well calibrated station should be less than about .2 magnitude units. It seems likely that detection levels in the denser areas of the network should be nearly correct, since at the lowest magnitude levels detection is dominated by the few nearest stations. In addition, there tend to be more data available resulting in more accurate calibration where the network is most dense. Detection threshold errors in excess of .5 magnitude unit seem unlikely.

On the other hand detection thresholds near the network periphery potentially involve many stations, greatly increasing the tendency toward threshold bias. Further, quaternary basin stations because of the low decay rate, q, tend to have relative high apparent sensitivity at greater distances. At sufficiently large distances, in fact, they dominate the threshold calculation. In reality the detection threshold considered as a function of distance for these stations should suffer a sudden drop in detection capability of nearly 1 magnitude unit at the associated basin margin. For these reasons it is possible that for more regional distances detection thresholds may be too low by more than 1 unit of magnitude. The areas of Southern California most likely to experience this problem are the continental borderland, northern Baja, and the eastern and northeastern portions of the region of principal coverage outlined in Figure 9.

Another problem with the current state of the analysis is that it does not take into account the effect of stations becoming inoperative for some period of time due to equipment failure. Typically about 5% of all stations are inoperative at any given time. Since the event detection threshold tends to be dominated by a few stations, especially when considering low thresholds near dense parts of the network, the loss of a key station can have a substantial effect. One way to look at station drop out is as periods of infinite noise. In any case the detection contours presented in this chapter presume a totally functional network.

One further note of warning concerns the time dependent

character of the actual detection thresholds. In the above analysis the sensitivity of various sensors are treated as being completely independent. This is of course an oversimplification. Noise level tends to be correlated from site to site with higher cultural noise during daylight hours and an increase in weather related noise and enhanced microseism activity during the winter months. In a sense the detection contours can be thought of as being dynamic, expanding at night and contracting during the day. These complications underline those areas where more work is required in order to properly understand the detection capabilities of real time event detectors like the one used in the CEDAR system.

CONCLUSIONS

A method has been developed to permit the *a priori* analysis of the detection capability of the real-time event detector utilized by the CEDAR system given a particular configuration of stations within the detection scheme. Although the development of this method is still somewhat primitive, it is, nevertheless, capable of revealing many gross inadequacies of a proposed detection configuration. Although this is its primary task, it would be quite useful to be able to examine detection homogeneity for other purposes, such as seismicity studies, as well. In order to acquire this capability several further developments are required.

The current state of development can be looked upon as the first of three stages. It encompasses the general formulation of the problem and its relationship to magnitude systematics. The

completion of this first stage is predicated on a better understanding of noise processes and their effect on the joint probability distribution governing the likelihood of detecting an event of a given magnitude at a particular place and time. The efficiency of these results could be checked by means of a Monte-Carlo simulation of the detection process. This second stage of development might become expedient for the primary function of performance prediction should the development of the required probability distributions prove to be sufficiently intractable. The final stage of development deals with the comparison of *a posteriori* detection thresholds based on an analysis of detected events with those predicted above. This stage, which is necessarily delayed until a sufficient record is established, may prove to be particularly enlightening.

PART II

SEISMOTECTONICS OF THE IMPERIAL VALLEY OF SOUTHERN CALIFORNIA

CHAPTER 4

HISTORICAL SEISMICITY AND FAULT RELATIONSHIPS IN THE IMPERIAL VALLEY

INTRODUCTION

In the following discussion we will attempt briefly to review the seismic history of the last 50 years for the Imperial Valley of Southern California. The development will synthesize seismicity data from several sources and attempt to relate them to recent geodetic observations as well as the major faults comprising the tectonic framework of the Gulf of California and its landward extensions into the Salton Trough. It is not intended to provide a complete review of geophysical observations in the Imperial Valley. Rather, we will concentrate on those areas that are required to support a more detailed discussion of the nature of earthquake swarms in Chapter 5. The main emphasis will be on the tectonic framework, spatial characteristics of epicentral distributions, and coherent variations of seismicity with time.

The region selected for detailed analysis is shown as the shaded area in Figure 1. This region runs in latitude from 32°30' to 33°30'N, and is bounded by meridians at 115° and 115°50'W. There are several compelling reasons for selecting this region in particular for a detailed study. The seismicity in the Imperial Valley is dominated by earthquake swarms. Surprisingly little is known about these phenomena. They frequently are associated with oceanic ridges, volcanic regions, and geothermal areas. More generally, earthquake swarms seem to demonstrate a tectonic affinity for regions of extensional tectonics. Weaver and Hill (1978) have documented a tendency for swarms to be associated with the extension arising between dextrally offset members of right-lateral fault zones.

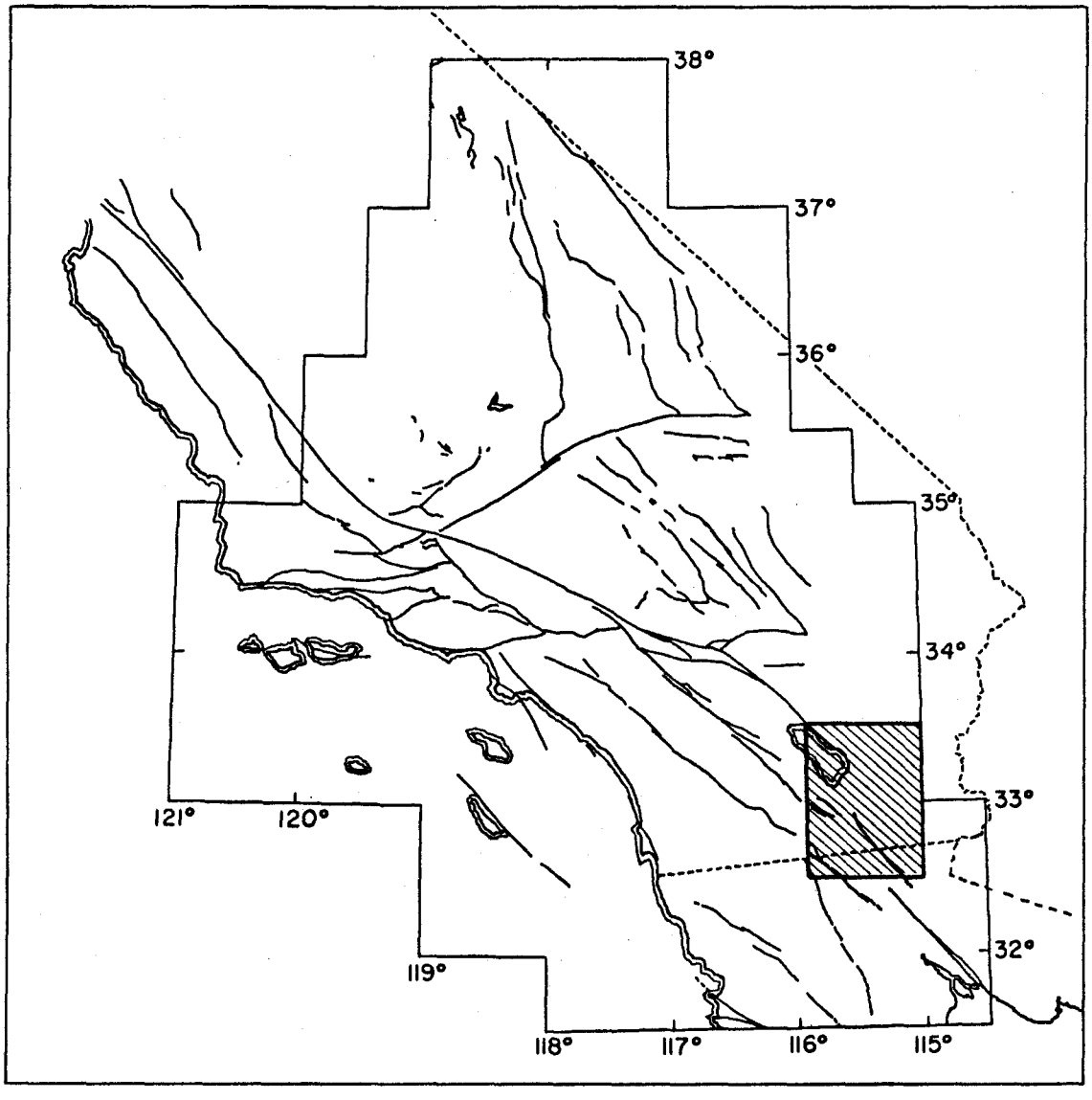

Figure 1. Index map showing area of detailed study (shaded box).

Presumably sinistral offsets of left-lateral fault systems manifest similar phenomena, as evidenced by a small swarm at Koehn Lake on the Garlock Fault in October, 1978. It is suggested that swarms may in a general way be related to the low fracture strength of crustal rocks under extension. The desire to elucidate the tectonic structures and physical mechanisms, giving rise to earthquake swarms motivated much of the effort represented by this dissertation.

From a more specific point of view the Imperial Valley and the dextral offset between the Imperial Fault and the San Andreas Fault in particular is a region of high seismicity adjacent to a quiet section of the San Andreas Fault that appears active but has not broken in a major earthquake in historical times. It is possible that a large event on this southernmost section of the San Andreas might be preceded by anomalous earthquake activity in the Imperial Valley. Another significant problem area relates to the understanding of gulf tectonics and ridge processes more generally. Although in some respects the Imperial Valley is quite unlike ridges elsewhere, it is likely that results obtained from this more easily instrumented region may be of general applicability. Furthermore, the Imperial Valley is a major area of developing geothermal potential. An understanding of contemporaneous seismotectonic processes is requisite if the effect of extraction of heat and re-injection of cooled brines is to be correctly anticipated. Finally, it is hoped that an understanding of basic fault processes in the Imperial Valley might contribute to the better understanding of the physics of faulting more generally. Such knowledge is absolutely essential if the technology of

earthquake prediction is to rest on a firm scientific foundation.

INSTRUMENTATION AND ANALYSIS

The earthquake epicenters discussed in this chapter are based on arrival times obtained from the network of short-period vertical seismometers monitored by Caltech since 1932. With time, the number of stations has increased considerably so that, in general, the magnitude cutoff for homogeneous coverage has gradually improved. Prior to 1956, station coverage in the Imperial Valley was not sufficient to provide reasonably accurate epicenters. Not only was the Imperial Valley outside of network closure (GAP > 180°), but the nearest station was beyond the P_n cross-over distance of about 80 km (Hadley, 1978) for earthquakes near Brawley. Moreover, the arrival of P_n is emergent so that larger events tend to be picked earlier. For smaller events, the P_n phase was occasionally missed altogether and the first P arrival was attributed to the onset of P_g.

This problem manifests itself as a distinctly bimodal distribution of travel time residuals for stations at intermediate distances. The closest station prior to 1956 was PLM at a distance of about 140 km. PLM has been in continuous operation since 1939. The situation was somewhat mitigated by the installation of a continuously recording station at HAY (80 km) and a strong motion station (10 km) at ECC in 1956. The effectiveness of the station ECC was, however, compromised by the lack of recordings for the smaller events associated with earthquake swarms, a tendency for the trace to be off scale when triggered, and a station clock with a high drift rate. The problem of network

closure persisted until the installation of permanent stations at GLA (65 km) in 1966 and RHM (100 km) in 1969. Beginning around 1965 many of the stations of the southern California network were telemetered to Caltech, providing a much more reliable basis for relative timing than was previously possible. A detailed history of the station distribution prior to 1973 is provided by Hileman and others (1973).

A quantum leap in location ability occurred in 1973 with the installation of the Imperial Valley network by the U.S.G.S. This network has been described in detail by Hill et al. (1975b). Data from this array have been processed and analyzed in a cooperative effort between the U. S. Geological Survey and Caltech since its installation. Most of the discussion of Imperial Valley seismicity herein is concerned with the last five years, since the installation of the high density network. It is fair to say that the observations and conclusions of this and the following chapter would have been impossible without the existence of the Imperial Valley network. Stations within the Imperial Valley are shown in Figure 6 through Figure 27 for those periods during which they were in routine operation. In this set of figures the increase in resolvable details of the seismicity patterns with increasing station coverage is obvious.

The most recent improvement in location capability came with the implementation of the CEDAR system in January of 1977, as discussed in the preceding three chapters. This system makes available digitized records for analysis and permits a routine relative timing accuracy of about 20 msec as compared to about 50 ms obtainable from routine

analysis of develocorder records.

Methods of location and magnitude assignment have varied considerably since 1932. Prior to about 1961 epicentral assignments were constructed by graphical techniques. Later, iterative computer programs were developed, permitting the location of more events than was feasible when all processing was done by hand. Between 1961 and 1972 routine locations were computed on a Bendix G-15D computer using a program developed by Nordquist (1964). From 1973 through 1976 locations were calculated using HYPO71 as discussed by Lee and Lahr (1975). From 1977 to the present hypocentral estimation has utilized a generalized inverse location program as part of the CEDAR system software support package discussed in Chapter 1. This program has been substantially expanded, modified, and fully documented by Klein (1978).

Epicentral data discussed in this chapter were obtained from the Southern California local earthquake catalogs (Hileman et al., 1973; Friedman et al., 1976) and recent preliminary bulletins. The quality of these epicentral locations has been uniformly high since the installation of the dense array in 1973. The bulk of the following discussion will deal with this recent time period.

At one point an effort was initiated to relocate all recent Imperial Valley events using a master event approach. This endeavor was abandoned when it was discovered that the resultant slight improvements in epicentral control did not contribute significantly to the general discussion of seismicity presented in this chapter. However, a master event approach was found to be absolutely essential

in the following chapter in order to obtain the resolution necessary to support the structural interpretations presented there.

Earthquakes prior to 1973 and the larger subsequent events were assigned local magnitudes, M_L, using the methods described by Richter (1958). Subsequently most of the events through 1976 were timed and located by U.S.G.S. personnel, with magnitude assignments based upon the coda duration method developed by Lee et al. (1972). From 1977 to the present all timing was accomplished using the CEDAR system software (Chapter 1), and magnitude assignment was by means of the coda amplitude technique developed in Chapter 2. Epicentral maps and graphical material presented in this and the following chapters were prepared utilizing analytical extensions of the basic CEDAR system software package. These software tools are discussed in greater detail in Chapter 5.

TECTONIC FRAMEWORK

The Imperial Valley, or more generally the Salton Trough, lies at the head of the Gulf of California physiographic province, a remarkably linear and narrow structural depression over 1400 km in length (Sharp, 1972). In terms of the plate tectonics paradigm, faulting in the Imperial Valley is part of the zone of deformation associated with the boundary between the American plate and the Pacific plate. Such interpretations for gulf tectonics were offered by Larson and others (1968). Atwater (1970) developed several models for the tectonic evolution of the Gulf and San Andreas fault systems based on a study of sea floor magnetic anomaly patterns. Typically such

studies suggest a motion of the Pacific plate relative to the American plate of about 6 cm/yr.

South of Baja California, the plate boundary is delineated by the East Pacific Rise. Where it enters the mouth of the Gulf this ridge is typical of fast-spreading ridges elsewhere in the world with fairly low related earthquake activity (Isaaks and others, 1968; Reichle and Reid, 1977). The change in trend to accommodate that of the Gulf is expressed in an increase in the length of the transform faults offsetting relatively short ridge segments. Deformation also becomes predominantly strike-slip with large earthquakes in the lower two thirds of the Gulf occurring as mainshock sequences associated with the major transforms (Reichle and Reid, 1977) and with mechanisms that are chiefly strike-slip (Sykes, 1967, 1968, 1970).

Reid and others (1973) discovered that microearthquake swarms were commonly associated with spread-centers in the Gulf; however, such activity could rarely be attributed to the transform faults. Furthermore, major earthquake swarms are not observed teleseismically in the southern Gulf.

The situation changes somewhat in the northern Gulf. Although mainshock sequences are still observed, major earthquake swarms near reputed ridge segments make up a significant portion of the seismicity. The detailed study of these swarms has demonstrated the style of faulting can be quite varied. One swarm studied by Tatham and Savino (1974) produced both strike-slip and dip-slip mechanisms. Thatcher and Brune (1971) reported a large component of normal faulting for a swarm in the Wagner Basin in 1969. Similar results were obtained

by Reichle and Reid (1977) for a swarm associated with the Delfin Basin, although they noted that northern Gulf swarms frequently manifest a strike-slip character.

Reichle and Reid (1977) attributed the increase in swarm activity to depression of the geotherms resulting from increasing sedimentation rates as one approaches the mouth of the Colorado River at the head of the Gulf. This interpretation is consonant with their observation that Gulf swarms and microearthquake activity are restricted to the sedimentary section and possibly the shallow crust. The sediment cover in the northern Gulf, deepening to over 6 km in the Imperial Valley (Biehler and others, 1964), encumbers a direct plate tectonic interpretation of fault relationships. Lomnitz and others (1970) proposed one such interpretation, shown in Figure 2, that extends the general tectonic pattern observed in the southern Gulf as far north as the Salton Sea and the southern termination of the San Andreas Fault. While recent studies have disagreed with some of the details of this model (e.g., Elders and others, 1972; Henyey and Bischoff, 1973; Bischoff and Henyey, 1974), there appears to be general accord with respect to the underlying concepts.

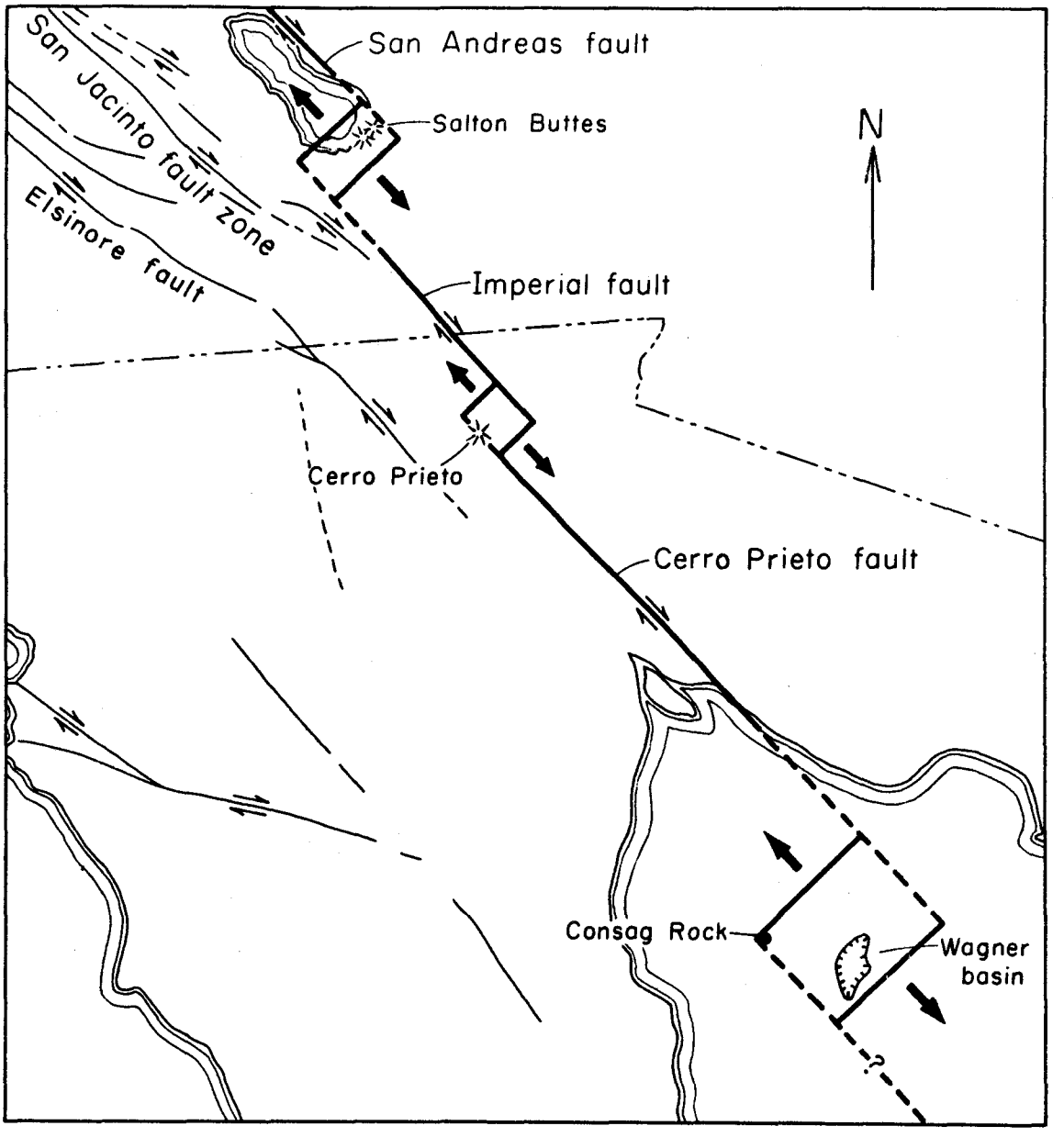

Figure 2. Diagram illustrating the relationship between Imperial Valley tectonics and that of the Northern Gulf of California as discussed by Lomnitz and others (1970), adapted from their Figure 3.

Earthquake activity within the Imperial Valley appears to be identical in all major respects with seismicity described for the Gulf of California by Reichle and Reid (1977). To illustrate this, preliminary epicenters for 1977 together with related fault structures are shown in Figure 3. The seismicity pattern is dominated by concentrations of swarm activity marking the dextral offsets of the northwest-trending strike-slip faults. Where depth control is obtainable, earthquake activity is confined to the 6 km thick sedimentary section and the first 2 or 3 km of the underlying crust. The Imperial fault broke along its entire mapped length in 1940 with a magnitude 7.1 right-lateral earthquake with maximum displacements approaching 4 m. The central portion of this break where displacements were highest is now largely aseismic. The diffuse band of earthquakes linking the northern Imperial Fault with the southern San Andreas, together with its associated fault structures, is the main topic of the remainder of this thesis.

Focal mechanisms for the Imperial Valley are also varied. One swarm in 1975 studied by Johnson and Hadley (1976) was dominated by strike-slip solutions with a cluster of thrust mechanisms at the northern end. Fuis and Schnapp (1977) also reported a variety of mechanisms for a swarm near Obsidian Butte in November, 1976. Normal earthquakes are only occasionally observed in Imperial Valley swarms. Neither the variety of mechanism nor the overall distribution of epicenters supports a simple model of a ridge segment perpendicular to its associated transforms. The concept of a "leaky" transform suggested for the Imperial Valley by Hill (1977) appears to be more

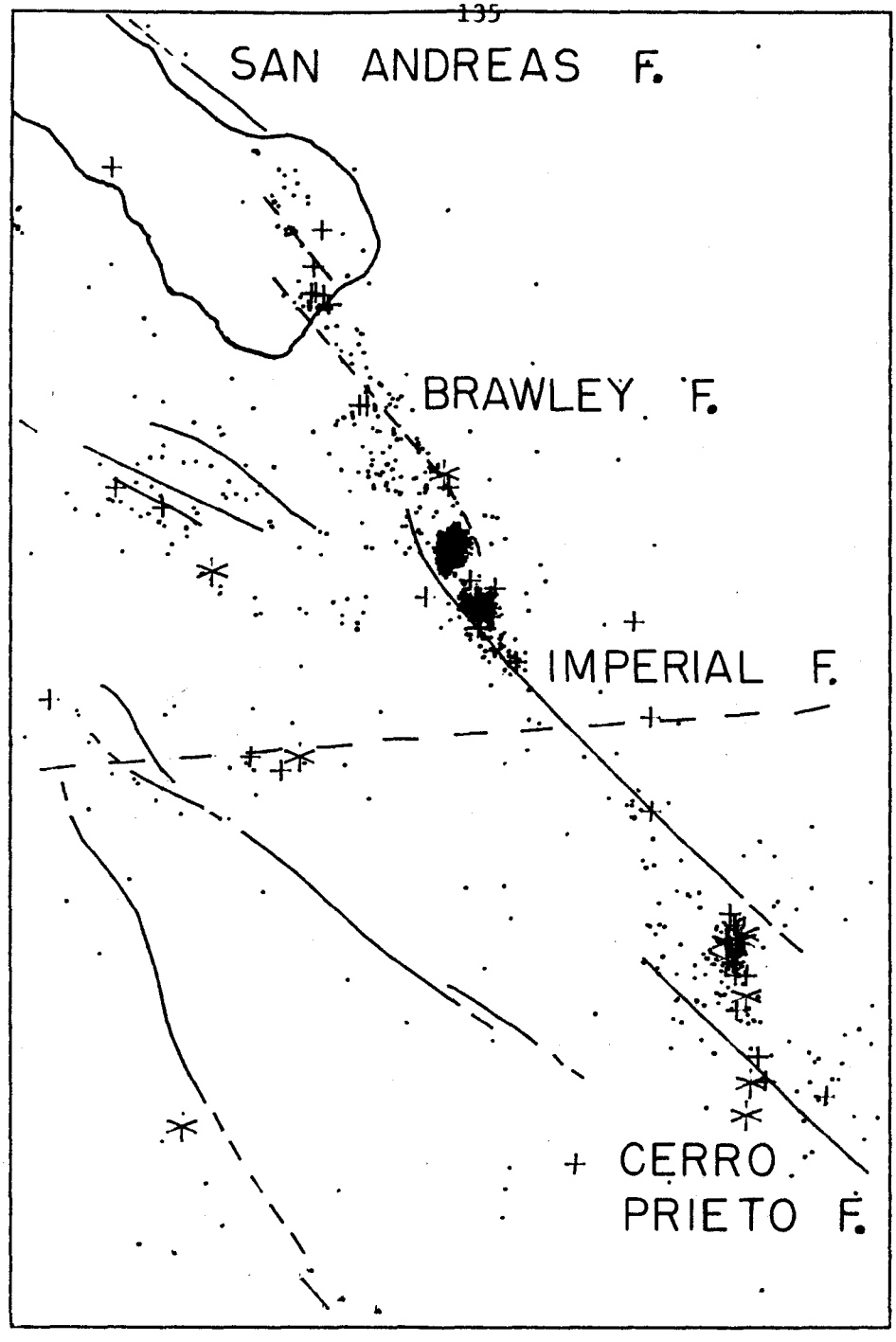

Figure 3. Relationship between seismicity and major fault structures in the Imperial Valley, Southern California. Plus symbols represent events greater than M_L = 3.0, asterisks denote events exceeding M_L = 4.0. A tendency for seismicity to concentrate at offsets in the major strike-slip faults is evident. All events for 1977 are shown regardless of location quality.

consistent with observed seismicity patterns. It should be kept in mind, however, that we are actually looking at failure in the shallow crust in response to a stress field driven by aseismic processes at greater depth. The constraints one can put on these deeper processes from observations of seismicity appear, at present, to be relatively mild.

North of the Imperial Valley the San Andreas Fault beginning along the eastern shore of the Salton Sea, a notable closed depression, runs nearly the entire length of the state of California for a distance of nearly 1400 km. Although great earthquakes have occurred along the northern two thirds of the San Andreas in 1857 and 1906, the southern section adjacent to the Imperial Valley has not broken historically Allen, 1968), although accumulated offsets of 250 km documented by Crowell (1962) suggest considerable tectonic significance. This figure is remarkably similar to that reported by Rusnak and others (1964) for the overall opening at the mouth of the Gulf. The extremely low level of microearthquake activity reported by Brune and Allen (1967) is similar to that along sections of the San Andreas that are known to have broken in 1857. Evidence for continuing activity on the southern San Andreas (Mission Creek-Banning branch) comes from the observation of about 1 cm of surface displacement observed following the 1968 Borrego Mountain earthquake (Allen et al., 1972). By inference, this displacement occurred at the time of the 1968 shock as sympathetic creep. North of the Imperial Valley, the east-west extensional tectonics superimposed on the predominantly strike-slip character of the plate boundary in the Gulf of California is replaced

by the north-south compression of the transverse range (Pechman, 1979).

Also related to the tectonic structure of the Imperial Valley are a series of right-lateral faults trending away from the trough axis into the penninsular ranges to the west. One of these, the San Jacinto, appears to be the most active in southern California in the range of small to moderate earthquakes (Brune and Allen, 1967). Although this structure is undoubtedly a contributor to inter-plate deformation, its relative tectonic significance may be more reliably indicated by its substantially smaller overall displacements of about 24 km (Sharp, 1972) as compared with 250 km on parallel sections of the San Andreas to the east. The question of relative significance is largely unresolved at the present time.

One model relating these faults to the axial ridge-transform system was proposed by Lomnitz et al. (1970). In this interpretation differential right-lateral motion occurs on extensions of the transform faults past their associated ridge segments due to decreasing spreading rate for more northerly spreading centers. Elders et al. (1972) pointed out that this model implies a complementary set of unobserved left-lateral faults to the east unless the ridge segments themselves are allowed to migrate. This could provide an explanation for several fold belts in the Imperial Valley as well as the current distribution of geothermal areas, some of which are at considerable distances from inferred active ridge segments. An undeformed region to the east is also consistent with the nearly total absence of seismicity east of the trough axis. Moreover, Bischoff and Henyey (1974) concluded that the Guaymas Basin,

for example, has been active for only the past 60,000 years. They inferred that ridge segments in the central gulf were not fixed for extended periods of time, but rather were somewhat mobile.

In summary, it is apparent that the Imperial Valley plays a key role with respect to the tectonics governing deformation of Southern California. An understanding of the seismotectonic processes in the Imperial Valley and the Gulf of California more generally is a necessary step in developing a more complete understanding of the southern San Andreas fault system.

IMPERIAL VALLEY SEISMICITY

In this and the next two chapters we will be conducting a detailed investigation of the seismotectonic processes occurring in the dextral offset between the northern end of the Imperial Fault and the southern end of the San Andreas. Well located epicenters for this region during the past five years are shown in Figures 4 and 5. All sufficiently well-located events occurring in the mapped area during this time period are plotted as a common symbol regardless of magnitude. Figure 4 includes all events thought to have a relative epicentral error of less than 2.5 km, while Figure 5 includes a subset of these for which the relative epicentral error is less than about 1 km. The instrumentally determined epicenter of the magnitude 6.7 (M_s = 7.1) El Centro earthquake of 1940 (Richter, 1958) is shown as an open circle near the Imperial Fault. The magnitude 6.5 Superstition Hills earthquake of 21 October 1942 is designated by a smaller filled circle. These

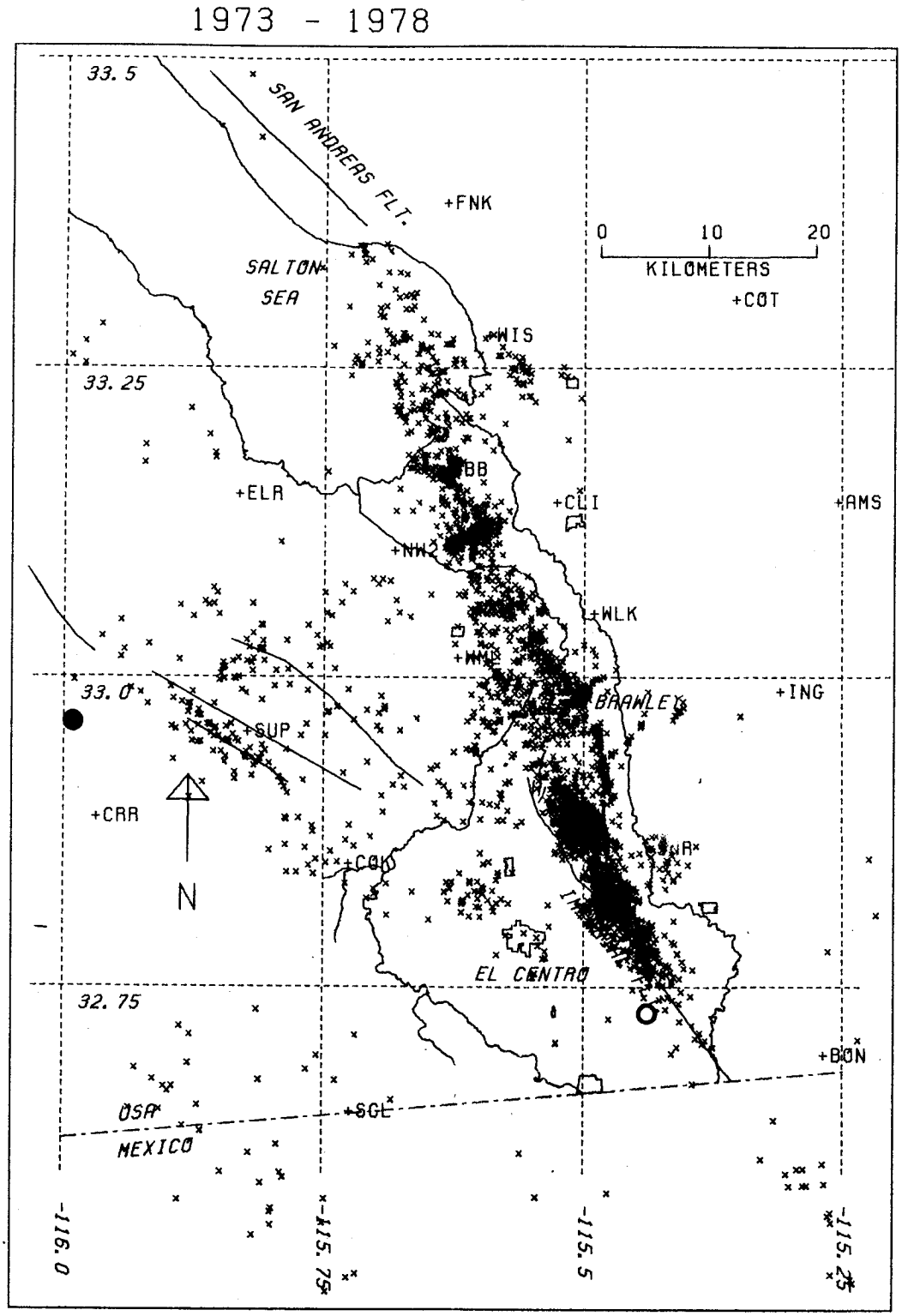

Figure 4. Epicenter plot showing all "A" and "B" quality epicenters (horizontal error less than 2.5 km) for the period June 1973 through November 1978. The open circle marks the instrumental epicenter of the 1940 El Centro earthquake (M_L = 7.1). The 1942 Superstition Mountain earthquake (M_L = 6.5) is shown as a filled circle.

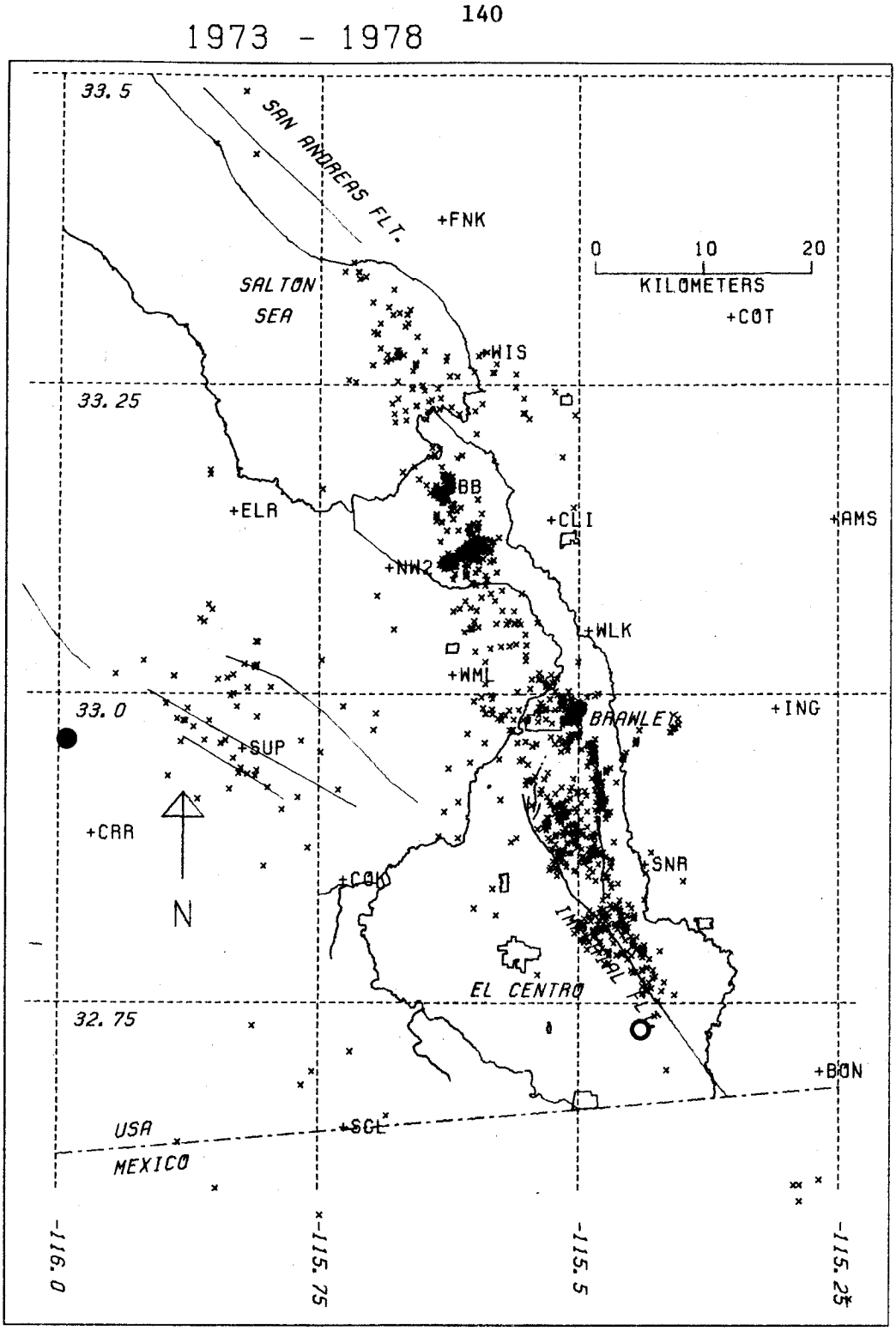

Figure 5. Epicenter plot showing all "A" quality epicenters (horizontal error less than 1.0 km) for the period June 1973 through November 1978. The open circle marks the instrumental epicenter of the 1940 El Centro earthquake (M_L = 7.1). The 1942 Superstition Mountain earthquake (M_L = 6.5) is shown as a filled circle.

are the only events with magnitudes greater than 6 to have occurred in the mapped area since the Southern California catalog was instituted in 1932.

Several intriguing observations regarding the spatial distribution of events in the Imperial Valley can be made directly from Figure 4. The remarkably well-defined, sharply bounded seismogenic zone running from the instrumental epicenter of the 1940 El Centro earthquake to the southern terminus of the San Andreas fault is surprising. In order to distinguish this spindle-shaped epicentral distribution from the nomenclature of individual causative faults we will refer to it as the Brawley seismic zone. This seismic trend was first recognized by Hill et al. (1975a) as a diffuse pattern of epicenters associated with the Brawley fault, based on an analysis of data from the first year of operation of the 16-station Imperial Valley network. The accumulation of data for the subsequent four years has lent considerable support to this interpretation, in addition to providing substantially more information regarding structural details. Another more diffuse pattern which was associated with an extension of the San Jacinto Fault has failed to emerge as a prominent feature, although distinctly higher seismicity is evident in Figure 4 along this trend (near SUP and northwest of El Centro). It is also clear from Figure 4 that the Brawley seismic zone marks the boundary between a region of moderate diffuse seismicity to the west and a nearly aseismic region at a magnitude 2 threshold to the east. This includes a dearth of events in the vicinity of the Glamis and Dunes geothermal areas, as was noted also by Hill et al. (1975a). It appears likely that the Brawley

seismic zone marks a fundamental east-west transition with respect to the tectonic processes giving rise to the observed seismicity pattern.

A number of fine structural details can also be seen in Figure 4, although they are somewhat more obvious in Figure 5. Several zones of concentrated activity cross the Brawley seismic zone and tend to be truncated by its boundaries. These trends, which appear to be transverse fault structures activated during some of the larger swarms, are discussed in considerable detail in Chapter 5. Another mild lineation paralleling the Imperial Fault to the east can be seen in Figure 5 at the southern end of the Brawley seismic zone. Swarms along the Imperial Fault tend to originate on a vertical plane coincident with this trend subsequently migrating north or south. In Chapter 5 this plane is interpreted as the sub-surface expression of the Imperial Fault. The offset of the corresponding seismic trend from the surface trace can easily be attributed to consistent mislocation due to lateral changes in crustal structure.

One final observation concerns the abrupt cessation of activity at the instrumental epicenter for the 1940 El Centro earthquake. Co-seismic offsets of less than 1 m north of this point rapidly increased to more than 3 m to the south. Richter (1958) and Trifunac and Brune (1970) have suggested that the 1940 mainshock may have ruptured unilaterally to the south followed by rupture to the north 75 minutes later during a magnitude 5.5 aftershock. This aftershock was considerably more damaging to the community of Brawley than was the mianshock. Possibly the 1940 earthquake initiated at a point where fault properties are somewhat discontinuous. In the following

chapter we conclude that much, if not all, swarm activity within the Brawley seismic zone is related to structures that are transverse to the Imperial fault trend, while these major structures participate in Imperial Valley tectonics by means of aseismic creep and occasional large events. The absence of seismic activity south of the 1940 epicenter may simply be associated with a lack of seismic transverse structures.

Figures 6 through 11 show epicentral maps prior to the installation of the dense Imperial Valley array in June of 1973. This period is broken down into periods of fairly homogeneous coverage separated by the times when new stations were installed and location capability was increased. All events with epicentral errors less than 15 km were selected for plotting during this period. It is difficult to compare seismicity prior to 1973 directly with current patterns due to the greater scatter in locations. However, a tendency of activity to shift toward the south during the period 1950 through 1972 is suggested in Figures 8 to 10. This trend also emerges from the discussion of the spatial characteristics of accumulated moment in the following section.

Beginning in 1973 (Figures 11 to 27) improvement in epicentral control revealed that over time periods of several weeks activity tends to be highly localized into discrete clusters. These clusters are swarms of earthquakes with most activity occurring over a period of a few hours to a few days. Normal aftershock sequences are rarely observed. Several such clusters tend to occur sporadically in close proximity within the Brawley seismic zone during time periods ranging

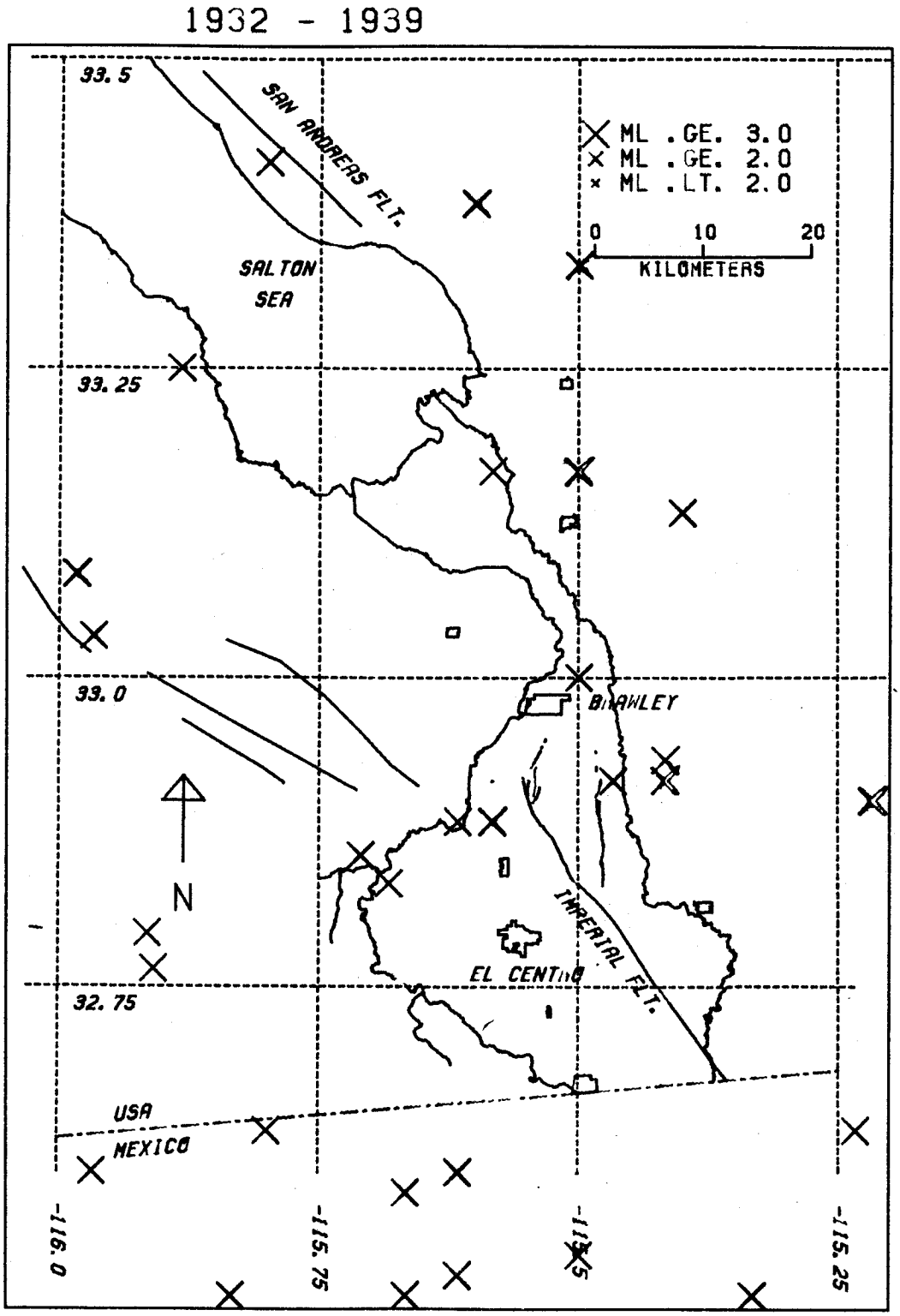

Figure 6. Imperial Valley seismicity including "A", "B", and "C" quality locations for the period 1932 thorugh 1939.

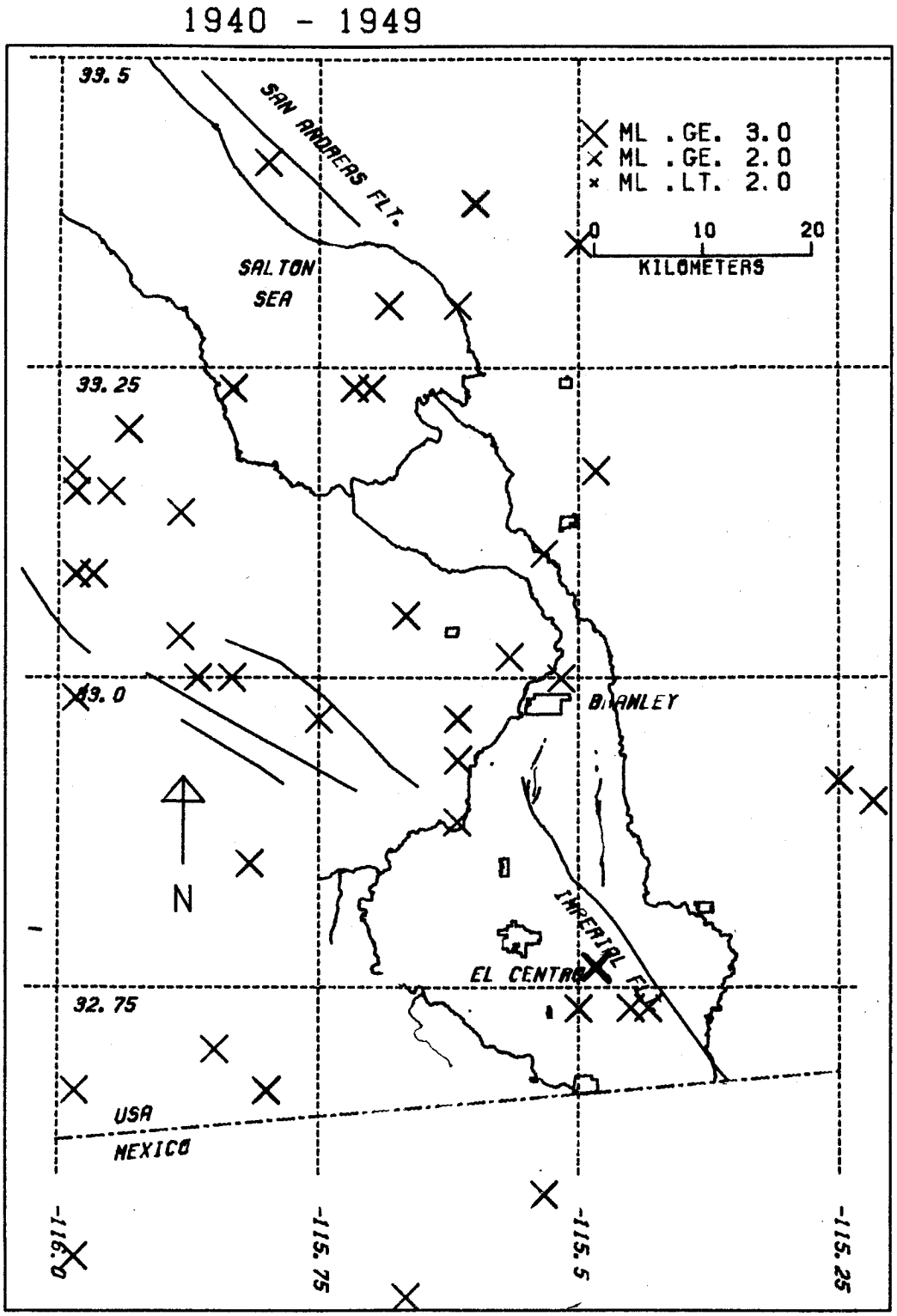

Figure 7. Imperial Valley seismicity including "A", "B", and "C" quality locations for the period 1940 through 1949.

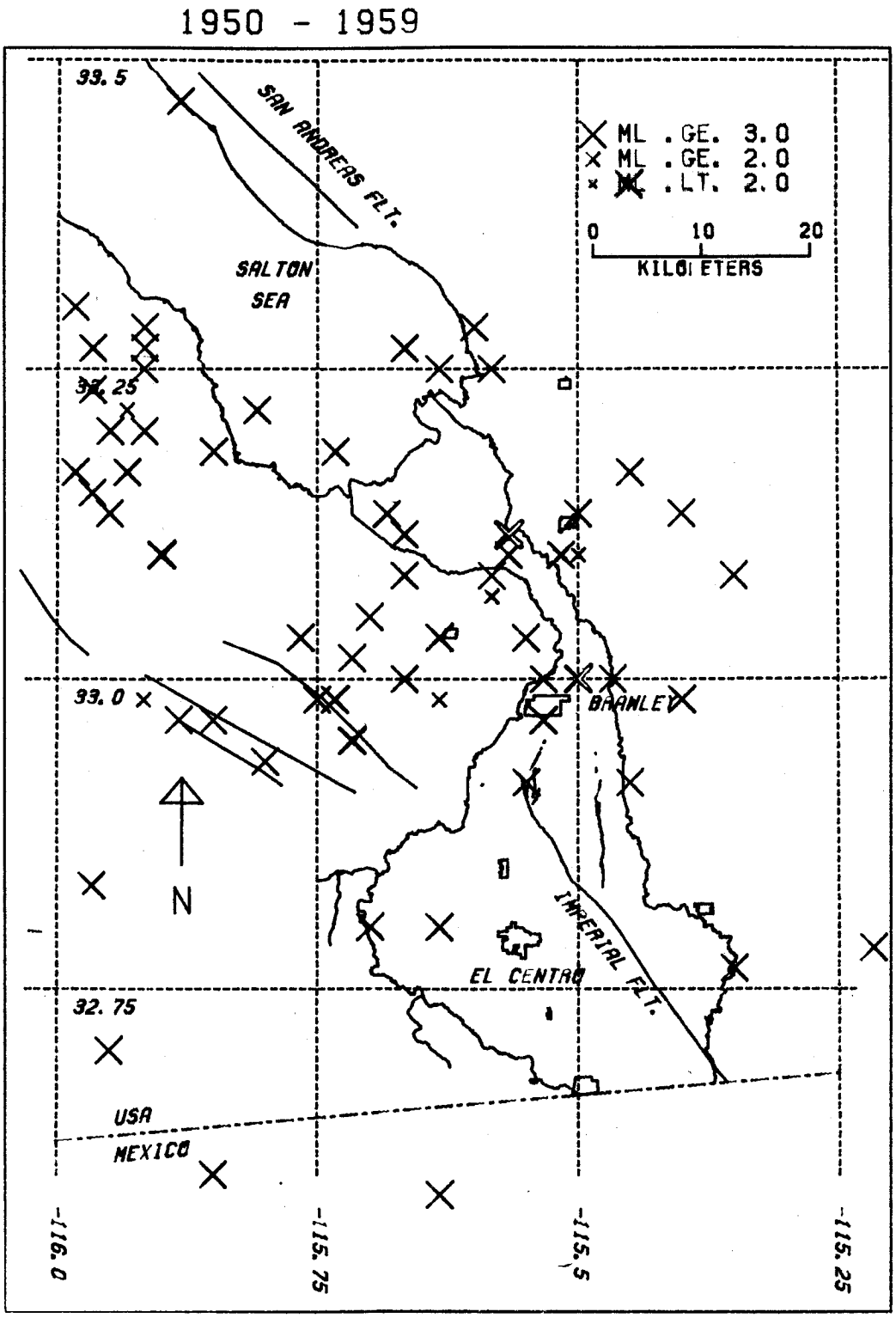

Figure 8. Imperial Valley seismicity including "A", "B", and "C" quality locations for the period 1950 through 1959.

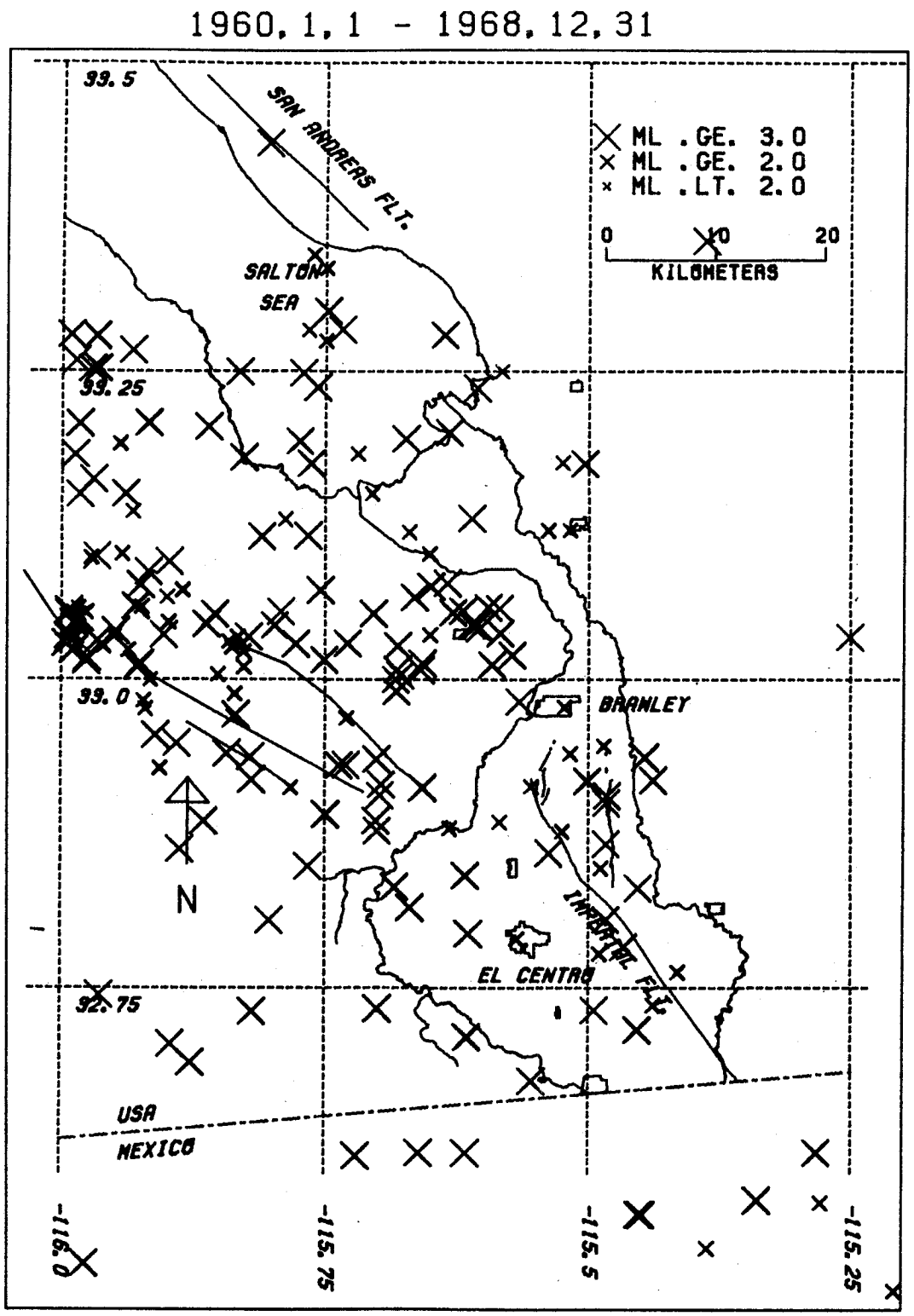

Figure 9. Imperial Valley seismicity including "A", "B", and "C" quality locations for the period 1960 through 1968.

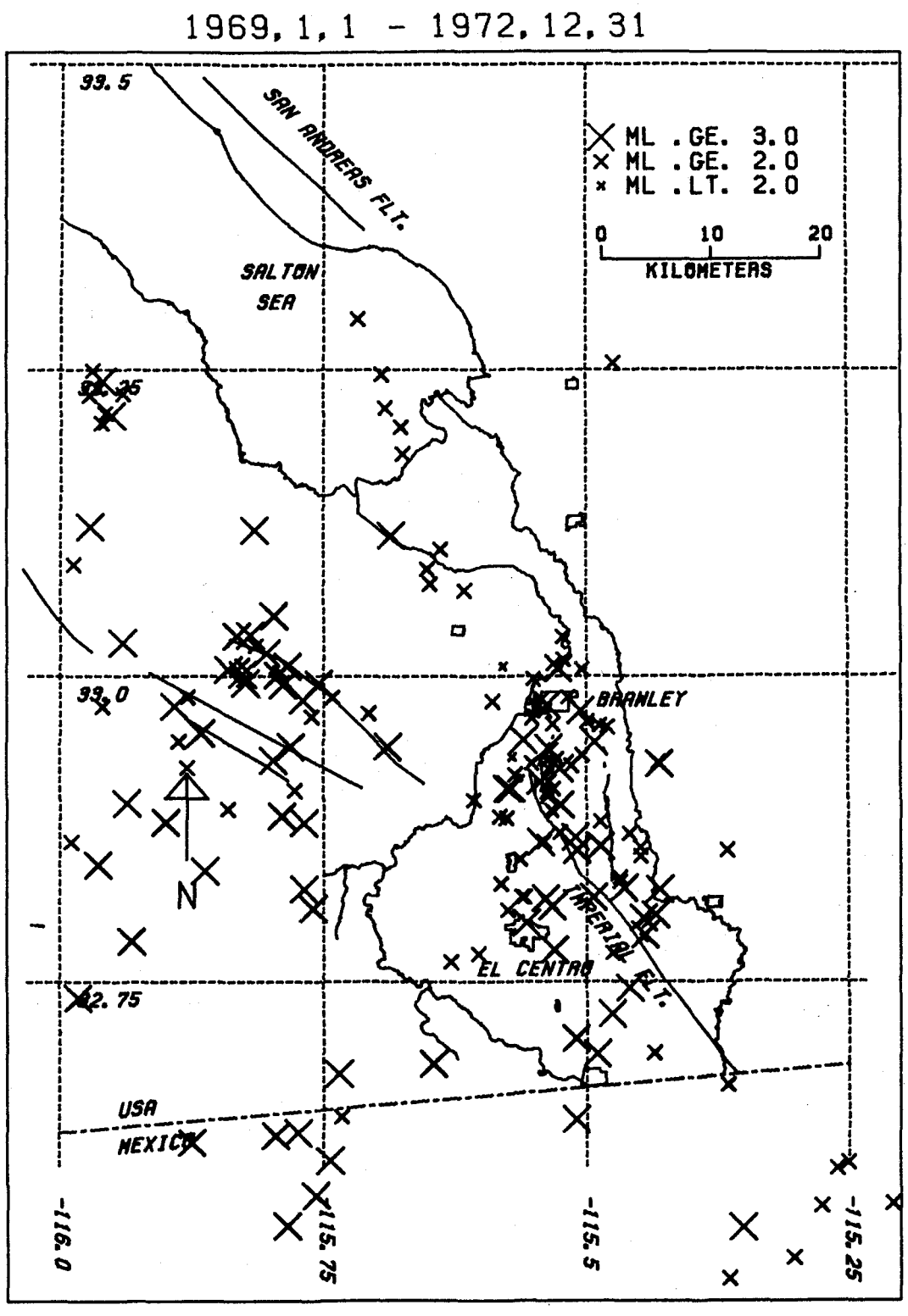

Figure 10. Imperial Valley seismicity including "A", "B", and "C" quality locations for the period 1969 through 1972.

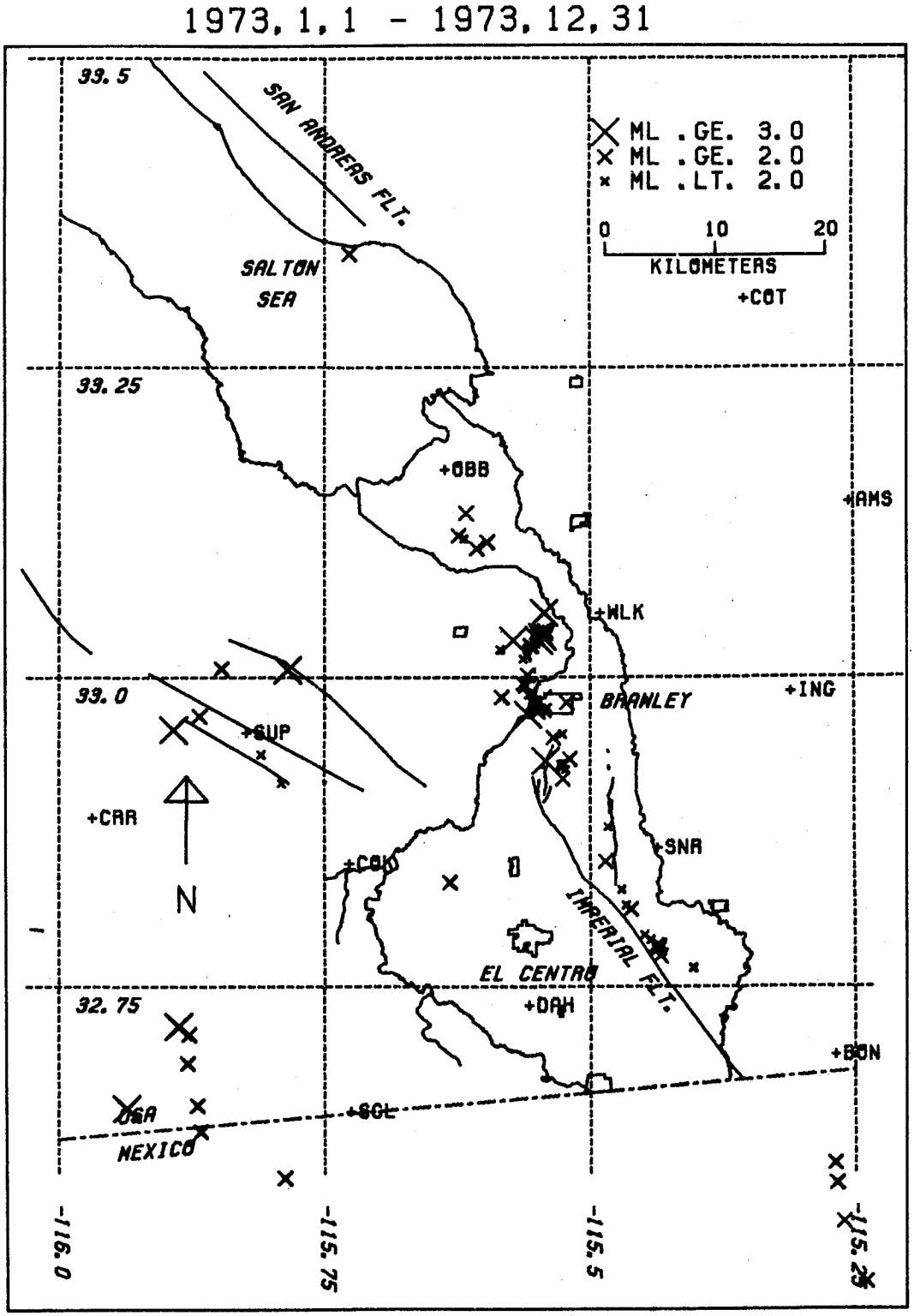

Figure 11. Imperial Valley seismicity including "A" and "B" quality locations for the period January 1973 through December 1973.

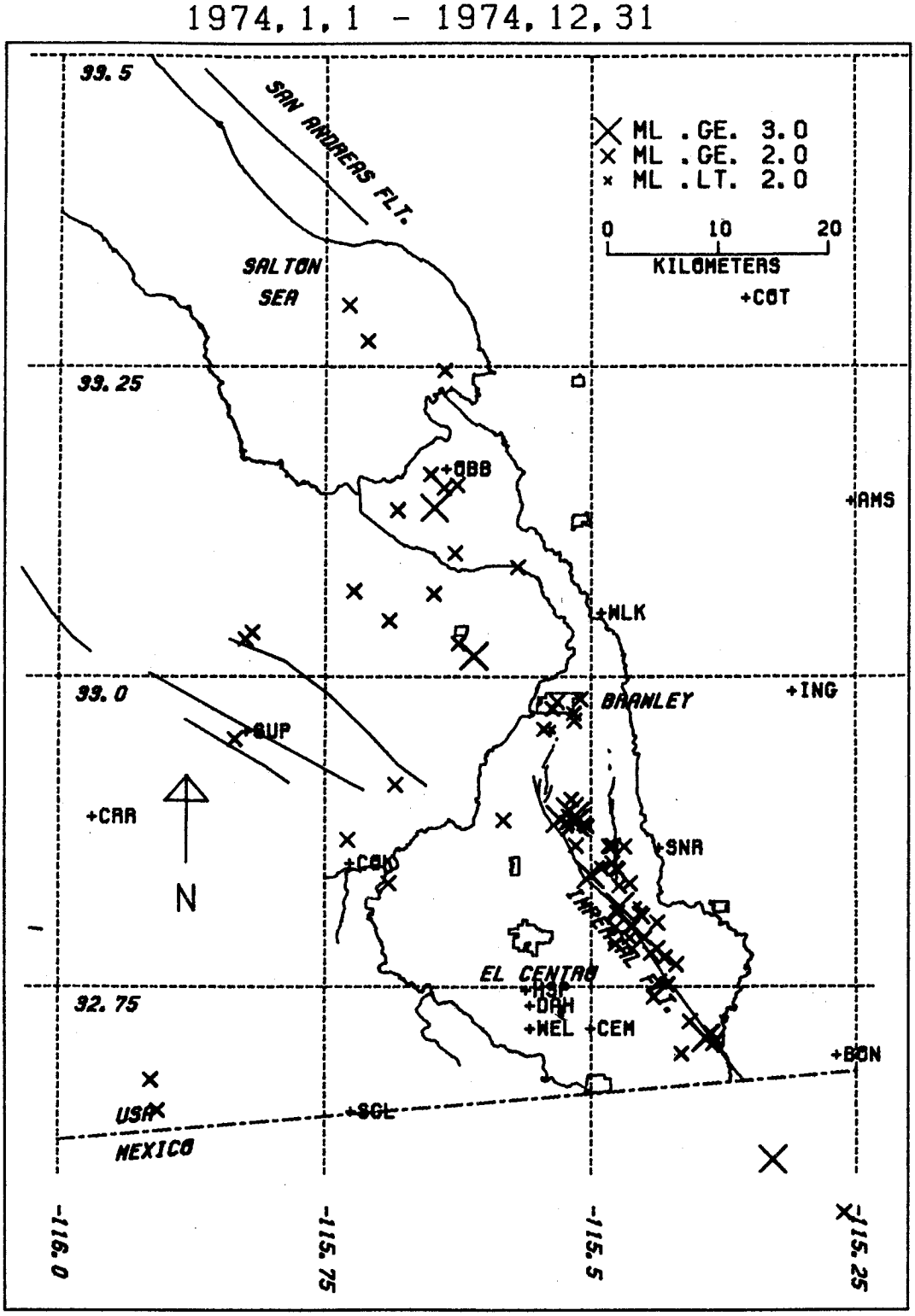

Figure 12. Imperial Valley seismicity including "A" and "B" quality locations for the period January 1974 through December 1974.

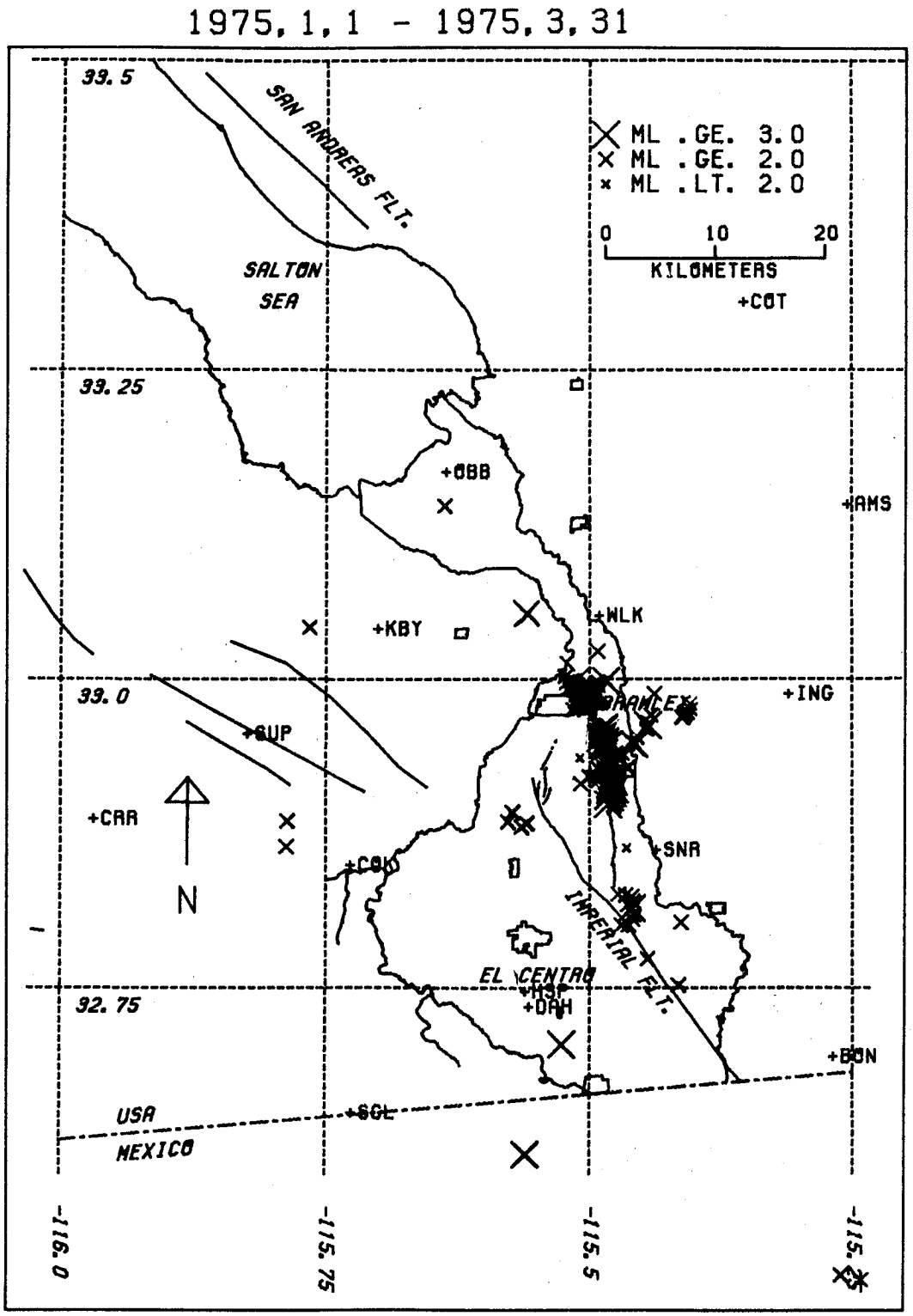

Figure 13. Imperial Valley seismicity including "A" and "B" quality locations for the period January 1975 through March 1975.

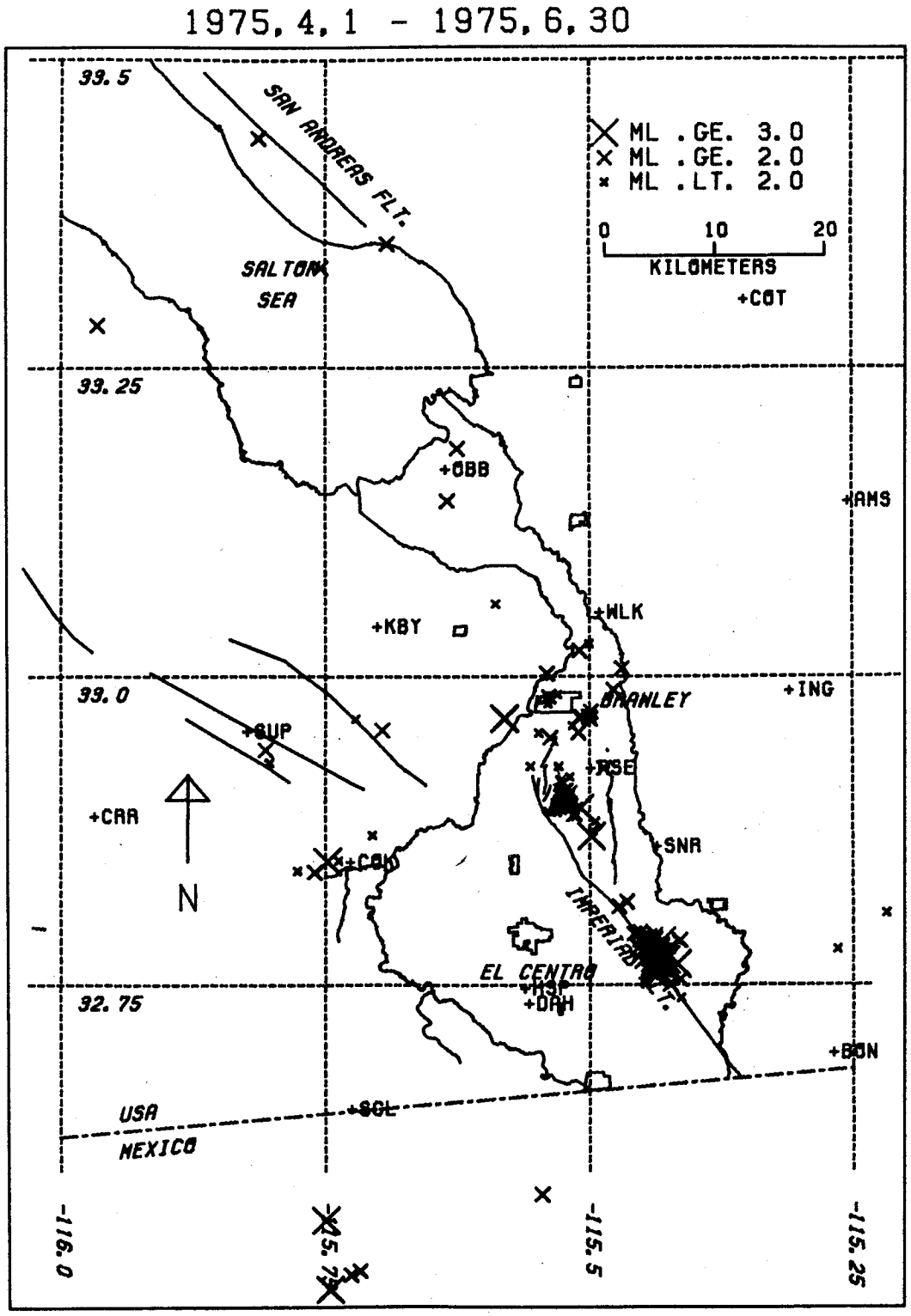

Figure 14. Imperial Valley seismicity including "A" and "B" quality locations for the period April 1975 through June 1975.

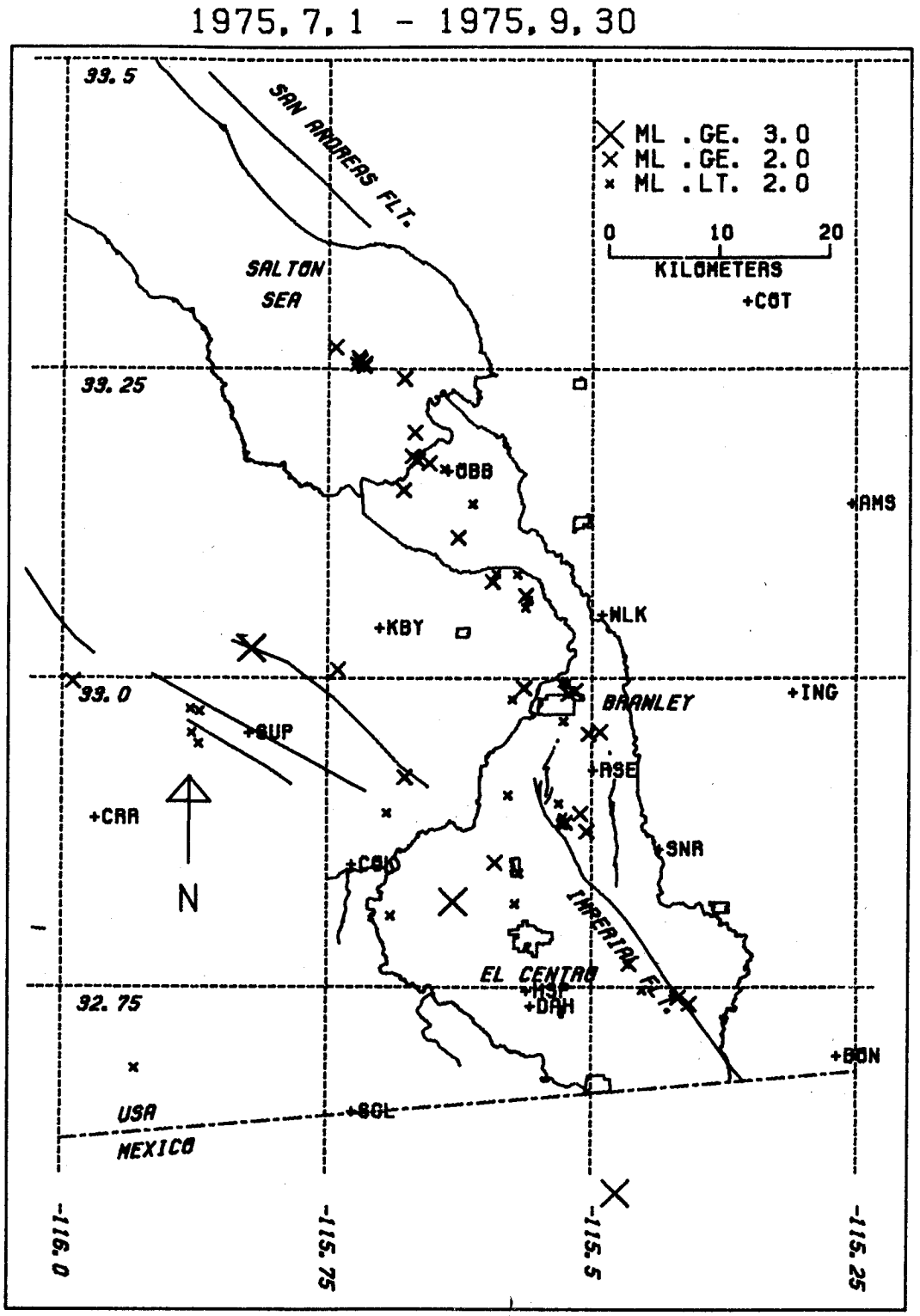

Figure 15. Imperial Valley seismicity including "A" nad "B" quality locations for the period July 1975 through September 1975.

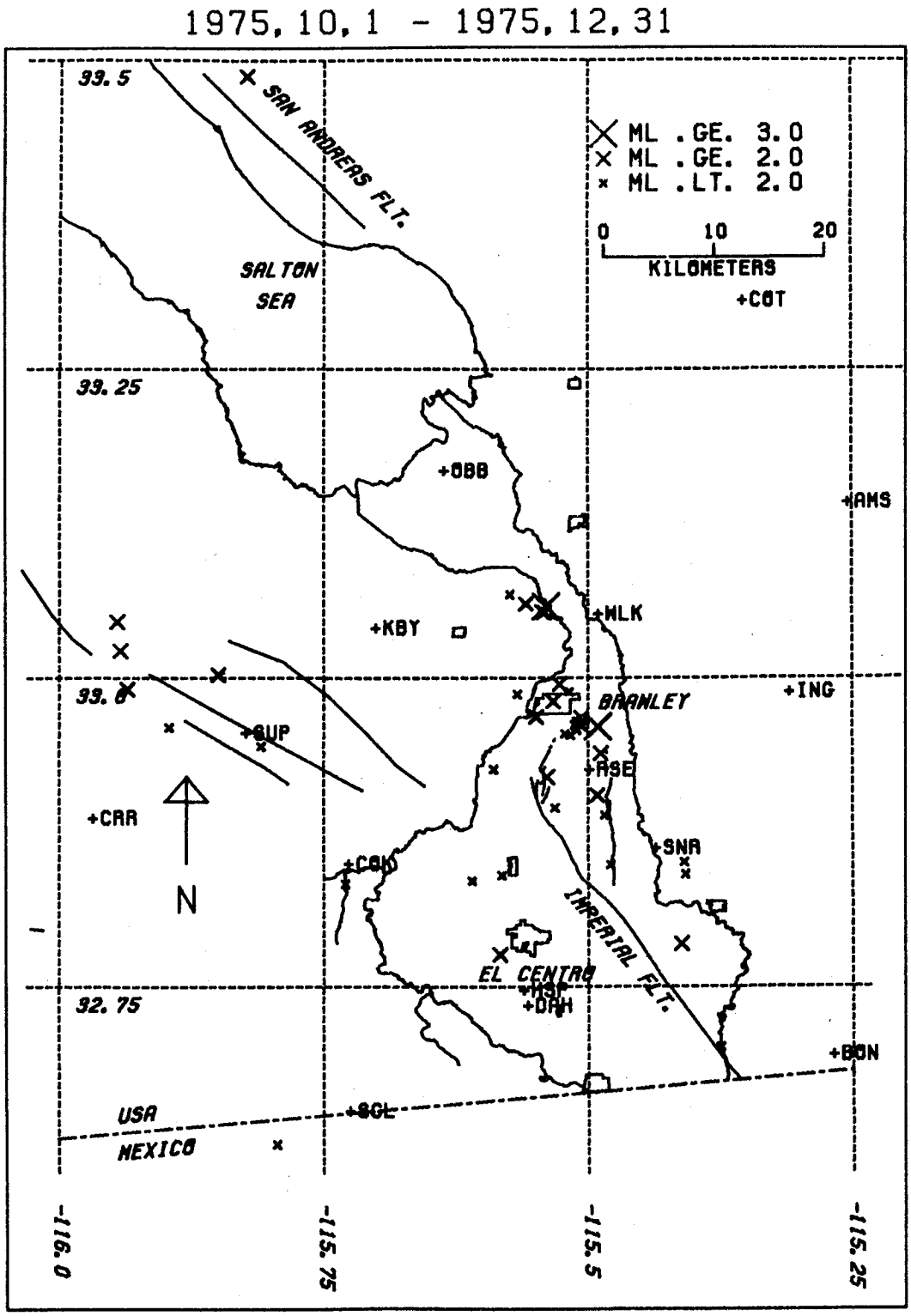

Figure 16. Imperial Valley seismicity including "A" and "B" quality locations for the period October 1975 through December 1975.

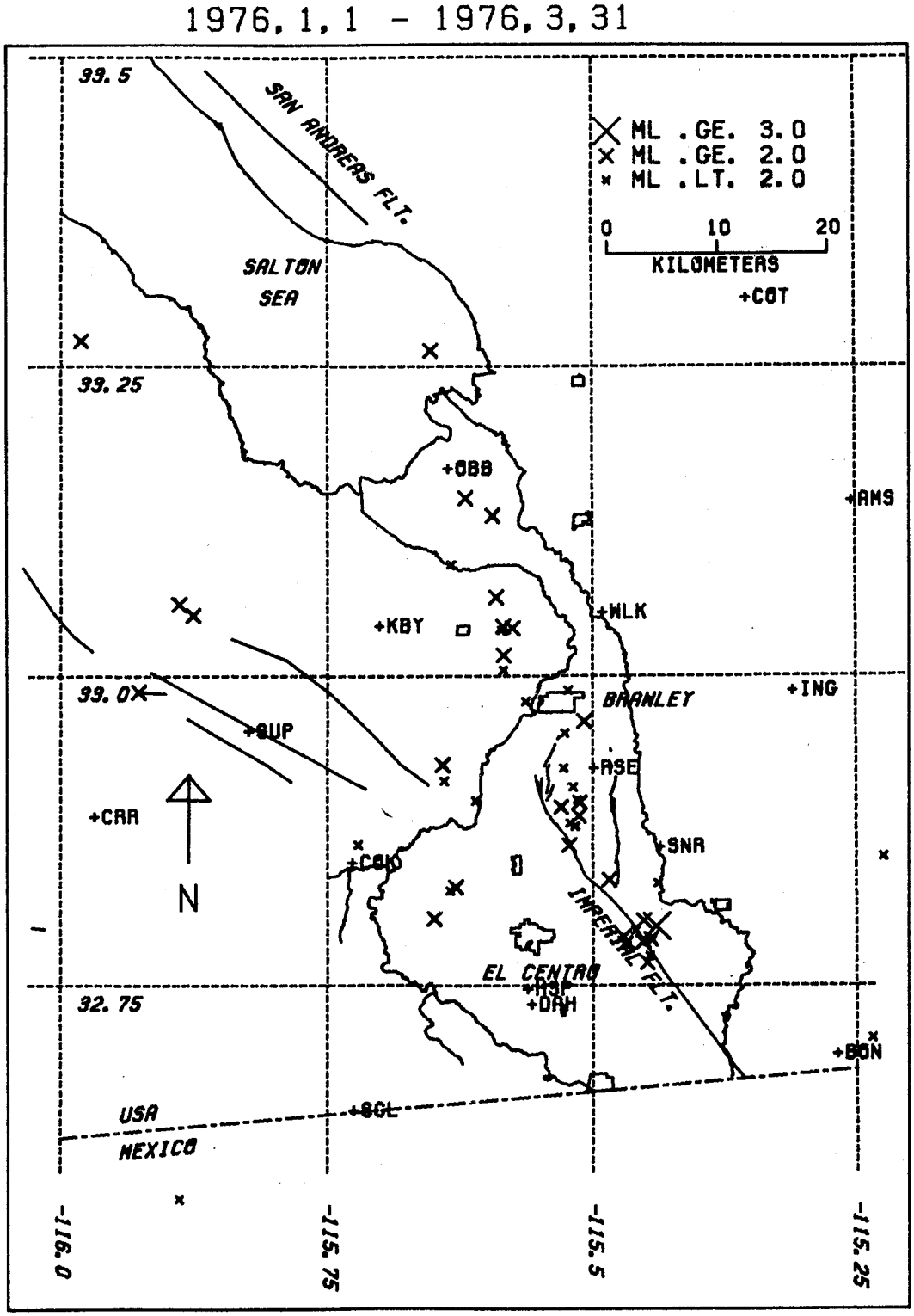

Figure 17. Imperial Valley seismicity including "A" and "B" quality locations for the period January 1976 through March 1976.

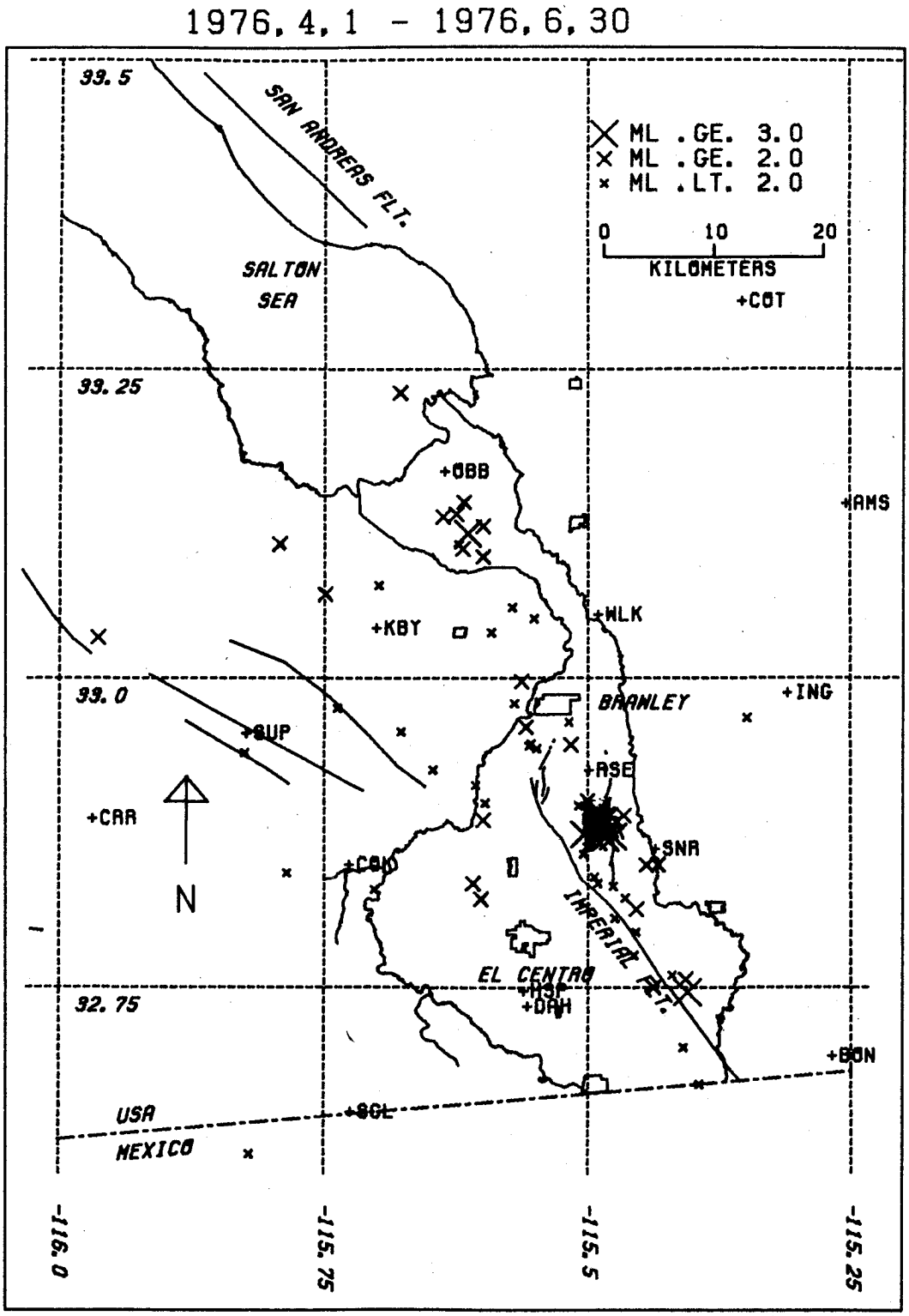

Figure 18. Imperial Valley seismicity including "A" and "B" quality locations for the period April 1976 through June 1976.

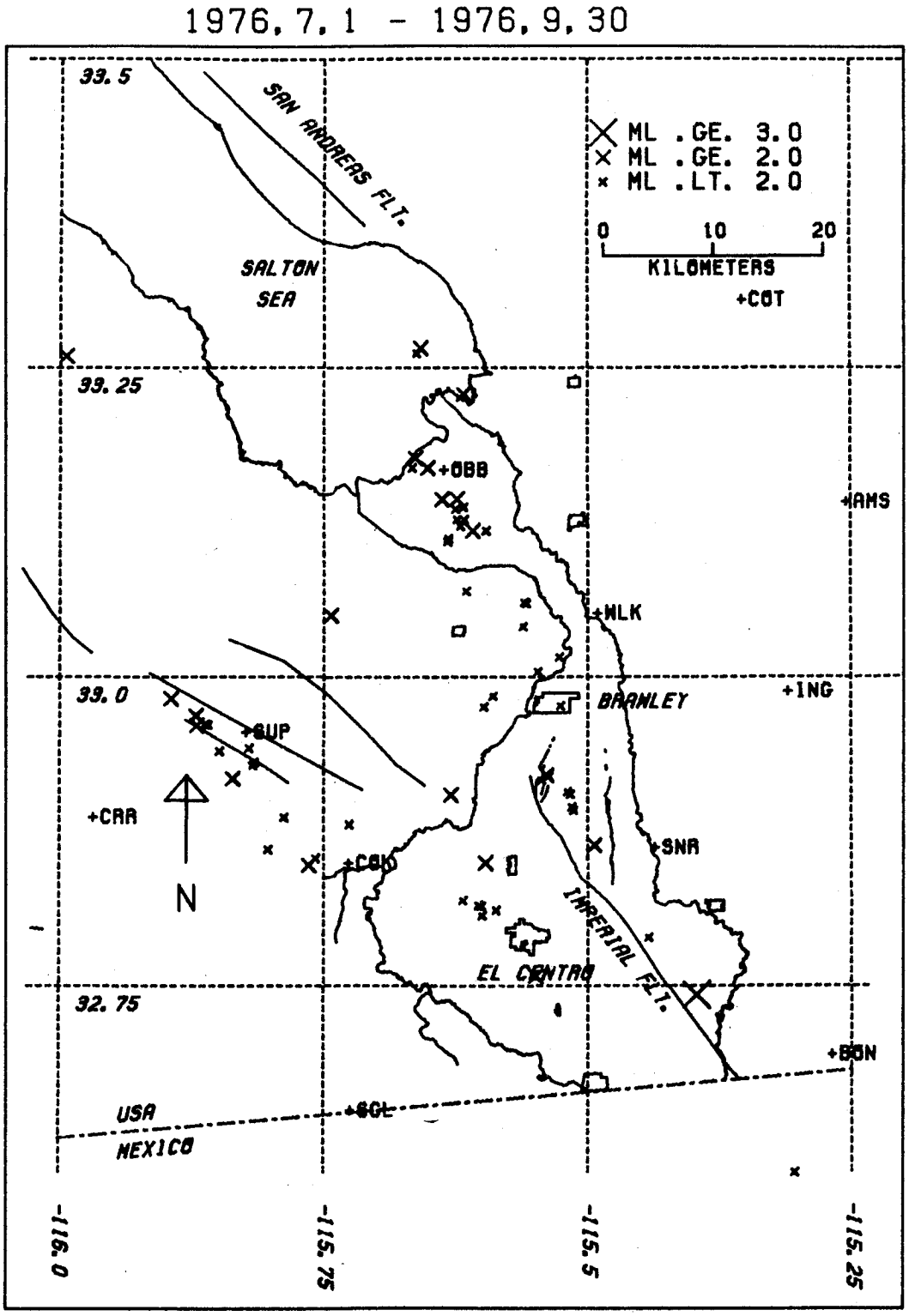

Figure 19. Imperial Valley seismicity including "A" and "B" quality locations for the period July 1976 through September 1976.

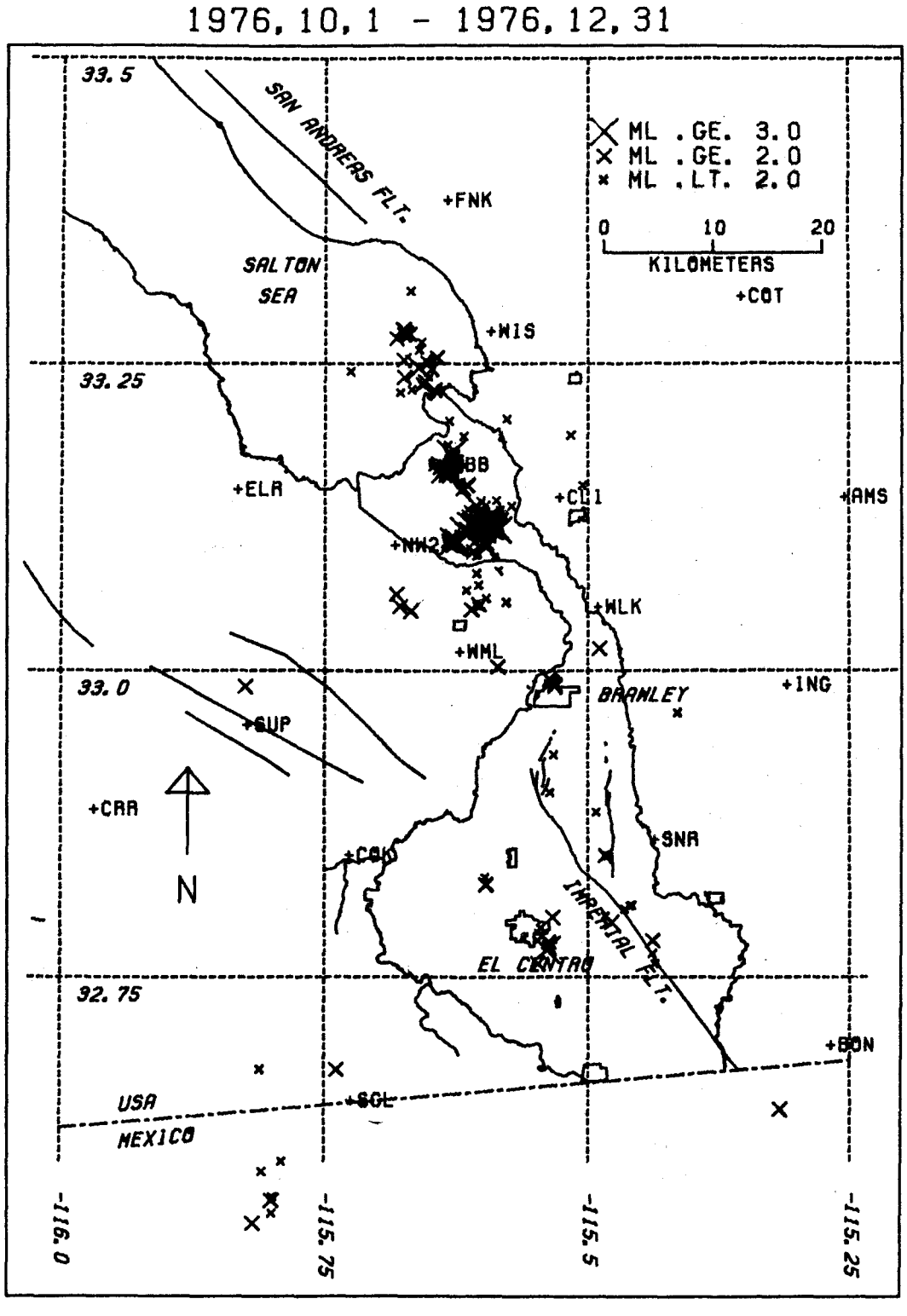

Figure 20. Imperial Valley seismicity including "A" and "B" quality locations for the period October 1976 through December 1976.

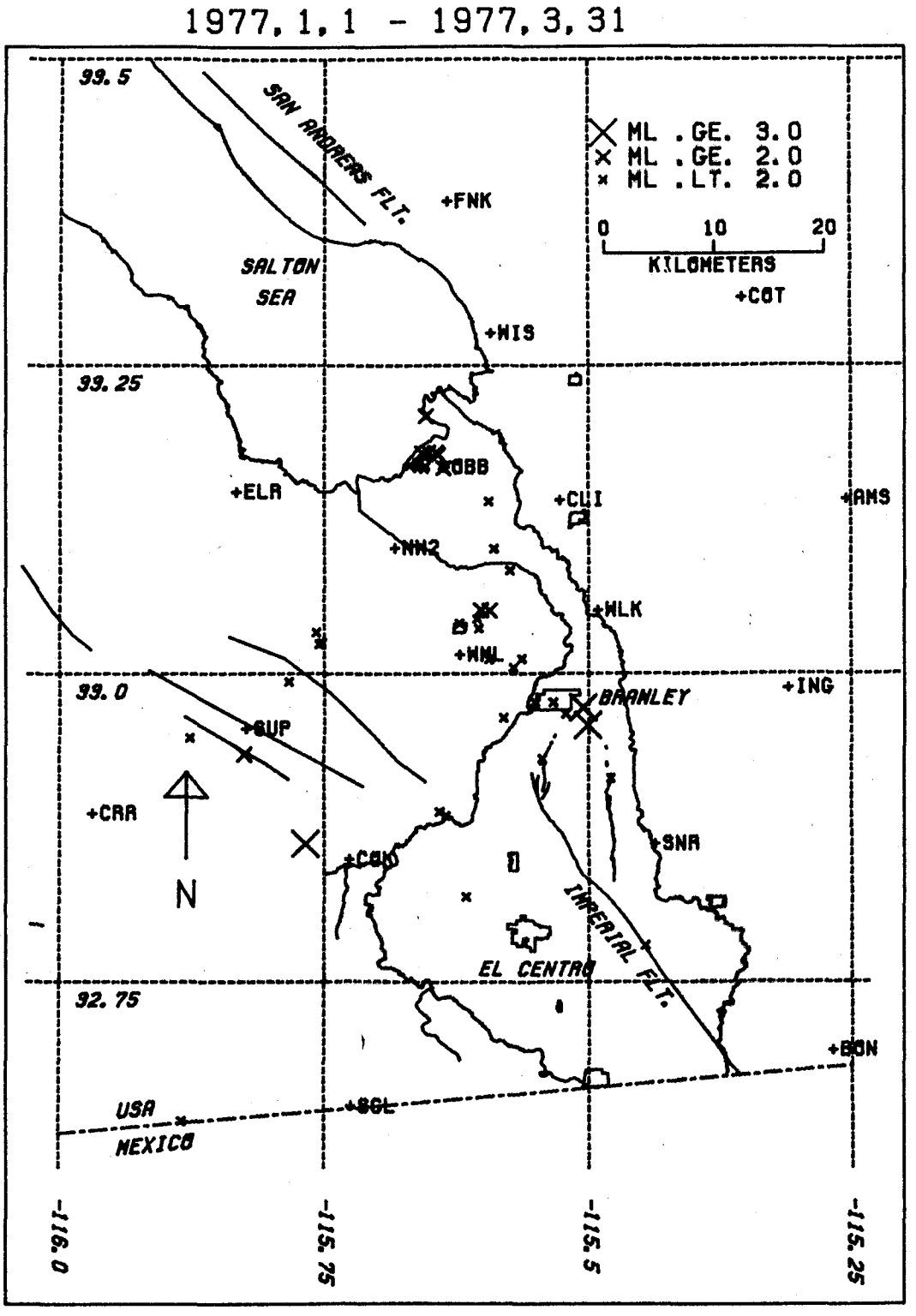

Figure 21. Imperial Valley seismicity including "A" and "B" quality locations for the period January 1977 through March 1977.

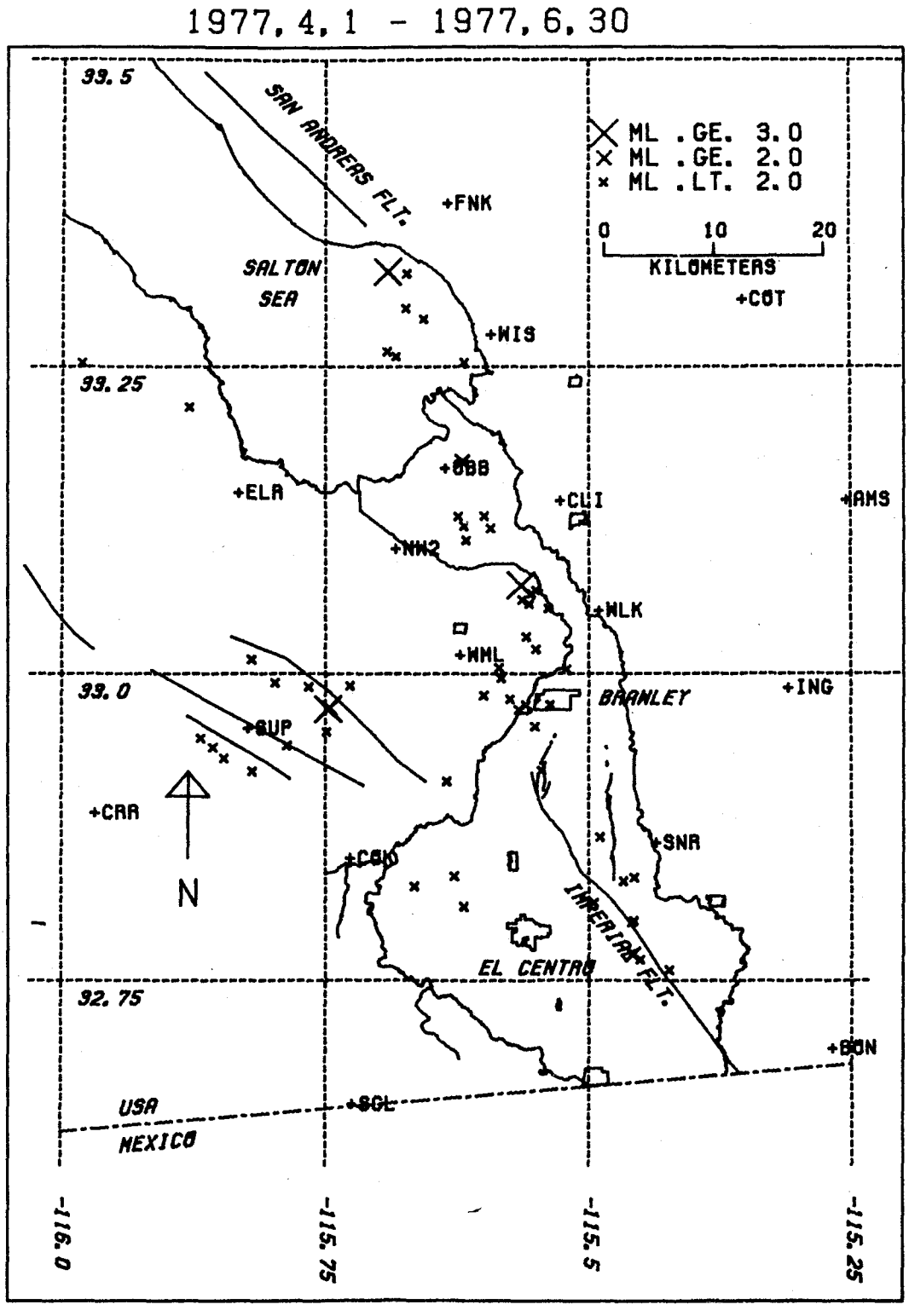

Figure 22. Imperial Valley seismicity including "A" and "B" quality locations for the period April 1977 through June 1977.

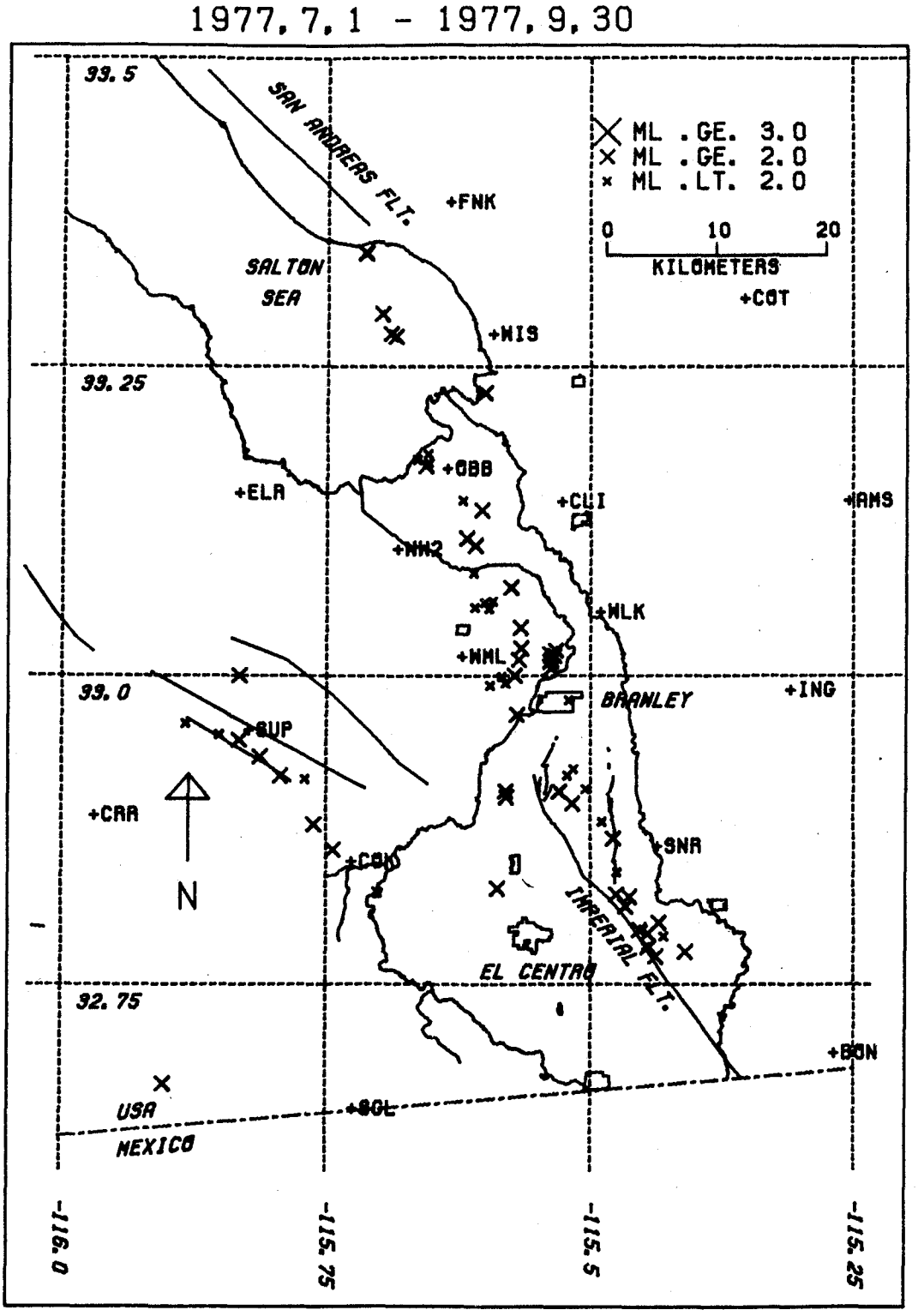

Figure 23. Imperial Valley seismicity including "A" and "B" quality locations for the period July 1977 through September 1977.

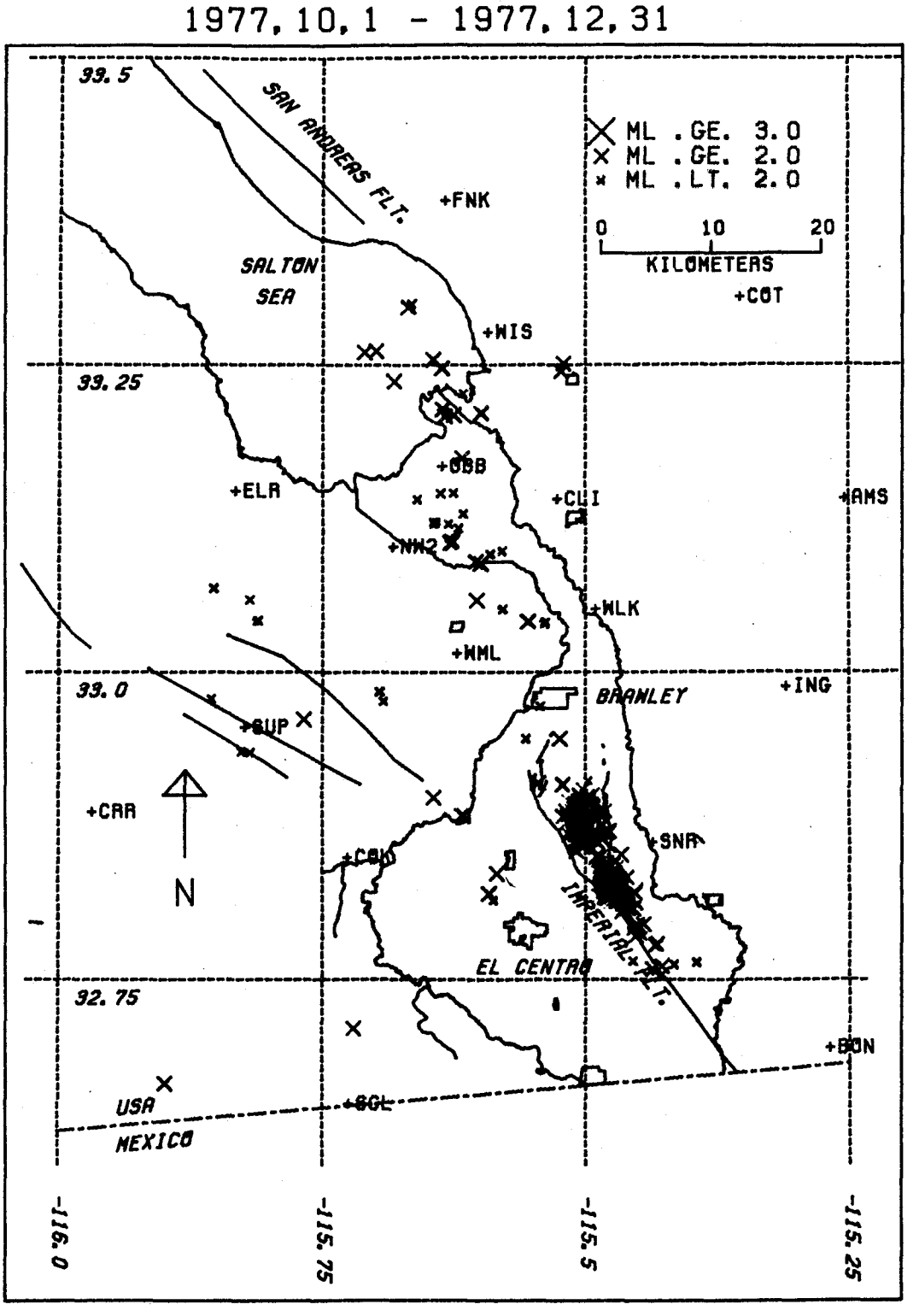

Figure 24. Imperial Valley seismicity including "A" and "B" quality locations for the period October 1977 through December 1977.

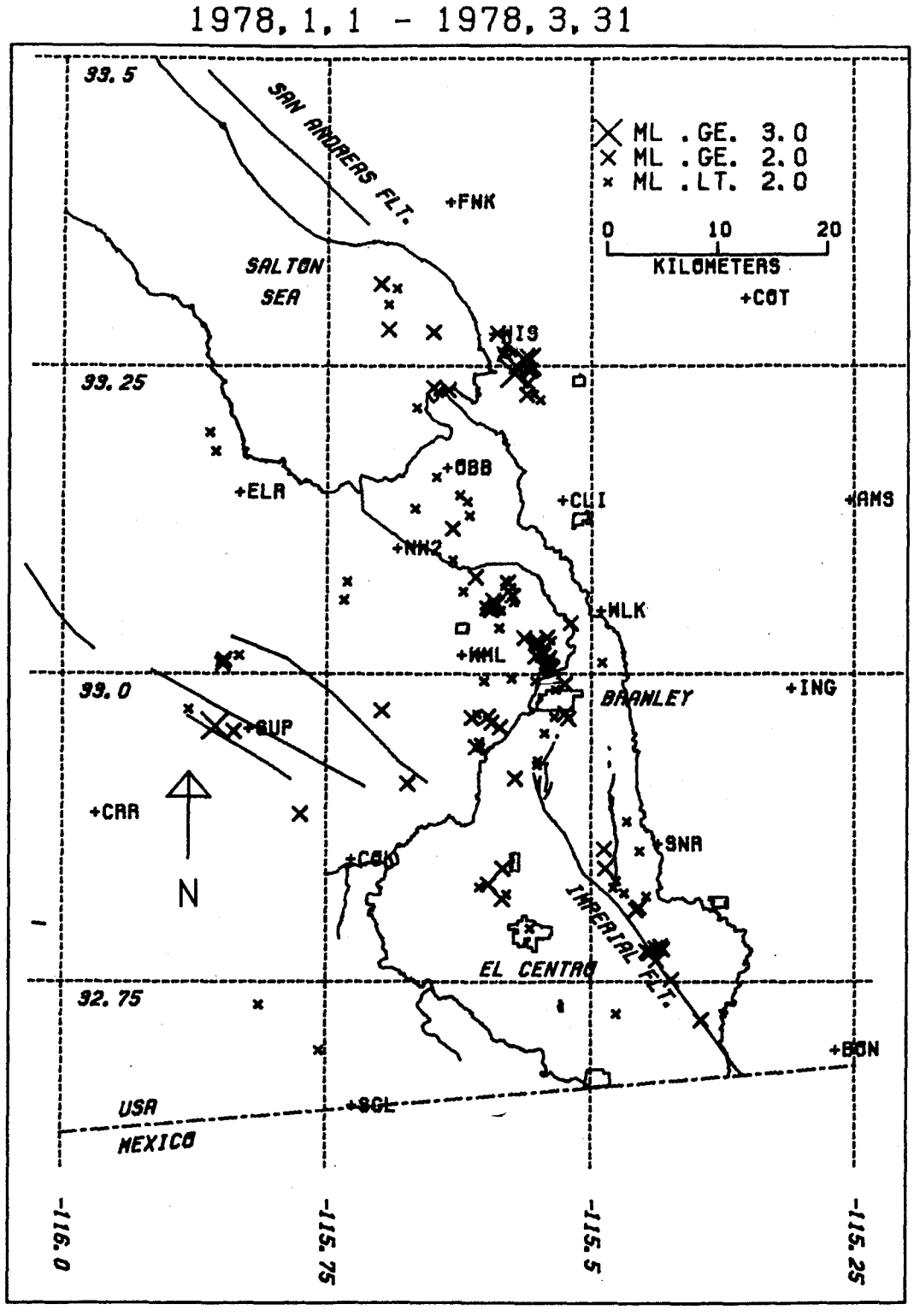

Figure 25. Imperial Valley seismicity including "A" and "B" quality locations for the period January 1978 through March 1978.

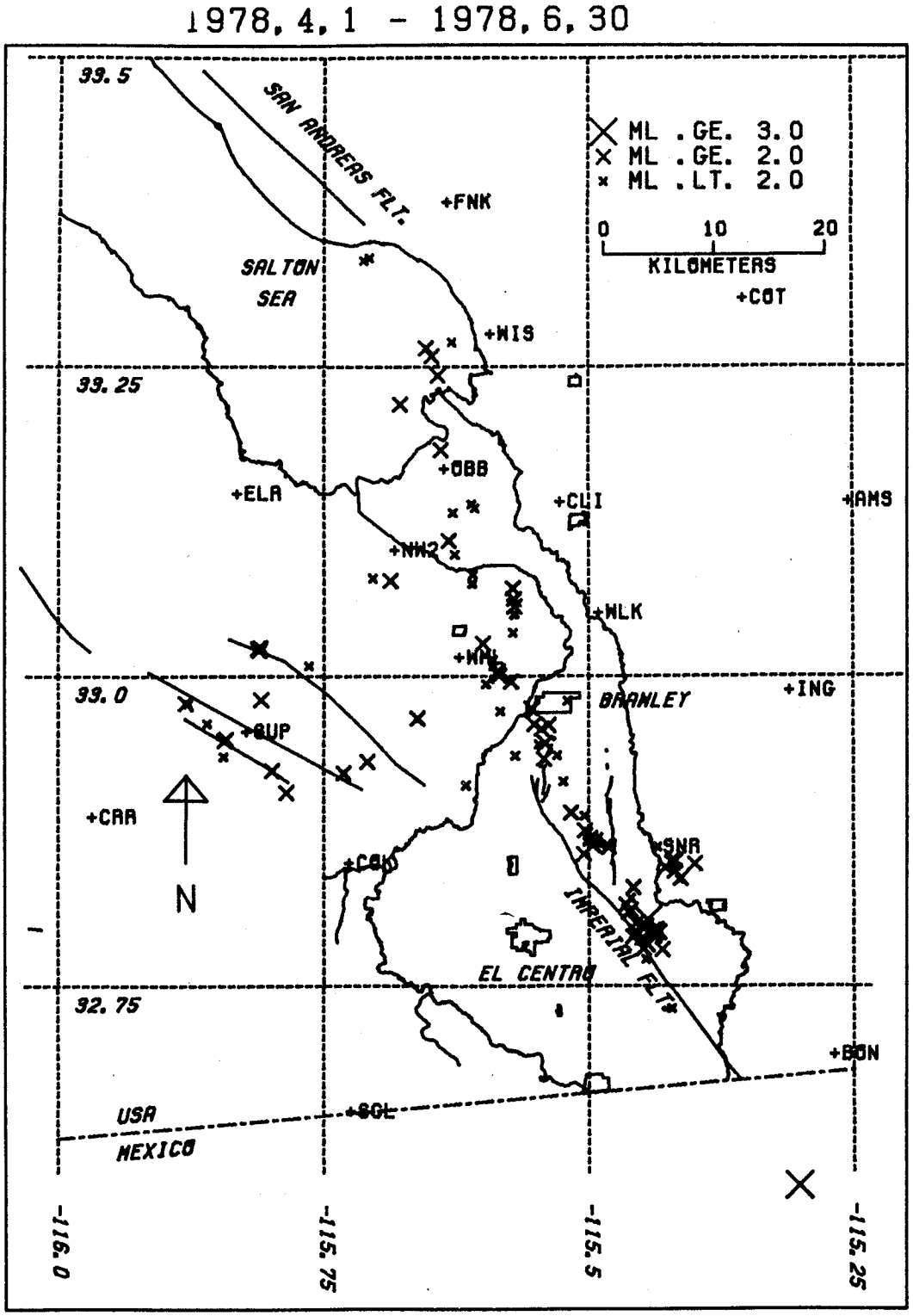

Figure 26. Imperial Valley seismicity including "A" and "B" quality locations for the period April 1978 through June 1978.

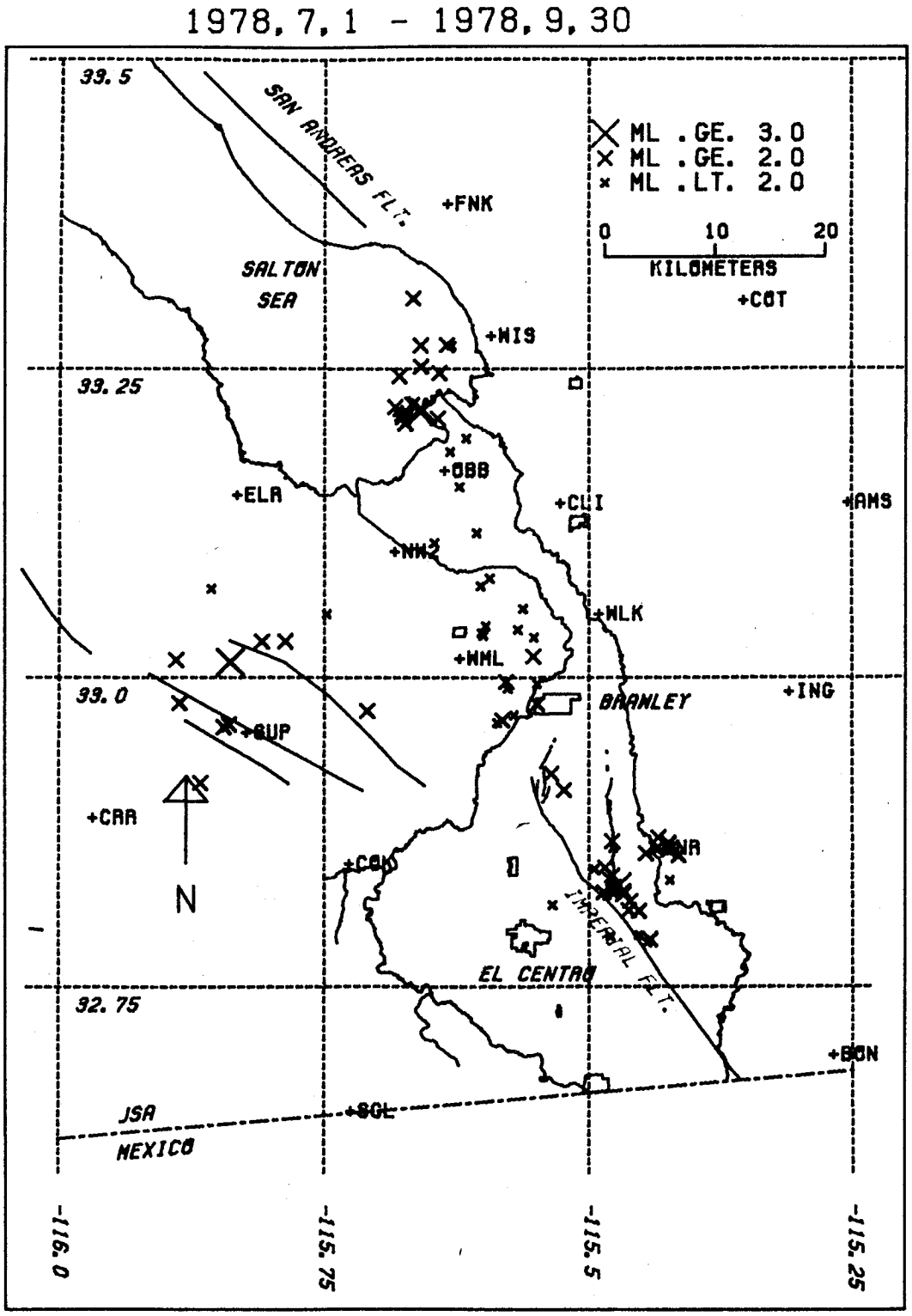

Figure 27. Imperial Valley seismicity including "A" and "B" quality locations for the period July 1978 through September 1978.

up to about 1 month, preceded and followed by periods of relative quiescence. The temporal and spatial proximity of these clusters suggests a physical relationship which will be the main subject of the following chapter.

It seems possible that the occasional isolated events and event pairs are simply the largest events of swarms for which most of the events are below our observational threshold. This was apparently the case for two swarms in 1975 near Obsidian Buttes studied by Gilpin and Lee (1978) using a tight array of portable seismographs. The first consisted of 31 events with magnitudes ranging from 1 to 1.5. None of these were recorded on a sufficient number of stations of the Imperial Valley network to warrant location during routine analysis procedures. Of the 253 events recorded during 72 hours for the second swarm, only 9 can be found in the Southern California catalog. It appears that there is considerable coherent seismicity occurring below our current detection capability.

It is intriguing that while over short time spans the seismicity within the Brawley seismic zone is highly clustered, during longer intervals (five years in Figure 4) the distribution is surprisingly uniform. Initially we had anticipated that swarm activity would arise periodically associated with several "hot spots" that would represent points of concentration of the regional secular strain. The observations, however, seem to require the contrary. The tendency appears to be more suggestive of "gap filling" leading to a spatial homogenization of seismicity with time. Very few instances were found that could be interpreted as the reactivation of a

tectonic structure associated with a preceding swarm. This suggests that in areas such as the Imperial Valley, the monitoring of seismicity for periods of a few months in order to establish a seismic background level is misleading. Such surveys have been conducted in connection with the development of geothermal resources so that subsequent seismic phenomena can be correctly ascribed either to natural processes or to human intervention. A more extensive period of monitoring leading to a detailed physical model is suggested when assessing the risks associated with those activities that might alter the seismicity pattern.

TEMPORAL VARIATIONS

Temporal variations of Imperial Valley seismicity can be examined more directly by compiling several time-series representations of recent events. One of these considers the accumulated moment calculated from local magnitude using the relationship $\log_{10}M_o = 1.5\ M_L + 16$ of Thatcher and Hanks (1973). Events were selected for this purpose from a quadrilateral with vertices at 32.2°, -115.8°; 33.2°, -115.0°; 32.67°, -115.0°; and 32.67°, -115.6°. The resulting plot is shown in Figure 28 for the period 1932 to the present. Accumulated moment is clearly dominated by the 1940 earthquake. The contribution of the 1940 mainshock is 1.1×10^{26} dyne-cm based on a catalogued magnitude of 6.7 (Hileman et al., 1973). Using a more representative value of $M_s = 7.1$ (Richter, 1958), gives a moment of 4.5×10^{26} dyne-cm which is comparable with the averaged value of 5.6×10^{26} dyne-cm listed by Kanamori and Anderson

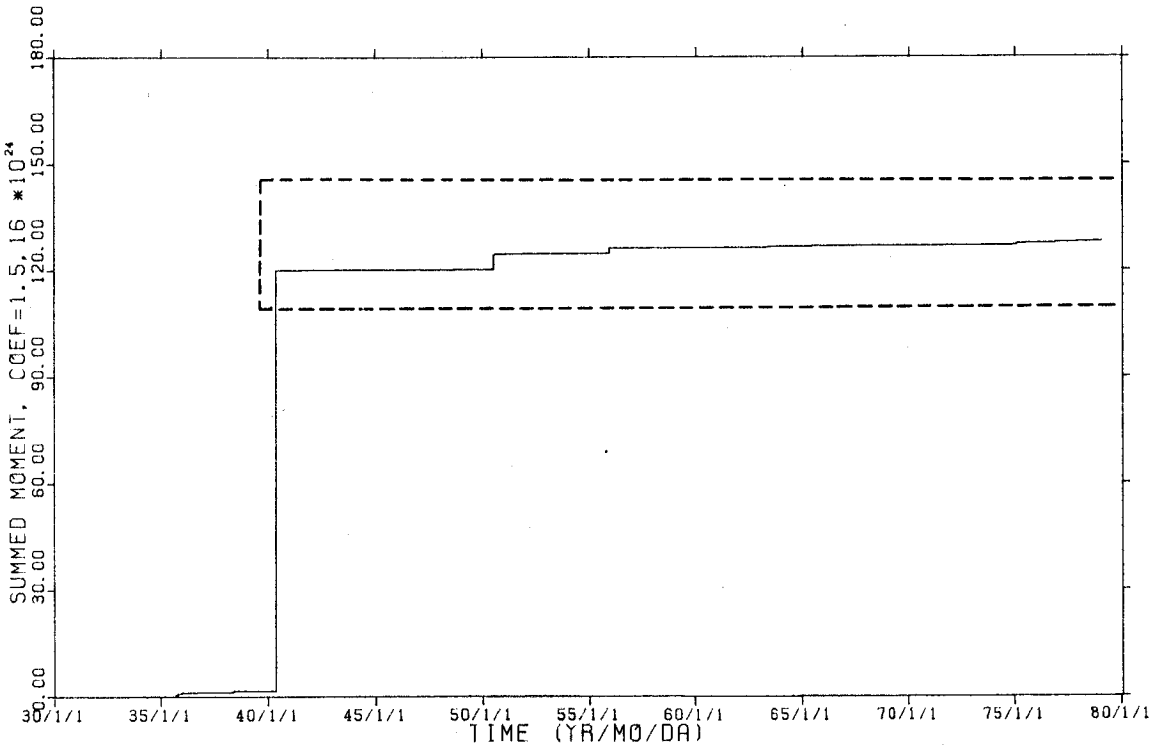

Figure 28. Integrated seismic moment for the Imperial Valley calculated using the relationship, $\log_{10} M_o = 1.5\ M_L + 16$. The region enclosed by broken lines is shown in greater detail in Figure 29.

(1975). This more realistic moment is about 4 times that used in preparing Figure 28, making its contribution to the accumulated moment proportionately greater. Plotted at the scale of Figure 28 the only additional outstanding feature is a sudden increase in moment rate in 1950 followed by a gradual return to the previous rate over a period of about 8 years. The style of seismicity in the Imperial Valley also changed at the time of the 1940 quake. Rather unexpectedly earthquake swarms which previous to 1940 had been common became virtually nonexistent until 1950 when the calm was broken by the largest swarm ever recorded in the Imperial Valley (Richter, 1958). This swarm, which contained 22 earthquakes of magnitude 4 and greater, was located about midway between Brawley and the Salton Sea and accounts for the first step in accumulated moment associated with the 1950 moment rate increase in Figure 28. The reduction in swarm activity after 1940 may be related to the observation that the aftershocks themselves resembled swarms (Richter, 1958).

Figure 29 shows a vertical exaggeration of the dashed region of Figure 28, revealing a second abrupt change in moment rate about 1975 (shown in still greater detail in Figure 30). While the 1950 change was related to an increase in activity in the northern and central portions of the Brawley seismic zone, the second reflects an increase in swarm activity south of Brawley.

The spatial change in moment rate is explored further in Figure 31 where accumulated moment is plotted as equivalent annual slip over 10 km fault sections as a function of distance for three periods following the 1940 earthquake. These periods were chosen to correspond

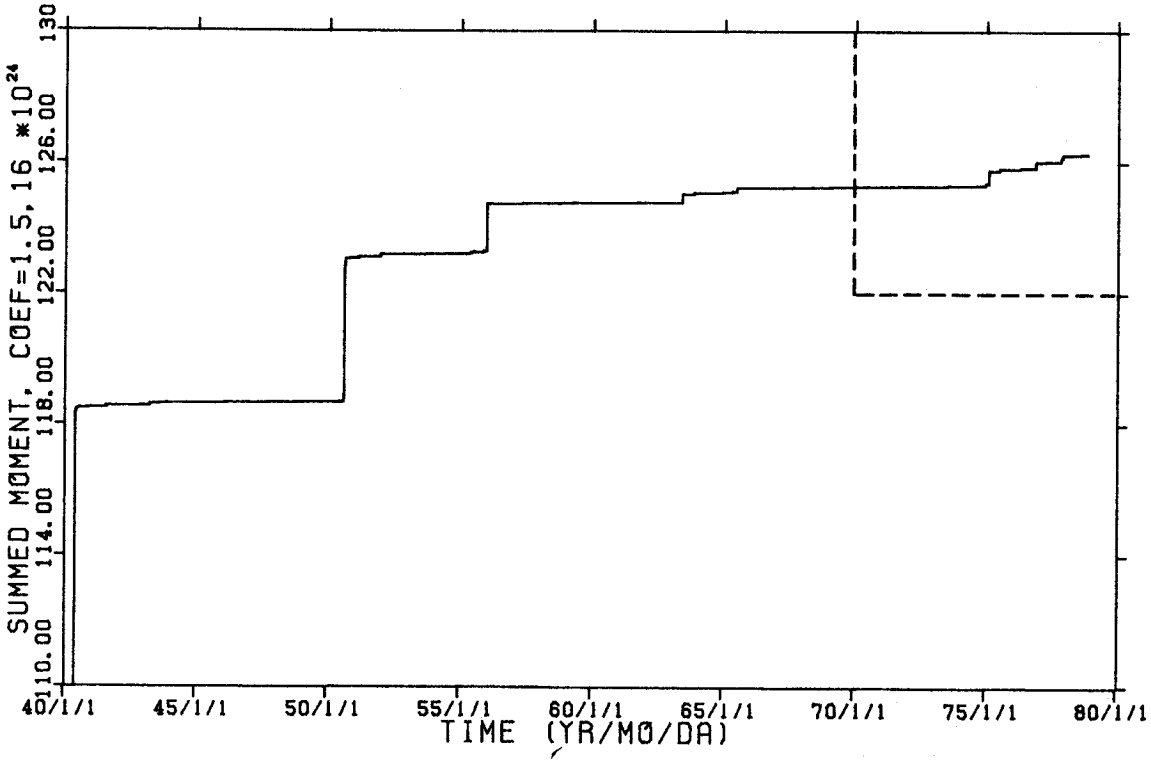

Figure 29. Integrated seismic moment for the Imperial Valley calculated using the relationship $\log_{10} M_o = 1.5\ M_L + 16$. The region enclosed by broken lines is shown in greater detail in Figure 30.

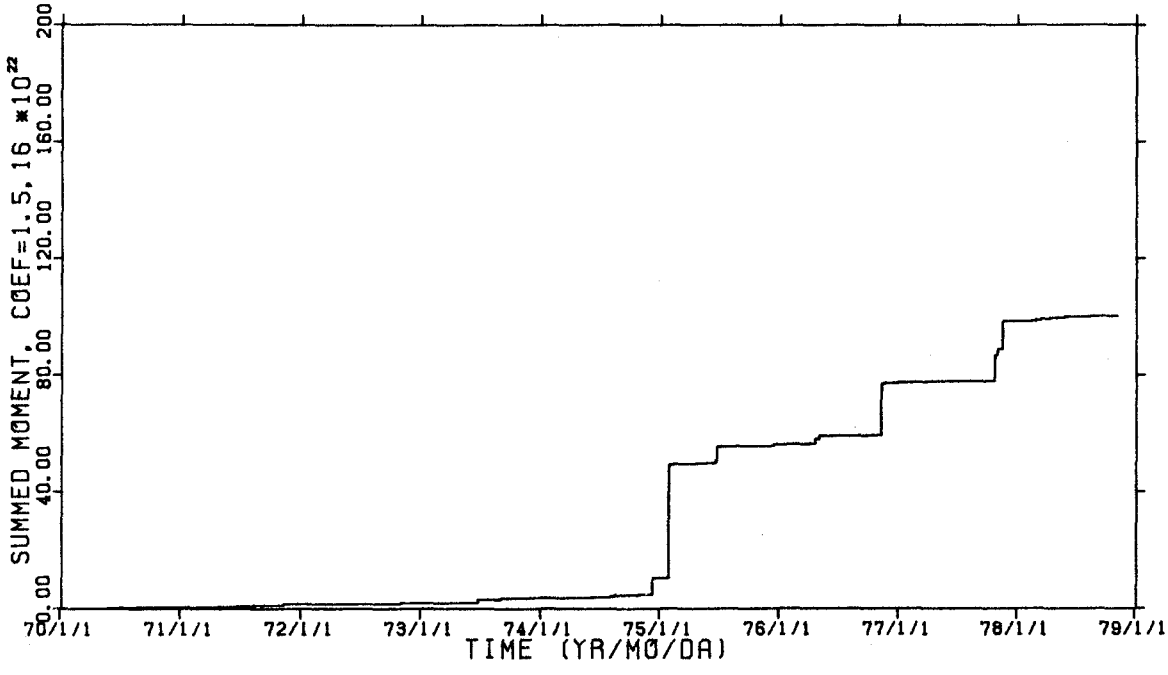

Figure 30. Integrated seismic moment for the Imperial Valley for the last nine years calculated using the relationship $\log_{10} M_o = 1.5\ M_L + 16$.

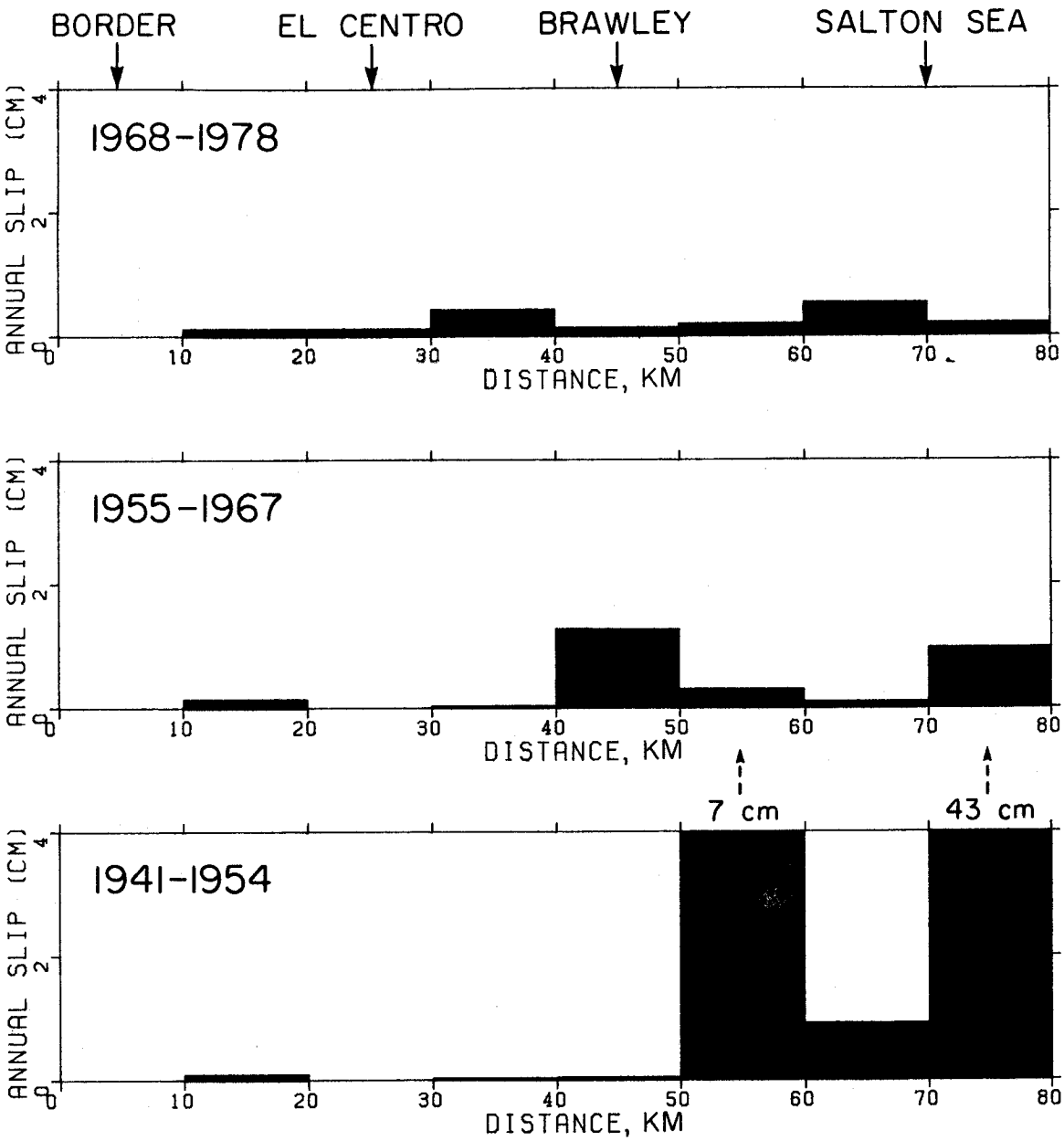

Figure 31. Seismic moment summed over 10 km sections of the Brawley Seismic Zone during three intervals bounded by triangulation surveys of the geodetic network reported by Thatcher (1979). Moment is calculated from local magnitude using the relationship $\log_{10} M_o = 1.5\ M_L + 16$, and plotted as equivalent slip on a fault surface of 50 km^2. Distance is measured from the point 32.65°N, 115.26°W.

to intervals between triangulation surveys of the Imperial Valley geodetic network reported by Thatcher (1979) in order to facilitate a direct comparison of these two studies. Slip is calculated from the relation $M_o = S\mu D$, where M_o is the accumulated moment (dyne-cm), S is the area of a fault section (5×10^{11} cm^2), μ is the shear modulus (2×10^{11} dynes/cm^2) and D is the calculated displacement (cm). The vertical extent of the seismogenic zone was taken to be 5 km. An encroachment of seismicity from north to south is evident. Averaged over the past 38 years the maximum annual slip that could be attributed to seismicity near the southern shore of the Salton Sea is about 6 mm/yr. This is in fair agreement with a deformation rate of 5 to 6 mm/yr. reported by Savage et al. (1974). The latter study, however, indicates a much more uniform rate with time than one would infer from the variations in seismicity.

A slightly different representation of these changes is shown in Figure 32 where we have plotted accumulated moment by year. This plot is in a sense the derivative of that in Figure 28 and tends to emphasize times of significant activity. The reduction of activity at the time of the 1940 quake is clear, followed by the major swarm in 1950. A general decline in average moment rate is also apparent. A similar presentation is provided in Figure 33 where the number of earthquakes with magnitudes of 4 and greater are summed by year. The increase in activity during the last 3 years reflects an apparent recent increase in the number of discrete swarms, though the accumulated moment for any particular swarm appears to have decreased considerably when compared to those from 1950 through 1965.

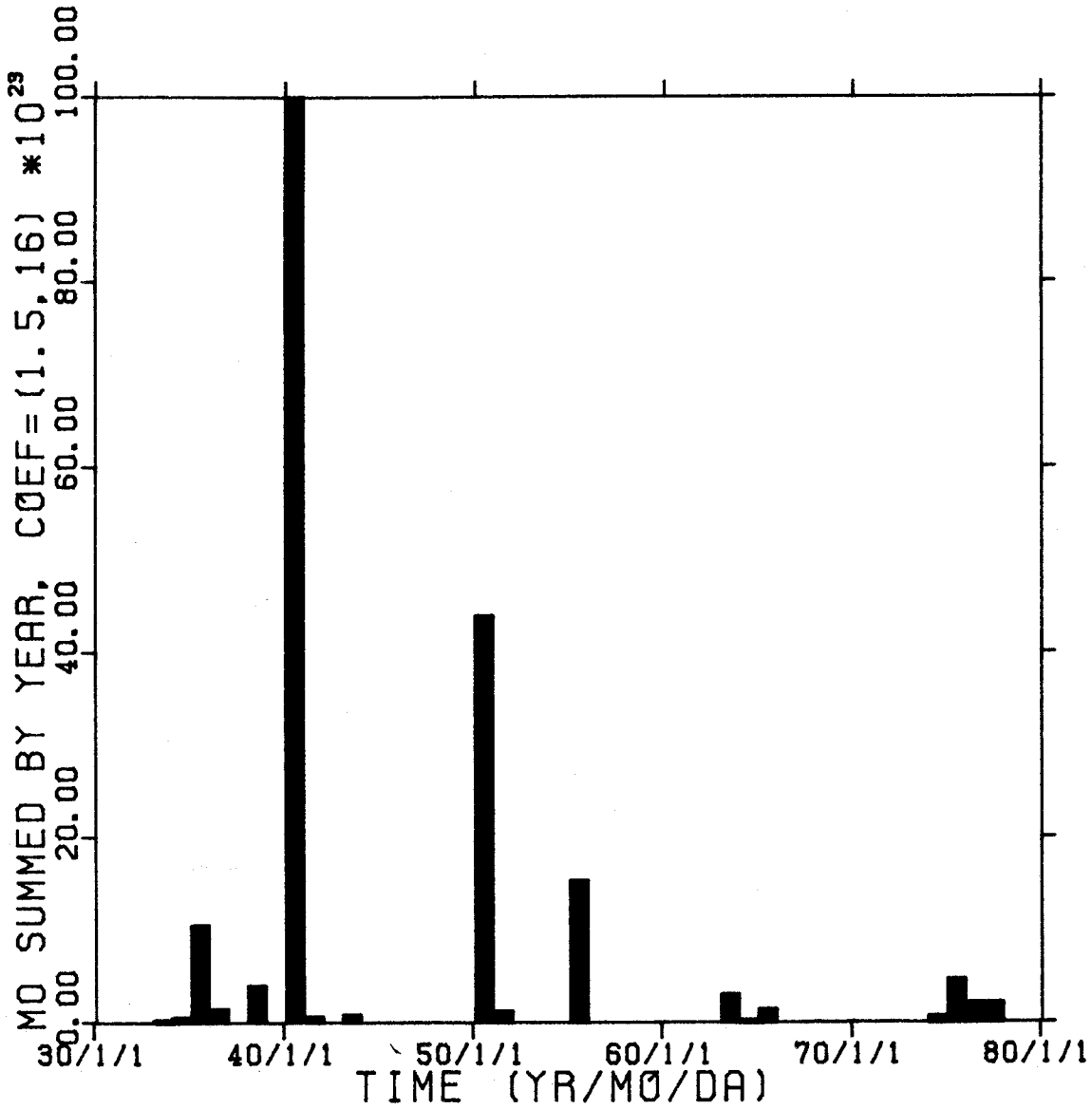

Figure 32. Histogram showing annual seismic moment in the Imperial Valley for the period 1932 to the present. Moment is estimated from local magnitude using the relationship $\log_{10} M_o = 1.5\ M_L + 16$.

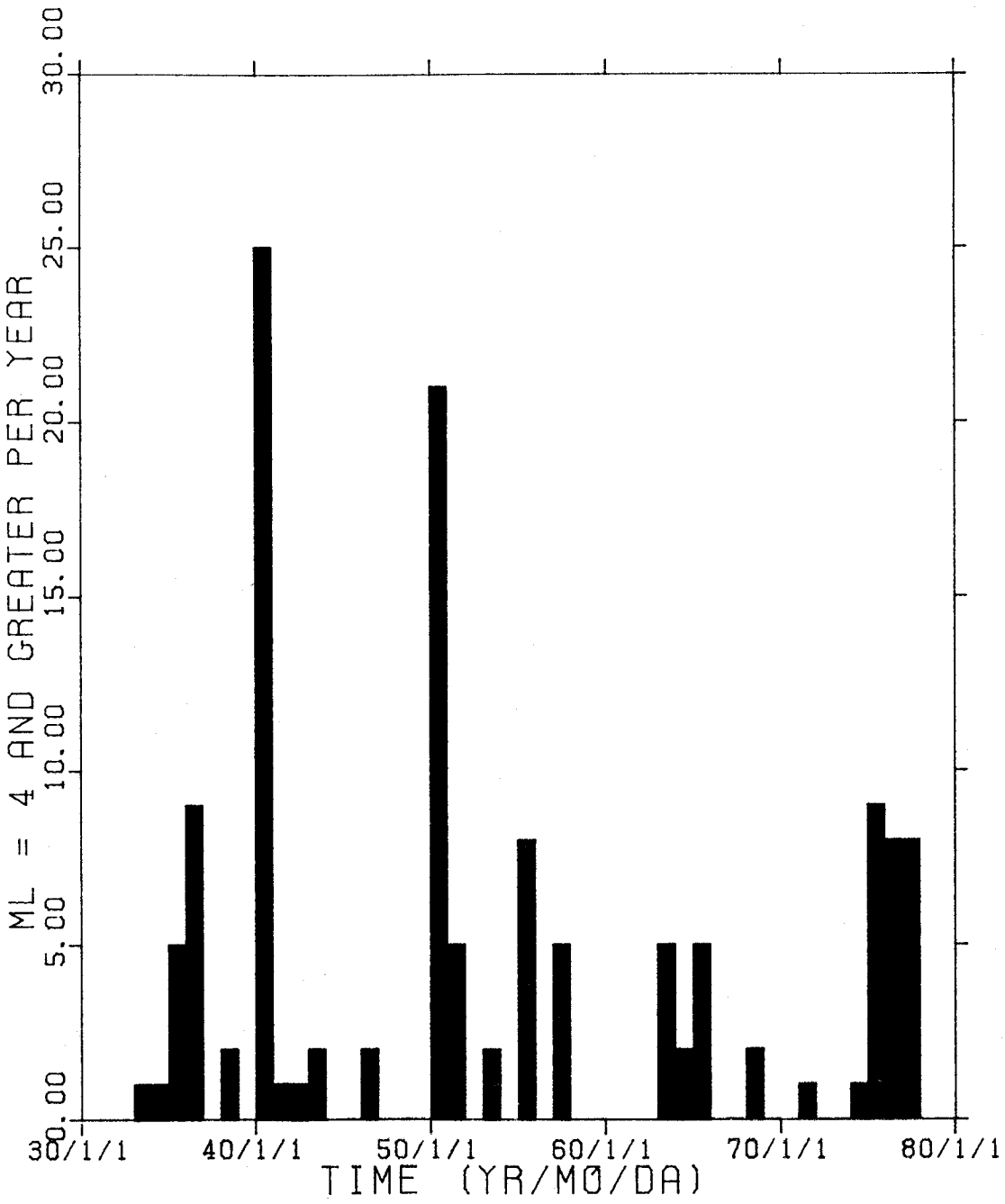

Figure 33. Histogram showing the yearly number of earthquakes in the Imperial Valley exceeding M_L = 4 for the period 1932 to the present.

The comparison of moment rate in the Imperial Valley with the geodetic results reported by Thatcher (1979) is intriguing. The 13-year period ending in 1941 is clearly dominated by the co-seismic deformation associated with the 1940 quake. Although the surface offset dies out north of the instrumental epicenter, the survey results suggest that at depth displacements as large as 4 m continue considerably further north. During the following 13 years large buried displacements along the entire length of the Brawley seismic zone are indicated, although substantial near-surface slip is apparently excluded by the geodetic data. One successful model requires 2 m of offset at depths exceeding 10 km over the co-seismic portion of the Imperial Fault and a northward extension along the Brawley Fault to its apparent merger with the San Andreas near the south end of the Salton Sea. Thatcher (1979) pointed out that this suggests a rather unusual mechanism for post-seismic recovery following the 1940 earthquake. From 1954 to 1967 the strain field is less coherent and it appears that most of the post 1940 recovery was completed prior to 1954. The greatest seismic moment rate north of the Imperial Fault falls within the same period (1941 to 1954) that substantial slip was occurring at depth. The accumulated seismic moment north of the Imperial Valley from 1941 through 1954 was about 4.2×10^{24} dyne-cm, or about two orders of magnitude less than that of the 1940 mainshock, with an equivalent magnitude of 5.7. This discrepancy suggests that most of the strain observed geodetically must be occurring aseismically in the Imperial Valley, although the seismicity does appear to be modulated by the strain rate.

The seismicity of the Imperial Valley during the past 50 years can be summarized in four discrete episodes of activity. These are:

(1) A period of intermittent earthquake swarms preceding 1940,

(2) ten years of low level seismicity after 1940,

(3) the resumption of swarm activity at the northern end of the Brawley seismic zone in 1950, and

(4) the spreading of activity into the southern end of the Brawley seismic zone beginning around 1969, with a significant increase in seismic moment rate in 1975. It is conceivable that the current situation is comparable to that preceding the 1940 earthquake, although verification of this is beyond the limits of earlier data.

Since 1973 the detection threshold in the Imperial Valley has decreased substantially, permitting a more detailed analysis of day-to-day variations in seismicity. Figures 34 through 39 provide a daily log of number of located events since the installation of the dense Imperial Valley network in June of 1973. A general increase in the number of detected events appears to be real, although some of this change must be associated with changes in station distribution and the implementation of the CEDAR system in January, 1977. The most obvious features in this series of histograms are many prominent spikes emerging from a background seismicity of two or three events per day. These spikes represent earthquake swarms lasting for several days.

The swarms associated with the largest seismicity spikes are spatially restricted to regions less than 10 km in extent. The

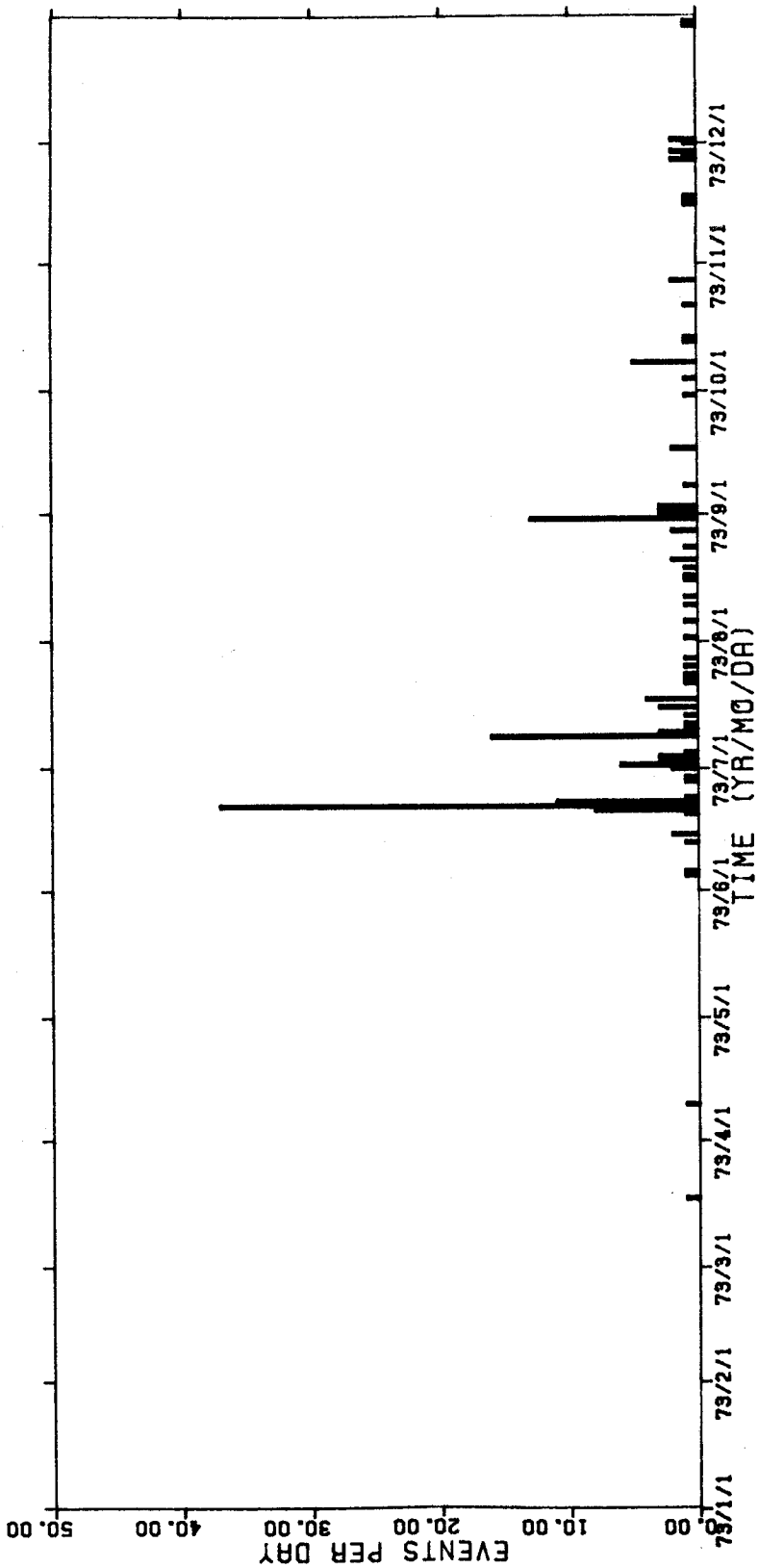

Figure 34. Histogram showing the number of earthquakes per day regardless of magnitude occurring in the Imperial Valley during 1973. The apparent increase in seismicity in June 1973 is due to the enhnaced detection capability provided by the installation of the 16-station Imperial Valley Network by the U. S. Geological Survey. The large "spikes" in this and the following five figures generally correspond to earthquake swarms.

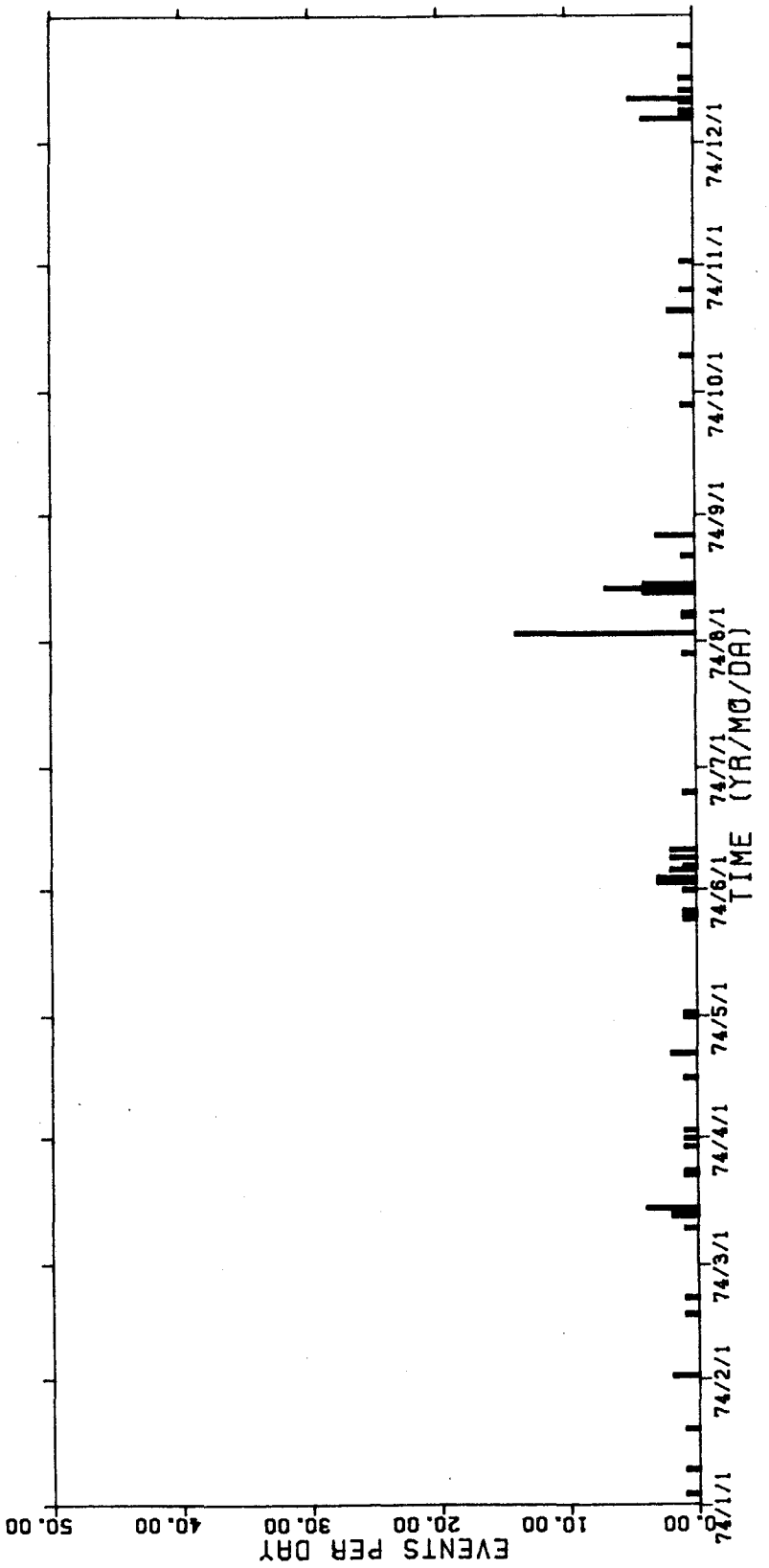

Figure 35. Histogram showing the number of earthquakes per day regardless of magnitude occurring in the Imperial Valley during 1974.

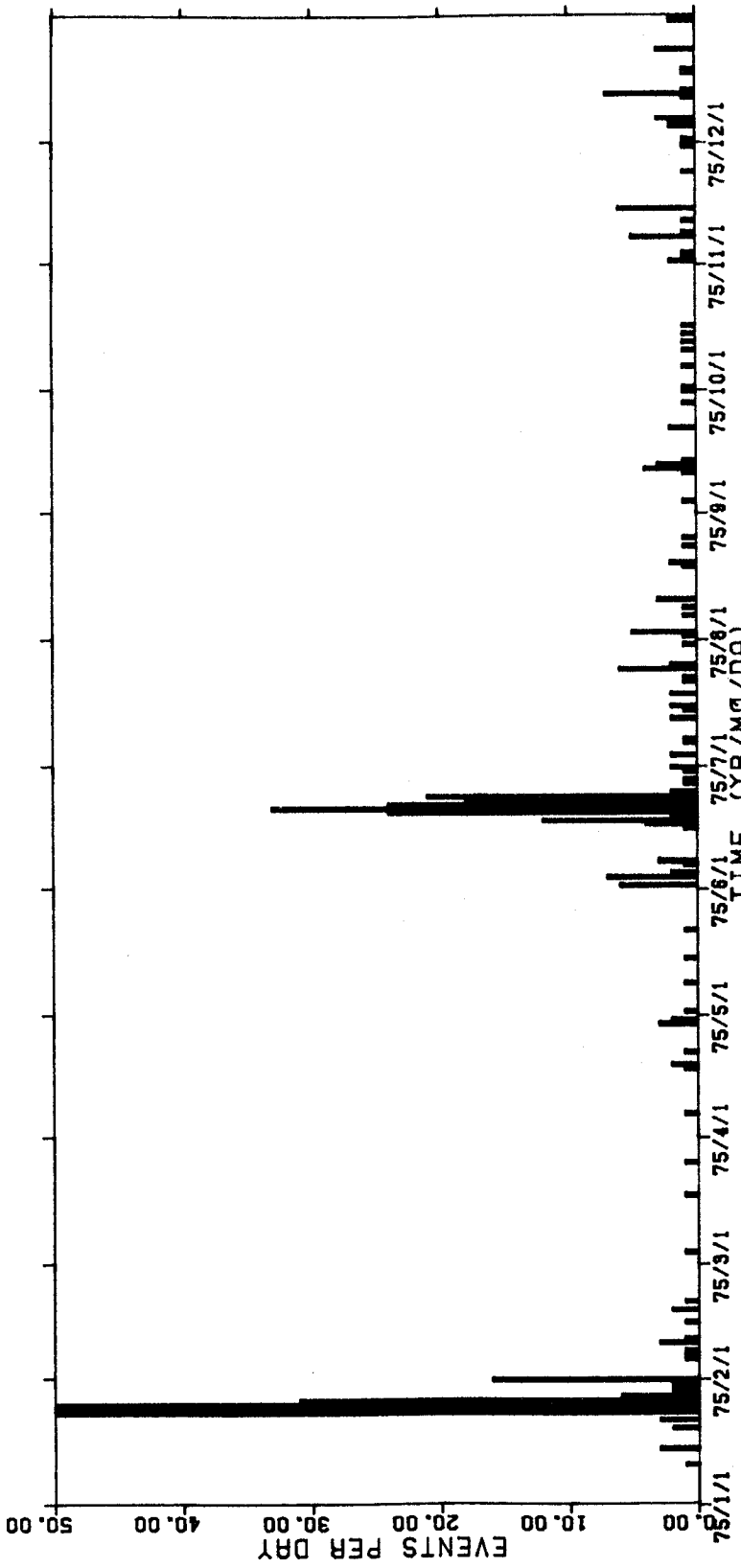

Figure 36. Histogram showing the number of earthquakes per day regardless of magnitude occurring in the Imperial Valley during 1975.

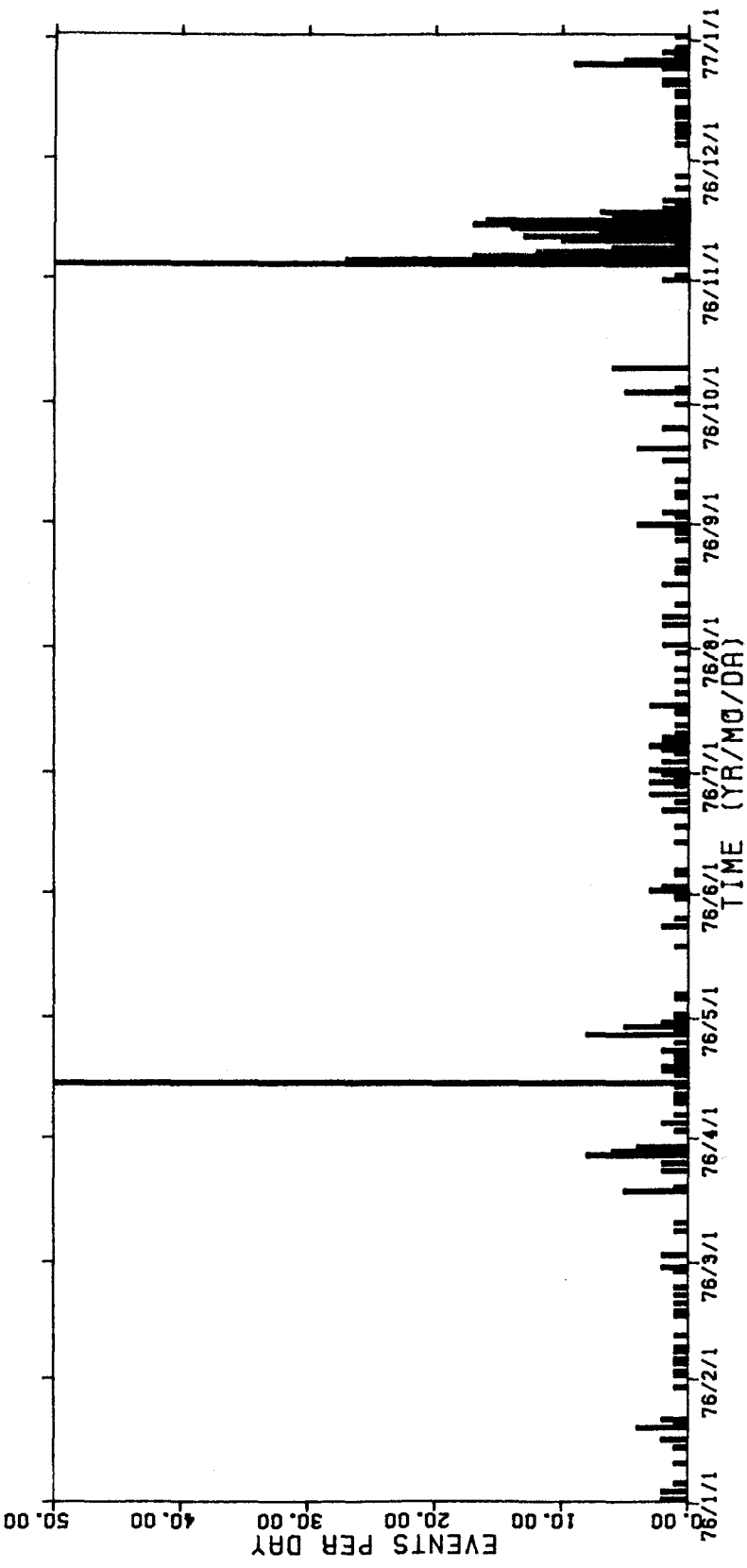

Figure 37. Histogram showing the number of earthquakes per day regardless of magnitude occurring in the Imperial Valley during 1976.

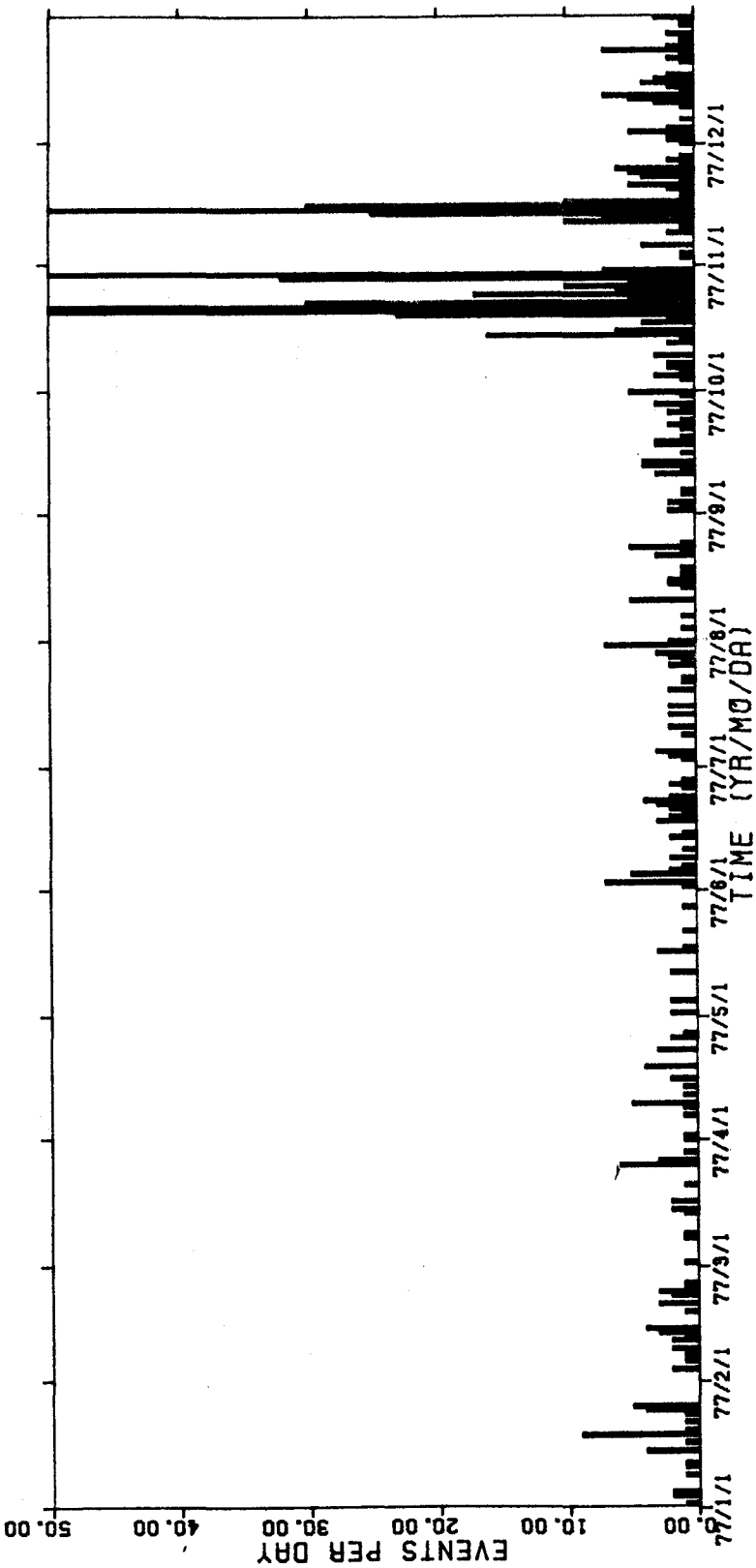

Figure 38. Histogram showing the number of earthquakes per day regardless of magnitude occurring in the Imperial Valley during 1977.

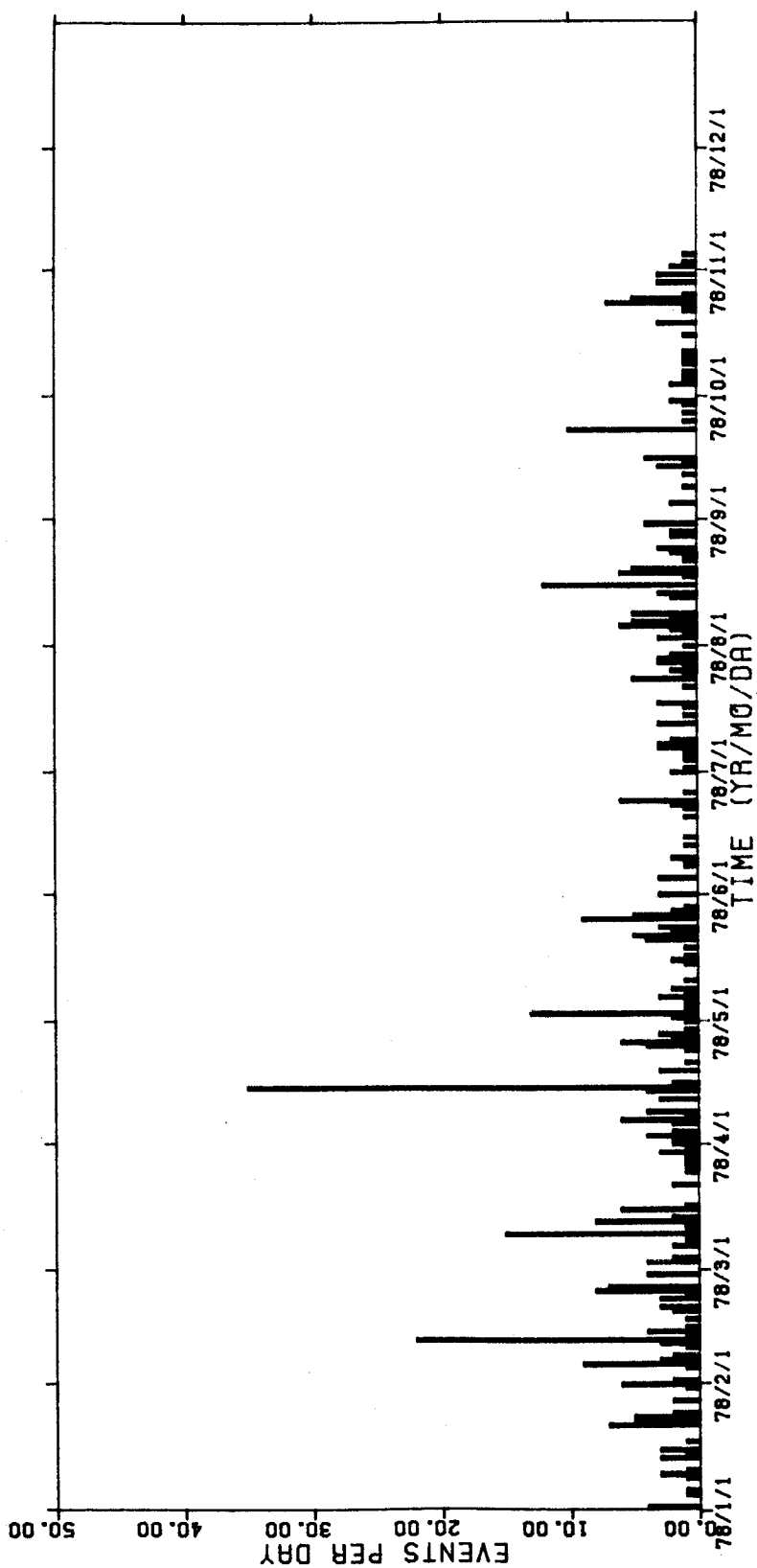

Figure 39. Histogram showing the number of earthquakes per day regardless of magnitude occurring in the Imperial Valley during 1978.

detailed analysis of the tectonic structures giving rise to these swarms is the subject of Chapter 5.

There seems to be essentially two discrete time scales that are important with respect to seismicity in the Imperial Valley. The shortest is on the order of several days and is related to the duration of individual swarms. Superimposed on this is a long-term periodicity of roughly 12 to 13 years marked by peaks of more intense activity from 1940 to 1943, 1950 to 1955, 1963 to 1965, and 1975 to the present. This periodicity is most clearly evident on Figure 32. A similar periodicity was noted for the recurrence of moderate earthquakes ($M_L > 6$) on the southern San Jacinto Fault by McNally (1977). In this case events in 1942, 1954, and 1968 were separated by intervals of very low seismicity with an increase in cluster activity several years before each event. Moreover the only other earthquake with a magnitude exceeding 6 in the study area since 1932 occurred in the Borrego Valley area near the southern end of the San Jacinto just two years after the 1940 quake. To date there has been no event on the San Jacinto Fault that could be related to the most recent increase in Imperial Valley seismicity. The possibility of coupling between the Imperial Valley seismicity and that of the San Jacinto Fault zone is intriguing and deserving of extensive further study.

SUMMARY AND CONCLUSIONS

The Imperial Valley appears to be related more closely to the Gulf of California tectonic province than to the rest of Southern California. In both areas seismicity is punctuated by infrequent

large strike-slip events associated with major northwest-trending transform faults with normal aftershock distributions. Earthquake swarms are more common, but are generally confined to the dextral offsets between the strike-slip faults. Swarm events appear to occur within recent sediments or possibly the upper few kilometers of basement. Focal mechanisms associated with the swarms are varied with a particularly large representation of strike-slip mechanisms, although both thrust and normal faulting is occasionally seen.

Earthquake epicenters in the Imperial Valley are concentrated in a narrow, spindle-shaped region connecting the northern end of the Imperial Fault with the southern end of the San Andreas Fault. This zone, designated the Brawley seismic zone, is 75 km long and 10 km wide at its widest point. The sharp boundaries of the Brawley seismic zone suggest possible fault control. If so, the western edge could most easily be associated with a northward extension of the Imperial Fault, while the eastern edge may reveal the subsurface location of the Brawley Fault. This zone is not what one would expect for a ridge segment perpendicular to its associated transforms, but does seem consistent with the notion of a "leaky" transform fault as suggested by Hill (1977). Seismicity within the Brawley seismic zone occurs almost exclusively as earthquake swarms. Although over time periods of several years activity is remarkably homogeneous, when viewed over time periods of a few months activity is highly clustered. The overall patterns are not apparent without several years of monitoring. This emphasizes the need for the continuation of established networks both before and during any activities that might

alter seismicity pattern or provoke damaging earthquakes. Short-term seismicity surveys of a few months appear to be of limited usefulness in connection with determining background seismicity levels in areas like the Imperial Valley.

Temporal fluctuations of Imperial Valley seismicity manifest two significant time scales. The first is associated with sudden increases in seismic activity by several orders of magnitude lasting for periods of from several days to a week. There is also apparently a longer period variation associated with the resurgence of significant activity every 12 to 13 years. A similar periodicity may also describe seismicity on the adjacent southern section of the San Jacinto Fault zone.

REFERENCES

Allen, C. R. (1968). The tectonic environments of seismically active and inactive areas along the San Andreas Fault System, in Proceedings of Conference on Geologic Problems of San Andreas Fault System, W. R. Dickson and A. Gantz (eds.), Stanford Univ. Press, Palo Alto, Calif., 70-82.

Allen, C. R., M. Wyss, J. N. Brune and R. E. Wallace (1972). Displacements on the Imperial, Superstition Hills and San Andreas Faults triggered by the Borrego Mountain earthquake, U. S. Geol. Surv. Prof. Paper 787, 87-104.

Atwater, T. (1970). Implications of plate tectonics for the Cenozoic tectonic evolution of western North America, Bull. Geol. Soc. Am., 81, 3513-3535.

Biehler, S., R. L. Kovach and C. R. Allen (1964). Geophysical framework of the northern end of the Gulf of California structural province, in Marine Geology of Gulf of California, T. Van Andel and G. Shor (eds.), Am Assoc. Petrol. Geologists Mem., 3, 126-156.

Bischoff, J. L. and T. L. Henyey (1974). Tectonic elements of the central part of the Gulf of California, Bull. Geol. Soc. Am., 85, 1893-1904.

Brune, J. N. and C. R. Allen (1967). A low stress-drop, low magnitude earthquake with surface faulting: the Imperial, California earthquake of March 4, 1966, Bull. Seism. Soc. Am., 57, 501-514.

Crowell, J. C. (1962). Displacement along San Andreas fault, Californa, Geol. Soc. Am. Spec. Paper 71, 61 pp.

Elders, W. A., R. W. Rex, T. Meidav, P. T. Robinson and S. Biehler (1972). Crustal spreading in Southern California, Science, 178, 15-24.

Friedman, M. E., J. H. Whitcomb, C. R. Allen, and J. A. Hileman (1976) Seismicity of Southern California region, 1 January 1972 to 31 December 1974, Seismological Laboratory, California Institute of Technology, Pasadena, 64 pp.

Fuis, G. and M. Schnapp (1977). The November-December 1976 earthquake swarms in northern Imperial Valley, California: seismicity on the Brawley Fault and related structures, Trans. Am. Geophys. Un., 58, 1188.

Gilpin, B. and T. Lee (1978). A microearthquake study in the Salton Sea geothermal area, California, Bull. Seism. Soc. Am., 68, 441-450.

Hadley, D. M. (1978). Geophysical investigation of the structure and tectonics of Southern California, Ph.D. Thesis, California Institute of Technology.

Henyey, T. L. and J. L. Bischoff (1973). Tectonic elements of the northern part of the Gulf of California, Bull. Geol. Soc. Am., 84, 315-330.

Hileman, J. A., C. R. Allen and J. M. Nordquist (1973). Seismicity of the Southern California region, 1 January 1932 to 31 December 1972, Seismological Laboratory, California Institute of Technology, Pasadena, 405 pp.

Hill, D. P. (1977). A model for earthquake swarms, J. Geophys. Res., 82, 1347-1352.

Hill, D. P., P. Mowinckel, and L. G. Peake (1975a). Earthquakes, active faults, and geothermal areas in the Imperial Valley, California, Science, 188, 1306-1308.

Hill, D. P., P. Mowinckel, and K. M. Lahr (1975b). Catalog of earthquakes in the Imperial Valley, California, U. S. Geol. Surv. Open-File Report, Washington, D.C. 29 pp.

Isaaks, B., J. Oliver and L. Sykes (1968). Seismology and the new global tectonics, J. Geophys. Res., 73, 5855-5899.

Johnson, C. E. and D. M. Hadley (1976). Tectonic implications of the Brawley earthquake swarm, Imperial Valley, California, January 1975, Bull. Seism. Soc. Am., 66, 1133-1144.

Kanamori, H. and D. L. Anderson (1975). Theoretical basis of some empirical relations in seismology, Bull. Seism. Soc. Am., 65, 1073-1095

Klein, F. W. (1978). Hypocenter location program hypoinverse, U. S. Geol. Surv. Open-File Report, 78-694, 113 pp.

Larson, R., W. Menard, and S. Smith (1968). Gulf of California: a result of ocean-floor spreading and transform faulting, Science, 161, 781-784.

Lee, W. H. K. and J. C. Lahr (1975). HYPO71 (revised): A computer program for determining hypocenter, magnitude and first motion pattern of local earthquakes, U. S. Geological Surv. Open-File Report, Washington, D.C. 113 pp.

Lee, W. H. K,, R. E. Bennet, and K. L. Meagher (1972). A method of estimating magnitude of local earthquakes from signal duration, U. S. Geol. Surv. Open-File Report, Washington, D.C., 28 pp.

Lomnitz, C., F. Mooser, C. Allen, and W. Thatcher (1970). Seismicity and tectonics of the northern Gulf of California region, Mexico. Preliminary results. Geofis. Int., 10, 37-48.

McNally, K. C. (1977). Patterns of earthquake clustering preceding moderate earthquakes, Central and Southern California, Trans. Am. Geophys. Un., 58, 1195.

Nordquist, J. M. (1964). A catalog of Southern California earthquakes and associated electronic data processing programs, Bull. Seism. Soc. Am., 54, 1003-1011.

Pechman, J. C. (1979). Tectonic implications of small earthquakes in the Central Transverse Ranges, California (in press).

Reichle, M. and I. Reid (1977). Detailed study of earthquake swarms from the Gulf of California, Bull. Seism. Soc. Am., 67, 159-171.

Reid, I., M. Reichle, J. Brune, and H. Bradner (1973). Microearthquake studies using sonobuoys: preliminary results from the Gulf of California, Geophys. J., 34, 365-379.

Richter, C. F. (1958). Elementary Seismology, W. H. Freeman and Co., San Francisco.

Rusnak, G. R., Fisher and F. Shepard (1964). Bathymetry and faults of the Gulf of California in Marine Geology of the Gulf of California-A Symposium, T. Van Andel and G. Shor (eds.), Am. Assn. Petrol. Geol. Mem. 3, 59-75.

Savage, J. C., D. Goodreau, and W. H. Prescott (1974). Possible fault slip on the Grawley Fault, Imperial Valley, California, Bull. Seism. Soc. Am., 64, 713-715.

Sharp, R. V. (1972). Tectonic setting of the Salton Trough, in The Borrego Mountain earthquake of April 9, 1968, U. S. Geol. Surv. Prof. Paper 787, 3-15.

Sykes, L. (1967). Mechanism of earthquakes and nature of faulting on mid-ocean ridges, J. Geophys. Res., 72, 2131-2153.

Sykes, L. (1968). Seismological evidence for transform faults, sea-floor spreading and continental drift, in History of the Earth's Crust, a NASA Symposium, R. A. Phinney, Ed., Princeton Univ. Press, Princeton, N. J., 120-150.

Sykes, L. (1970). Earthquake swarms and sea-floor spreading, J. Geophys. Res., 75, 6598-6611.

Tatham, R. and J. Savino (1974). Faulting mechanism for two oceanic earthquake swarms, J. Geophys. Res., 79, 2643-2652.

Thatcher, W. (1979). Horizontal crustal deformation from historic geodetic measurements in Southern California, J. Geophys. Res., 84 (in press).

Thatcher, W. and J. N. Brune (1971). Seismic study of an oceanic ridge earthquake swarm in the Gulf of California, Geophys. J., 22, 473-489.

Thatcher, W. and T. C. Hanks (1973). Source parameters of southern California earthquakes, J. Geophys. Res., 78, 8547-8576.

Trifunac, M. D. and J. N. Brune (1970). Complexity of energy release during the Imperial Valley, California earthquake of 1940, Bull. Seism. Soc. Am., 60, 137-160.

Weaver, C. S. and D. P. Hill (1978). Earthquake swarms and local crustal spreading along major strike-slip faults in California, Pageoph, 117, 51-64.

CHAPTER 5

AN APPARENT RELATIONSHIP BETWEEN EPISODIC FAULT CREEP AND EARTHQUAKE SWARMS IN THE IMPERIAL VALLEY, SOUTHERN CALIFORNIA

INTRODUCTION

In this chapter several specific observations and inferences are presented regarding the nature of earthquake swarms in the Imperial Valley of Southern California. This study will be focused on those swarms comprising the Brawley seismic zone described in the preceding chapter with the aim of understanding the mechanical properties of this region as they are revealed by precise location of the events making up the swarms. Seven swarm sequences are analyzed at varying levels of detail, followed by an attempt to synthesize common properties into a physical model.

Initial interest in Imperial Valley earthquake swarms grew out of a study of a swarm in January, 1975 reported by Johnson and Hadley (1976). During the course of the 1976 study it became clear that if arrival times were measured with sufficient care, it was possible to resolve considerable detail with respect to the fault structures activated during the swarm. Following several months of rather tedious timing of Develocorder records, an intriguing picture emerged; the temporal development of the 1975 swarm was highly structured and progressive with time. Clustered activity appeared to resolve fault planes that were transverse to the purported Brawley fault, with focal mechanisms fully supporting these interpretations. Bursts of seismicity -- the swarms -- were in essence providing flash pictures of the active members of the Imperial Valley fault system. The activation of these structures, together with evidence from additional earthquakes which were attributed to the Brawley fault itself, revealed a well-defined, bilateral migration pattern with a uniform propagation rate

of .5 km/hr.

These observations allow an interpretation whereby the earthquakes making up a swarm are simply the seismically observable part of a more pervasive, underlying physical process. For the January 1975 swarm, it was suggested that the advance of seismic activity marked the propagation of a bilateral fault creep event along the proposed northwest-trending Brawley fault. The observations supporting this conclusion are presented below. One way to test this idea, or more generally to constrain the candidate physical process, is to look at other swarms comprising the Brawley seismic zone. This is especially required by the inferential nature of our conclusions.

Clearly the task of deriving physical insight into a process from the sound that it makes can only be partially successful. Hopefully we can proceed far enough with inferences based on observations of the swarms so that further progress can be made by means of additional non-seismic observations and experiments.

DATA ANALYSIS

The analysis procedures employed in the study of Imperial Valley earthquake swarms were similar to those described by Johnson and Hadley (1976). The most significant change in procedure concerns the implementation of a location program based on the generalized inverse method as formulated by Wiggins (1972). Since we are concerned with the smallest resolvable details that can be obtained with respect to identifying planar structures in a spatial seismicity distribution, it is absolutely essential to have a firm grasp of

the orientation of the model null-space; without this information deficiencies in the problem, such as an inadequate station distribution can show up and be interpreted as planar fault structures. This location program was then applied within the context of a master event scheme to obtain a target relative location precision of roughly 200 m.

The most consistent results were obtained when the master event itself was located upon the structure being resolved. Consequently it became expedient to establish a network of master events with each located either in an absolute sense or relative to a previously established master event. To accomplish this, the earthquakes were divided into 15 space-time intervals containing the swarms being studied. These bounds, listed in Table 1, were chosen so as to include the most spatially extensive swarms in the past five years. The master events used in each region are listed in the corresponding row of Table 2. If a given master event was itself located relative to one preceding, this is noted by the index in the column headed "Previous Master".

There has been some change in station distribution over the last five years. Furthermore, it is occasionally necessary to establish relative delays for stations that were temporarily inoperative at the time a particular master event was recorded. In order to establish such delays, a procedure is used whereby the events in a particular region are located relative to a partial master. Residuals for stations not recorded by the master event are not constrained, so that the median of the resulting distribution of travel-time residuals

TABLE 1

REGION IDENTIFICATION		TREND	NO. OF EVENTS	REGION DEFINITION			MASTER EVENT
				TIME INTERVAL (Yr/Mo/Da	LATITUDE RANGE	LONGITUDE RANGE	
1	73JUN-1	Imperial	28	73/06/01-73/07/31	32.75-32.90	115.40-115.60	6
2	73JUN-2	Imperial	20	73/06/01-73/07/31	32.90-33.00	115.40-115.60	7
3	74AUG	Imperial	25	74/08/01-74/08/30	32.75-32.95	115.40-115.60	7
4	75JAN-1	Brawley	127	75/01/01-75/02/31	32.75-32.96	115.40-115.60	1
5	75JAN-2	Brawley	160	75/01/01-75/02/31	32..6-33.10	115.45-115.55	2
6	75JUN-1	Imperial	94	75/06/01-75/06/30	32.70-32.85	115.40-115.60	7
7	75JUN-2	Imperial	61	75/06/01-75/06/30	32.85-33.00	115.40-115.60	6
8	76MAR-1	Imperial	20	76/03/01-76/04/30	32.70-32.85	115.40-115.60	7
9	76MAR-2	Imperial	71	76/03/01-76/04/30	32.85-32.95	115.40-115.60	6
10	76NOV-1	Brawley	263	76/10/01-77/03/31	33.00-33.15	115.50-115.75	3
11	76NOV-2	Brawley	100	76/10/01-77/03/31	33.15-33.20	115.50-115.75	4
12	76NOV-3	Brawley	29	76/10/01-77/03/31	33.20-33.30	115.50-115.75	5
13	77OCT-1	Imperial	251	77/10/01-77/10/27	32.855-33.00	115.40-115.60	6
14	77OCT-2	Imperial	172	77/10/28-77/11/30	32.855-33.00	115.40-115.60	6
15	77OCT-3	Imperial	435	77/10/01-77/11/30	32.75-32.855	115.40-115.60	7

TABLE 2

No.	ORIGIN TIME (GMT) (Yr/Mo/Da	HrMn)	North Latitude	West Longitude	Depth	Previous Master
1	75/01/23	1230	32°56.00'	115°28.88'	4.00	--
2	75/01/25	1431	32°59.15'	115°30.02'	5.96	1
3	76/11/06	213	33° 8.06'	115°35.93'	5.03	--
4	76/11/11	321	33°10.63'	115°38.92'	4.55	3
5	76/11/18	749	33°14.15'	115°39.35'	3.75	4
6	77/10/21	612	32°53.19'	115°30.17'	6.29	--
7	77/11/14	205	32°49.47'	115°28.43'	5.01	6

can be taken to be a central estimate of the delay had a particular station been timeable for the original master. By this means a "completed" master event is constructed and used to relocate the events in the region.

The crustal model used for all locations was that described by Johnson and Hadley (1976). This model was a smoothed version of the Westmoreland profile obtained by Biehler and others (1964).

The analytical and graphical tools used in this study, including the above location procedure, are a part of the general software support for the CEDAR system as discussed in Chapter 1. The problem of organizing large volumes of arrival-time data into a file structure that permits efficient relocation under competing assumptions is identical to that encountered in the final stages of routine analysis. A procedure called "winnowing" is used to assemble all arrival-time data meeting certain specified criteria into a disc file called a "Control Module". Various programs make it easy to treat such a collection of data under a common set of assumptions, such as relocating all events relative to a particular master event. The rows of Table 1 each correspond to an individual Control Module assembled in this fashion. The data have been segregated so that events within a Control Module are spatially and temporally localized so as to permit relocation with a common master event. Event sequences that are spread over a sufficiently large region require more than one Control Module. For example, in Table 1 the swarm sequence that occurred in June 1975 along the Imperial trend (explained below) is treated in two discrete files identified

as 75JUN-1 and 75JUN-2.

The manipulation of event data within a Control Module is provided by a data editing program called QED1. In addition to permitting the addition, modification, and delection of arrival-time data, QED1 allows for the creation and testing of master events. Individual events within the Control Module can then be relocated relative to these "trial" master events in order to reveal timing errors that would contaminate subsequent relative locations. The need for an interactive approach in this application is emphasized if one considers the alternatives provided by more traditional approaches. If the data had been compiled on punched cards, then over 50 boxes of cards (2000 per box) would have been required. Not only would this have been inconvenient and time-consuming, but just the logistics of transporting such a massive data set would have been prohibitive.

Once the data have been organized and a suitable master event has been established, relative locations for the remaining events can be calculated quickly and without further interaction. Following location, the resulting hypocentral data are compiled into a collection of earthquake catalogs, again using the CEDAR system software. Subsequent analysis, including the generation of nearly all of the figures contained in this and the preceding chapters, is carried out using a system of four programs. Strictly speaking, these routines are not a part of the CEDAR system support package. Rather, they are the current embodiment of a rapidly developing software system designed to facilitate efficient access to and processing of CEDAR

system data. The heart of the sub-system dealing with the manipulation and graphical analysis of hypocentral data is a general earthquake sorting routine named "QSORT". This program efficiently compiles a sub-catalog from an input collection of earthquake catalogs, based on a set of selection criteria. The output can then be analyzed by any of three subsequent programs, MAPS, QUAKEPLOT, AND STEREO. MAPS is a general approach to producing epicenter maps utilizing a variety of projections with extensive capabilities for annotation and labeling. It is an extension of the program HYPERMAP (written by Robert L. Parker at U.C.S.D.). QUAKEPLOT implements the analysis of catalog data in the form of a time-series producing graphs, bargraphs, and scatter plots in two dimensions. Input transformations provide for the accumulation of parameters over fixed ranges of another parameter (usually time), non-linear or logarithmic axes, and arbitrary functions of hypocentral parameters through user-written subroutines. STEREO provides for the construction of hypocentral scatter plots through the generation of a stereoscopic pair which can be viewed through any of several devices available for use with stereoscopic photographs. A collection of hypocenters and line drawings (representing faults or cultural referents) can be observed from an arbitrary viewpoint. This capability has proven to be particularly useful for the analysis and presentation of the progressive nature of the swarms through the generation of successive pairs showing the particular spatial relationships that occur as the swarm develops. Three of the swarms discussed below were analyzed in this fashion. Since many individuals have difficulty fusing stereoscopic images,

we have tried to include an adequate amount of supporting material that does not require this faculty. The basic projection subroutines used by STEREO were developed by Don Eckelmann at Colgate University.

GENERAL PROPERTIES OF IMPERIAL VALLEY EARTHQUAKE SWARMS

Before embarking on a detailed discussion of individual swarms, it should prove useful to anticipate some of the inferences and conclusions that will later be drawn from the observations. In particular, an observational description of the class of objects we have been referring to as swarms appears to be in order. Swarms, in general, are conceived to be sequences of earthquakes that lack a well-defined mainshock (e.g., Mogi, 1963). Seismic activity generally builds gradually to a peak and then slowly subsides. In the Imperial Valley several apparently isolated swarms occurring over a period of a few weeks with intervening intervals of quiescence are sufficiently closely juxtaposed in time and space as to appear mechanically related. We have chosen to call such an aggregate of swarms a swarm sequence whenever it is necessary to distinguish it from the individual swarms comprising it.

Spatially the swarms associated with each of the seven swarm sequences discussed below are distributed along north-northwest trends paralleling the strike of the major transform faults. The activation of the component swarms is progressive, manifesting either unilateral or bilateral migration along this trend. Individual swarms, which are isolated in both space and time, appear to define structures that are transverse to the north-northwest trends. Development of seismicity

on these structures is also progressive, although propagation is generally unilateral away from the associated trend. One gets the distinct impression that discrete swarms, or bursts of seismic activity, are associated with the development of a single fault. During the past five years there is scant evidence for the reactivation of a particular transverse structure in a subsequent swarm.

There are two major trends or lineations in the Imperial Valley capable of supporting the development of swarm sequences. One of these, the Imperial Trend, lies along the northern end of the surface trace of the 1940 earthquake. This trend also seems to form the western boundary of the Brawley seismic zone. The other trend, referred to as the Brawley trend, extends from south of Brawley to the Salton Sea along the eastern boundary of the Brawley seismic zone. Of the seven swarm sequences discussed in detail below, two were associated with the Brawley trend while five lie along the Imperial trend.

The regions associated with the two seismic trends are shown in Figure 1 surrounded by dashed boundaries. The Imperial trend is the more westerly of the two. Figure 1 also shows the epicentral distribution of earthquakes larger than $M_L = 3.0$ in the past five years. Although the overall seismicity also shows some indication of two offset linear trends striking north-northwest, the primary motivation for segregating the seismicity in this manner comes from the spatial distribution of the individual swarm sequences. The asterisks near the southern end of the two regions in Figure 1 are the reference points for calculating distances.

Figure 1. Distribution of earthquakes greater than M_L = 3. occurring in the Imperial Valley during the past 5 years. The two dashed parallelograms illustrate the regionalization of seismicity into the Imperial Trend (west) and the Brawley Trend (east). The asterisks along the bottom edge of these two regions are used as a distance reference in Figures 2 through 7 as well as elsewhere in this chapter.

IMPERIAL VALLEY, ML .GE. 3.0, 1973 - 1978

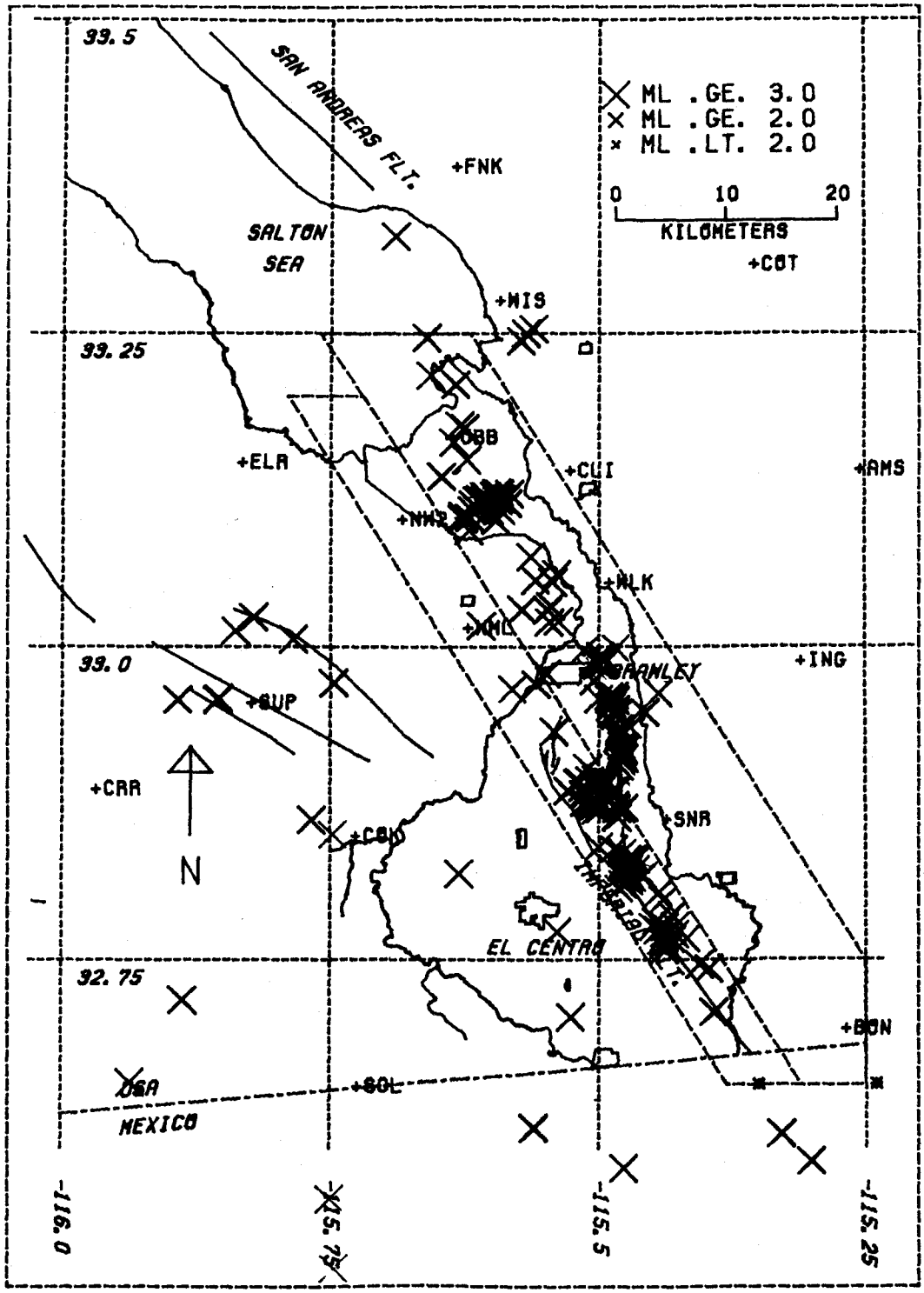

While swarm sequences along the two principle trends are similar in many respects, there are also some differences. In particular, the two swarm sequences studied on the Brawley fault are separated by a 15-km-long section along which no migration has been observed. Swarms along this section of the Brawley trend, such as one reported by Hill and others (1975a) that occurred in June of 1973, do not appear to be part of a more extended sequence. By contrast, swarm sequences on the Imperial trend overlap to a considerable extent. There is one section in fact that is included in all of the five sequences studied. In addition, swarms along the Brawley trend tend to begin more precipitously with accumulated moment series more closely resembling mainshock sequences. Swarms on the Imperial trend characteristically are comprised of discrete bursts of seismic activity beginning and ending abruptly, with durations of a few hours.

The tendency of swarms to aggregate into swarm sequences along the proposed trends is illustrated in the time-distance scatter plots shown in Figures 2 through 7. Distance has been calculated from the reference points in Figure 1. We have only included "A" and "B" quality locations in these figures, so all of the swarms discussed below cannot be observed. Characteristic swarm sequences along the Brawley trend can be seen in January 1975 and November 1976 and along the Imperial trend in August 1974, June 1975, and October 1977. It can also be noted that activity along one trend shows no particular correlation with activity along the other. A singular exception to this rule can be seen in Figure 4, where a small swarm on the Imperial trend followed one on the Brawley trend

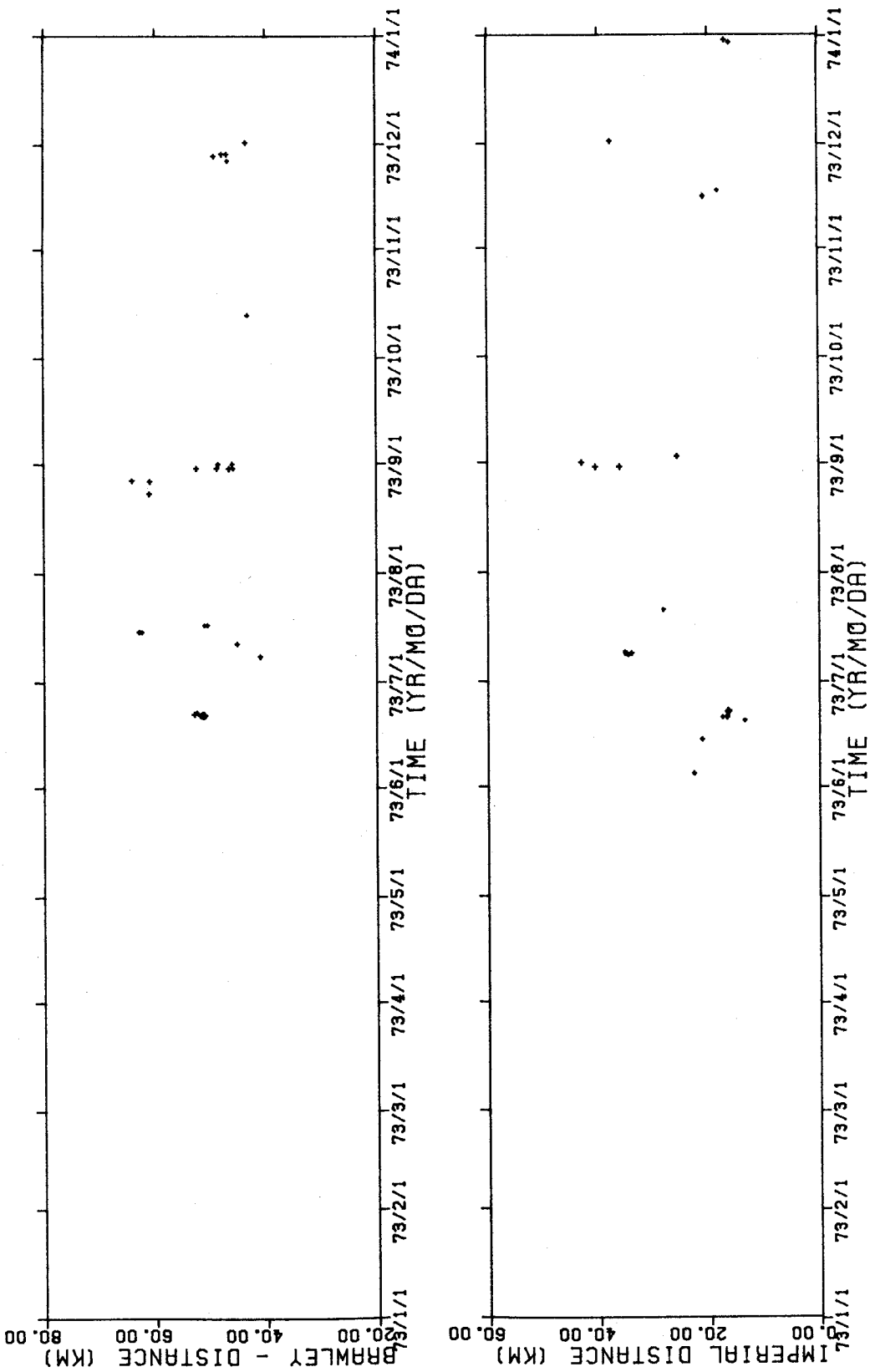

Figure 2. Time-distance scatter plot showing the spatio-temporal relationships for all quality "A" or "B" epicenters along both the Brawley Trend (upper frame) and the Imperial Trend (lower frame) for 1973.

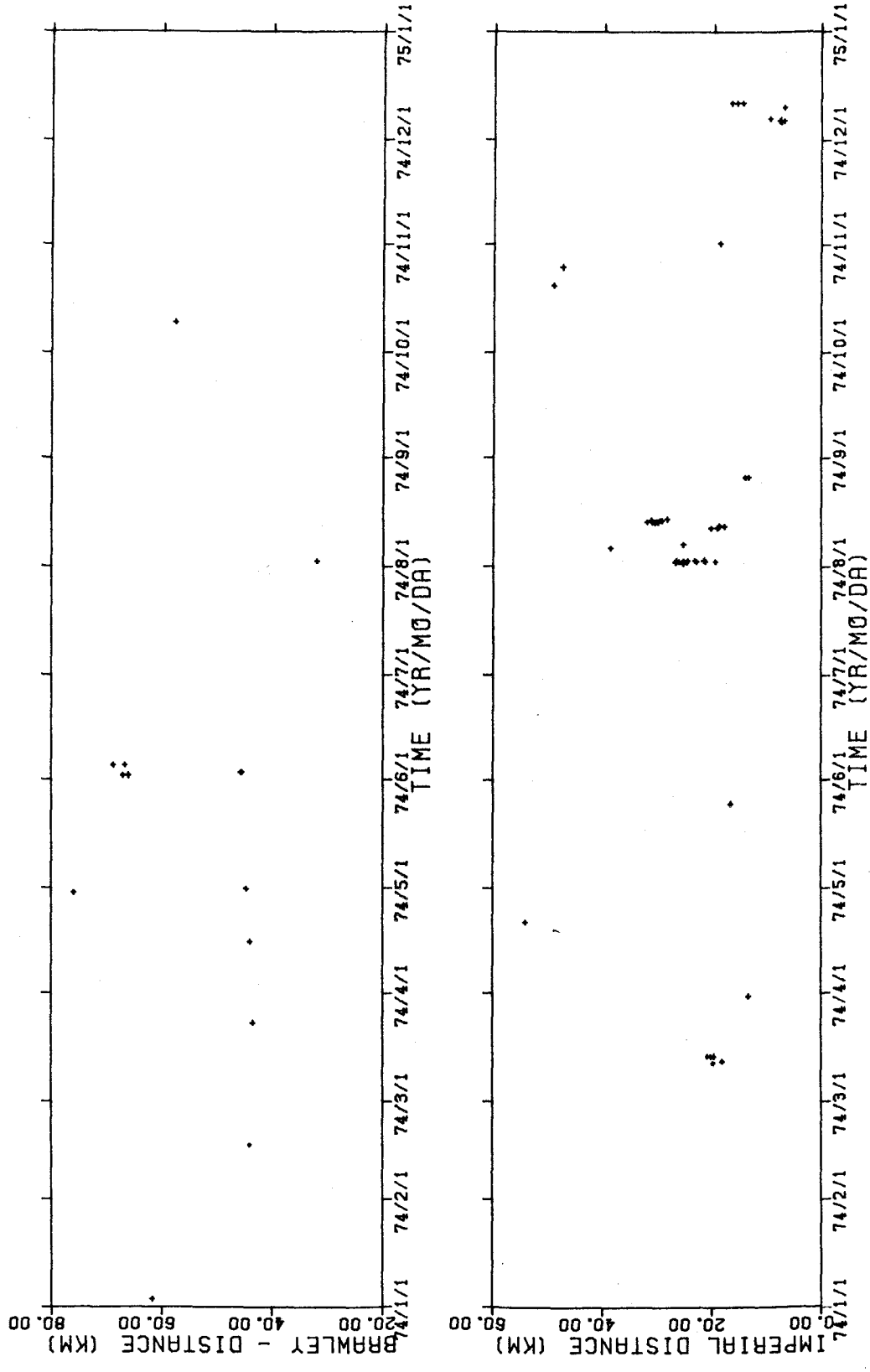

Figure 3. Time-distance scatter plot showing the spatio-temporal relationships for all quality "A" or "B" epicenters along both the Brawley Trend (upper frame) and the Imperial Trend (lower frame) for 1974.

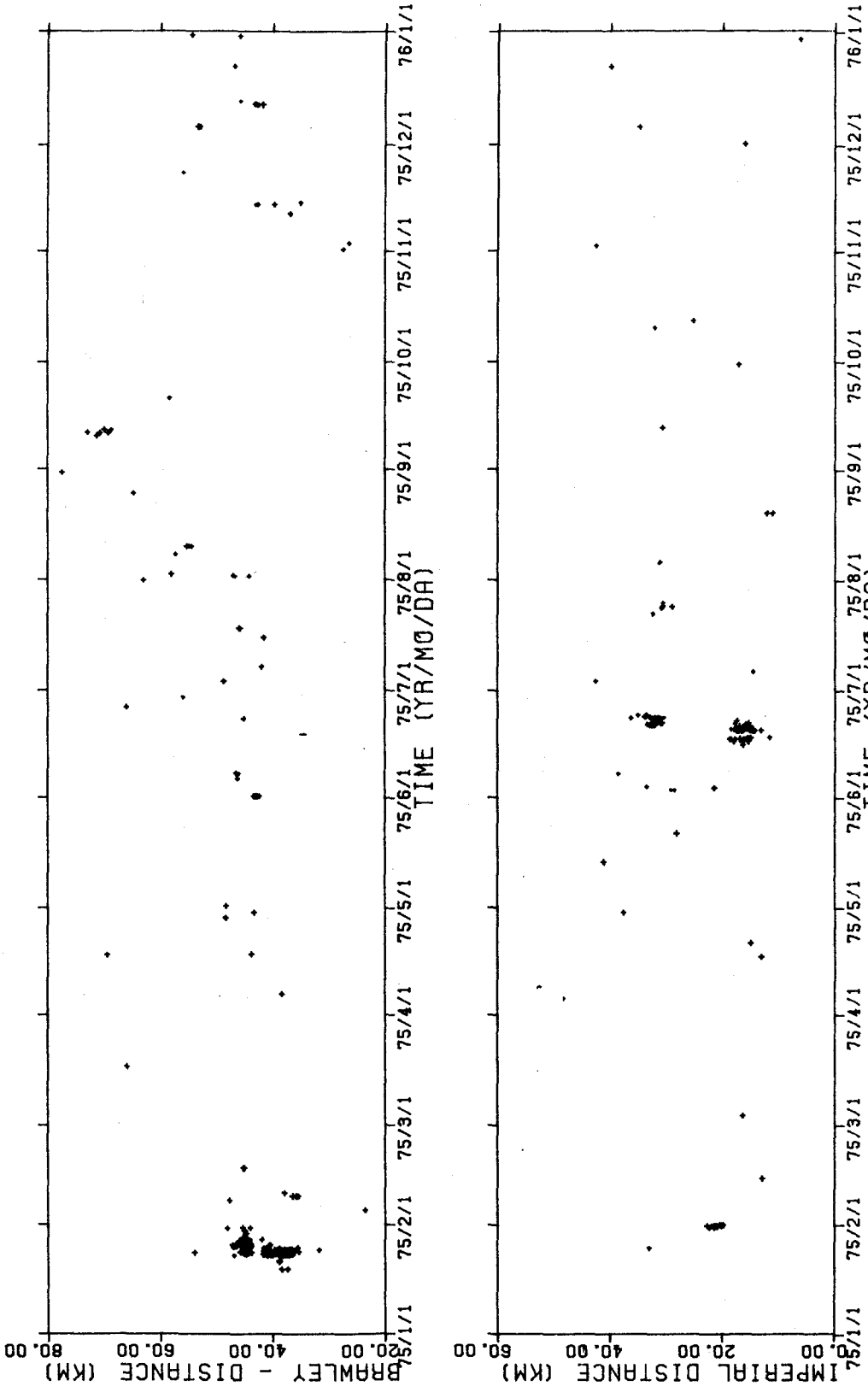

Figure 4. Time-distance scatter plot showing the spatio-temporal relationships for all quality "A" or "B" epicenters along both the Brawley Trend (upper frame) and the Imperial Trend (lower frame) for 1975.

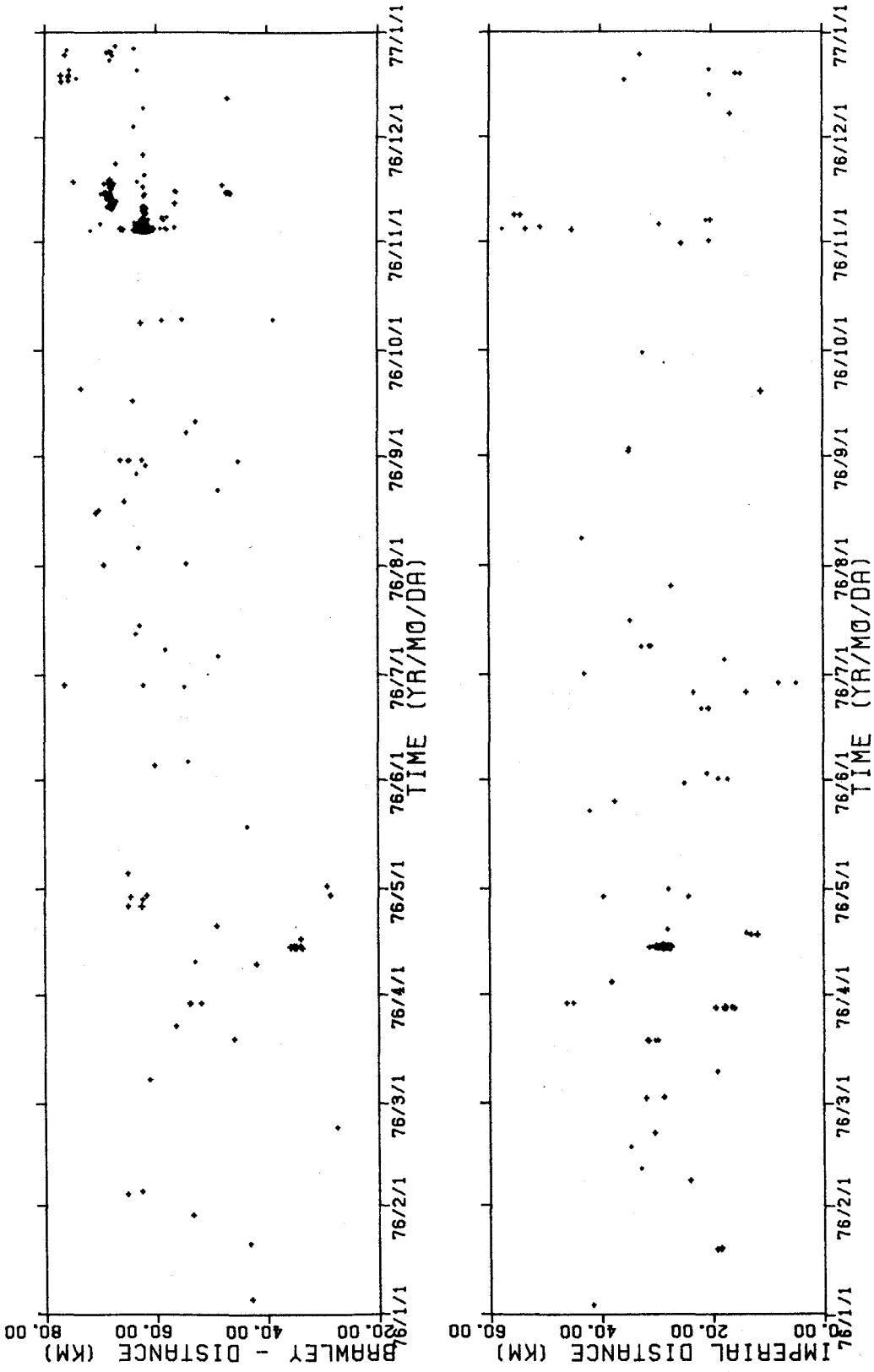

Figure 5. Time-distance scatter plot showing the spatio-temporal relationships for all quality "A" or "B" epicenters along both the Brawley Trend (upper frame) and the Imperial Trend (lower frame) for 1976.

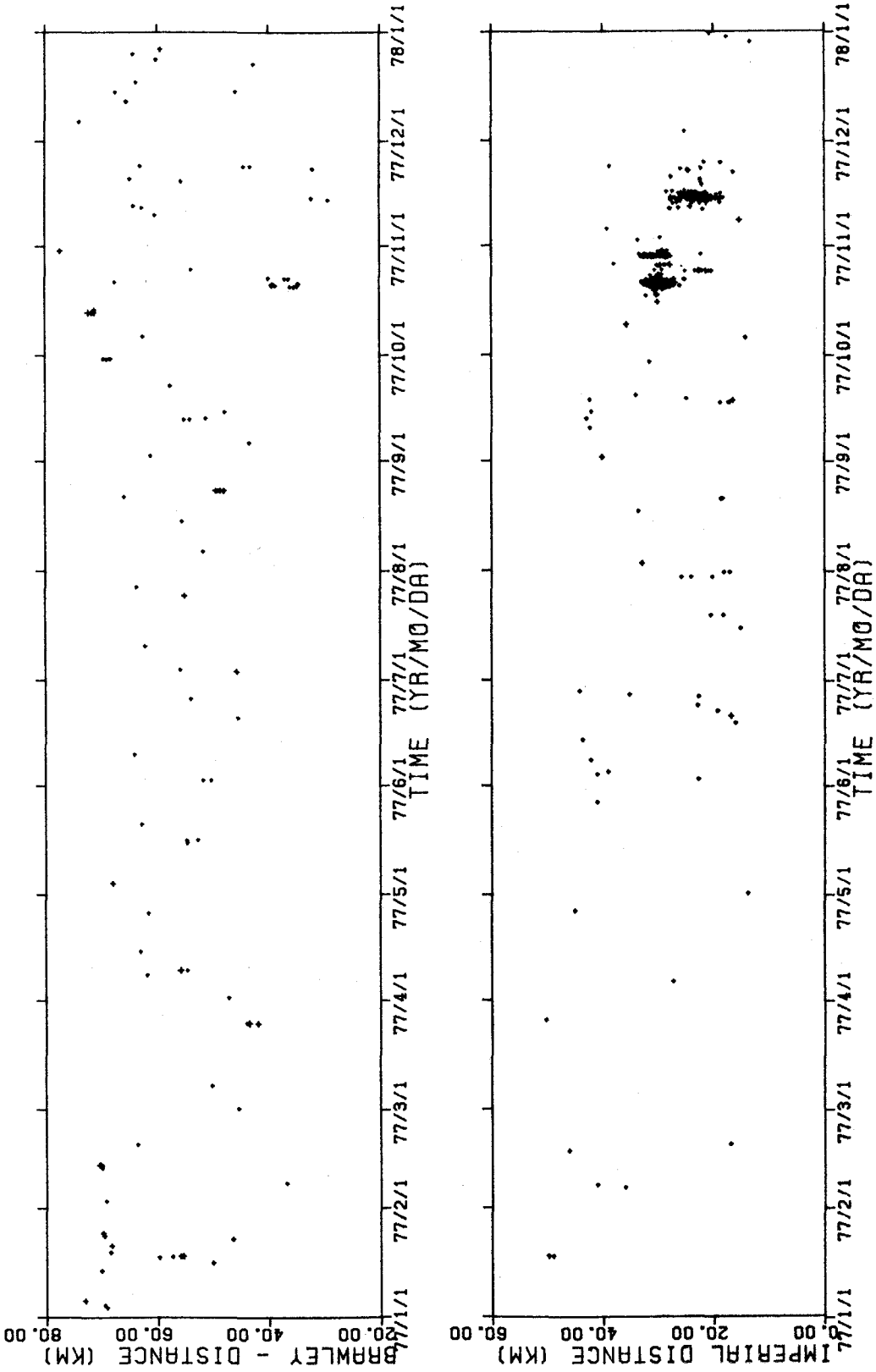

Figure 6. Time-distance scatter plot showing the spatio-temporal relationships for all quality "A" or "B" epicenters along both the Brawley Trend (upper frame) and the Imperial Trend (lower frame) for 1977.

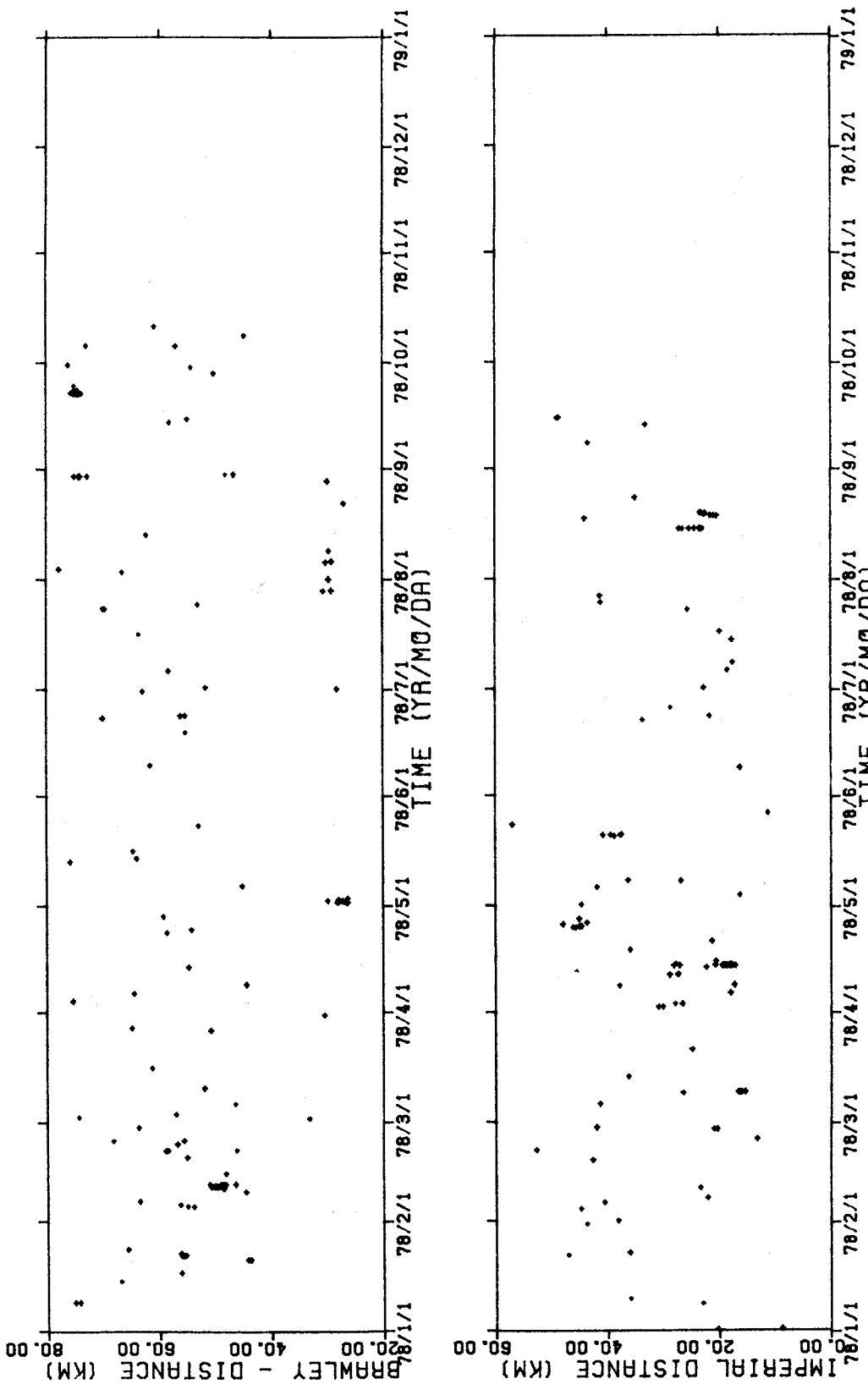

Figure 7. Time-distance scatter plot showing the spatio-temporal relationships for all quality "A" or "B" epicenters along both the Brawley Trend (upper frame) and the Imperial Trend (lower frame) for 1978.

near the point where they appear to merge east-northeast of El Centro.

EARTHQUAKE SWARMS ON THE BRAWLEY TREND

Two swarms attributed to the Brawley trend have been studied in considerable detail. The first, in January 1975, occurred at the southern end just southeast of the community of Brawley (Figure 8). This swarm was studied in the greatest detail (Johnson and Hadley, 1976) of the seven swarm sequences reported in this chapter. The intriguing progressive development of this swarm with the suggestion of a coherent, underlying process were the primary motivating factors behind this thesis. Earthquakes associated with the January 1975 swarm occurred over a period of about 3 weeks, with the most intense activity taking place between January 23 and January 26. More than 250 events were analyzed for this swarm with 75 events larger than M_L = 3.0. The largest event, M_L = 4.7, occurred near the northern end of the swarm. The January 1975 swarm was seismically active along a 12-km-long section of the Brawley trend, with an additional 10 km if the surface breaks mapped by Sharp (1976) south of the seismically active stretch are included. This swarm is the only one with demonstrable surface expression the past five years.

January 1975 Sequence

The epicenters of the events comprising the January 1975 swarm are plotted in Figure 8 together with topographic contours, the concurrent surface breakage mapped by Sharp (1976), and the surface faulting associated with the 1940 Imperial Valley earthquake. Three

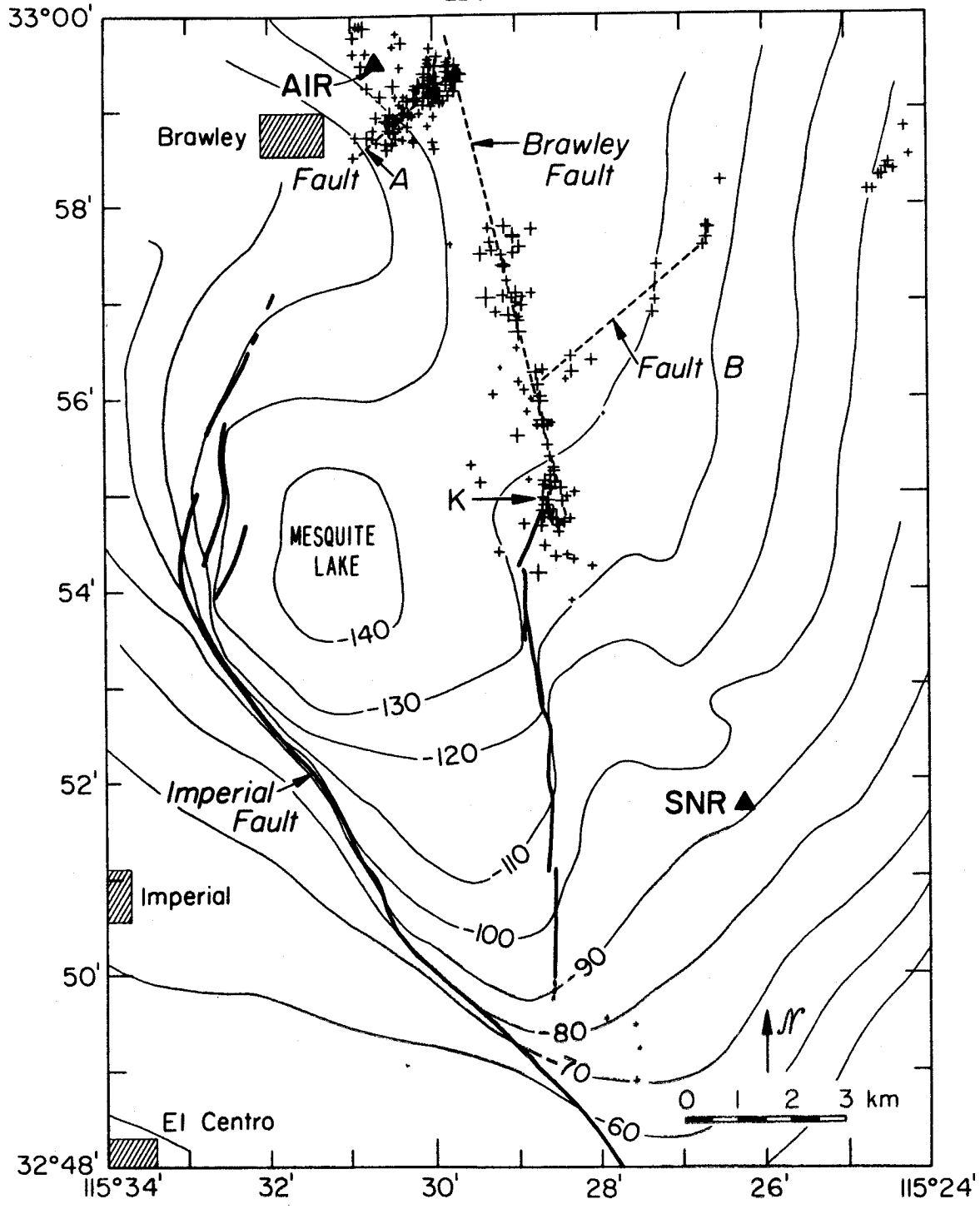

Figure 8. Detailed map showing epicenters associated with the 75 JAN sequence on the Brawley Trend (plus signs, size proportional to magnitude), observed surface faulting (heavy lines), faults inferred from seismicity (broken lines) and topographic contours (light lines). The letter "K" indicates the point where the surface faulting coincident with the 75 JAN sequence crossed Keystone Road (from Johnson and Hadley, 1976; Figure 2).

distinct lineations, indicated by broken lines, are apparent in the epicentral distribution. With the additional evidence provided by focal mechanisms, three fault structures have been inferred from these lineations, although no surface expression has been observed. The absence of surficial features is not surprising considering recent sedimentation and agricultural modifications in this part of the Imperial Valley.

The prominent northwest-trending lineation is identified as the Brawley Fault discussed by Hill and others (1975a, 1975b). Its strike of about N 8° W is compatible with those of the focal mechanisms for events 1 through 6 of Figure 11. These events are associated spatially with the Brawley Fault (Figure 10), and the mechanisms require right-lateral motion on a nearly vertical fault plane. To the south this trend is continued by the surface cracks reported by Sharp (1976) to a point about 1.4 km north of its apparent intersection with the Imperial Fault northeast of El Centro. The character of these cracks, according to Sharp, implies a tectonic origin with right-lateral offset. The total absence of epicenters along that portion of the Brawley Fault where cracks were observed implies that their development was associated with an aseismic process such as creep. As pointed out by Sharp, the occurrence of surficial cracks was coincident with that portion of the Brawley Fault manifesting a well-developed scarp. This is also apparent in Figure 8 from the correlation between topography and surface faulting. The 1.4-km gap between the southern end of the observed cracks and the Imperial Fault was filled by a sequence of four events ($M \leq 3.2$) on January 31 (Figure 8), seven days

after the beginning of the swarm.

The two northeast-striking lineations have been designated Faults "A" and "B" as they are labeled on Figure 8 for reference purposes in the following discussion. Events 7, 8, 9, 12, 13, 14, 15 and 16 of Figure 11 are representative of focal mechanisms calculated for events associated with Fault "A". The strike of Fault "A" is on trend with northeast-trending splay faults that formed at the northern end of the ground breakage associated with the 1940 Imperial Valley earthquake (Ulrich, 1941; Buwalda and Richter, unpublished manuscript).

The most intriguing phenomena observed for the January 1975 swarm are related to its progressive development with time. The overall development of the swarm is shown in the upper frame of Figure 9 where the magnitude of each event is plotted as a function of time. The low-level foreshock activity beginning around January 10 is nearly fifty times greater than what could be considered an average background level for this area. The rapid development of the swarm, coupled with a slow decay, now appears to be typical of swarms along the Brawley trend as compared to those along the Imperial trend. In a sense this distribution is closer to a foreshock-mainshock pattern, although a clear mainshock is not present. In the lower frame of Figure 9 accumulated moment has been graphed in order to reveal times of peak seismicity. Seismic moment is calculated from magnitude using the expression, $\log_{10} M_o = 1.5\ M_L + 16$, developed by Thatcher and Hanks (1973) and plotted as total slip on an arbitrary 33 km^2 fault surface, assuming

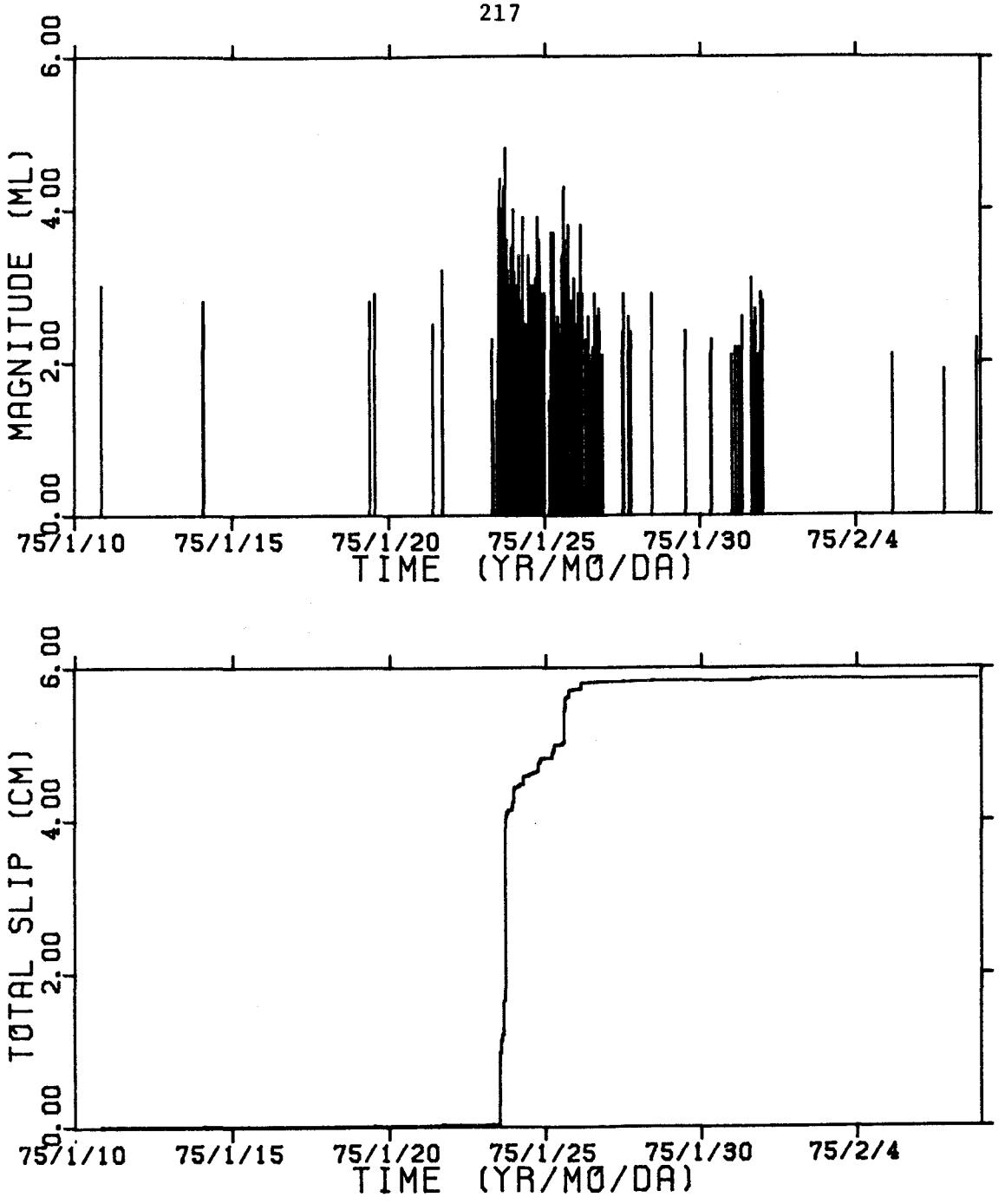

Figure 9. Two time-series representations illustrating the temporal development of the 75 JAN swarm sequence. In the upper frame events are represented by a vertical line proportional to magnitude plotted at the origin time. A tendency for larger events, exclusive of precursors, to occur early in the sequence is evident. The lower frame shows moment plotted as proportional slip on a 33 km^2 fault.

Figure 10. Spacio-temporal relationships associated with the events of the 75 JAN sequence near Brawley. In the lower portion of the Figure the distance along the Brawley Fault is plotted as a function of origin time (size proportional to magnitude). The first three days are divided into nine time frames separated by dashed lines. The epicenters of the evetns in each time frame are plotted in the upper portion of the Figure and in the form of stereoscopic pairs in Figures 13 through 21. The tick marks along the inferred faults (dashed lines) correspond to those marking the ordinate of the lower plot. The reference numbers associated with the focal mechanisms correspond to those in Figure 11. Solid quadrants are compressional. (From Johnson and Hadley, 1976, Figure 4).

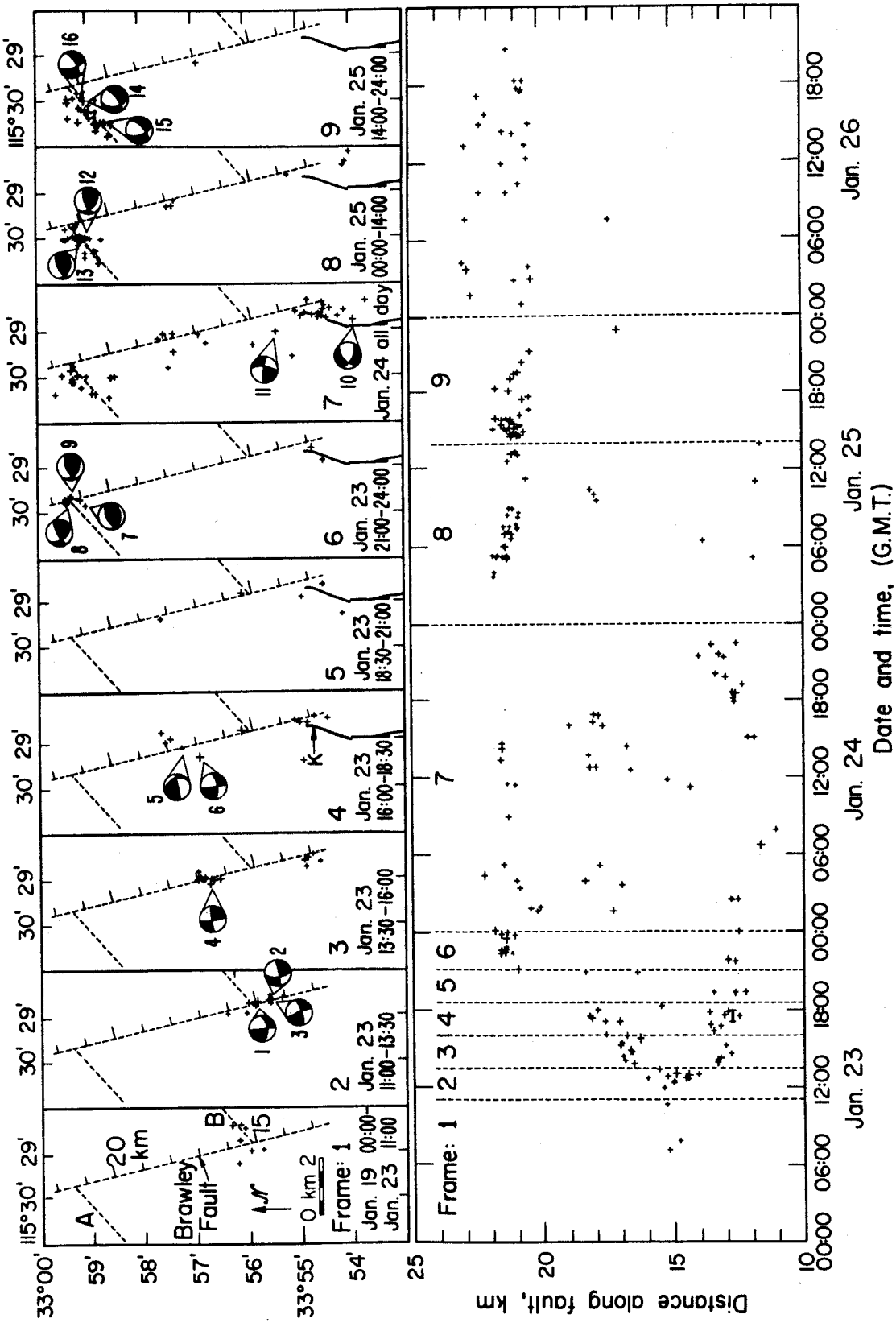
115°30' 29'
33°00'
59'
58'
57'
56'
33°55'
54'
A
B
20 km
Brawley Fault
0 km 2
Frame: 1
Jan. 19 00:00-
Jan. 23 11:00
2
Jan. 23
11:00-13:30
3
Jan. 23
13:30-16:00
4
Jan. 23
16:00-18:30
5
Jan. 23
18:30-21:00
6
Jan. 23
21:00-24:00
7
Jan. 24 all day
8
Jan. 25
00:00-14:00
9
Jan. 25
14:00-24:00
Frame: 1
2 3 4 5 6
7
8
9
25
20
15
10
Distance along fault, km
00:00 06:00 12:00 18:00 00:00 06:00 12:00 18:00 00:00 06:00 12:00 18:00
Jan. 23
Jan. 24
Jan. 25
Jan. 26
Date and time, (G.M.T.)

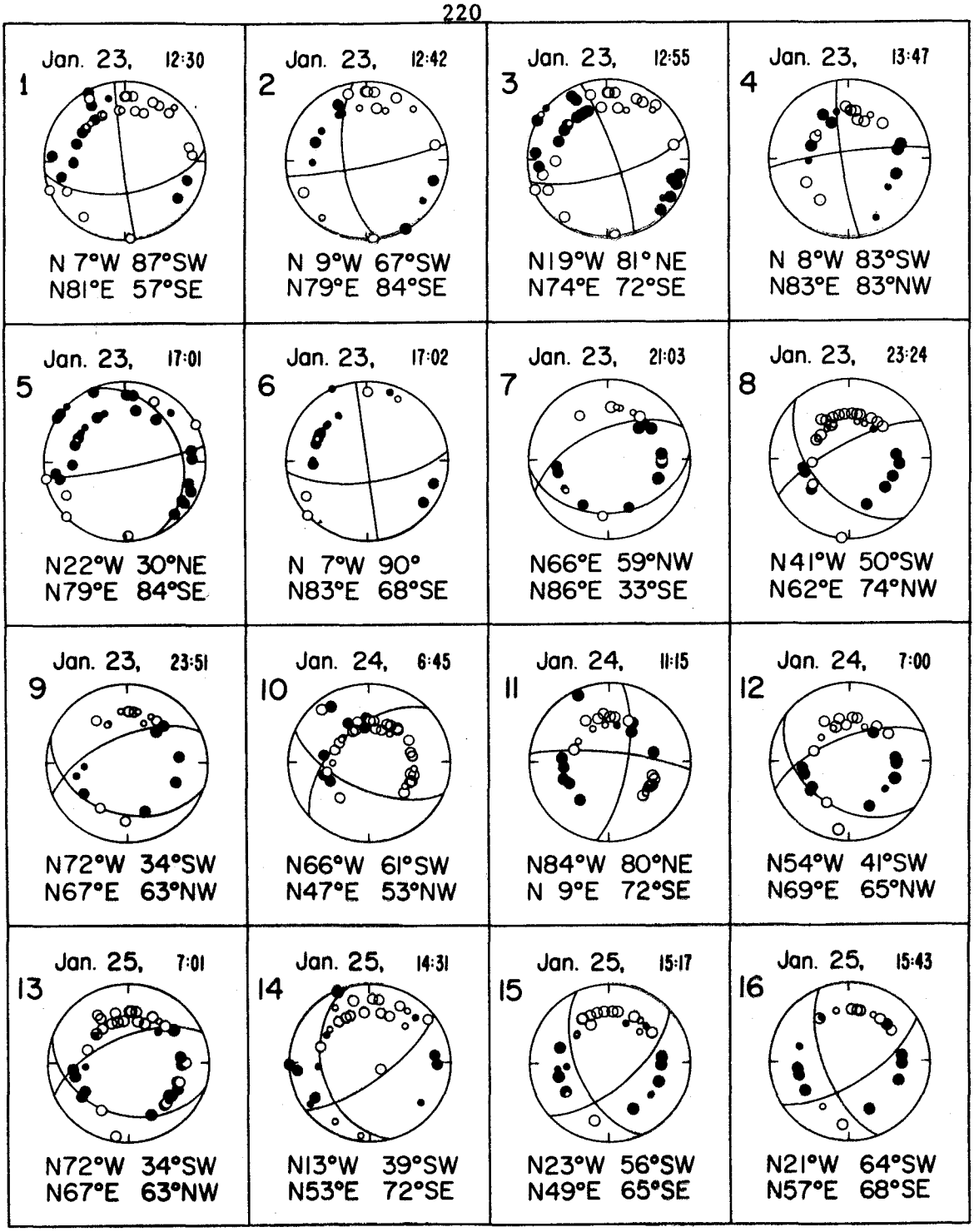

Figure 11. Lower hemisphere equal-area projection of first-motion data and focal mechanisms. Solid circles indicate compression, open circles indicate dilatation. The fault plane orientations are not listed in order of preference.

a shear modulus of 2×10^{11} dynes/cm^2. Identical assumptions were used in preparing plots similar to Figure 9 for each of the seven swarms discussed in this chapter. The most rapid increase in summed moment is associated with the onset of seismicity about mid-day on January 23. The second step in accumulated moment marks the activation of the transverse structure near Brawley.

Particular attention has been paid to revealing the details of the spatio-temporal development of the January 1975 swarm. Much of this information is contained in Figure 10. The lower portion of Figure 10 is a plot of the distance along the Brawley Fault as a function of origin time for the events occurring during the four days of peak activity. Distance along the Brawley Fault is defined as the epicentral distance from a point (32°48'N, 115°27'W) near the Imperial Fault on trend with the Brawley Fault. This plot has been divided into nine time frames spanning the first three days. The events occurring within each time interval are plotted in the corresponding plan view on the upper portion of Figure 10 showing the relationships to the inferred fault structures shown on Figure 8. The tick marks along the Brawley fault indicate the distance along the fault in kilometers and correspond to those marking the ordinate of the lower portion of the figure.

Further details of the spatio-temporal distribution are provided by a series of stereoscopic pairs in Figures 12 through 21. The observation point is located 275 km above the point 32°24'N, 115°33'W. Reference features include the outline of the community of Brawley, and the New River in the northwest corner, the Alamo River along the

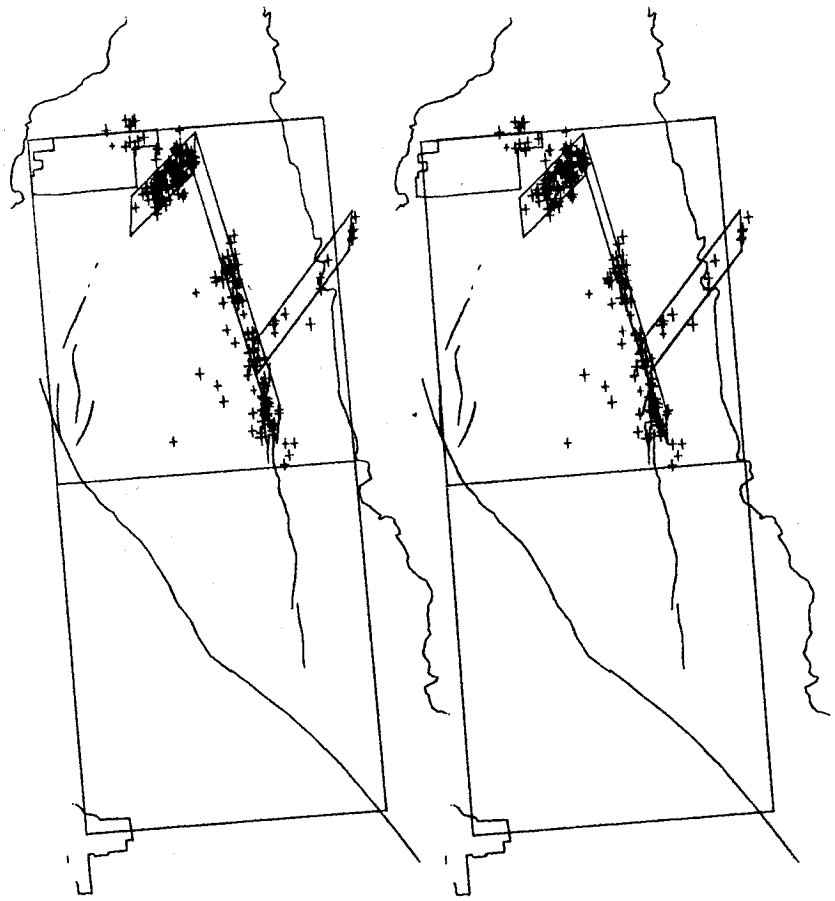

Figure 12. Stereo view showing all "A quality hypocenters for the 75 JAN swarm sequence on the Brawley trend. Cultural referents include the community of Brawley and the New River (upper left), the Alamo River (upper right) and El Centro (lower left). Both the 1940 surface faulting and the recent faulting along the Brawley Fault (Sharp, 1976) are shown. A reference grid, with sides of 0.1°, is plotted at a depth of 6 km. These features together with inferred fault planes are repeated in Figures 13 through 21. The view is from a point 275 km above 32°24'N, 115°33'W.

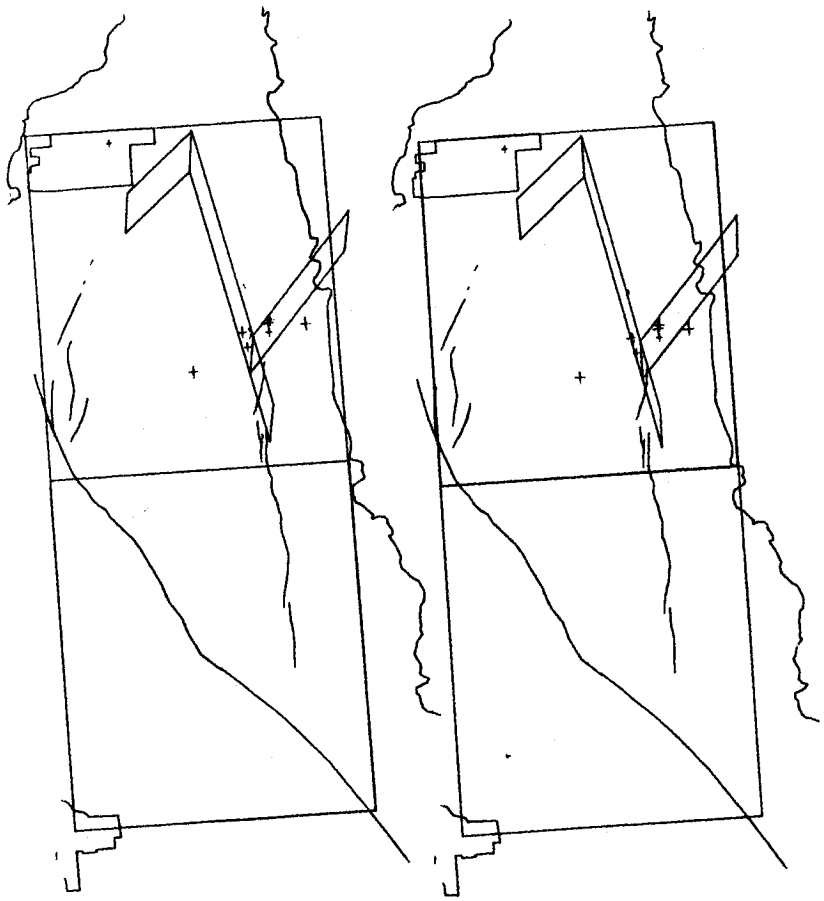

Figure 13. Stereo view showing all "A" quality hypocenters of the 75 JAN sequence occurring during the period 19 January 00:00 through 23 January 11:00 GMT (107 hours; frame 1 of Figure 10). These precursory events are generally shallower than subsequent events in the same area.

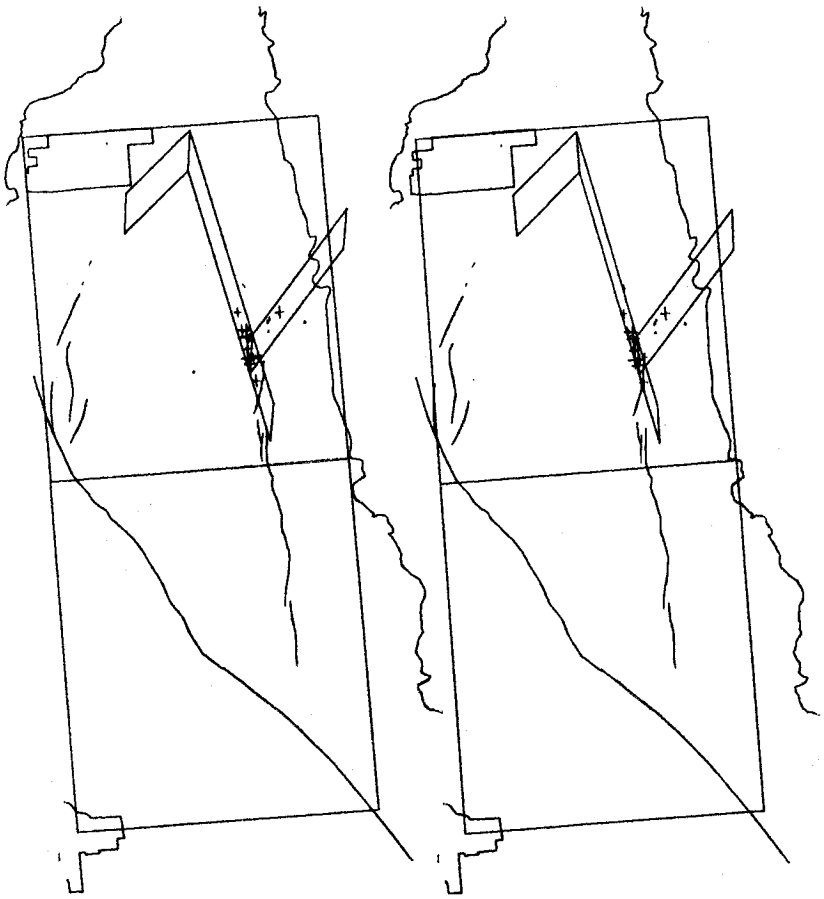

Figure 14. Stereo view showing all "A" quality hypocenters of the 75 JAN sequence occurring during the period 23 January 11:00 through 13:30 GMT (2.5 hours; frame 2 of Figure 10). This period brackets the sudden increase in moment rate shown in Figure 9. Through Figure 21, events preceding the specified intervals are represented for single points to accentuate migrational phenomena.

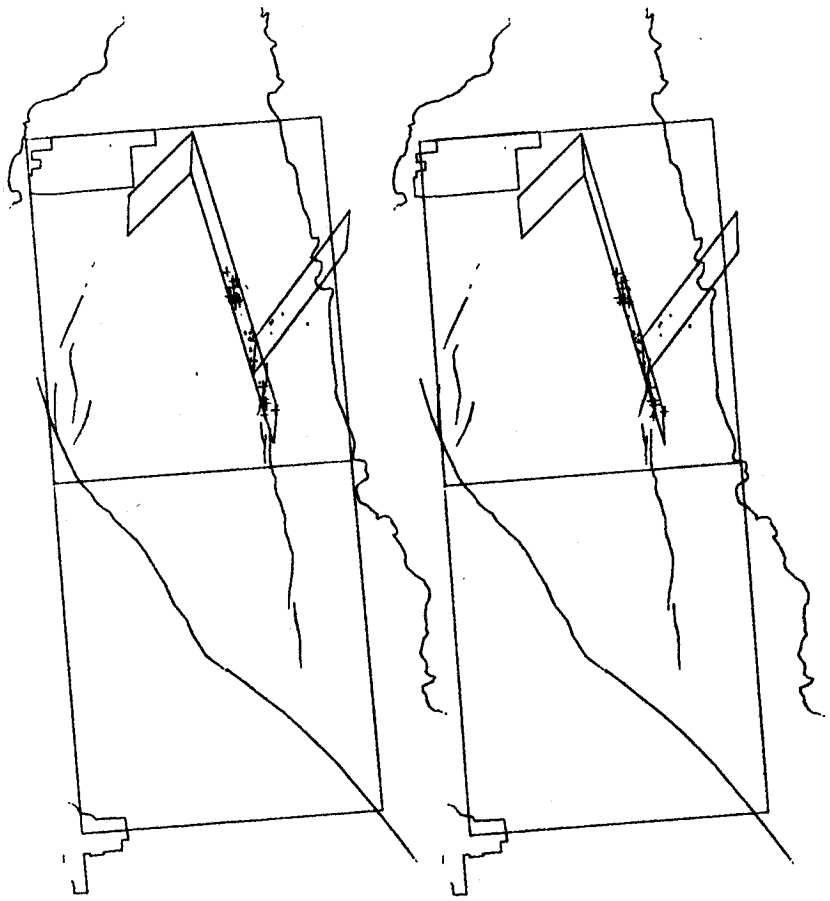

Figure 15. Stereo view showing all "A" quality hypocenters of the 75 JAN sequence occurring during the period 23 January 13:30 through 16:00 GMT (2.5 hours; frame 3 of Figure 10). The beginning of bilateral migration is now evident.

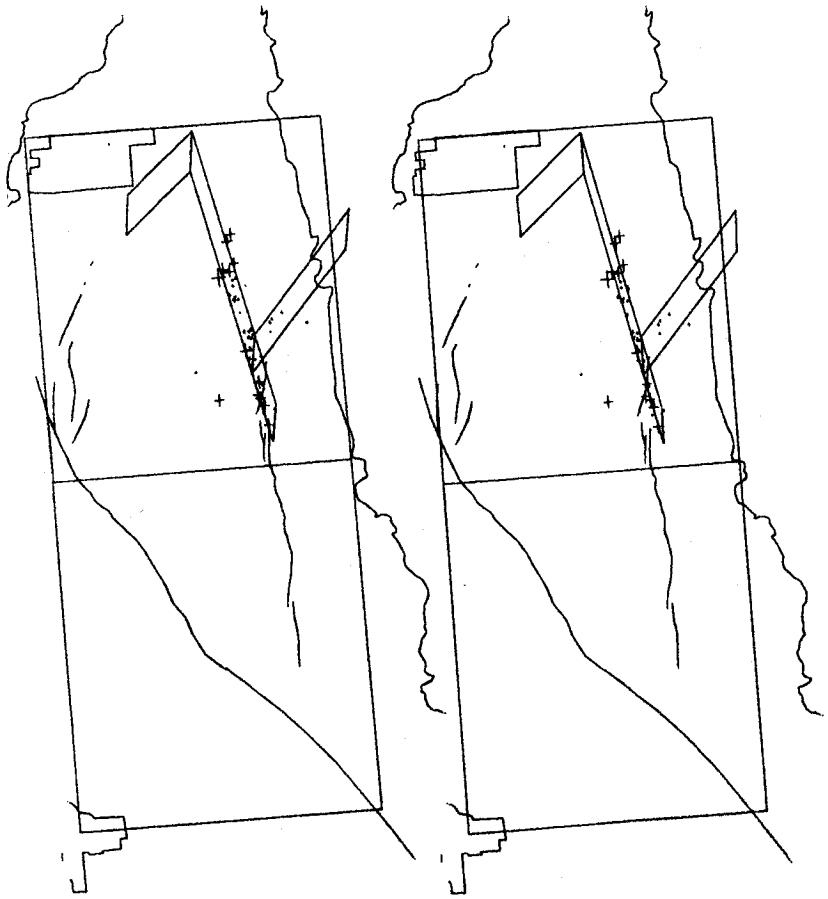

Figure 16. Stereo view showing all "A" quality hypocenters of the 75 JAN sequence occurring during the period 23 January, 16:00 through 18:30 GMT (2.5 hours; frame 4 of Figure 10). During this interval migration of activity to the south terminated with the formation of a scarp on the Brawley Fault where it crosses Keystone Road.

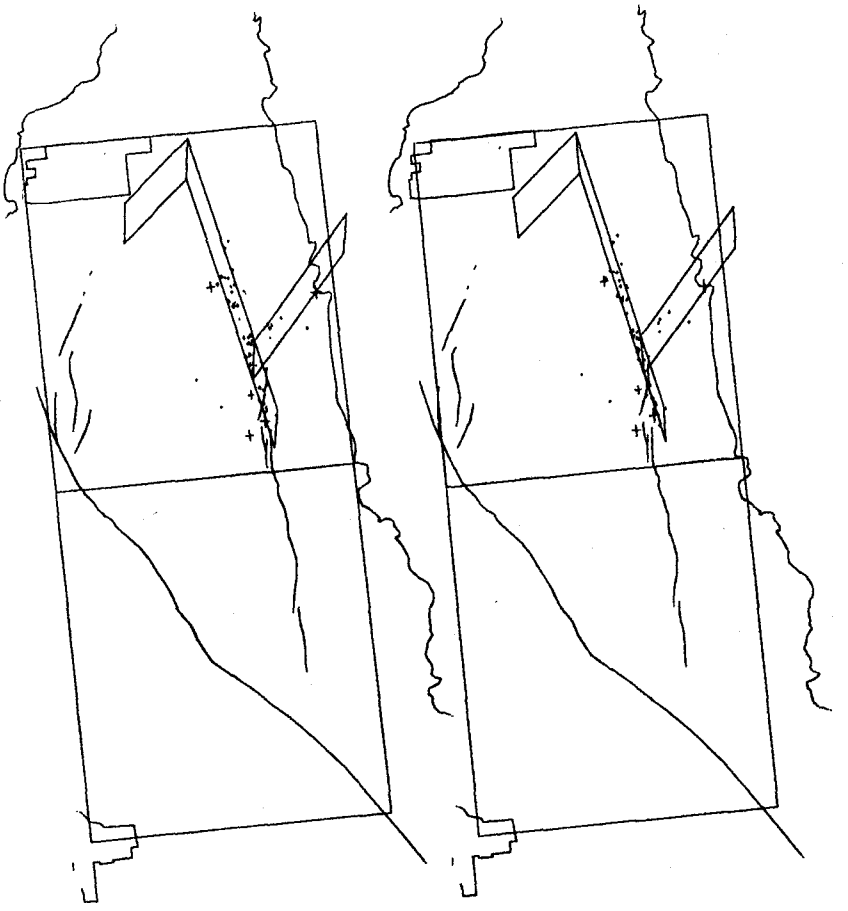

Figure 17. Stereo view showing all "A" quality hypocenters of the 75 JAN sequence occurring during the period 23 January 18:30 through 21:00 GMT (2.5 hours; frame 5 of Figure 10). The absence of activity corresponds to the crossing of a section of the Brawley Fault that was quiescent throughout the 75 JAN swarm sequence.

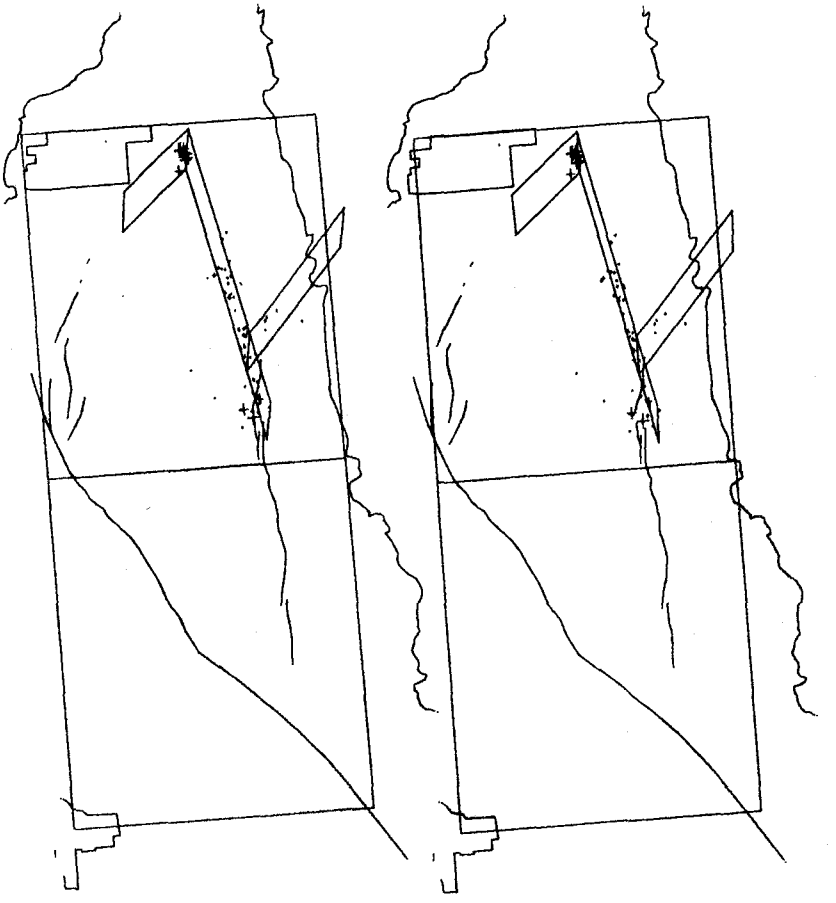

Figure 18. Stereo view showing all "A" quality hypocenters of the 75 JAN sequence occurring during the period 23 January 21:00 through 24:00 GMT (3 hours; frame 6 of Figure 10). During this interval northward migration along the Brawley Fault terminates with highly clustered seismicity near its intersection with Fault "A".

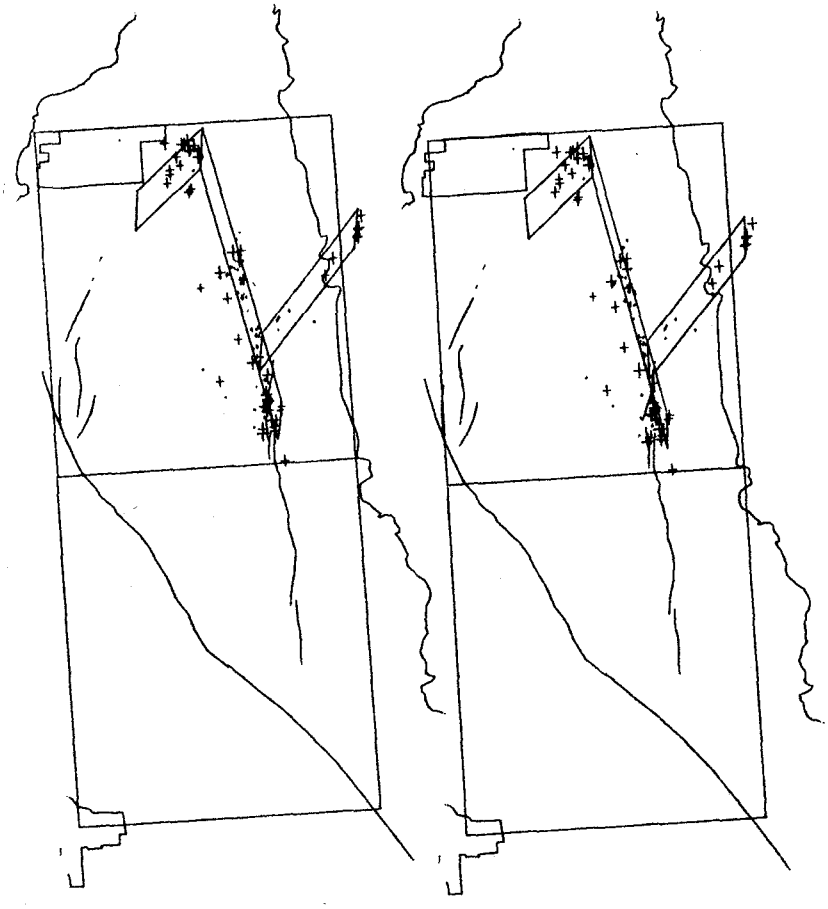

Figure 19. Stereo view showing all "A" quality hypocenters of the 75 JAN sequence occurring during the period 24 January 00:00 through 24:00 GMT (24 hours; frame 7 of Figure 10). The beginning of activity along the transverse structure designated Fault "A" can now be observed.

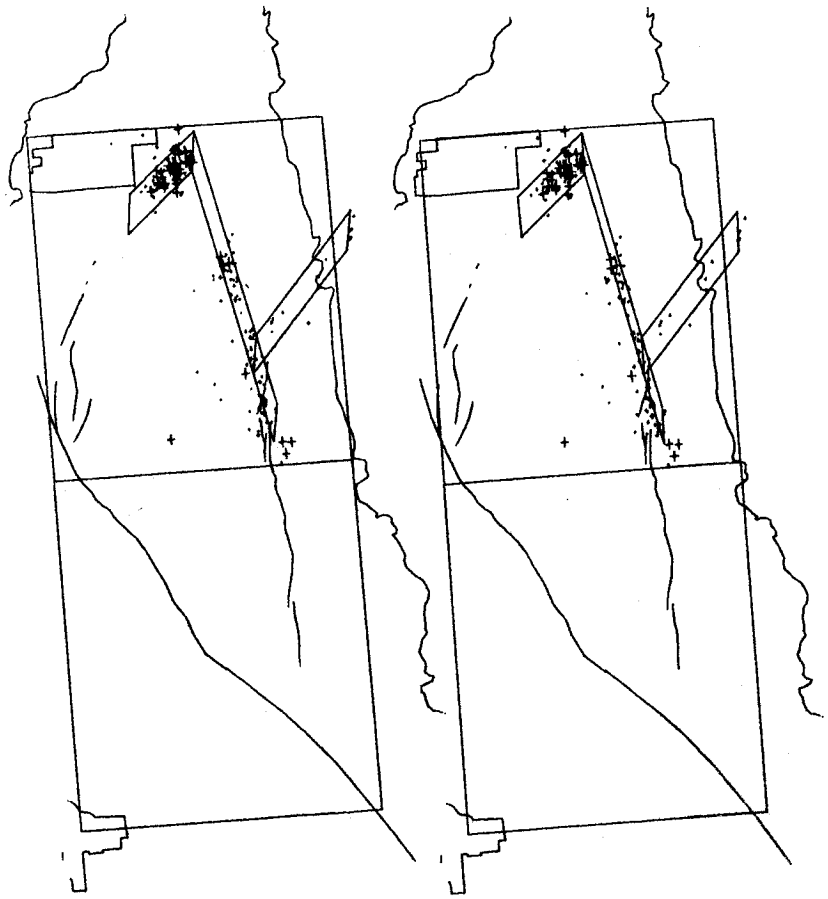

Figure 20. Stereo view showing all "A" quality hypocenters of the 75 JAN sequence occurring during the period 25 January 00:00 through 14:00 GMT (14 hours; frame 8 of Figure 10). This interval contains the first of two bursts of activity completing the activation of Fault "A".

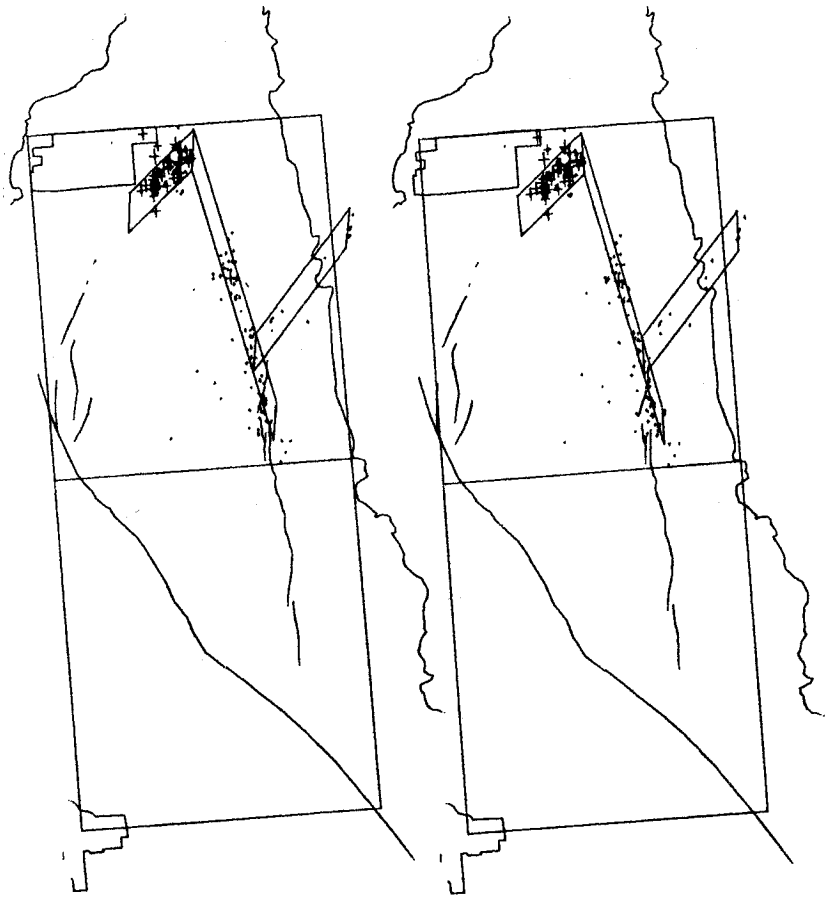

Figure 21. Stereo view showing all "A" quality hypocenters of the 75 JAN sequence occurring during the period 25 January, 14:00 through 24:00 (10 hours; frame 9 of Figure 10.)

eastern edge, and the outline of El Centro in the southwest corner. The large domino-shape figure is provided as a scale and depth referent. It is .1° on each side and is plotted at a depth of 6 km.

The surface trace of the 1940 earthquake and the ground breakage associated with the January 1975 swarm as mapped by Sharp (1976) are also shown. Fault members suggested by Johnson and Hadley (1976) are plotted from a depth of 3 km to a depth of 7 km. The most northerly trending of these is identified as a creeping (at depth) section of the Brawley fault. The transverse structure beneath Brawley, fault "A", is shown dipping to the south in agreement with normal faulting. This was done because the location accuracy did not permit greater resolution. Our preferred interpretation is that the events along fault "A" occurred as thrust events on two north dipping structures, one above the other. This interpretation is mechanically compatible with right-lateral creep south of Brawley encountering a "locked" section of the Brawley fault to the north.

The hypocentral distribution for all "A" quality events is shown in Figure 12. The remaining 9 stereoscopic pairs correspond on a one-to-one basis with the time frames shown on the upper portion of Figure 10. Events occurring during each interval are plotted as discrete symbols with sizes proportional to magnitudes. All events prior to the interval are plotted as points to make the progressive development of the swarm as visible as possible.

One of the most intriguing results of this study is the well-defined migration of the onset of seismicity bilaterally north and south along the Brawley fault from its point of inception near the

intersection of the Brawley fault and fault "B" as shown in frames 2 through 6. To the north the migration covered a distance of 6.5 km in about 13 hours, giving a propagation velocity of .5 km/hr. The swarm was preceded by a gradual increase in shallow seismicity ($h < 6$ km) in the immediate vicinity of the intersection of the Brawley fault and fault "B" (frame 1 and Figure 13) during the four days prior to the onset of peak activity. Spatially these events appear to lie on a steeply north dipping plane with strike coincident with fault "B". The character of the seismicity changed abruptly simultaneous with a sudden increase in the number and magnitude of events (frame 2 and Figure 14) at 1230 GMT on January 23. These and subsequent events were deeper ($h > 6$ km) with a distinct tendency to align along the strike of the Brawley fault. This trend is supported by the strike of the focal mechanisms. In order to better represent the onset of seismicity as it progressively involved the Brawley fault, the remainder of January 23 is divided into 2-1/2 hour intervals (frames 2 through 6 and Figures 14 through 18). The passage of the onset of seismicity was characterized by a sudden increase in activity followed by a return to relative quiet. Shallower events tended to trend off the strike of the Brawley fault in a manner suggestive of conjugate failure within the sediments. Sharp (1976) was able to bracket the time of the formation of the scarp at Keystone Road (marked with a "K" on Figure 8 and frame 4 of Figure 10) to the interval 1700-1800 hrs GMT on January 23. This interval is shown as a bracket on the lower portion of Figure 10. The development of the scarp occurred about 3 hours after the projected arrival of a disturbance

at a depth of about 5 km. The delay may be related to the propagation time from this depth to the surface. Unfortunately, the time of formation of the cracks farther south is not known.

Considering further the propagation to the north, the absence of events in frame 5 and Figure 17 is associated with the passage of the disturbance along a portion of the Brawley fault near kilometer 20 that was quiet throughout the swarm, as shown in Figure 2. The northward migration terminated at the intersection of the Brawley Fault and fault "A" with tightly clustered sequence of events shown in Frame 6 and Figure 18. Focal mechanisms and the alignment of these events indicate reverse faulting on a northeast striking plane dipping steeply to the north.

Frame 7 and Figure 19 show the diffuse pattern of events occurring on January 24. Of note is the onset of shallow seismicity ($h < 6$ km) along the strike of fault "A". This was followed on January 25 by two rather distinct bursts of activity (frames 8 and 9) with depths ranging from 6 to 8 km.

The progressive development of activity associated with fault "A" away from its inception at the intersection with the Brawley fault as evidenced in Figures 18 through 21, is especially intriguing. This was the first evidence suggesting the activation of a transverse structure by an essentually aseismic process propagating along the Brawley trend. The subsequent examination of other swarms in the Imperial Valley (discussed below) provided abundant further examples of similar behavior.

The change in mechanism from thrust to normal reported by

Johnson and Hadley (1976) and shown in frame 9 of Figure 10 does not appear to be particularly well-supported. The differences in focal mechanisms in events 11 through 16 of Figure 11 do not involve significant changes in the first motion patterns; rather it appears to reflect an instability associated with the absence of steep take-off angles. In light of more recent studies, it now seems more likely that all strike-slip displacement on the Brawley trend was converted to thrust faulting on fault "A", and that significant creep at depth along the Brawley fault did not continue farther north past the community of Brawley. This interpretation is also tectonically compatible with continued subsidence of the closed depresssion named Mesquite Lake (Figure 8).

November 1976 Sequence

A second major swarm sequence occurred along the Brawley trend near its northern end in November 1976. Preliminary results for this swarm were presented by Fuis and Schnapp (1977) and a more detailed analysis by these authors is currently in progress. The epicentral distribution for the November 1976 swarm is shown in Figure 22. The general tendency to elongate in several clusters along a northwest trend is again evident. The largest event was assigned a magnitude of 4.9, with more than 31 events exceeding magnitude 3.0 and 8 events larger than 4.0. Thus the November 1976 swarm was comparable in size to the January 1975 sequence which produced 75 earthquakes greater than 3.0 and 7 events greater than 4.0 with a maximum magnitude of 4.8. At the time of writing, final magnitude assignments for the November

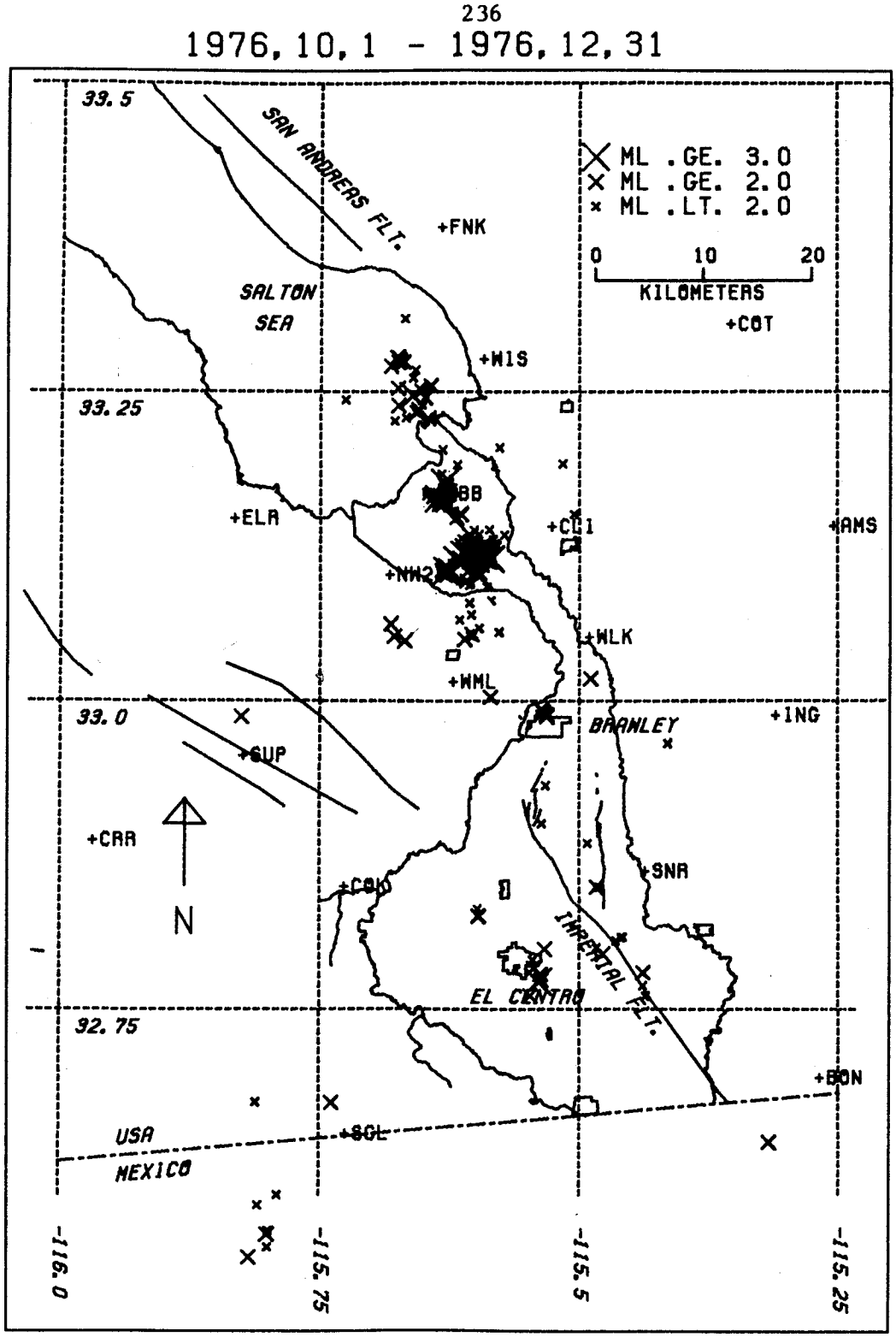

Figure 22. Epicentral plot of all "A" and "B" quality events during the fourth quarter of 1976 including the 76 NOV swarm sequence near the southern shore of the Salton Sea.

1976 swarm were not available, so some rearrangement of the number of events in each magnitude partition will probably occur.

The development of the November 1976 swarm sequence with time was in many respects similar to that of the January 1975 swarm. Figure 23 shows the same tendency for maximum moment rate to be strongly skewed toward the onset of the sequence. The localized build-up of seismicity before the swarm, however, was not observed. While the January 1975 swarm terminated with intense activity on a transverse structure, the November 1976 swarm began on a transverse structure near the southern end of the distribution shown in Figure 22. Based on the hypocentral distribution together with first-motion focal mechanisms reported by Fuis and Schnapp (1977), this structure has been interpreted as a nearly vertical fault striking east-northeast. First motions require left-lateral slip on this plane. A particularly well-constrained P-wave focal mechanism for the largest event of the sequence (M 4.9 at 1041 GMT, 4 November) gives a vertical plane striking N 64° E with an auxiliary plane striking N 26° W with a dip of 70°W (Heaton and Helmberger, 1978). The efficacy of this solution was subsequently confirmed by its use in the highly successful calculation of strong ground motion records recorded at Imperial College (d = 33 km) and El Centro (d = 36 km).

Further details of the temporal development of the November 1976 swarm are provided in the form of time-distance plots in Figures 24 and 25. Figure 24 is projected along an east-northeast line parallel to the transverse structure and perpendicular to the Brawley fault. Distance is measured from a point 33°3' N, 115°45'W east of the

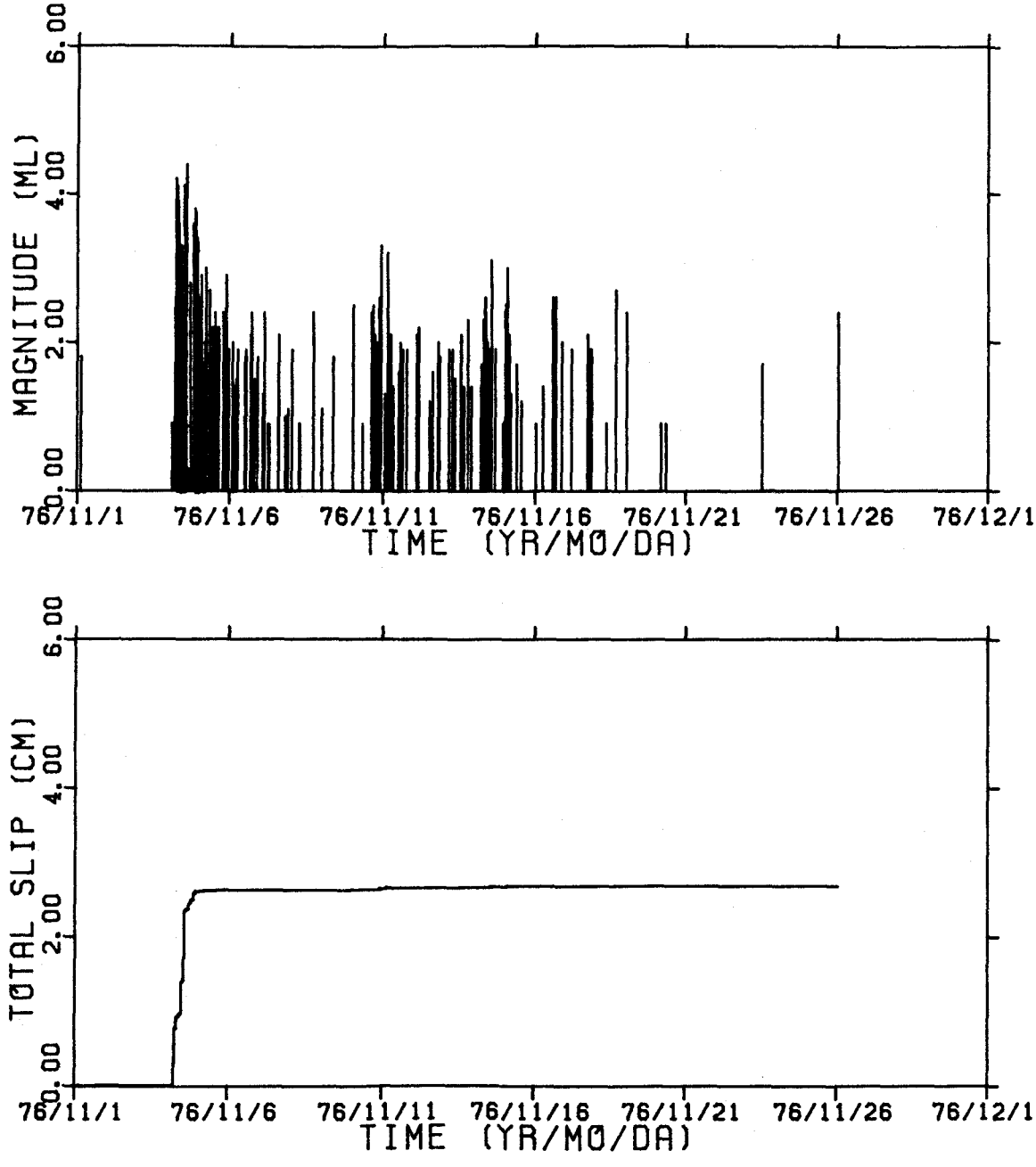

Figure 23. Two time-series representations illustrating the development of the 76 NOV swarm sequence. In the upper frame events are represented by a vertical line proportional to magnitude and plotted at the origin time. As appears typical for sequences along the Brawley trend there is a strong tendency for the larger events to occur near the beginning of the sequence. The lower frame shows moment plotted as proportional slip on a 33 km^2 fault.

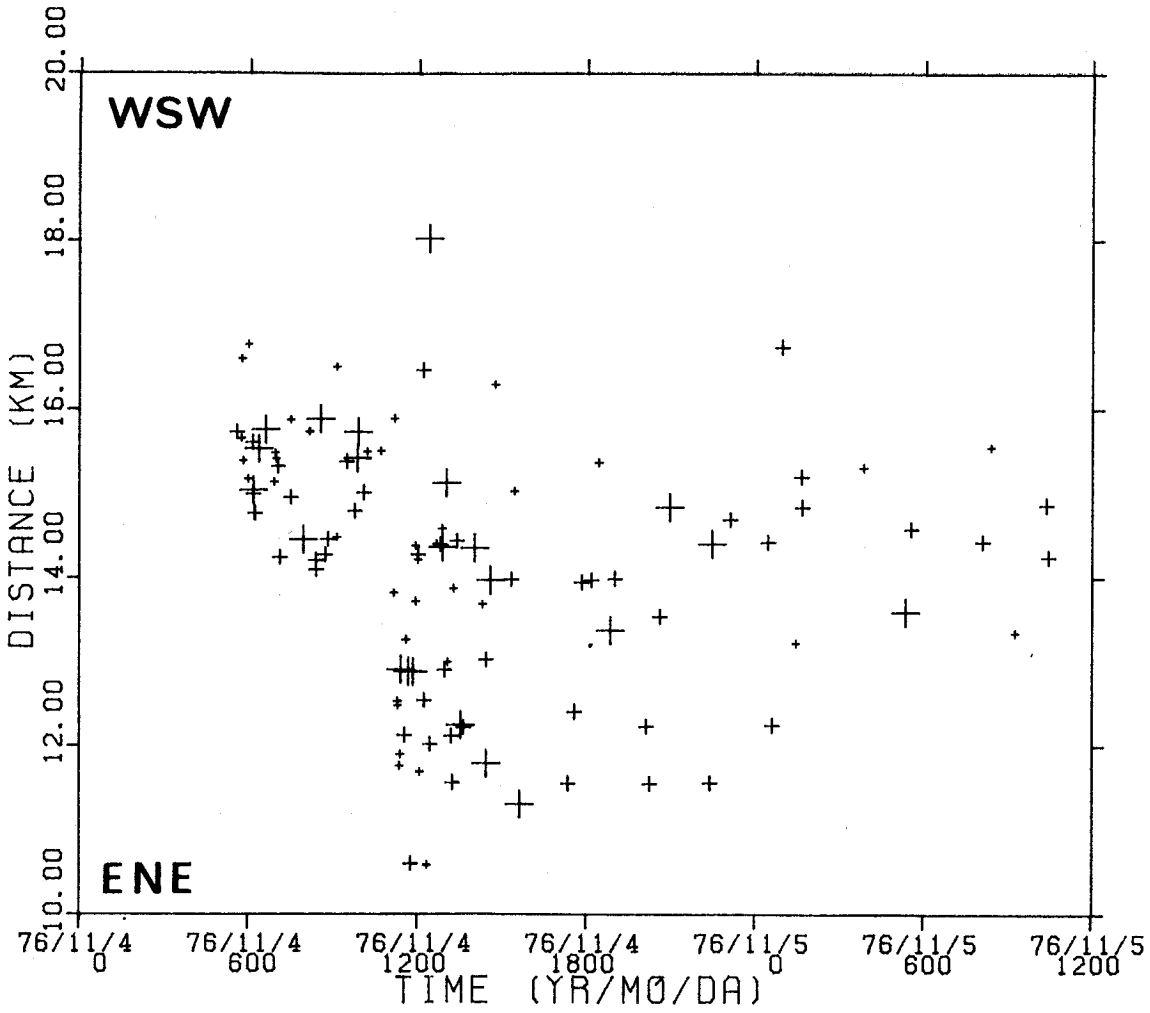

Figure 24. Time-distance scatter plot showing the migration of seismicity to the southwest along the transverse structure defined by the events initiating the 76 NOV swarm sequence. Events are represented by symbols with size proportional to magnitude. Distance is measured from the point 33°3'N, 115°45'W.

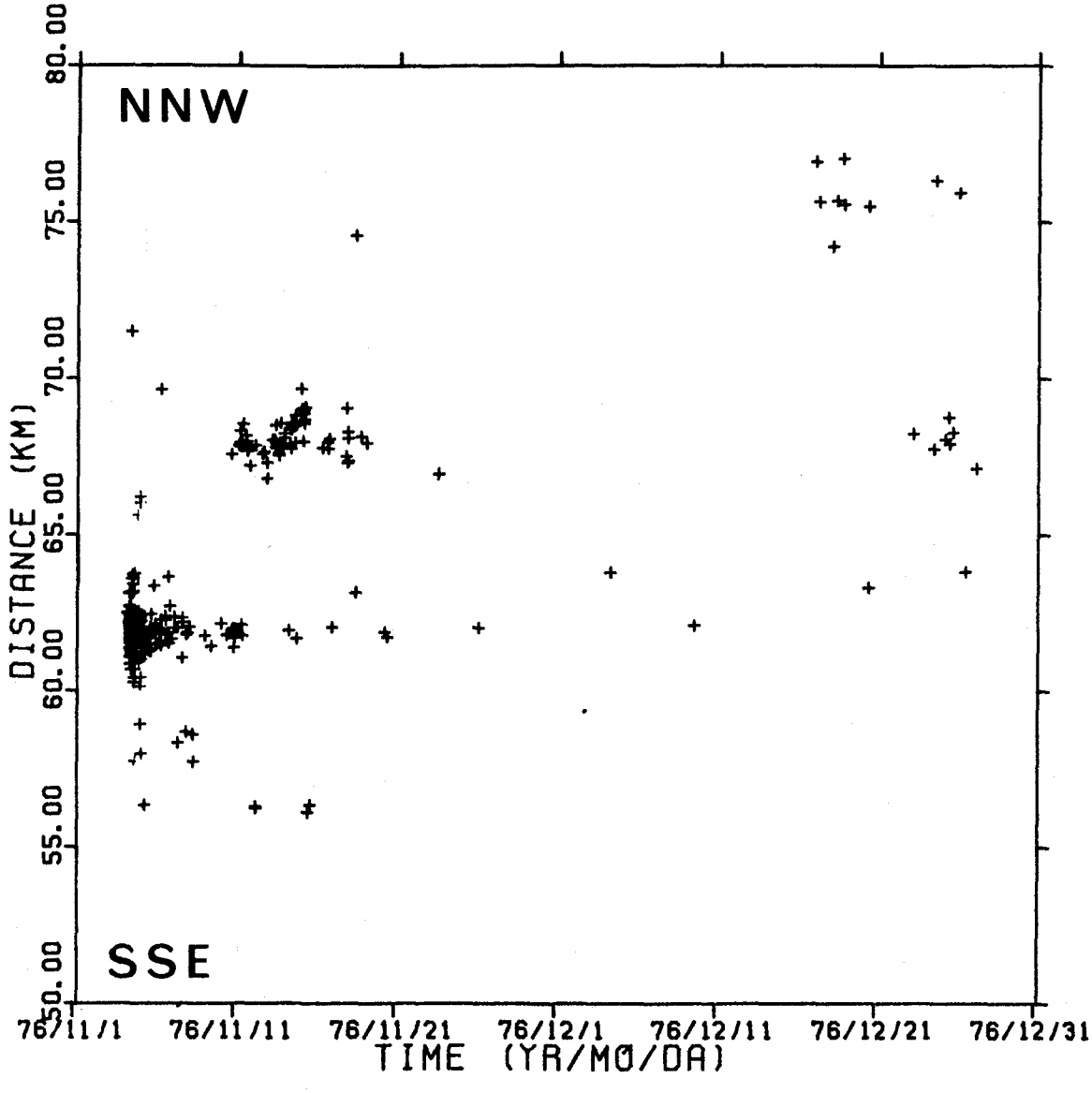

Figure 25. Time-distance scatter plot showing the migration of seismicity to the northwest along the trend of the Brawley Fault in the form of discrete clusters isolated in both space and time. Note the change in time scale from Figure 24.

epicenters. Events plotted in Figure 25 are projected on a north-northwest line paralleling the Brawley trend with distance measured from the reference point for Brawley trend events in Figure 1. Figure 24 demonstrates that the activity commenced at the eastern end of the transverse fault followed by subsequent unilateral migration to the west at a velocity of about .5 km/hr, a rate remarkably similar to that observed along the Brawley trend during the January 1975 swarm sequence. Initial activity was concentrated at the point where the transverse structure intersects the rather sharp eastern boundary of the Brawley Seismic Zone (Chapter 4). Westward migration was truncated at the western boundary of the Brawley Seismic Zone. Subsequent low-level activity south of this point is consistent with the conjecture that the western boundary of the Brawley Seismic Zone is controlled by a northward extension of the Imperial Fault.

Subsequent northward migration marked by the progressive activation of localized, isolated clusters is shown in Figure 25. Here again we see intervening regions which are aseismic throughout the swarm sequence. As before, this phenomenon is interpreted as indirect evidence for fault creep along the Brawley trend. A much slower migration rate of around .5 km/day is indicated, with a tendency toward decreasing rate with distance. A similar decrease in propagation rate for creep events in Central California has been reported by King and others (1973). Figure 25 also shows evidence for some migration to the south of events which in Figure 22 appear

to lie along the western edge of the Brawley seismic zone providing some support for the possibility of an active fault as discussed above.

A series of stereoscopic pairs in Figures 26 through 31 provide considerable details of the spatio-temporal development of the November 1976 swarm sequence, particularly with reference to the later stages of this process. All "A" quality solutions are plotted in Figure 26. This distribution, together with the "step-like" epicentral distribution shown in Figure 22 and general results from the January 1975 swarm sequence, were used to infer a framework of seven vertical fault planes shown in Figures 26 through 31. This structure is arranged so that aseismic processes (creep) are occurring on northwest trends while northeast elements are activated seismically. Of these, the only one which is reasonably well supported by observation is that associated with the transverse structure at the southern end of the distribution. While the remaining elements are regarded as highly plausible, we recognize the existence of a variety of alternative interpretations.

The stereoscopic pairs also contain a number of surficial details for reference purposes, including the southern shoreline of the Salton Sea, the Alamo River, and the New River to the south. The Salton Sea shoreline is shown on its 1943 position. Since that time it has encroached a considerable distance to the south. As before, hypocenters for consecutive time intervals are shown as discrete symbols in Figures 27 through 31. Events from preceding intervals are reduced in size to small dots in order to provide an

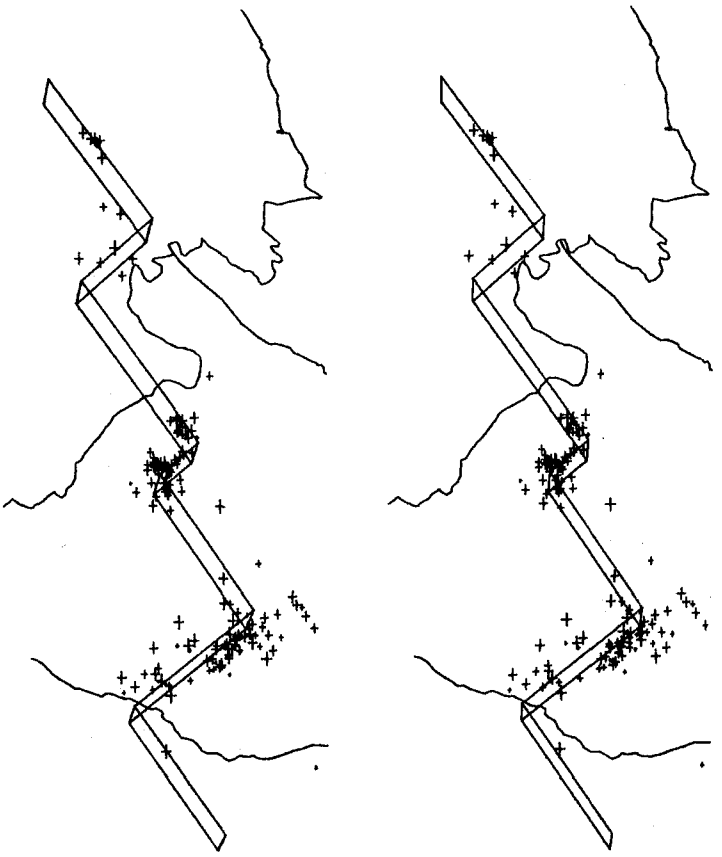

Figure 26. Stereo view showing all "A" quality hypocenters for the 76 NOV swarm sequence on the Brawley trend. Cultural referents include the southern shoreline of the Salton Sea and the mouth of the Alamo River (near top of Figure) and the New River (near bottom of Figure). The suggested fault structures represent one of several reasonable interpretations and are shown primarily for spatial reference purposes. The view is from a point 275 km above 32°39'N, 115°36'W.

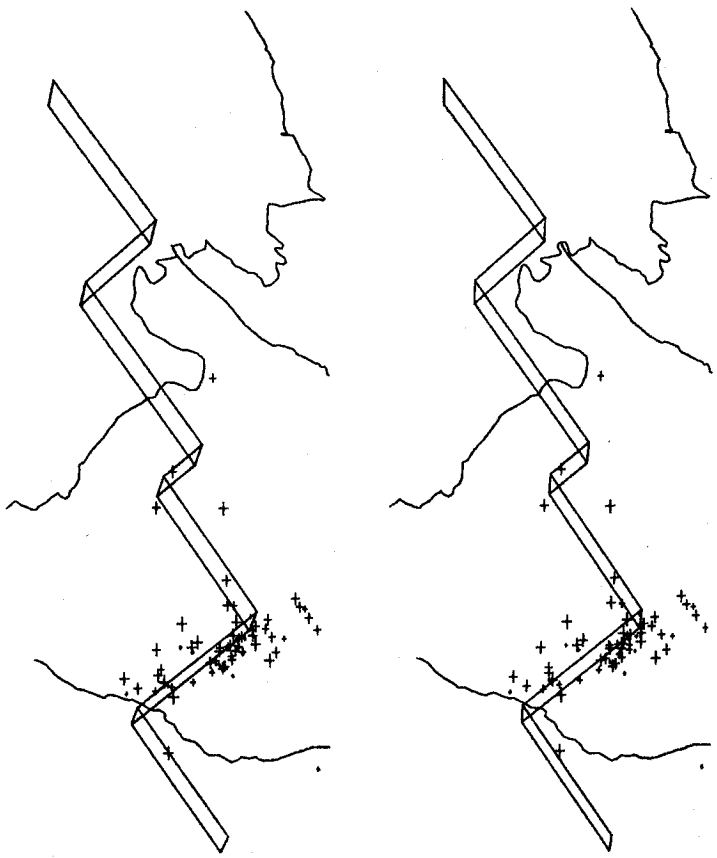

Figure 27. Stereo view showing all "A" quality hypocenters of the 76 NOV sequence occurring during the period 1 November through 10 November 1976 (10 days). During this period activity is largely confined to northeast trending transverse structure. As shown in Figure 24 initial development of activity on this sturcture proceeded from southwest to northeast.

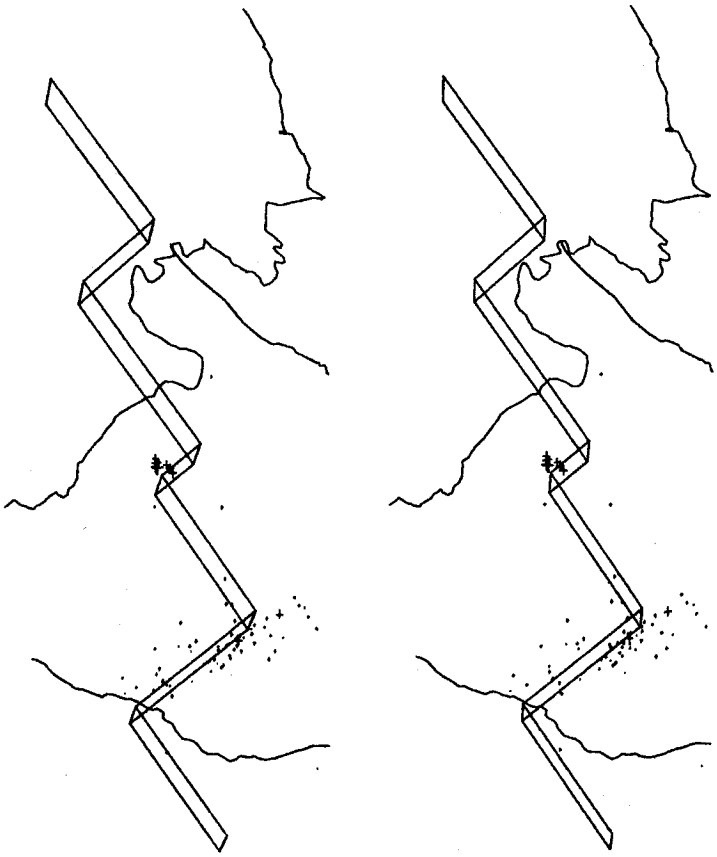

Figure 28. Stereo view showing all "A" quality hypocenters of the 76 NOV sequence occurring on 11 November 1976 (1 day). In this figure through Figure 31, events preceding the specified interval are represented as single points for reference purposes.

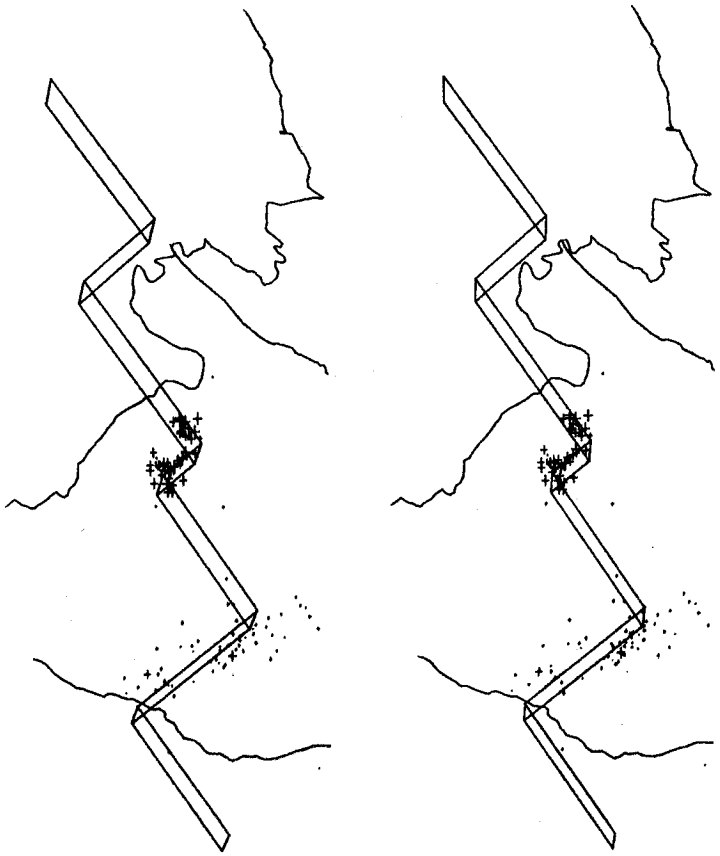

Figure 29. Stereo view showing all "A" quality hypocenters of the 76 NOV sequence occurring from 12 November through 17 November 1976 (6 days).

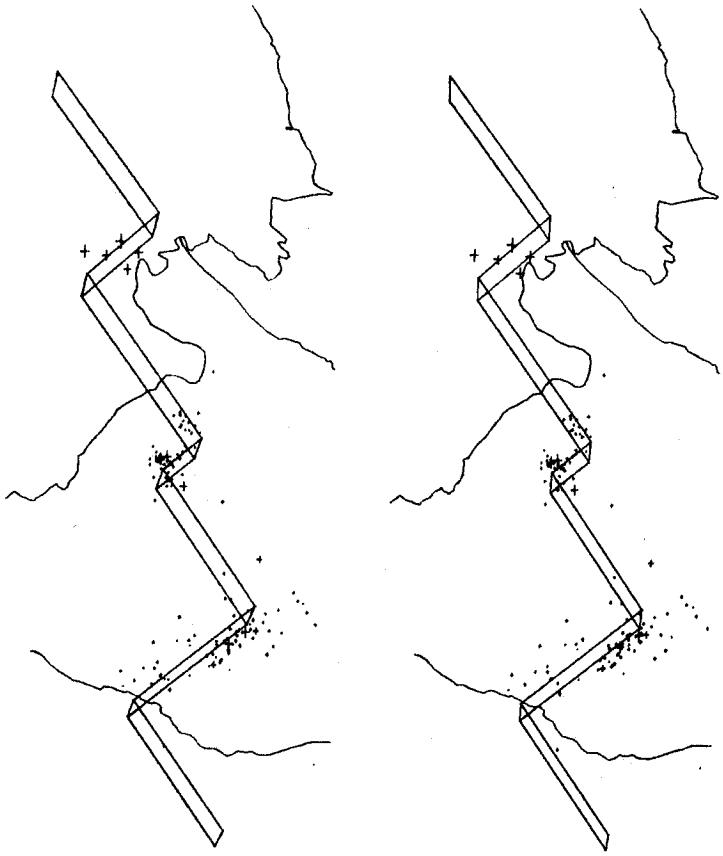

Figure 30. Stereo view showing all "A" quality hypocenters of the 76 NOV sequence occurring from 18 November through 18 December 1976 (31 days).

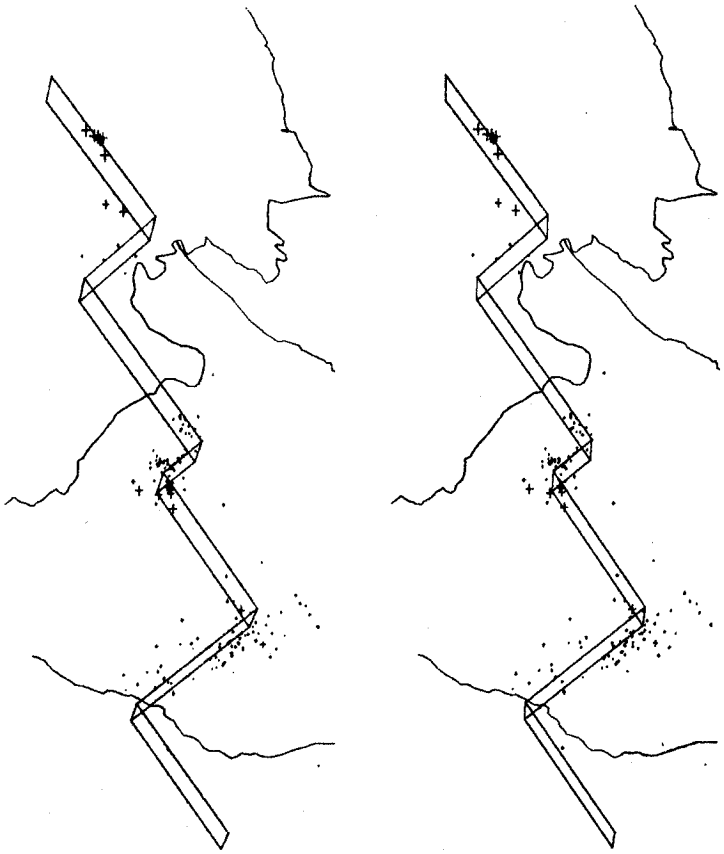

Figure 31. Stereo view showing all "A" quality hypocenters of the 76 NOV sequence occurring from 19 December through 31 December 1976 (12 days).

on-going reference to the progressive development of the swarm sequence. Intervals are of irregular duration and are arranged so as to emphasize the development of individual component swarms.

It is still somewhat conjectural as to whether or not there is a discrete, well-defined fault -- the Brawley Fault -- joining the January 1975 and November 1976 sequences. Certainly the sharply defined eastern boundary of the Brawley Fault could be explained by such a structure. The geodetic results reported by Thatcher (1979) are also consistent with the existence of a throughgoing fault at depth. However, both the trilateration studies and the lack of observed migration seem to require that if there is such a fault it is "locked" at depths shallower than 10 km from north of Brawley nearly to the Salton Sea. This inference is supported by the lack of localized deformation of cultural features such as roads and irrigation channels, although such deformation is common farther south along the Brawley trend and along the Imperial trend. This leaves open the possibility that the 15- to 20-km-long section of the proposed Brawley fault north of Brawley may break in a single event similar to the destructive earthquake in 1940. Should this occur, the length of possible faulting would render the occurrence of an event significantly larger than $M_L = 6$ unlikely.

Other Brawley Trend Sequences

Although during the past decade the Brawley trend has been relatively inactive as compared to the Imperial trend (Chapter 4), this has not always been the case. Most of the swarms reported by

Hileman (1978) seem to be related to the Brawley trend including major swarms in July 1950, December 1955, October 1963, and June 1965. Some of these earlier sequences produced significant surface effects. A swarm in July 1950 produced surface cracks and numerous sand boils (Murphy and Ulrich, 1952), with the most severe surficial effects occurring about 10 km west of Calipatria. Significantly, the intense activity marking the onset of the November 1976 swarm occurred within a few kilometers of this point, although in this case no surficial effects were observed. The expulsion of ground water was also a major factor in a swarm in April of 1957 (Brazee and Cloud, 1959). Ground cracks and sandblows formed in a region about 7 km southeast of the area affected in 1950. A line joining these two areas is coincident with the trend of the Brawley fault. These earlier sequences also shared the property of precipitous onset described above for the January 1975 and November 1976 swarm sequences.

EARTHQUAKE SWARMS ON THE IMPERIAL TREND

From the time of the 1940 El Centro earthquake (M_s = 7.1) until about 1965 the Imperial trend appears to have been relatively free of earthquake swarms. One of the earliest, in March of 1966, was accompanied by surface displacements reaching 1.5 cm along a 10-km section of the Imperial Fault (Brune and Allen, 1967). Although they associated this breakage with the largest event in the swarm (M_L = 3.6), making it the smallest known earthquake with documented surface displacement, the hypothesis that the primary cause of the surface displacement was coincident fault creep was not ruled out.

In light of more recent results, including the discussion below, we prefer the latter interpretation.

Prior to 1973 there is no evidence that individual swarms were occurring as part of more extensive swarm sequences. Although the location precision at the time was not capable of resolving individual clusters spatially, more recent swarms are often sufficiently separated in time that swarm sequences should have been identifiable from time-series. On the other hand, the magnitude threshold was such that some recent swarm sequences would have appeared as isolated events or swarms, provided they were not missed altogether. A careful analysis of records for the nearest stations at the times of reported events should help to resolve this point. However, from available evidence it appears that coherent sequences of swarms did not occur prior to about 1973. Also, swarm sequences since 1973 have generally tended to become larger with time.

Spatio-Temporal Relationships from Five Swarm Sequences

Five notable swarm sequences have occurred along the Imperial trend during the five years since the installation of the 16-station Imperial Valley network by the U.S.G.S. in June 1973 (Hill and others, 1975b). These swarms have been more or less evenly spaced in time, occurring in June 1973, August 1974, June 1975, March 1976, and October 1977. The first of these in June 1973 was recognized by Hill and others (1975a) in an analysis of the first year of operation of the Imperial Valley network, although its more general significance could not be fully appreciated until similar processes were repeated several times.

A graphical summary of the last five swarm sequences is provided in Figures 32 through 46. A similar set of three figures is repeated for each of the five sequences. The first figure in each set is an epicentral map. All events in the mapped region with qualities of "A", "B", or "C" (e.g. Lee and Lahr, 1975) during the specified time intervals are plotted. In each case a strong tendency for events to occur in a few highly localized clusters along a northwest trend can be noted. The somewhat higher scatter of the events for the August 1974 swarm plotted in Figure 35 seems to be attributable to improper or inaccurate timing procedures. This problem seems to afflict 1974 Imperial Valley epicenters generally, as evidenced by Figure 12 of Chapter 4.

The second figure prepared for each of the five swarm sequences (e.g., Figure 33 for the June 1973 sequence) provides a direct representation of time history. In the lower frame accumulated moment is plotted as slip ($S = 33$ km^2, $\mu = 2 \times 10^{11}$ dynes/cm^2) to emphasize times of greatest strain release. Since identical assumptions are used for each sequence, the total accumulated moment (or slip) over the appropriate time-interval can be used as a measure of relative "size". A general increase in intensity of the five swarms studied with time is apparent. The top frame shows the actual magnitude distribution with time, illustrating one of the major differences between swarms on the Imperial trend as compared to those on the Brawley trend. Imperial trend swarms are more accurately characterized by bursts of seismicity beginning and ending abruptly, rather than the more precipitous failure associated with transverse structures on the

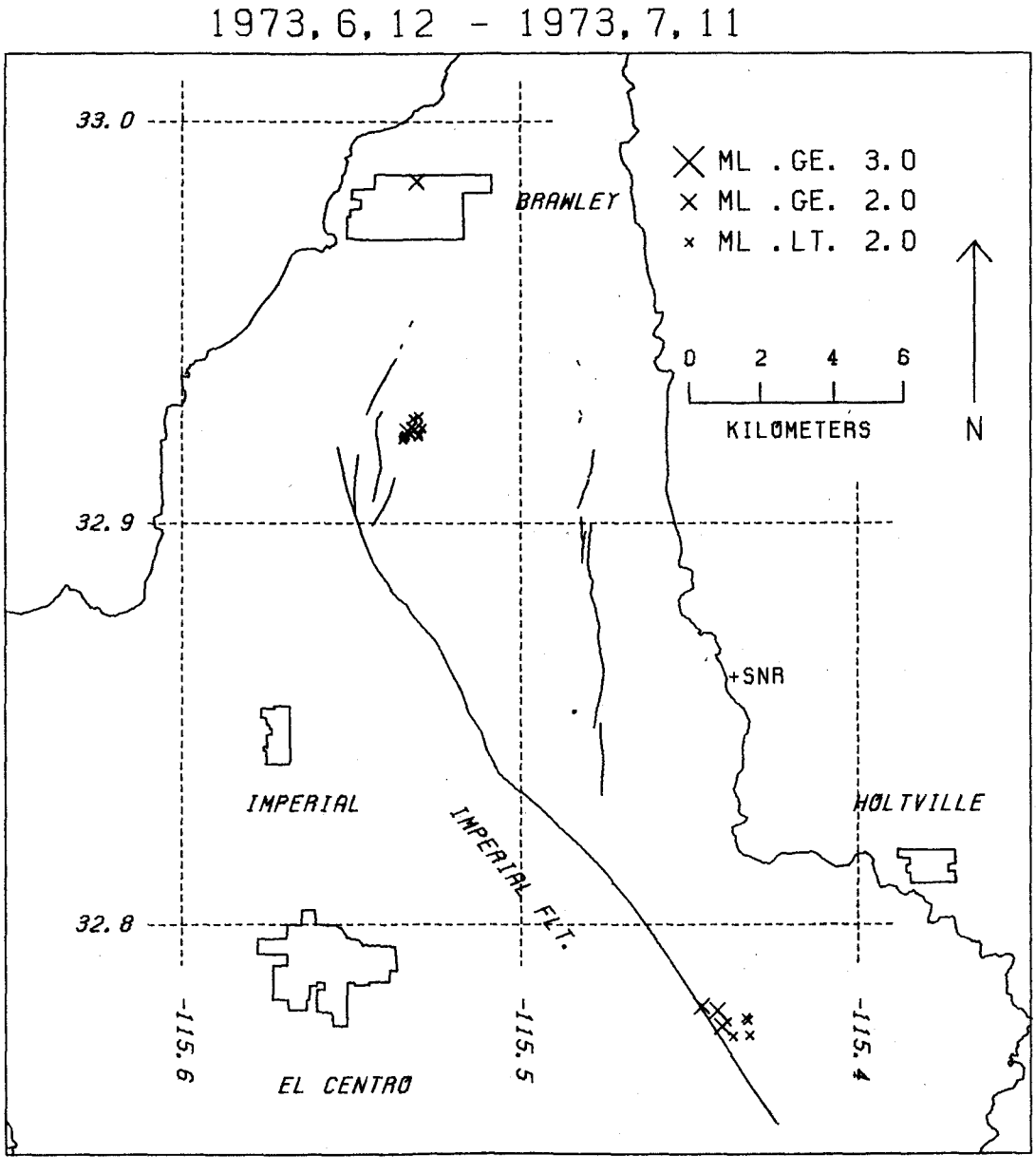

Figure 32. Map showing the distribution of all "A", "B", and "C" quality epicenters (plus signs proportional to magnitude) for events associated with the 73 JUN swarm sequence on the Imperial Trend. The 1940 surface faulting and the ground breakage associated with the 75 JAN sequence on the Brawley Trend are shown for reference.

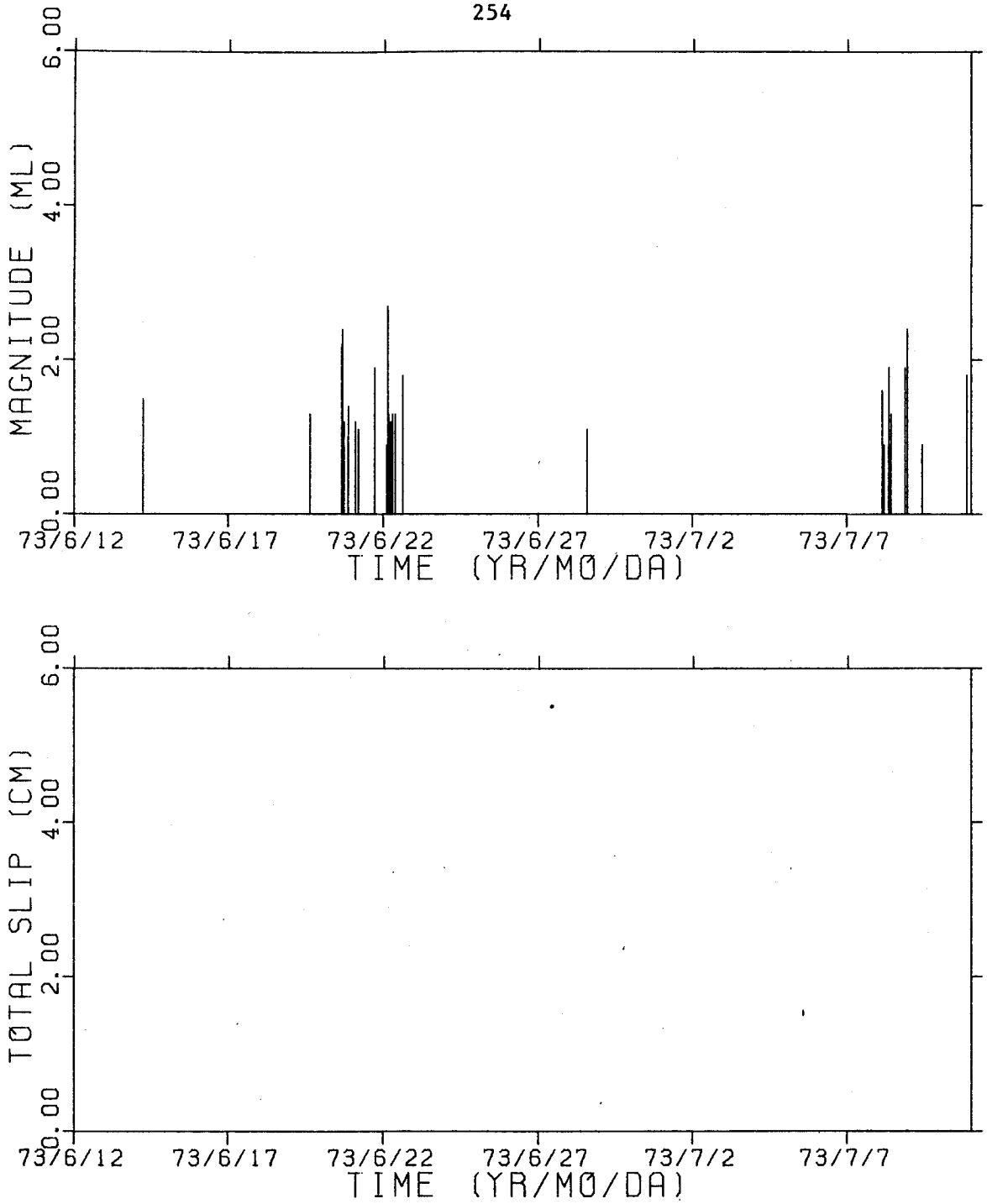

Figure 33. Two time-series representations illustrating the development of the 73 JUN swarm sequence. In the upper frame events are represented by vertical iines proportional to magnitude and plotted at the origin time. The lower frame shows accumulated moment plotted as proportional slip on a 33 km^2 fault. A common vertical scale used for comparison of the five Imperial Trend sequences studied resulted in the 73 JUN moment plot being indistinguishable from the time axis.

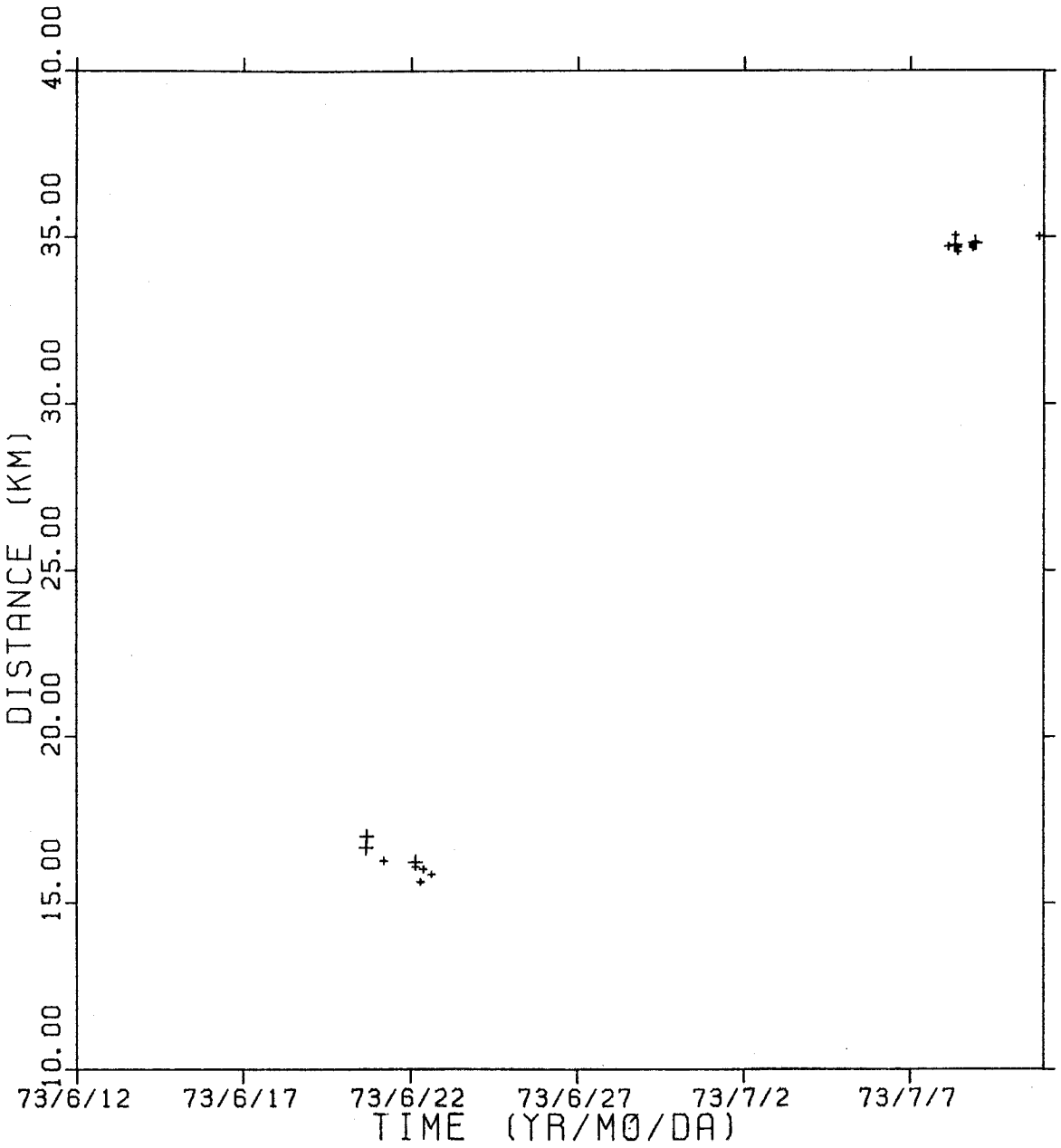

Figure 34. Time-distance scatter plot showing the spatio-temporal relationship among the discrete swarms comprising the 73 JUN swarm sequence along the Imperial Trend. Symbol size is proportional to magnitude.

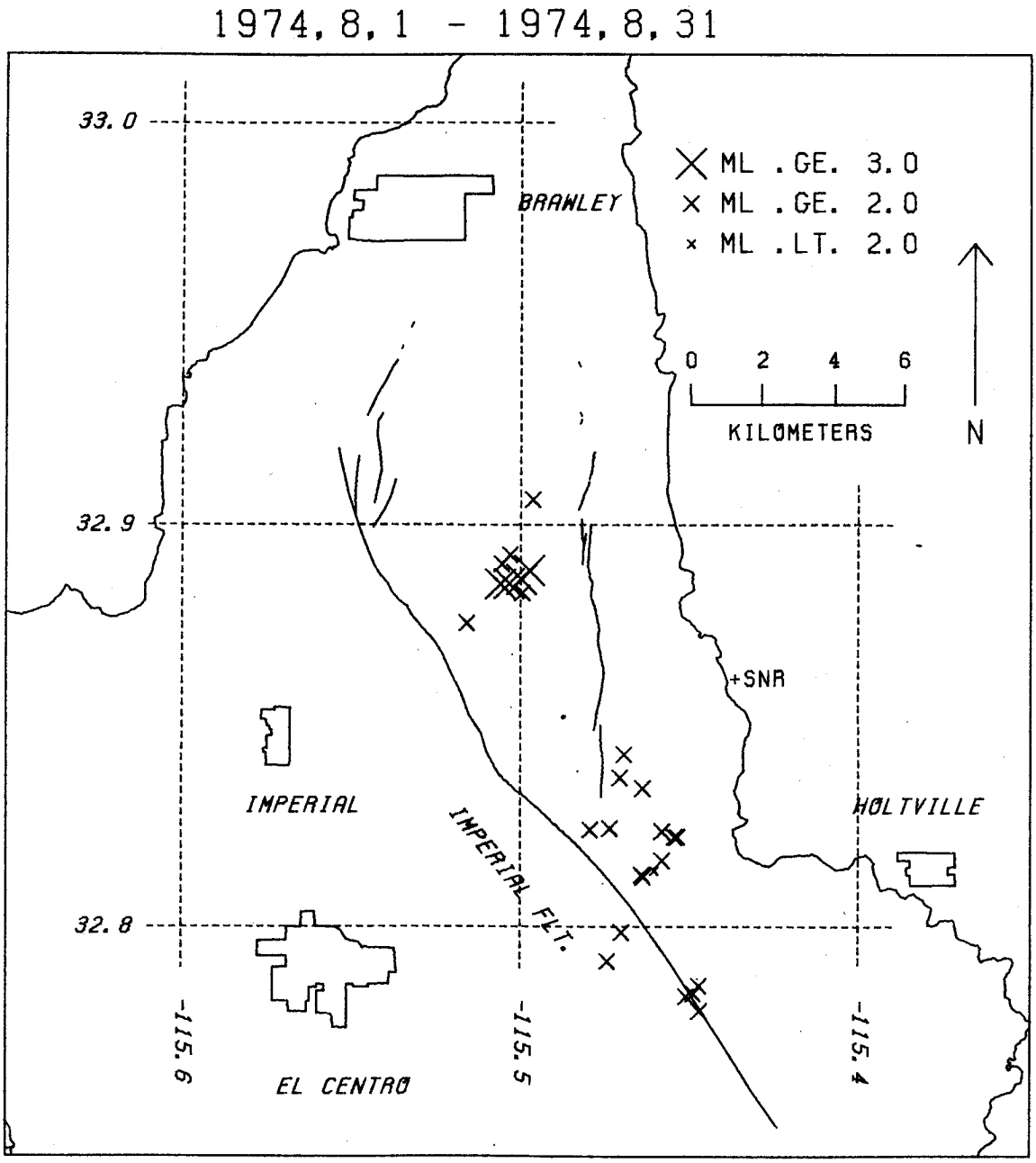

Figure 35. Map showing the distribution of all "A", "B", and "C" quality epicenters (plus signs proportional to magnitude) for events associated with the 74 AUG swarm sequence on the Imperial Trend.

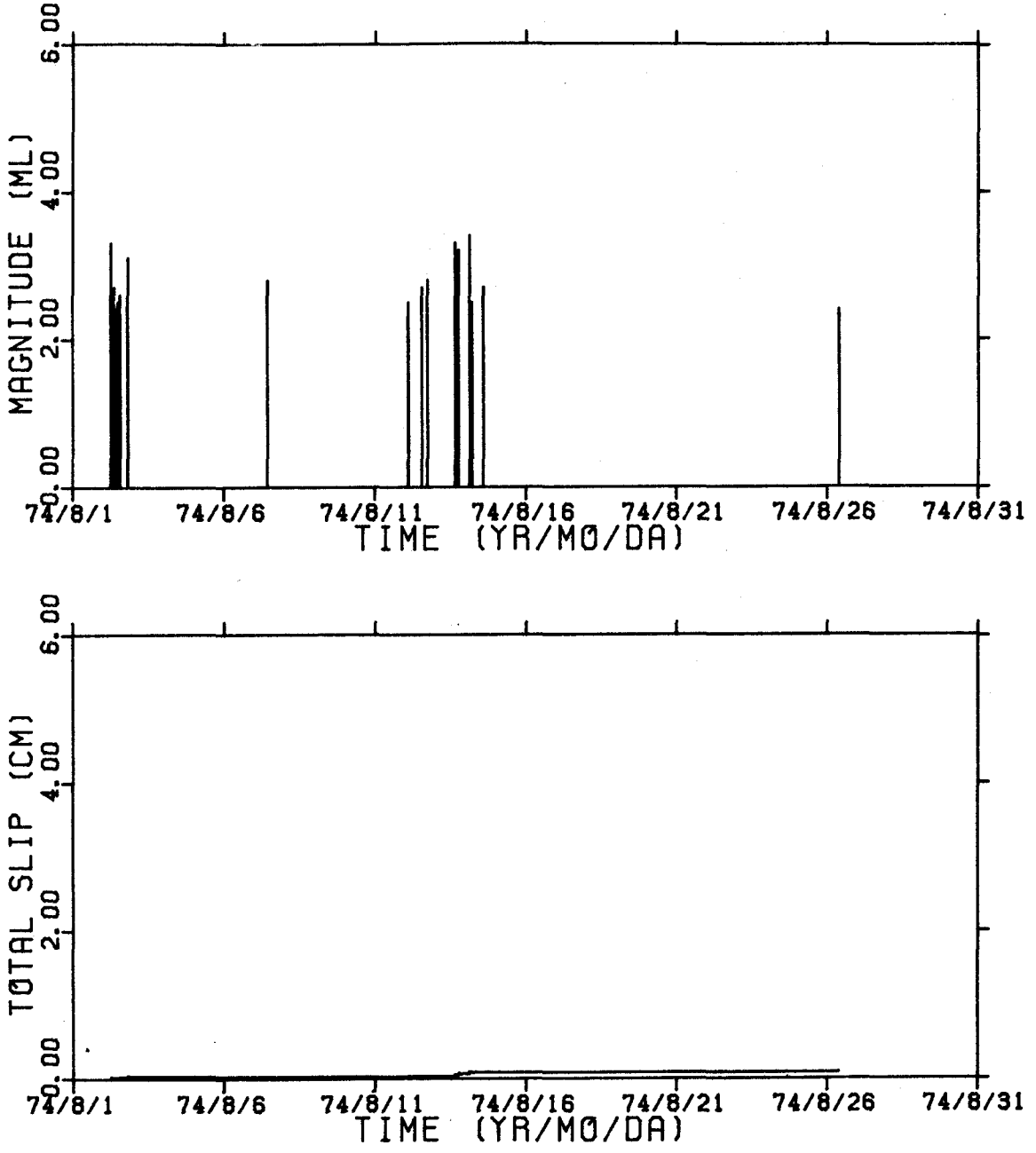

Figure 36. Two time-series representations illustrating the development of the 74 AUG swarm sequence. In the upper frame events are represented by vertical lines proportional to magnitude and plotted at the origin time. The lower frame shows accumulated moment plotted as proportional slip on an arbitrary 33 km^2 fault.

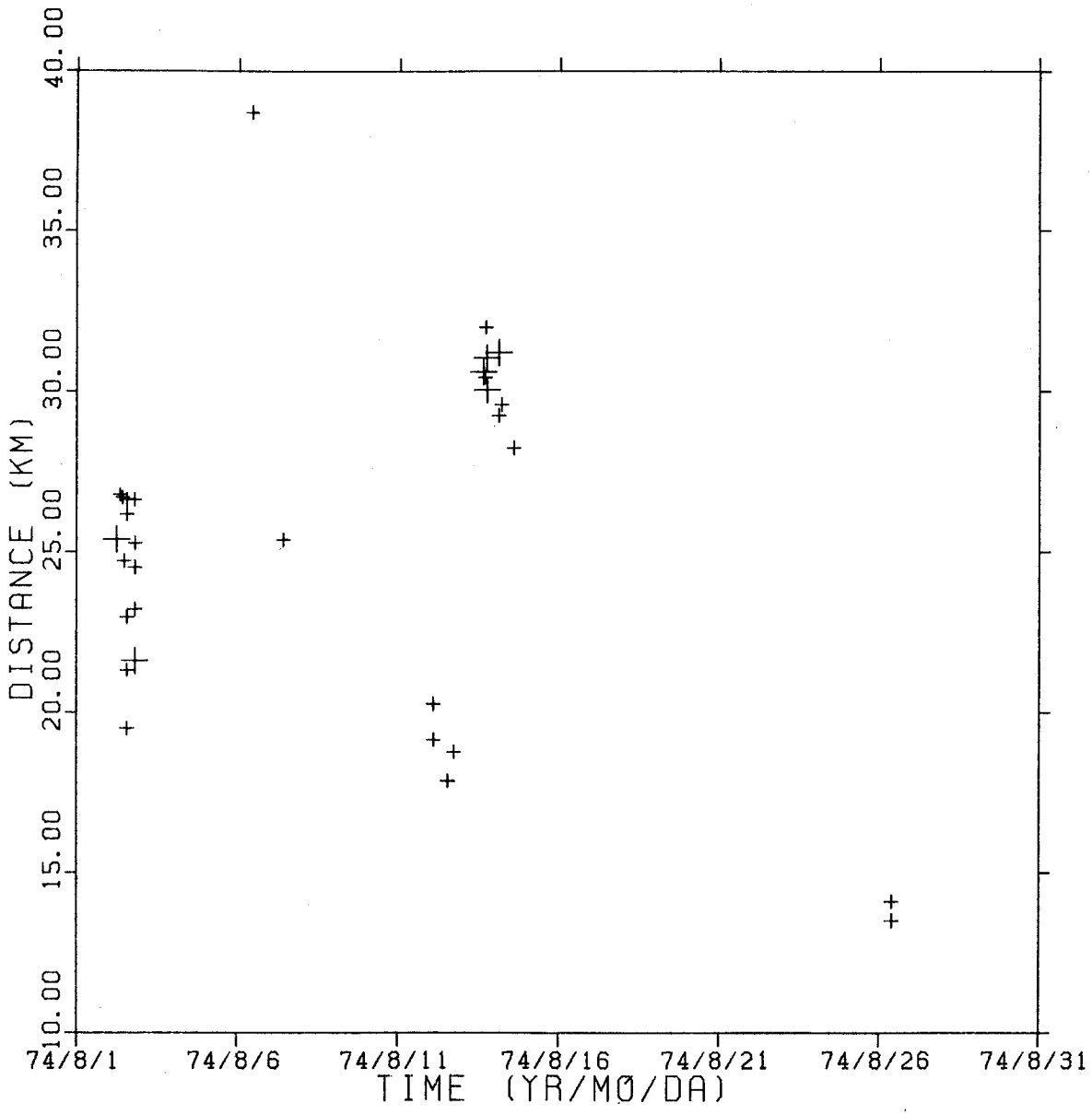

Figure 37. Time-distance scatter plot showing the spatio-temporal relationship among the discrete swarms comprising the 74 AUG swarm sequence along the Imperial Trend. Symbol size is proportional to magnitude.

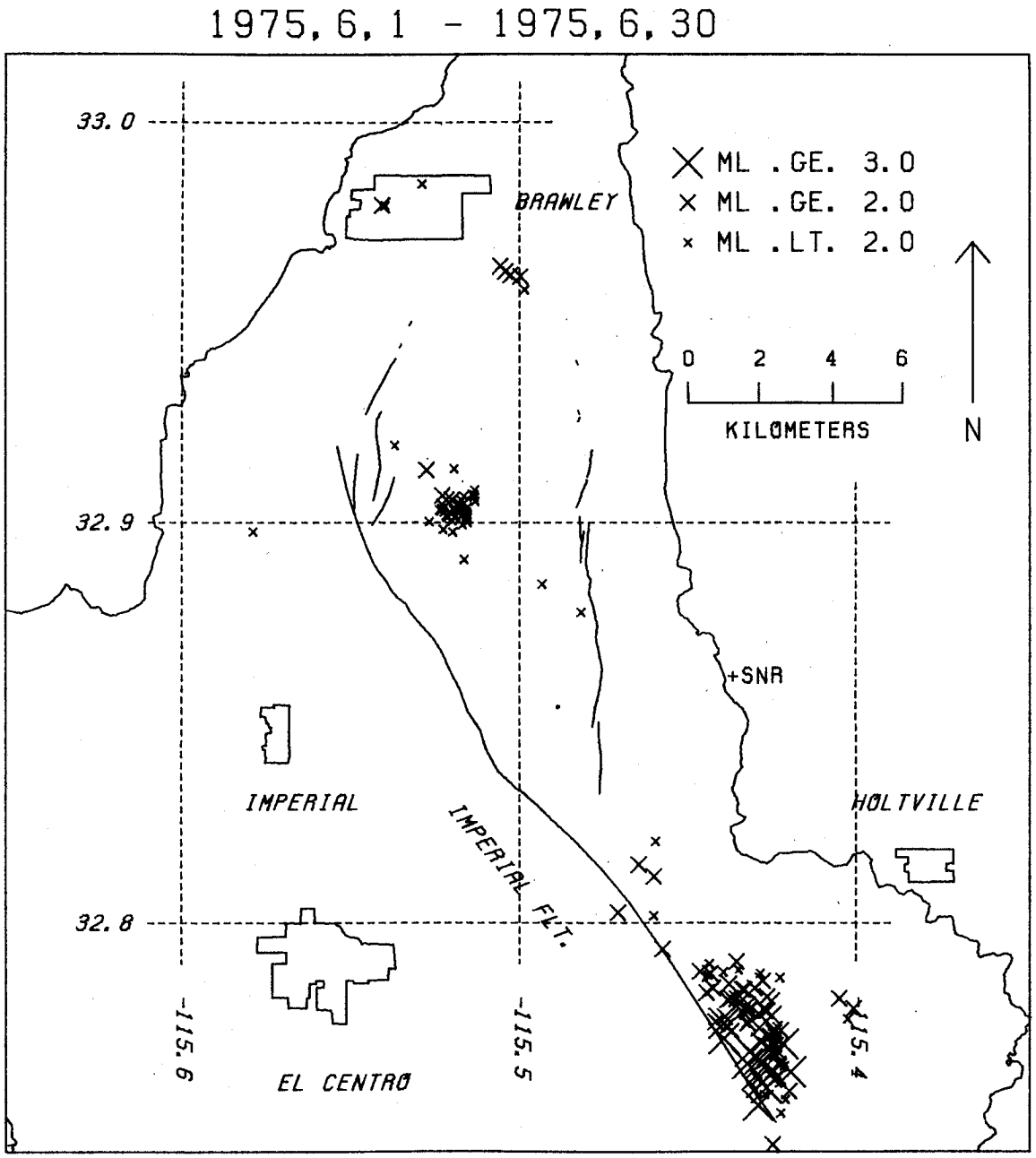

Figure 38. Map showing the distribution of all "A", "B", and "C" quality epicenters (plus signs proportional to magnitude) for events associated with the 75 JUN swarm sequence on the Imperial Trend.

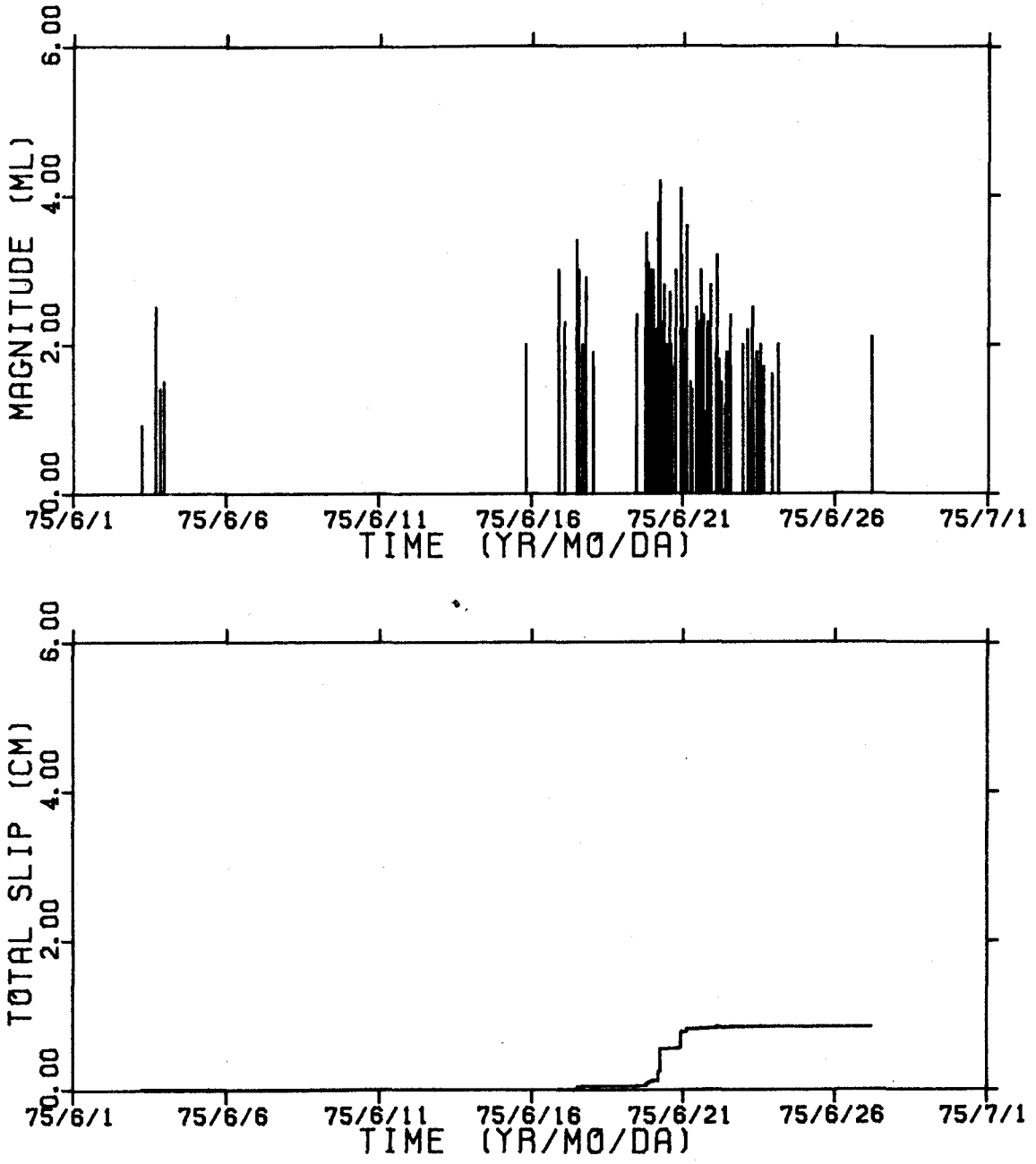

Figure 39. Two time-series representations illustrating the development of the 75 JUN swarm sequence. In the upper frame events are represented by vertical lines proportional to magnitude and plotted at the origin time. The lower frame shows accumulated moment plotted as proportional slip on an arbitrary 33 km^2 fault.

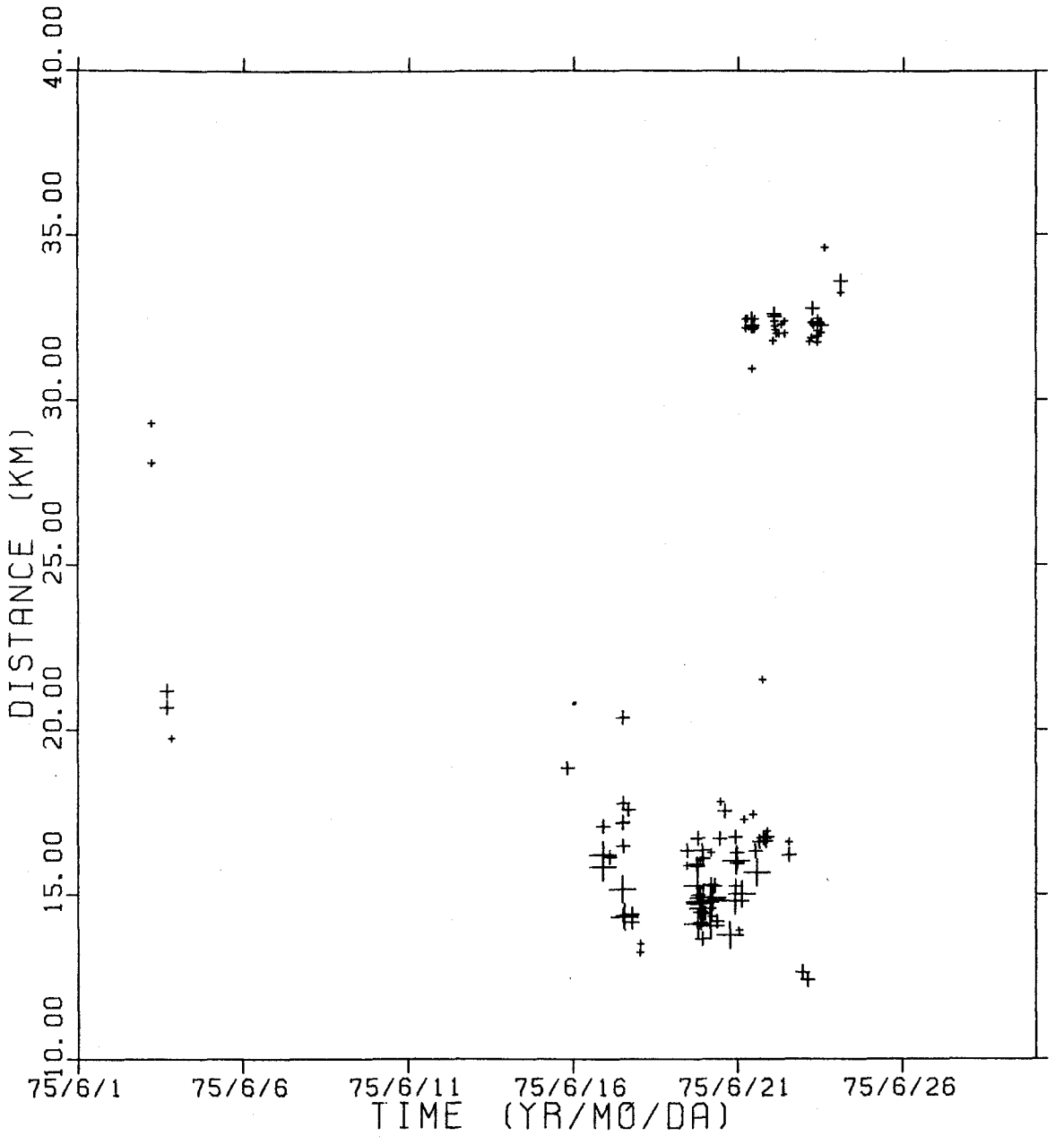

Figure 40. Time-distance scatter plot showing the spatio-temporal relationship among the discrete swarms comprising the 75 JUN swarm sequence along the Imperial Trend. Symbol size is proportional to magnitude.

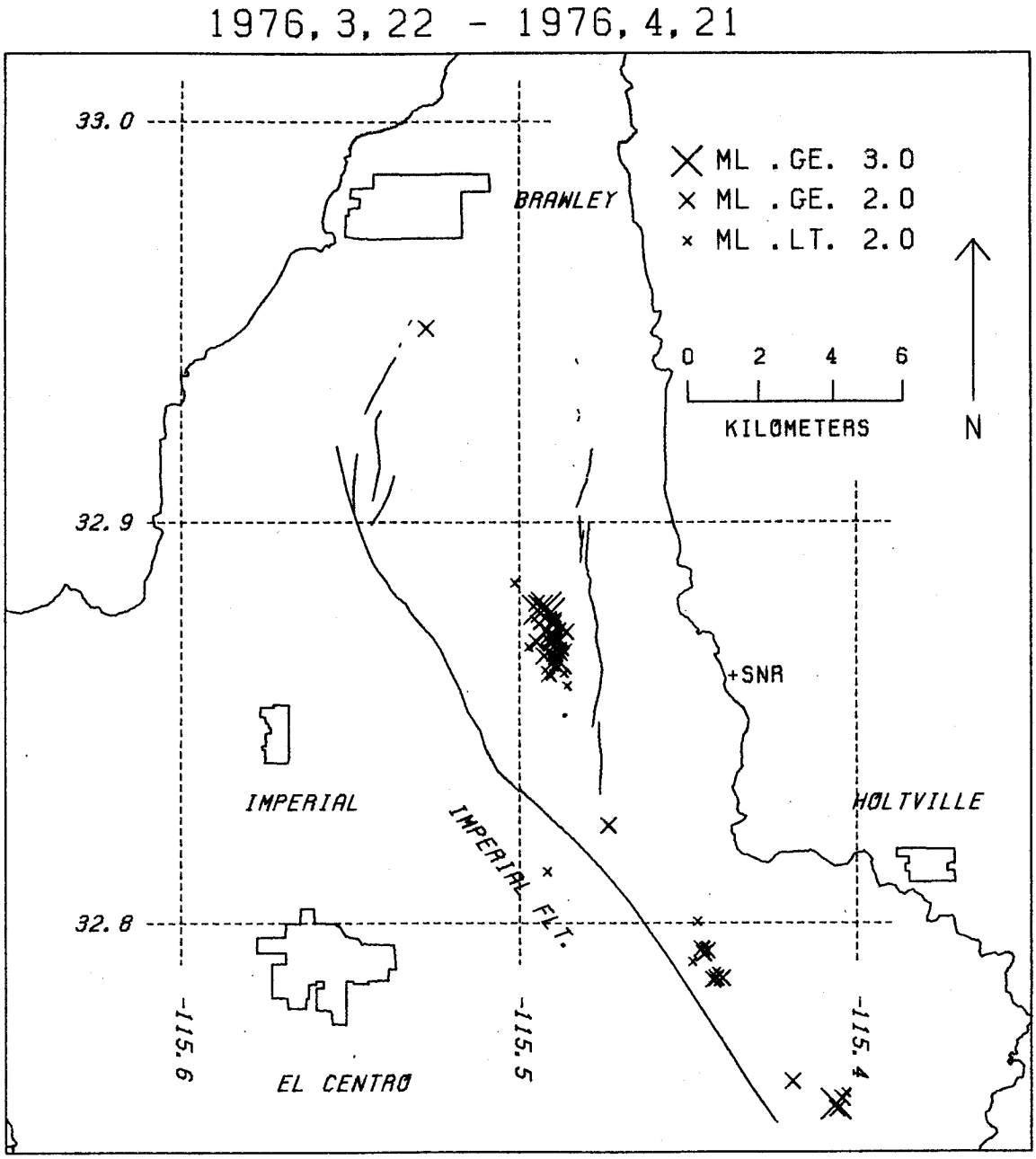

Figure 41. Map showing the distribution of all "A", "B", and "C" quality epicenters (plus signs proportional to magnitude) for events associated with the 76 MAR swarm sequence on the Imperial Trend.

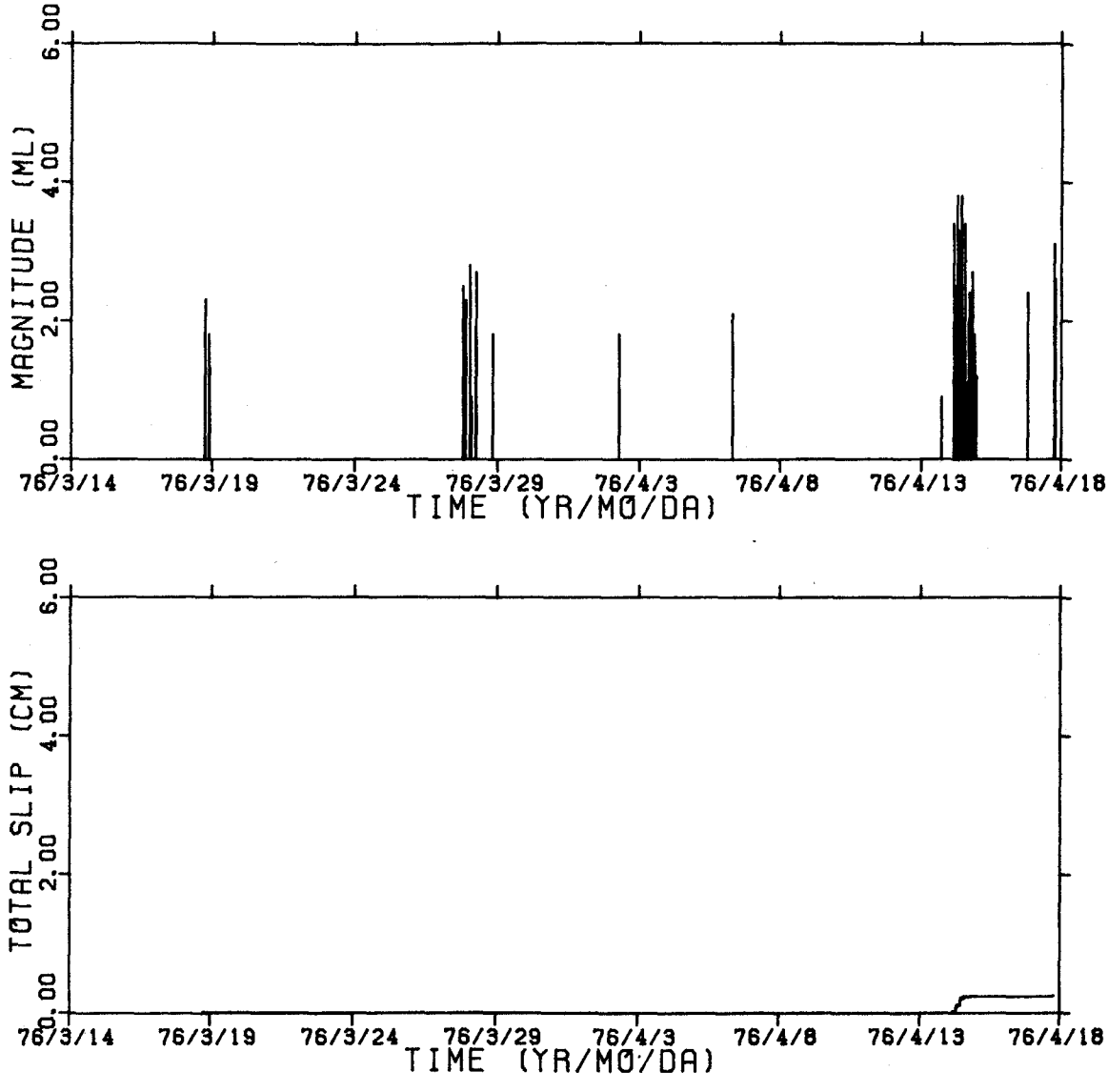

Figure 42. Two time-series representations illustrating the development of the 76 MAR swarm sequence. In the upper frame events are represented by vertical lines proportional to magnitude and plotted at the origin time. The lower frame shows accumulated moment plotted as proportional slip on an arbitrary 33 km^2 fault.

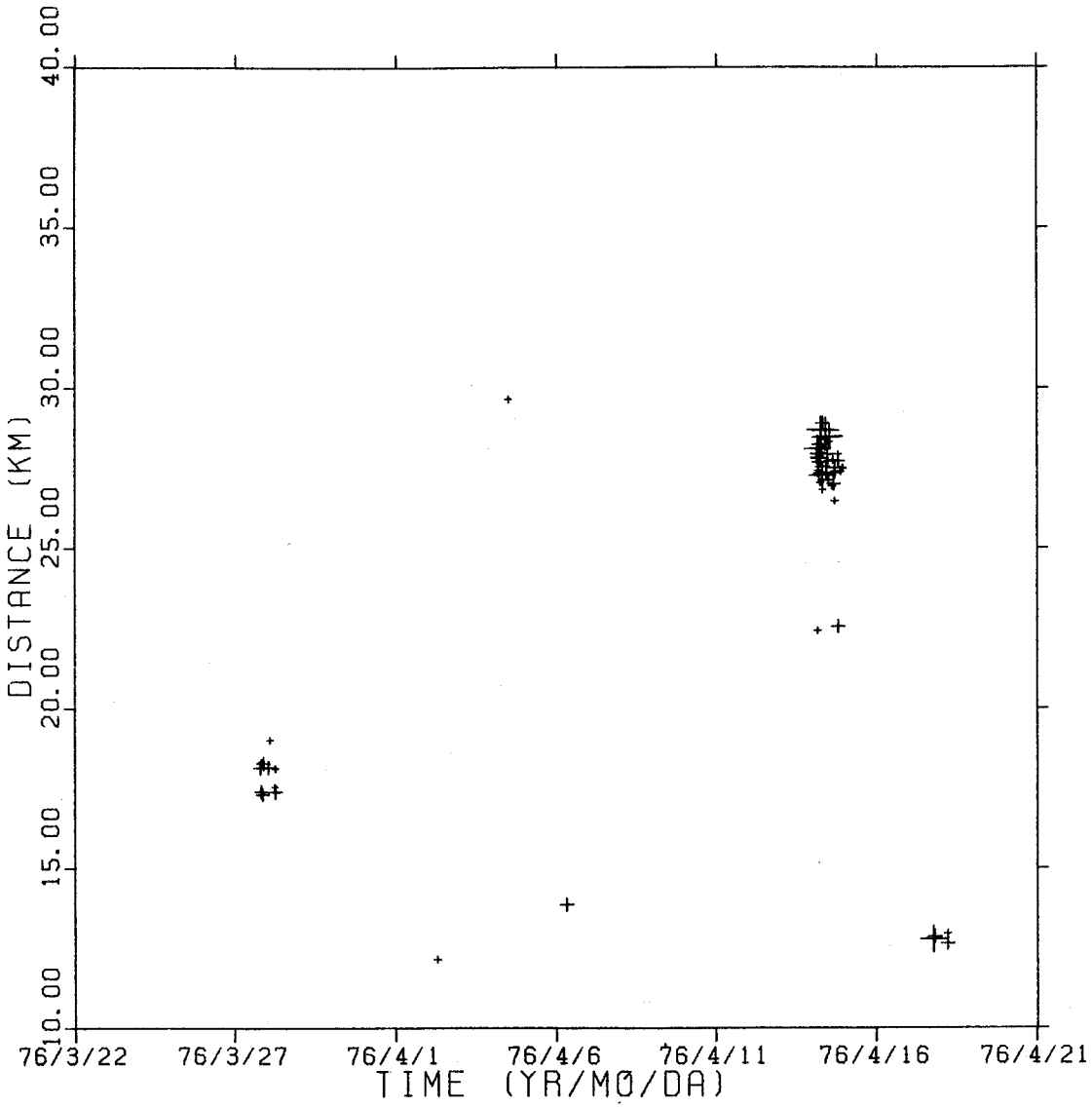

Figure 43. Time-distance scatter plot showing the spatio-temporal relationship among the discrete swarms comprising the 76 MAR swarm sequence along the Imperial Trend. Symbol size is proportional to magnitude.

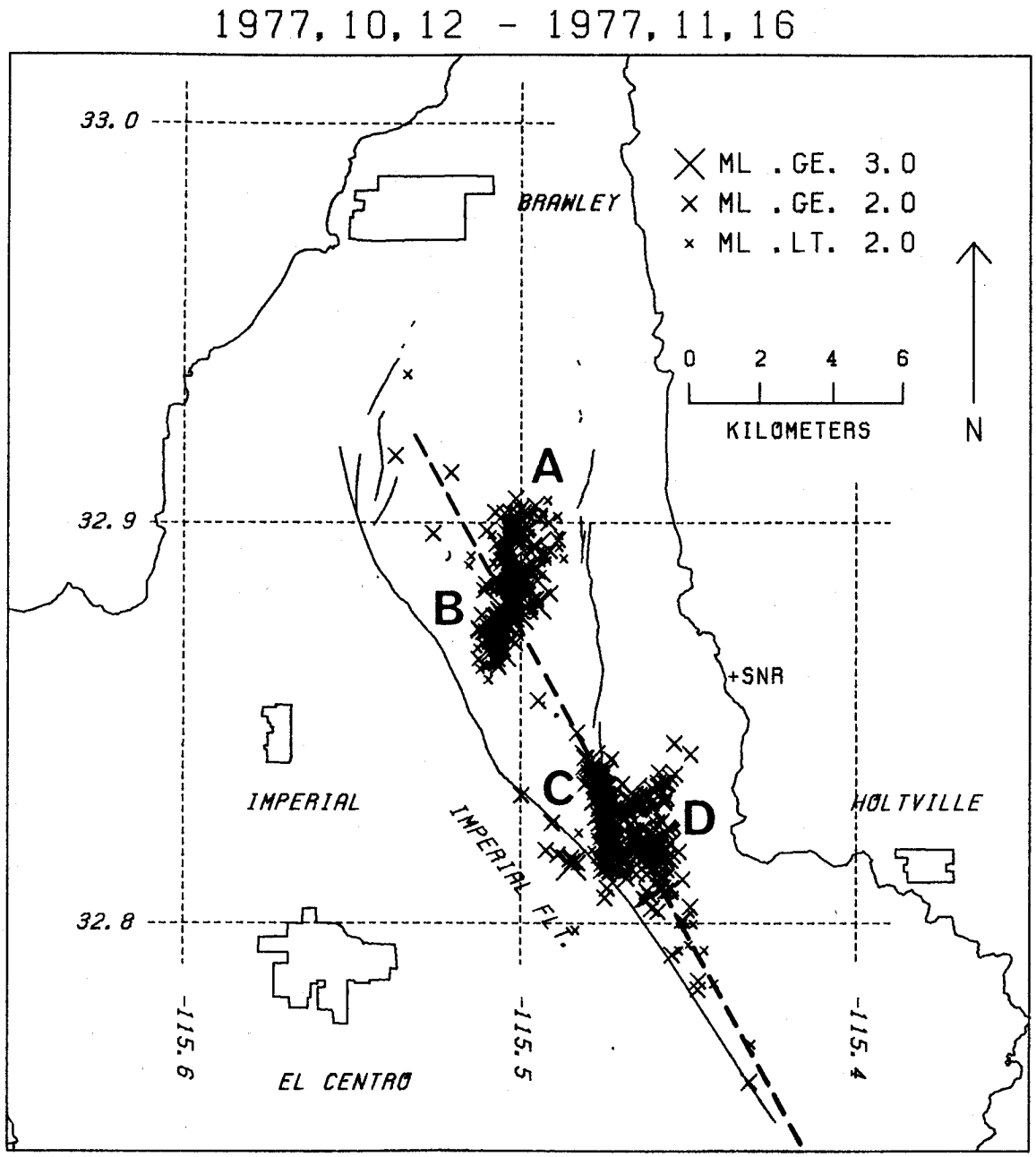

Figure 44. Map showing the distribution of all "A", "B", and "C" quality epicenters (plus signs proportional to magnitude) for events associated with the 77 OCT swarm sequence on the Imperial Trend. The individual swarms comprising this sequence are labeled A through D in order of occurrence. The dashed line represents the intersection with the free surface of the sub-surface plane of the Imperial Fault as suggested by the hypocentral distributions of all five Brawley Trend sequences.

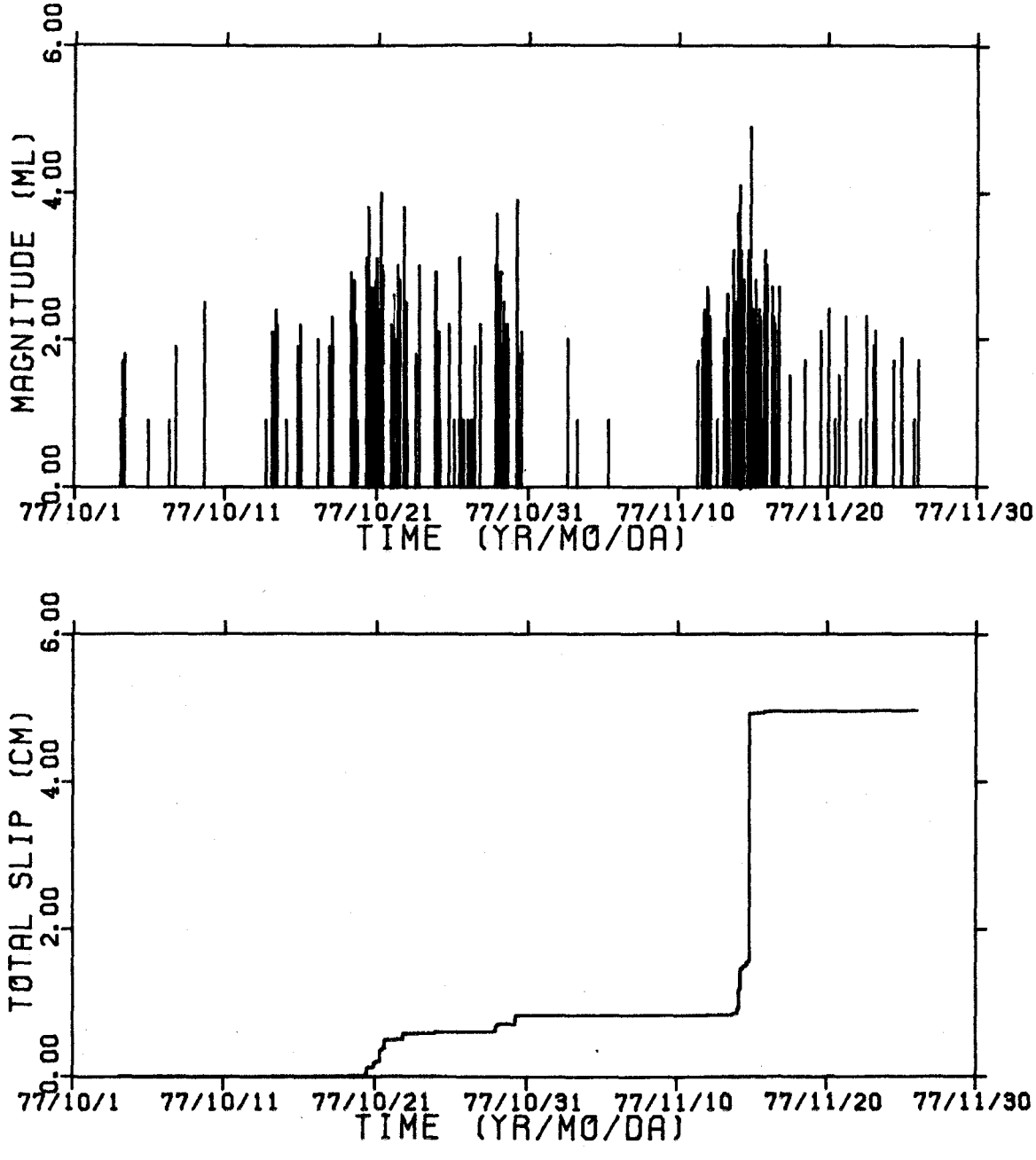

Figure 45. Two time-series representations illustrating the development of the 77 OCT swarm sequence. In the upper frame events are represented by vertical lines proportional to magnitude and plotted at the origin time. The lower frame shows accumulated moment plotted as proportional slip on an arbitrary 33 km^2 fault.

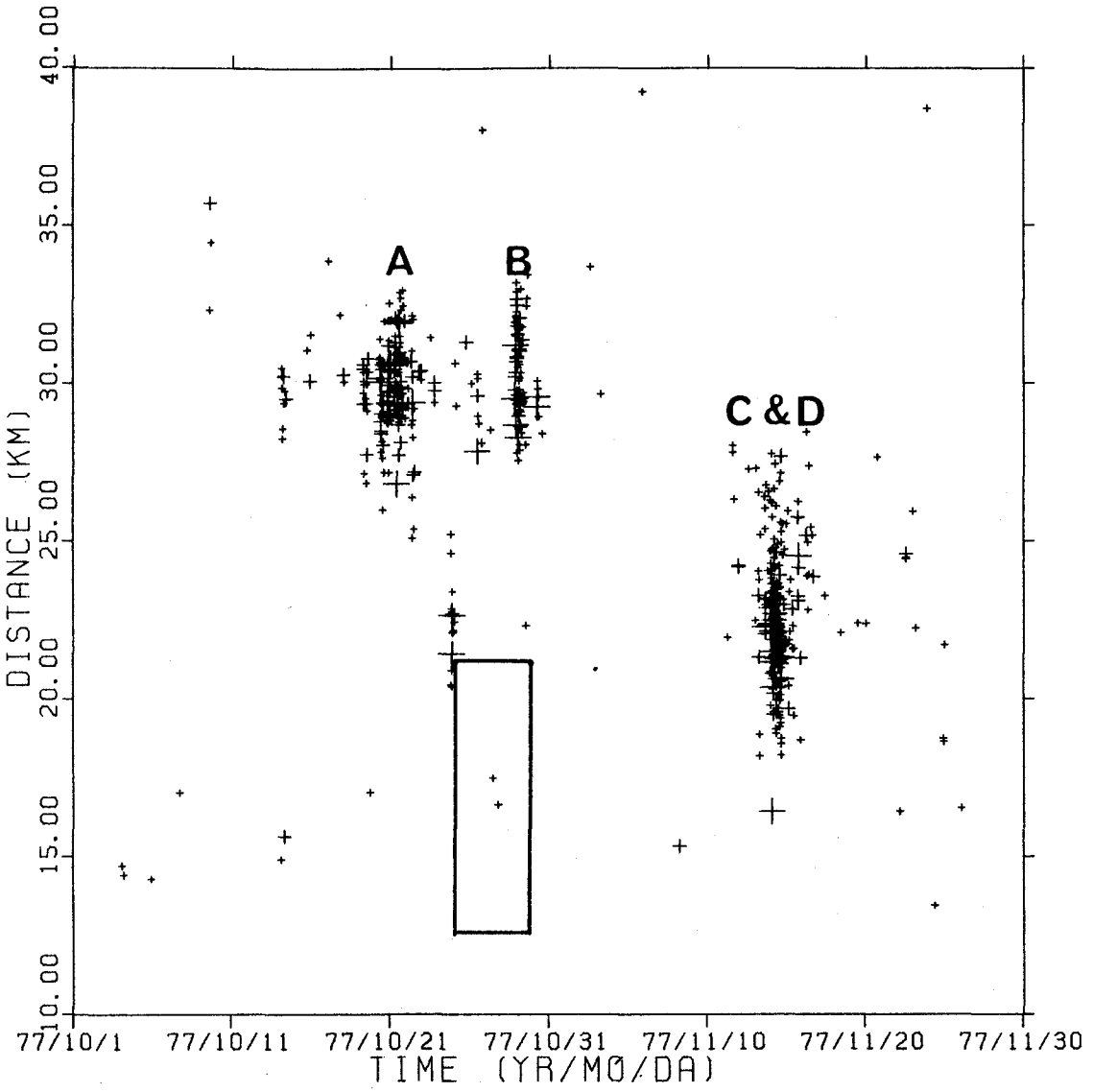

Figure 46. Time-distance scatter plot showing the spatio-temporal relationship among the discrete swarms comprising the 77 OCT swarm sequence along the Imperial Trend. Symbol size is proportional to magnitude. The individual swarms comprising this sequence are labeled A through D in correspondence with Figure 44. Unsuccessful attempt to predict the onset of related activity along the southern portion of the Imperial Trend.

Brawley trend.

The third figure in each of the five sets consists of a time-distance scatter plot along the Imperial trend where distance is measured from the Imperial trend reference point in Figure 1. The time axis covers the same period as the associated epicentral plot. The time span in each case is one month, with the exception of the last sequence (Figure 45), where two months are plotted.

The time-distance plots point out many of the similarities of swarms on the Imperial trend as compared to those on the Brawley trend. Again one sees individual swarms of earthquakes, highly localized in space and time, with individual clusters distributed along a northwest trend. There is ample evidence for the progressive activation of these clusters along the proposed trend. Plotted in this manner, it appears that swarm sequences along the Imperial trend are constituted of from 2 to 5 discrete event clusters. The concept of swarm pairs discussed by Johnson (1977, 1978) appears to be something of an over-simplification, although the swarm sequences do tend to be dominated by relatively large swarms at their limits of propagation. Occasionally, as in the case of the August 1974 sequence (Figure 37) and the June 1975 sequence (Figure 40), these terminating swarms are preceded by event clusters at intervening distances. For each of the five sequences studied, the two terminating swarms tend to be comparable in size, bracketing a common section of the Imperial trend near a distance of 25 km. The smallest swarms occurred as part of the June 1973 sequence with the greatest spatial separation, whereas the largest swarms, associated with the most recent sequence, were also

the least separated. Consequently, a model for the generation of earthquakes swarms must provide some mechanism for transmitting amplitude information along the Imperial trend. The manner in which amplitude information is transmitted appears to be such that for higher amplitudes the probability of precipitating a swarm at an early stage in propagation is enhanced. Thus, larger swarms would be expected to occur closer together. Further, it appears that once a swarm has been triggered along the Imperial trend, local conditions change such that the reactivation within a span of a few years is inhibited.

We can interpret these observations as evidence for the activation of swarms by a physical disturbance propagating along the Imperial Fault. Propagation appears to be bilateral from a point of initiation approximately due west of Holtville near where the apparently creep-related surface cracks mapped by Sharp (1976) after the January 1975 swarm sequence on the Brawley trend merged with the surface trace of the 1940 El Centro earthquake. This is simply a restatement of our conjecture that Imperial Valley swarms are but a part of a more pervasive physical process lasting for several weeks. If this interpretation is correct, then the five swarms sequences examined share a limited range of propagation rates from about .2 to .4 km/day. In the following section we will present the case for identifying this physical process as fault creep propagating along the plane of the Imperial Fault at depth.

The tendency for larger swarms to be more closely spaced can be explained if the probability of generating a swarm is enhanced for

higher amplitudes. If, as we suppose, the propagating disturbance is buried fault creep, then the amplitude information is presumably carried in the displacement amplitude of the creep events. The local probability for generating an earthquake swarm would then grow with the intensification of the stress field for larger creep events.

The box in Figure 46 represents at attempt to predict the second of a pair of terminal swarms. This prediction was predicated on the observation that in each of the preceding sequences significant swarm activity at one end of the active section of the Imperial trend was preceded by activity at the other. Clearly this prediction cannot be considered successful. On the other hand, the concept that swarms are part of a more extensive swarm sequence with coherent properties that can be anticipated was strongly supported.

October 1977 Sequence

We can now consider the set of observations relating to the details of the structures along the Imperial trend activated during swarms. For the Brawley trend these structures in many, if not all, instances appeared to be east-northeast striking transverse faults. Similar results are obtained for the Imperial trend, although in this case the transverse structures seem to be vertical faults oriented approximately due north. The observational support for this assertion comes from a study of the October 1977 swarm sequence. This sequence was selected for a particularly detailed analysis because of the availability of relatively high accuracy timing data from the CEDAR system discussed in Chapter 1. This data set permits a degree of

relative depth control that cannot be approached conveniently with data from earlier sequences.

The hypocentral distribution obtained in this analysis is presented in a series of stereo pairs in Figures 47 through 67. The viewpoint is 275 km above the point 32°24'N, 115°33'W. Irregular consecutive time intervals were chosen to encompass discrete bursts of seismicity. As evidenced by the stereo pairs, these bursts are associated with spatially highly localized activity. The cultural details, scale referents, implied faults, and point of view are identical to those shown in Figures 12 through 21 for the January 1975 sequence on the Brawley trend. The only additional feature of the current series is the inferred sub-surface position of the Imperial fault.

An attempt to infer the sub-surface location of the Imperial fault was made necessary by our interest in mechanisms that could couple a disturbance propagating along the Imperial trend with swarm activity on transverse structures. This problem was approached by considering the spatial distribution of the origin points for isolated clusters from the 5 swarm sequences studied in detail. Origin points were obtained as the median hypocenters of the first three or four well-located events initiating each cluster The resulting locations, shown in Figure 47, lie remarkably close to a vertical plane (also shown), which we suggest represents the sub-surface position of the Imperial fault. The strike of this plane agrees with that of the surface trace farther south. Apparently as the surface break approached Mesquite Lake it veered somewhat to the

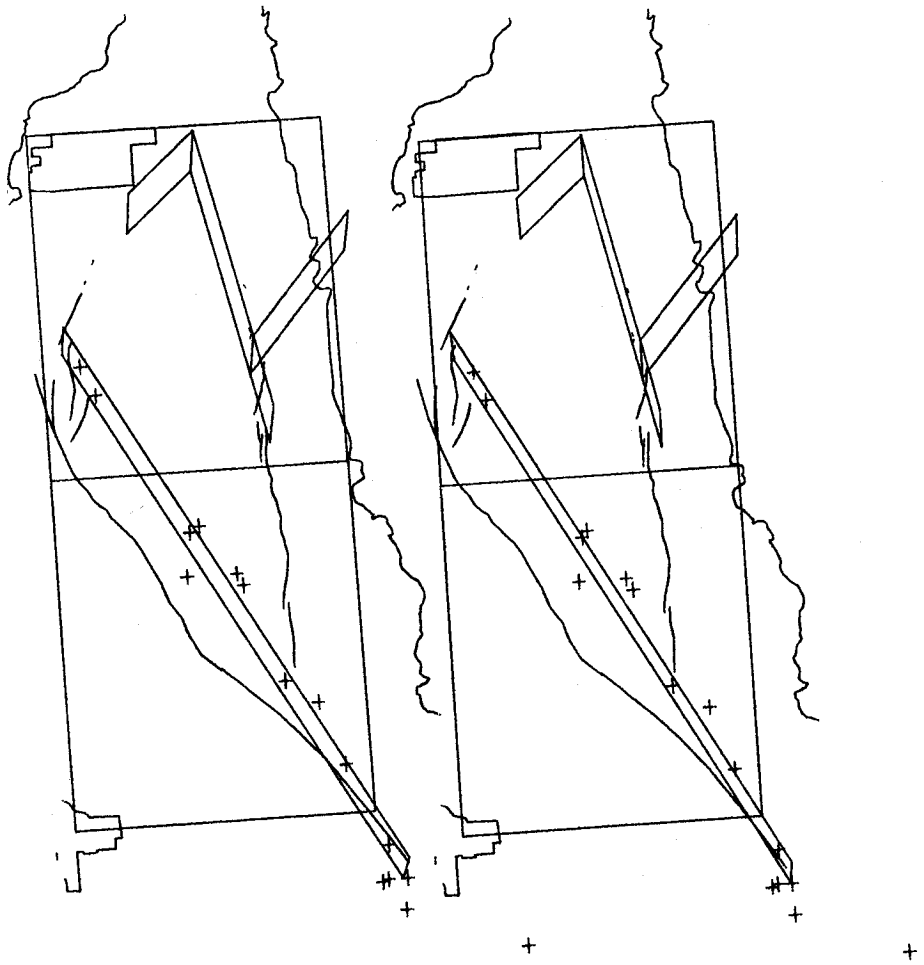

Figure 47. Stereo view showing the distribution of the median initiation points for all significant discrete swarms comprising the 5 sequences on the Imperial Trend studied in detail. This distribution was used to define the sub-surface expression of the Imperial Fault (also shown). Cultural referents include the community of Brawley and the New River (upper left), the Alamo River (upper right), and El Centro (lower left). Both the 1940 surface faulting and the faulting associated with the 75 JAN Brawley Trend sequence are shown. A reference grid, with sides of 0.1°, is plotted at a depth of 6 km. These features are repeated in Figures 49 through 67. The view is from a point 275 km above 32°24'N, 115°33'W.

west and then back to the east, ending in a series of northeast-trending splays, while maintaining a relatively straight course at depth. Once located in this manner it was surprising to discover that what we infer to be the sub-surface expression of the Imperial fault can be seen on an epicentral map of "A" quality events (Chapter 4, Figure 5) as a narrow lineation of epicenters. Apparently small swarms and background seismicity are occurring close to the plane of the Imperial Fault at depth. The Imperial fault, together with the fault structures inferred for the January 1975 swarm, define a crustal block. The active subsidence of this block is forming the closed depression known as Mesquite Lake.

The spatial distribution of hypocenters for the October 1977 sequence is shown in Figure 48. The development of this distribution with time occurred in four discrete episodes. These stages of development are labeled "A" through "D" in Figures 44 and 46, in order of occurrence. The intersection of the sub-surface Imperial fault with the free surface is shown in Figure 44 as a broken line sub-parallel to the 1940 surface break. While only two spatially separated clusters are apparent in the figures, the stereo pairs demonstrate that each of these developed as two discrete sub-clusters separated from each other by the plane of the Imperial fault. For the northern events this division is also evident in the time-distance plot, Figure 46. This is not as obvious for the southern events, most of which occurred during a burst of intense activity lasting less than 24 hours. The development of the October 1977 swarms was typical of other sequences along the Imperial trend

Figure 48. Stereo view showing all "A" quality hypocenters for the 77 OCT swarm sequence on the Imperial Trend.

in that activity commenced for each pulse of activity at a highly localized point near the Imperial fault plane, followed by progressive migration away from the Imperial fault along a north-south trend. In some respects the October 1977 swarm sequence behaved more like two swarm sequences. Previous sequences developed preferentially northeast of the Imperial trend for swarms along the northern half and southwesterly for those along the southern half. The October 1977 sequence was unusual in that development occurred on both sides of the fault along both the northern and southern sections. This behavior may be related to the intensity of the 1977 swarm sequence, which far exceeded any other in this area since the 1940 earthquake. With at least 43 events exceeding magnitude 3.0 and with eight of these in excess of 4.0, the October 1977 sequence was the only Imperial sequence comparable in size to the two large swarms on the Brawley trend in January 1975 and November 1976.

The development of swarm "A" from a small localized group of hypocenters can be followed in Figures 49 through 53. This sequence of figures, which begins on October 19, was preceded by a small swarm and minor activity beginning on October 14 (Figure 46). The epicenters are tightly clustered near the initiation point shown in Figure 49. They could not be included in a stereo pair since the nearest station, SNR, was out of operation and depth control was unobtainable. The tightly clustered activity for a protracted period early in the sequence make it similar to the January 1975 sequence on the Brawley trend, where shallow activity near the point of initiation continued for seven days. It would be interesting to know whether the

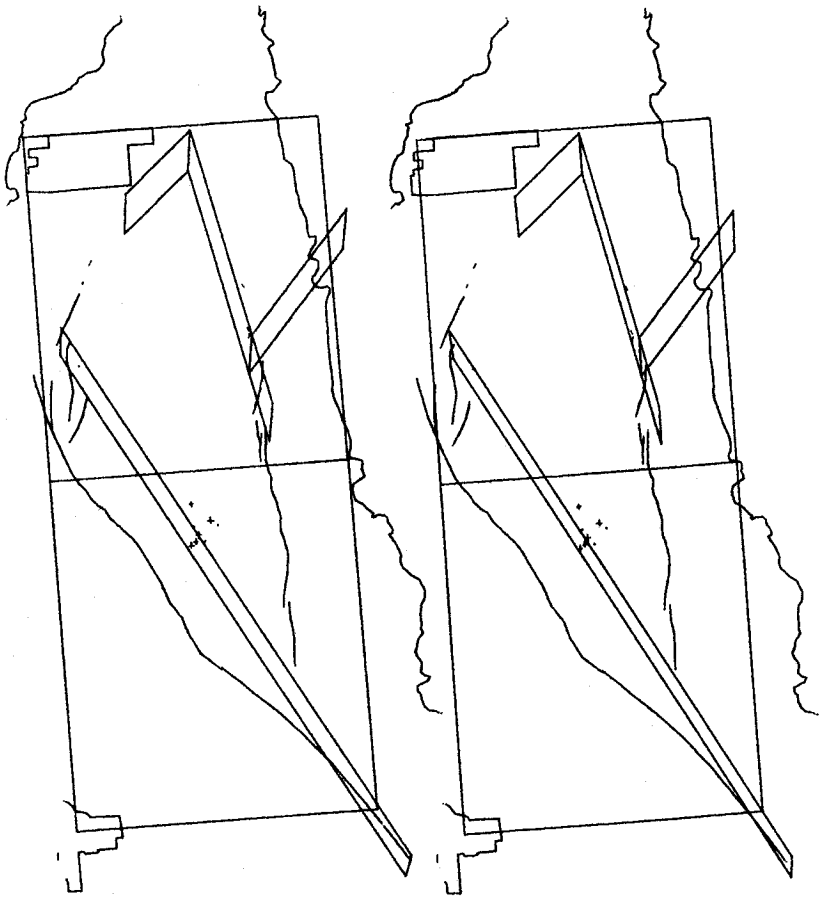

Figure 49. Stereo view showing all "A" quality hypocenters of the 77 OCT swarm sequence occurring during the period 19 October 00:00 through 20 October 9:00 GMT (33 hours). This initial, highly clustered activity was followed by rapid migration to the north.

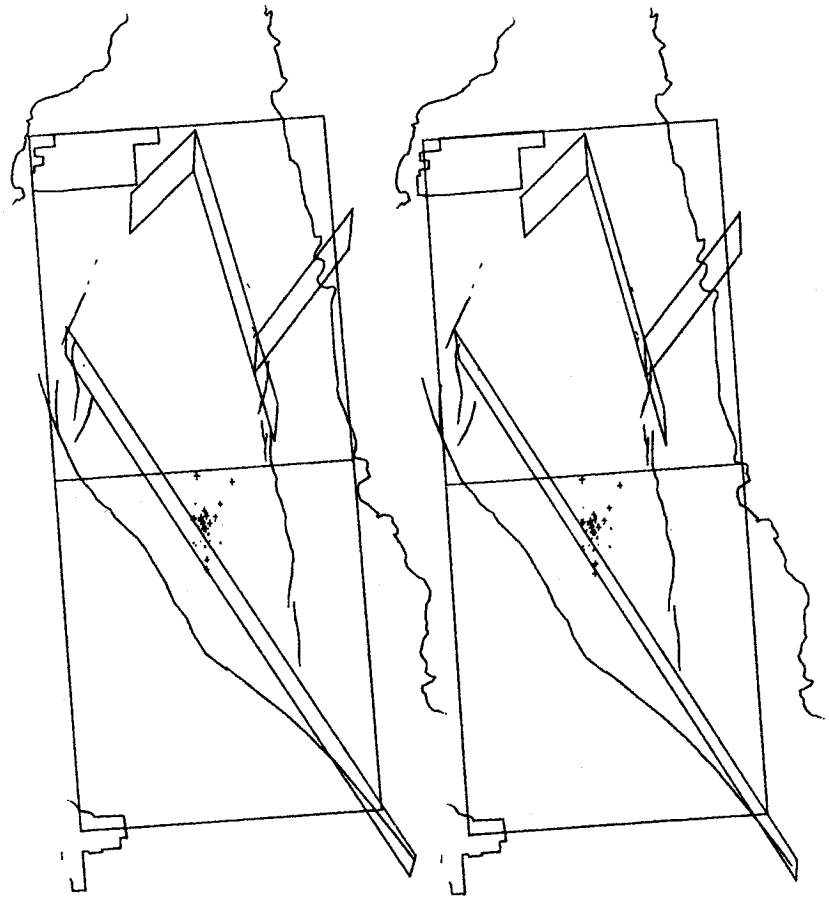

Figure 50. Stereo view showing all "A" quality hypocenters of the 77 OCT sequence occurring during the period 20 October 9:00 through 17:00 GMT (8 hours). Through Figure 67 events preceding the specified intervals are represented as single points to accentuate migrational phenomena.

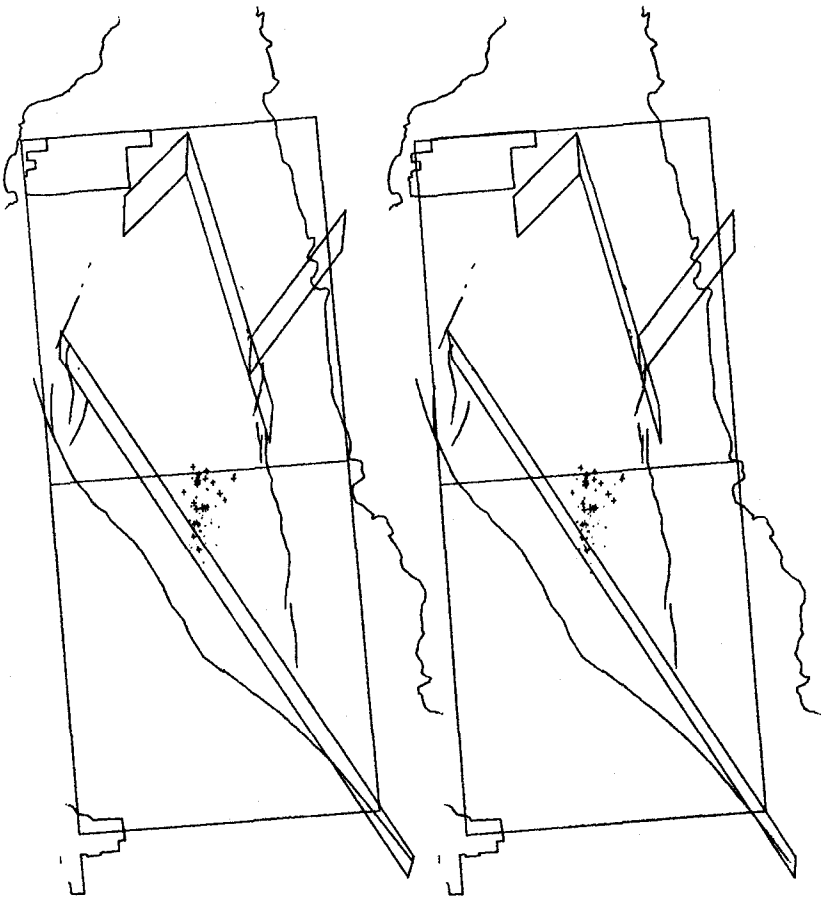

Figure 51. Stereo view showing all "A" quality hypocenters of the 77 OCT sequence occurring during the period 20 October 17:00 through 21 October 3:00 GMT (10 hours). Note that through Figure 53 most activity is associated with extension of the seismogenic volume leaving a wake of relative quiescence.

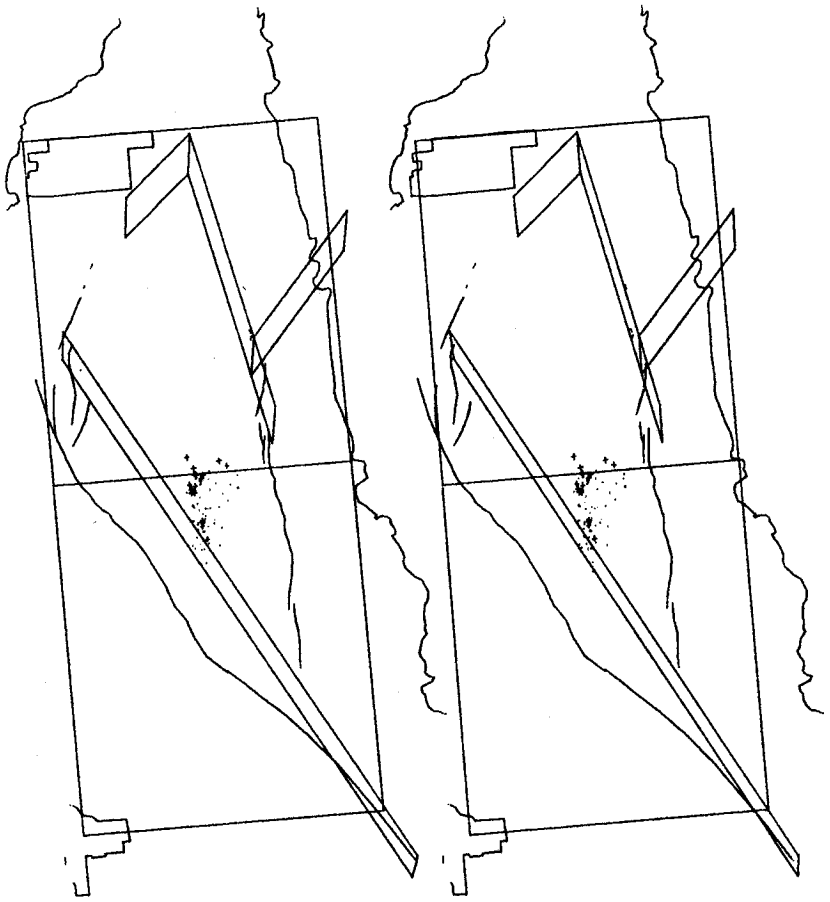

Figure 52. Stereo view showing all "A" quality hypocenters of the 77 OCT sequence occurring during the period 21 October 3:00 through 9:30 GMT (6.5 hours). The development of swarm A can be envisioned as a northward developing vertical fracture with attendant splay faulting to the northeast.

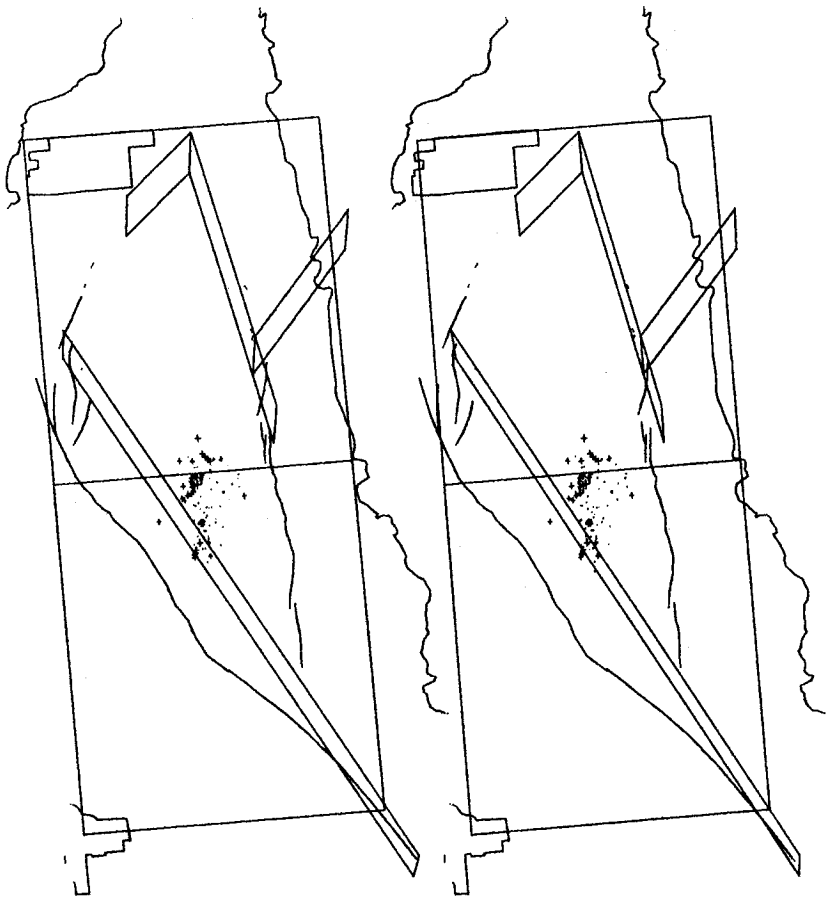

Figure 53. Stereo view showing all "A" quality hypocenters of the 77 OCT sequence occurring during the period 21 October 9:30 through 17:00 GMT (7.5 hours).

events precursory to the 1977 sequence were also shallower than those that followed.

The structures activated during the development of swarm "A" appear to be rather complex, although the progressive character of this process is clear from the figures. Our preferred interpretation calls for the northerly migration of activity along a north-south fault away from its intersection with the Imperial fault plane. Migration is accompanied by sympathetic failure on northeast-trending structures, similar to those of the January 1975 swarm, east of the developing fault. Although supported by focal mechanisms, this interpretation clearly pushes the limits of resolution and some readers may prefer any of a variety of possible local alternatives. The important observation, that development of this complex structure is progressive away from the Imperial trend, is unambiguous.

The earliest events that appear to be associated with swarm "B" southwest of the Imperial fault plane can be seen in Figures 53 and 54. This early activity was followed by seven days of very low seismicity (Figure 56) before the primary development of swarm "B" in Figures 57 and 58. Thus the seven days of minor activity followed by a short period of rapid progressive development mimics the development process of swarm "A". It seems likely that this similarity is significant. The structural complexity associated with swarm "B" is somewhat less than that for "A". A single vertical north-south plane with progressive development to the south is consistent with the observed distribution of hypocenters and their associated errors.

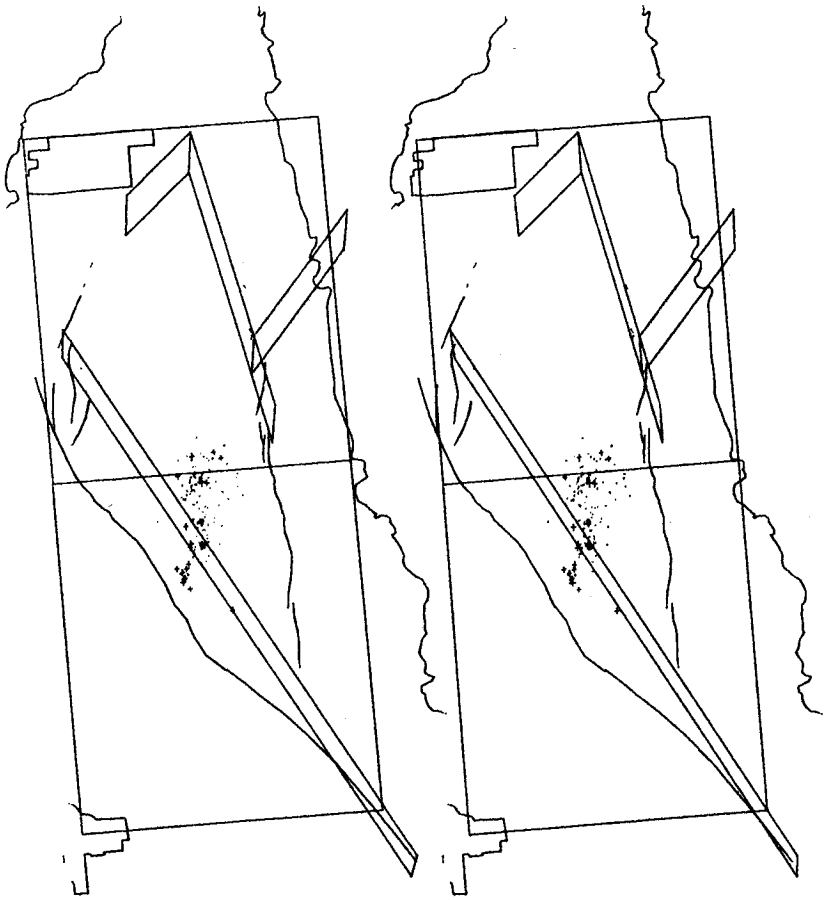

Figure 54. Stereo view showing all "A" quality hypocenters of the 77 OCT sequence occurring during the period 21 October 17:00 through 23 October 0:00 GMT (31 hours). Activity can be seen beginning in the area designated swarm "B". Further development of activity in this area, however was delayed for more than 10 days.

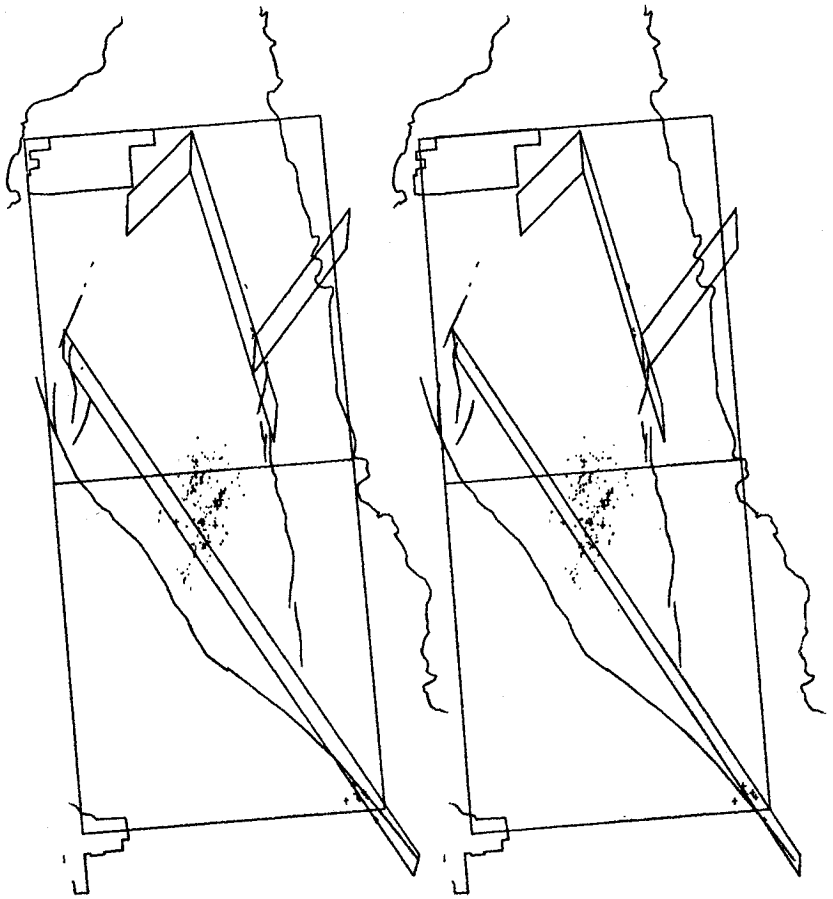

Figure 55. Stereo view showing all "A" quality hypocenters of the 77 OCT sequence occurring during the period 23 October 0:00 through 28 October 0:00 GMT (120 hours). Note the small cluster to the south in the area to become active in about 2 weeks. These events appear to be deeper than subsequent southern events of the 77 OCT sequence A marks the southern limit of migration as well.

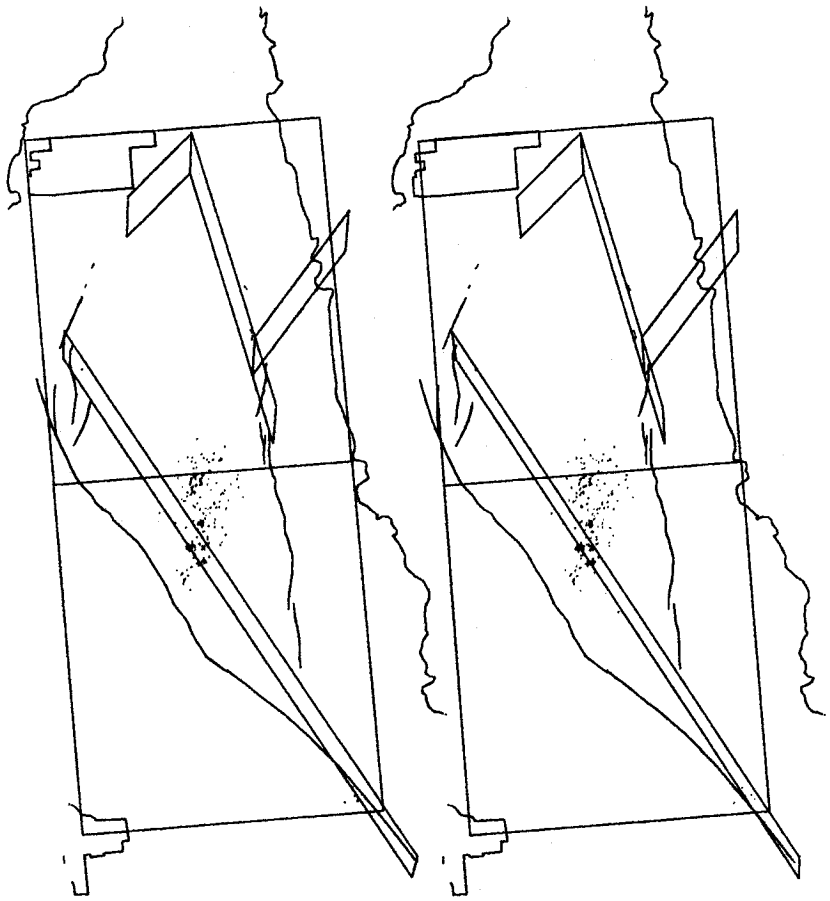

Figure 56. Stereo view showing all "A" quality hypocenters of the 77 OCT sequence occurring during the period 28 October 0:00 through 21:55 GMT (21.9 hours). This interval begins the rapid development of swarm B.

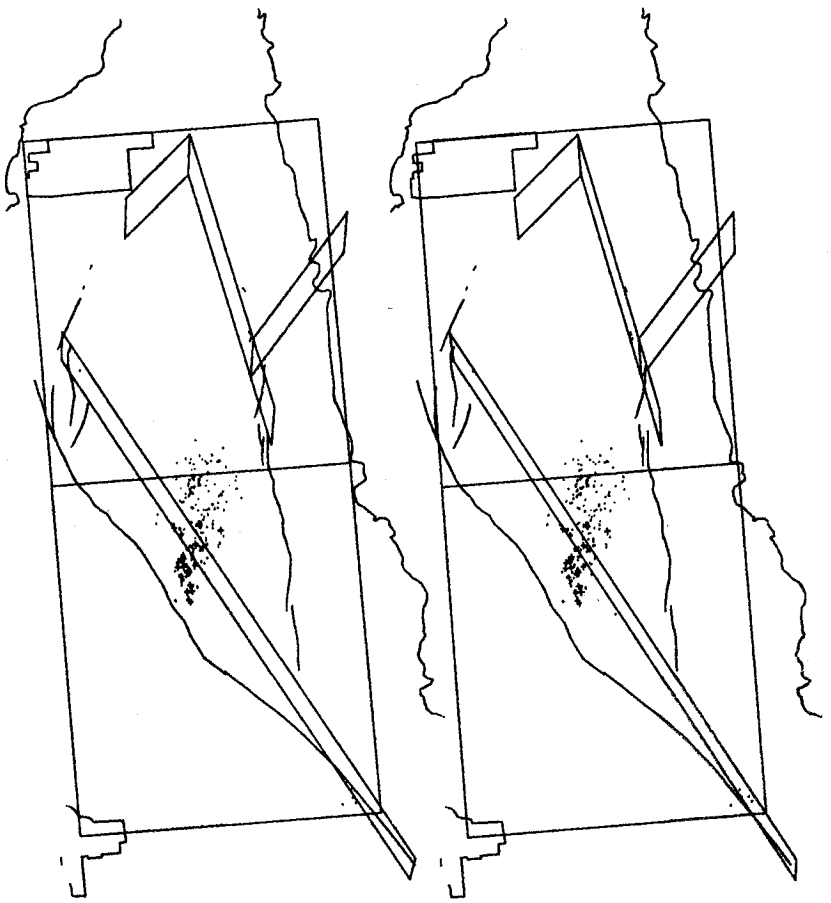

Figure 57. Stereo view showing all "A" quality hypocenters of the 77 OCT sequence occurring during the period 28 October 21:55 through 29 October 2:00 GMT (4.1 hours). Activity during this interval appears to continue the development begun in Figure 54.

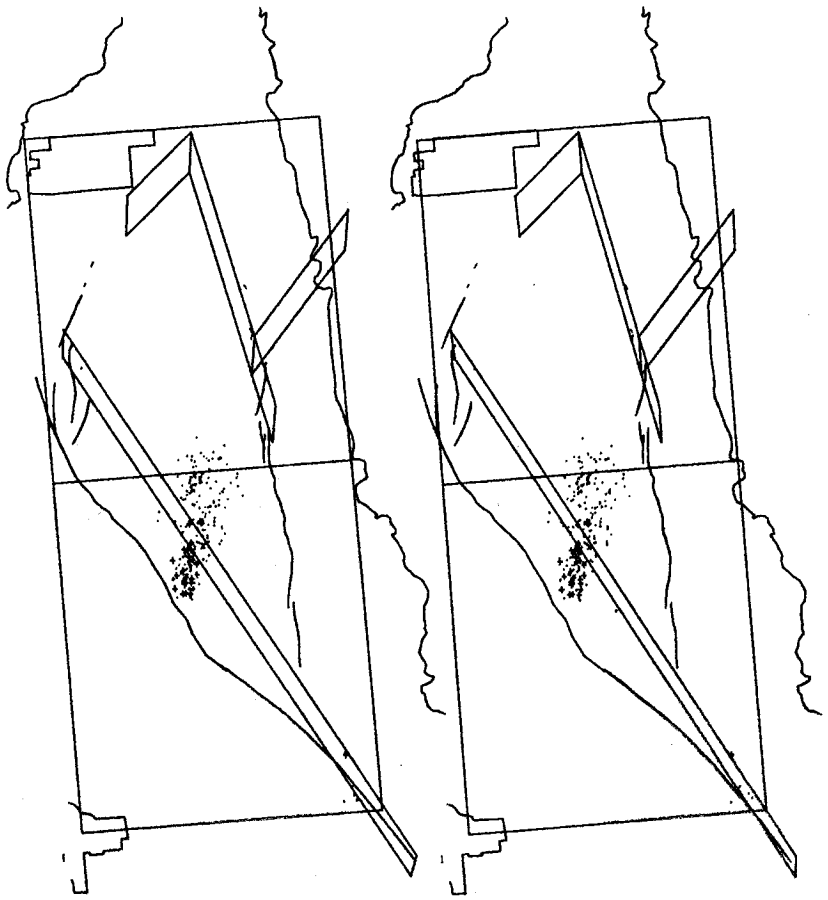

Figure 58. Stereo view showing all "A" quality hypocenters of the 77 OCT sequence occurring during the period 29 October 2:00 through 30 October 0:00 GMT (22 hours).

Figure 59 covers an extended period of low seismicity from October 30 through November 13. The most interesting aspect of Figure 59 is the tightly clustered group of events near the intersection of the 1975 surface cracks (Sharp, 1976) and the Imperial fault plane. This cluster occurred late in the day on November 13, near the end of the period plotted, and marks the beginning of swarm "C". The subsequent development of swarm "C" southward on a vertical plane trending slightly east of south can be followed in Figures 60 through 65. In each subsequent figure, the most recent events extend the distribution further south. In this case, the planar nature of the structure activated during swarm "C" is considerably more well-defined than for "A" and "B". Focal mechanisms, although not controlled due to the paucity of close stations, are consistent with this interpretation.

The origination of swarm "D", shown in Figure 63, occurred before the development of swarm "C" was completed. Swarm "D" also began near the Imperial fault plane, with subsequent development to the north in Figures 63 through 67. The resulting distribution appears to define a structure paralleling that associated with swarm "C". These two structures bound a region of diffuse seismicity probably associated with northeast trending structures similar to those inferred for swarm "A". Although discrete structures cannot be resolved, a general shoaling of events in Figures 63 through 66 is evident. The final epicentral distribution (Figure 48) for the southern swarms defines a crude letter "N". The cross-bar marks the position of the Imperial fault.

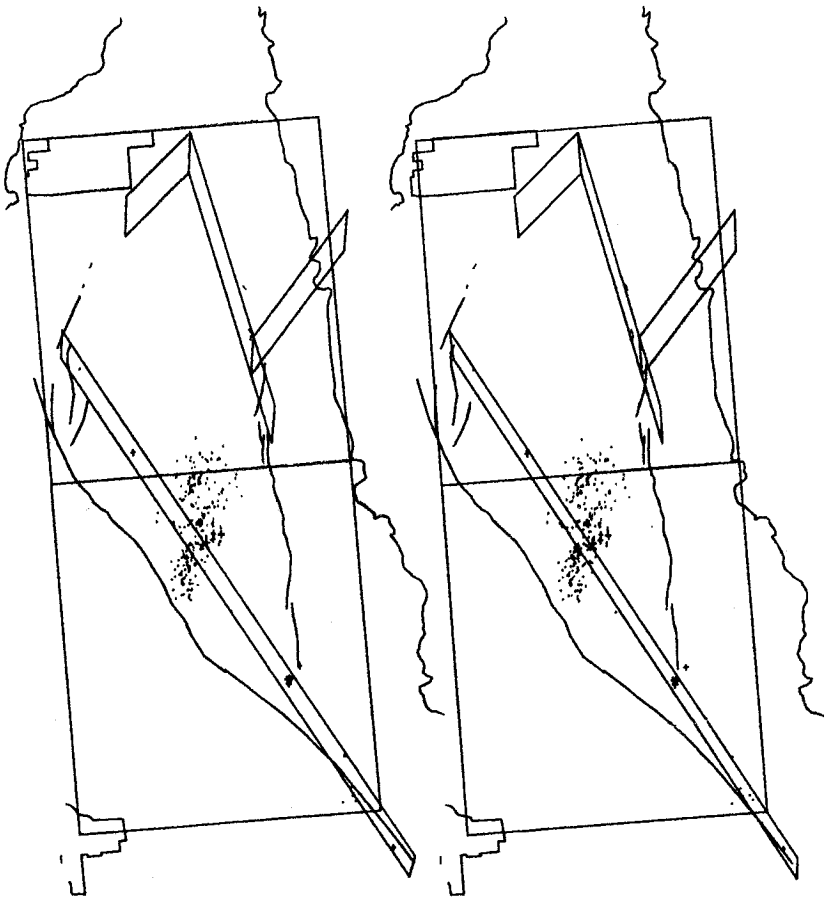

Figure 59. Stereo view showing all "A" quality hypocenters of the 77 OCT sequence occurring during the period 30 October 0:00 through 13 November 0:00 GMT (336 hours). Note the initiation of swarm C as a tight cluster on the proposed plane of the Imperial Fault.

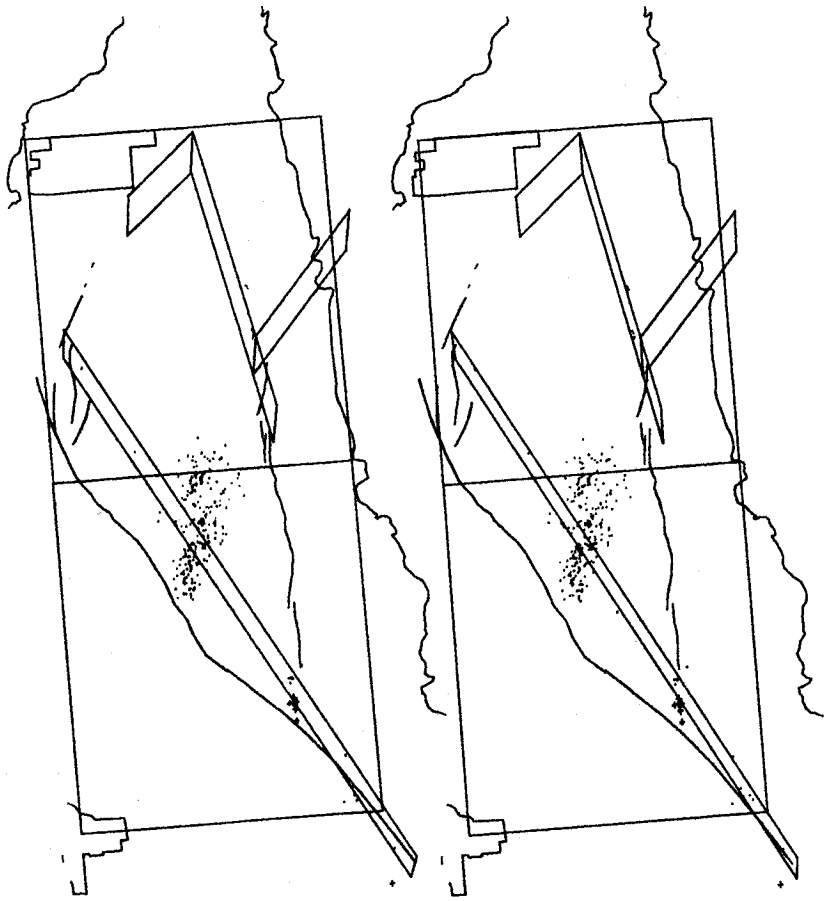

Figure 60. Stereo view showing all "A" quality hypocenters of the 77 OCT sequence occurring during the period 13 November 0:00 through 8:00 GMT (8 hours). The rapid development of swarm C to the south-southwest can be seen in this interval. This development continues through Figure 66 although most of its extent is defined after 4 hours. It is our contention that this migration marks the growth of a vertical fracture.

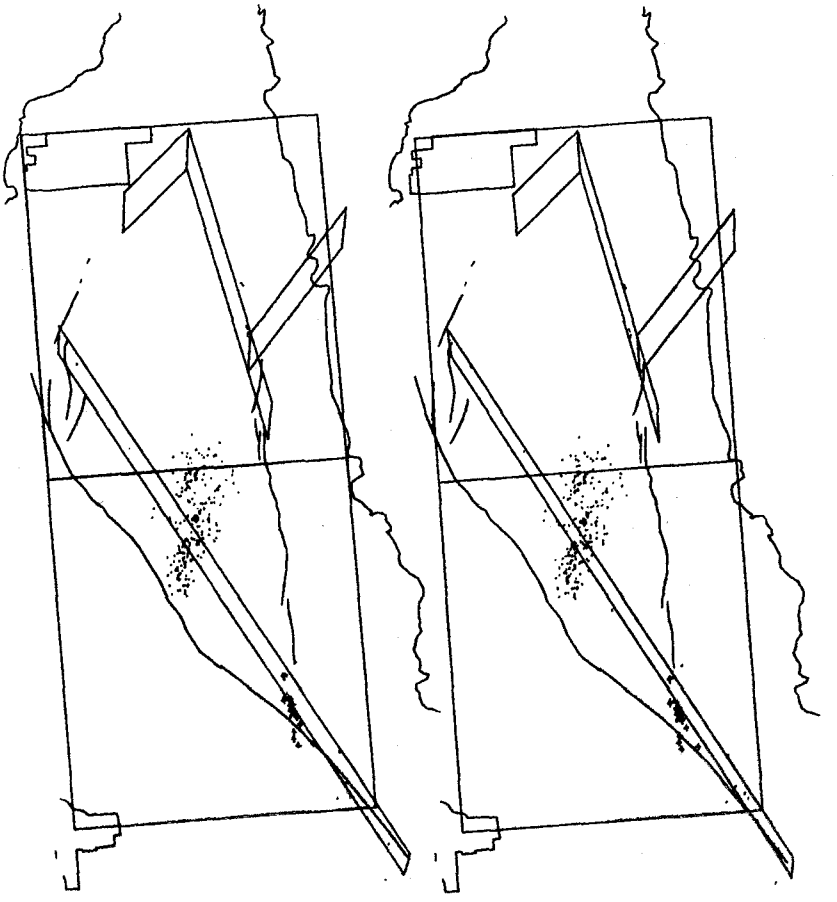

Figure 61. Stereo view showing all "A" quality hypocenters of the 77 OCT sequence occurring during the period 13 November 8:00 through 14 November 1:00 GMT (17 hours).

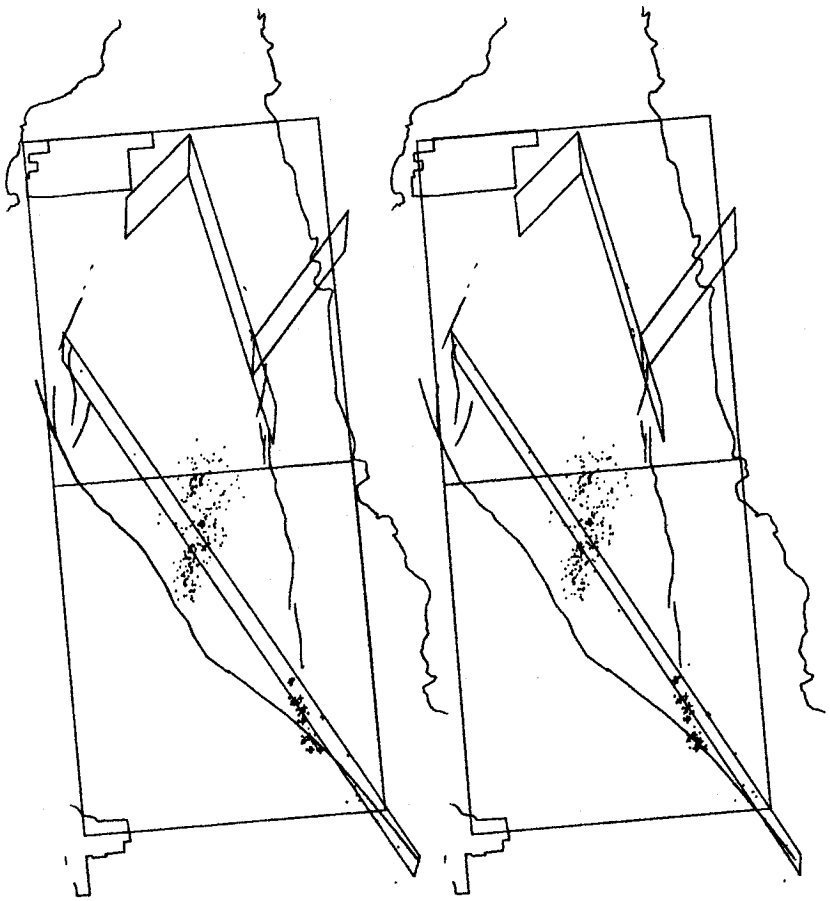

Figure 62. Stereo view showing all "A" quality hypocenters of the 77 OCT sequence occurring during the period 14 November 1:00 through 3:00 GMT (2 hours).

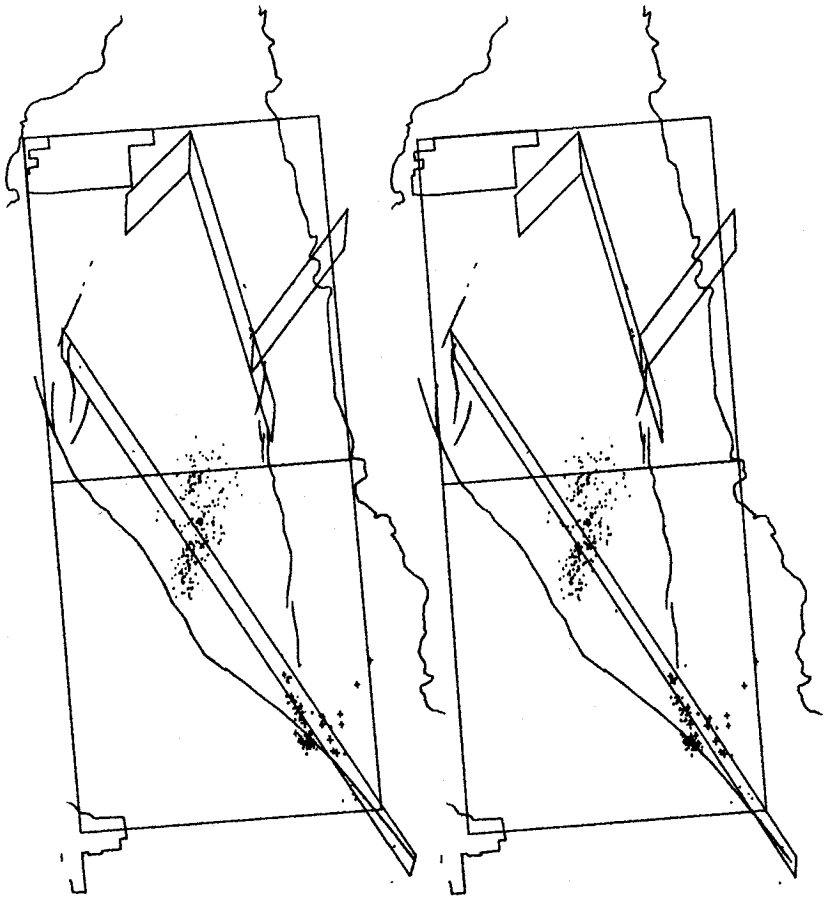

Figure 63. Stereo view showing all "A" quality hypocenters of the 77 OCT sequence occurring during the period 14 November 3:00 through 5:00 GMT (2 hours). Coincident with the continued development of swarm C, some activity can now be seen on the plane of the Imperial Fault between the initiation points of swarms A and B.

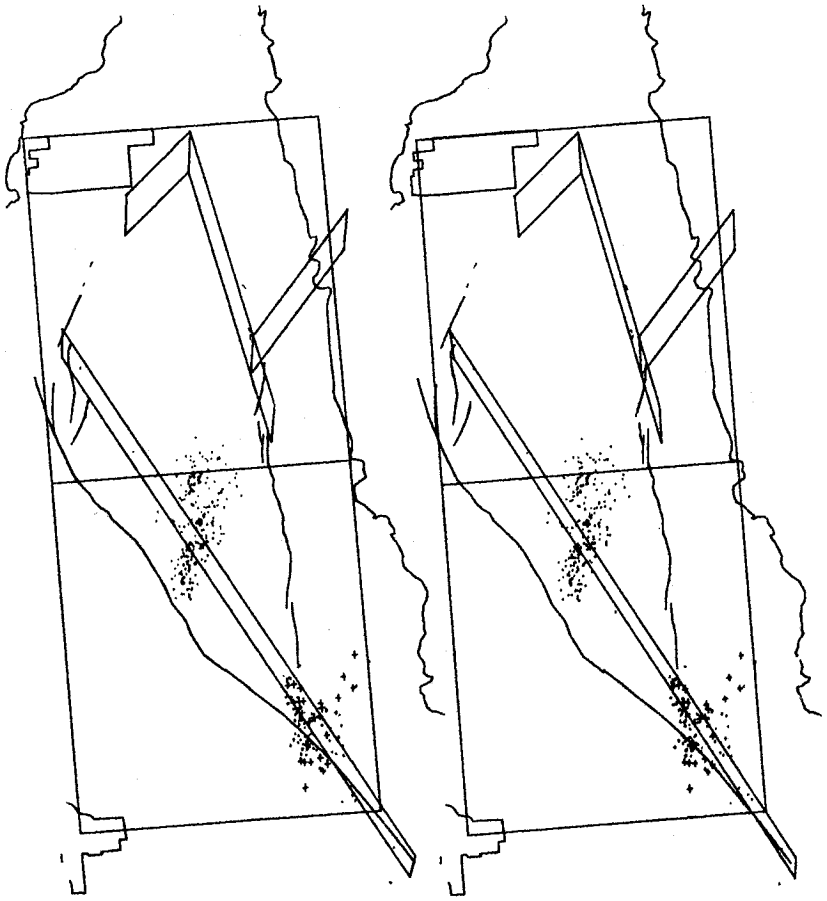

Figure 64. Stereo view showing all "A" quality hypocenters of the 77 OCT sequence occurring during the period 14 November 5:00 through 7:00 GMT (2 hours). The development of swarm D manifests a general shallowing of activity with time as can be seen in Figure 69 as well.

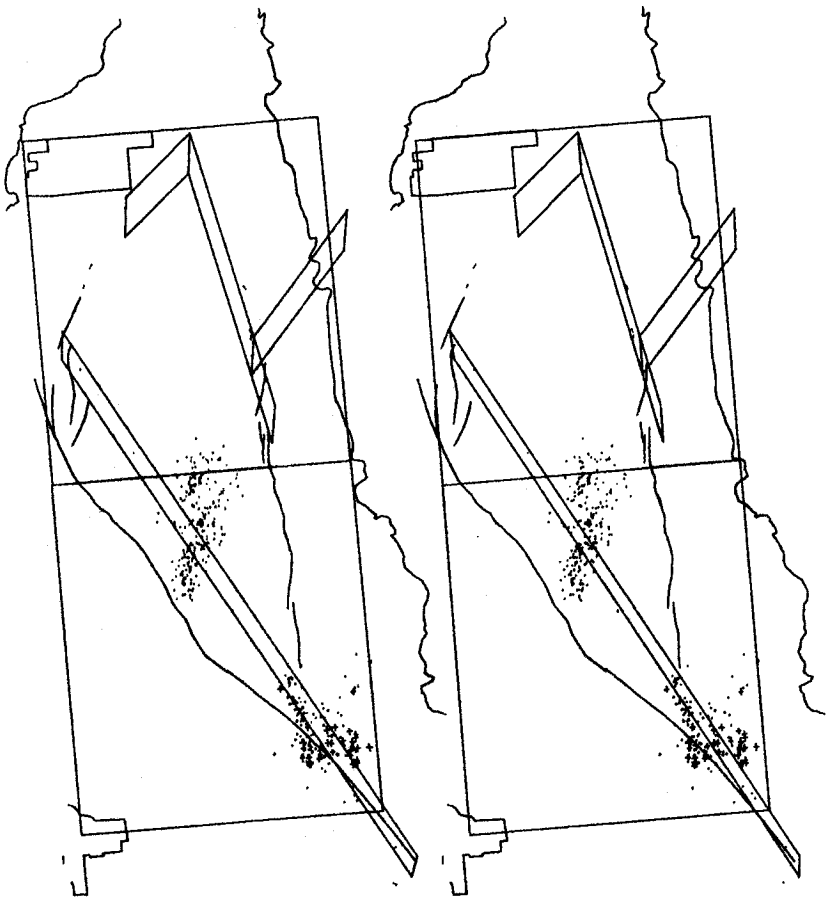

Figure 65. Stereo view showing all "A" quality hypocenters of the 77 OCT sequence occurring during the period 14 November 7:00 through 11:00 GMT (4 hours).

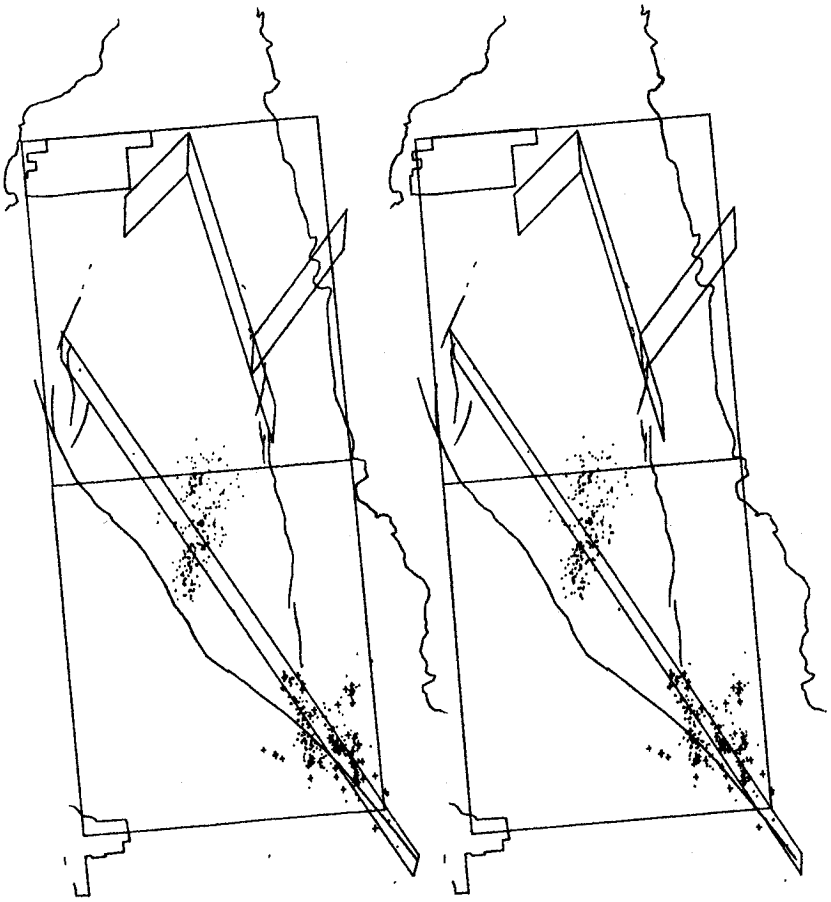

Figure 66. Stereo view showing all "A" quality hypocenters of the 77 OCT sequence occurring during the period 14 November 11:00 through 24:00 GMT (13 hours).

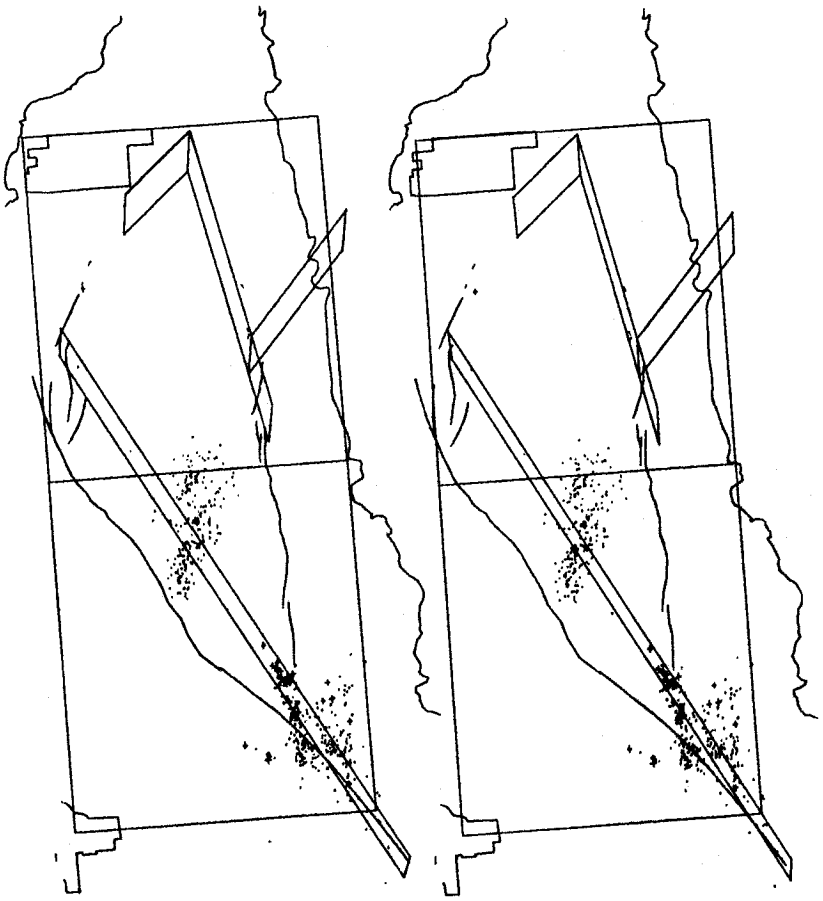

Figure 67. Stereo view showing all "A" quality hypocenters of the 77 OCT sequence occurring during the period 15 November 0:00 through 30 November 0:00 GMT (360 hours).

We interpret the structures activated during swarms "C" and "D" as growing vertical sheer cracks. To explore the progressive nature of the development of seismicity on these structures in more detail we have plotted the events associated with each in cross-section in Figures 68 and 69. Events were isolated to a particular structure using a narrow box 1.25 km wide. For each structure three consecutive time intervals are shown with events plotted as "+", "x" and "*" in increasing time order with "+" representing events prior to 12 November and with "*" those following 13 November. Distance is defined relative to the point 32°47'N, 115°27'W. The intersection with the inferred Imperial fault plane is shown as a solid vertical line. The progressive development of seismicity on these two planar structures is remarkable. The few exceptions to uniform extension can easily be attributed to mislocation or to the inadvertent inclusion of off-plane events. Migration of events associated with swarm "C" (Figure 68) proceeded horizontally at a fixed depth of about 5 km, near the base of the sediments. Migration in swarm "D" (Figure 69) shows a considerable vertical component with initial activity near 8 km shoaling to about 5 km. The conclusion that what we are witnessing is the progressive development of a set of vertical fractures is difficult to avoid.

DISCUSSION

Similarity to the Seismicity of the Reykjanes Ridge in Iceland

Few areas in the world exhibit the combination of high seismicity and tectonic setting one finds in the Imperial Valley. One such area

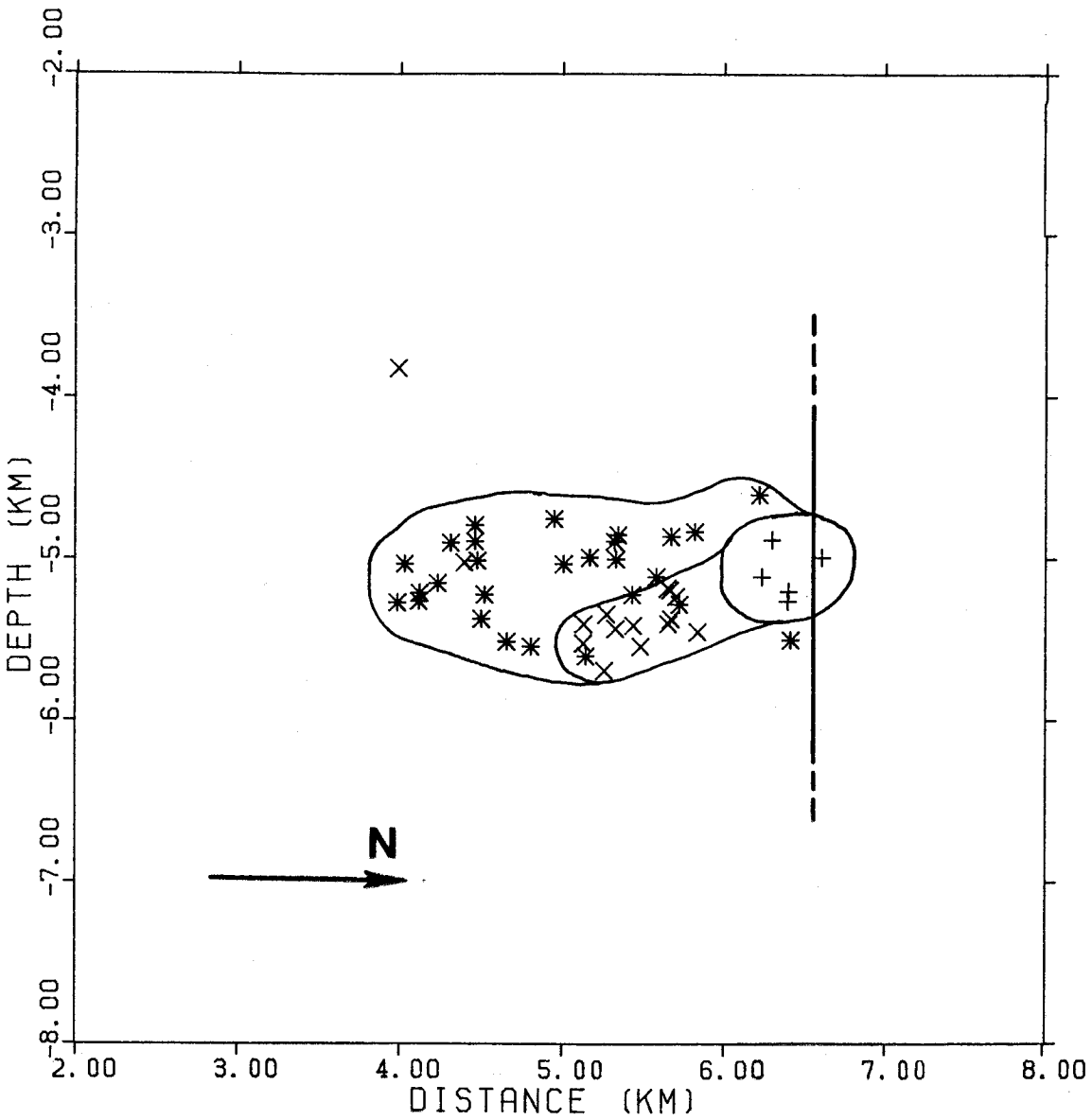

Figure 68. Growth of swarm C on a southerly trending vertical plane. The proposed intersection of the Imperial Fault with this plane is shown as a solid line. Events in three consecutive intervals (see text) are represented by the symbols "+", "x" and "*" respectively.

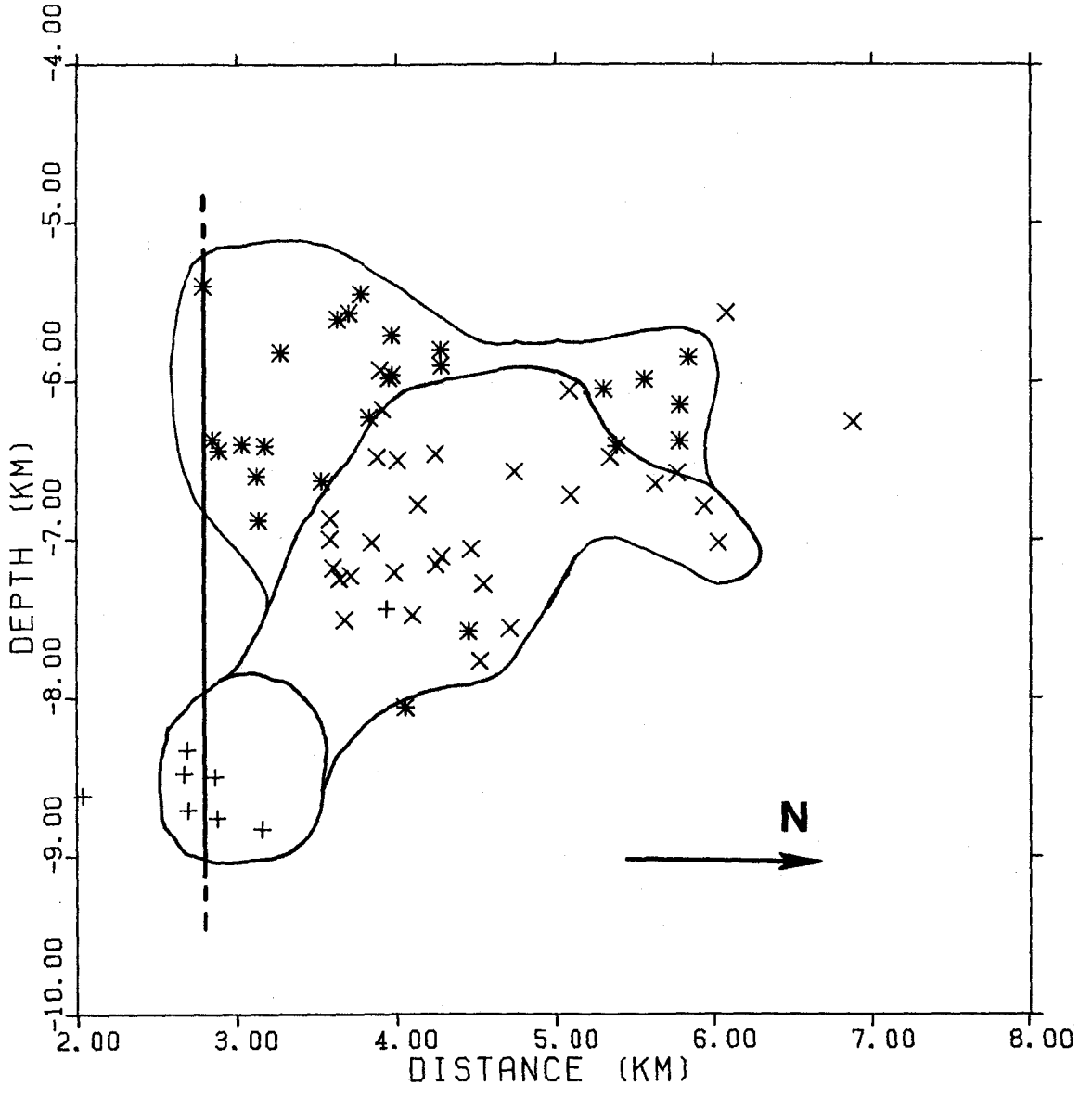

Figure 69. Growth of swarm D on a northerly trending, vertical plane. The proposed intersection of the Imperial Fault with this plane is shown as a solid line. Events in three consecutive intervals are represented by the symbols "+", "x" and "*" respectively.

is the Reykjanes Peninsula in Iceland; the similarity between these two seismotectonic provinces is intriguing. Seismicity on the Reykjanes Peninsula described by Tryggvason (1973) is confined to a narrow linear zone striking about N75°E along the axis of the peninsula. Multiple events and earthquake swarms are typical of this zone, making a direct comparison with the Brawley seismic zone discussed in Chapter 4 attractive. Faulting within this zone consists of an *en echelon* pattern of groups of open and volcanic fissures. The strike of these features varies from N35°E in the eastern part of the zone to about N45°E to the west. However, there appears to be no throughgoing transform fault exposed at the surface analogous to the Imperial fault in Southern California. Despite this difference, the linear trend of epicenters has been interpreted as marking the location of significant transform motion associated with the mid-Atlantic ridge. The existence of a buried transform is also supported by the occurrence of a large historic earthquake ($M > 7$) and a central distribution of strike-slip focal mechanisms along the inferred trace (Klein and others, 1977). Geothermal areas are distributed along the seismic trend in much the same ways as in the Imperial Valley. As with the Imperial Valley, the major deformation appears to be extensional, while a more vertical most compressive axis leads to tensional surface structures and volcanism. In the Imperial Valley a preponderance of strike-slip focal mechanisms suggests a more nearly horizontal, greatest compressive stress. It should be emphasized that both the Reykjanes Peninsula and the Imperial Valley represent landward extensions of oceanic ridges.

The similarity between the Reykjanes Peninsula and the Imperial Valley becomes even stronger when one compares the spatio-temporal characteristics of seismicity. A major swarm of earthquakes occurring in September 1972 on the Reykjanes Ridge has been described in considerable detail by Klein and others (1977). With six events greater than magnitude 4 and an equivalent magnitude of 4.9 calculated from accumulated moment, this swarm appears to be just slightly smaller than the largest swarms in the Imperial Valley discussed in the previous section. Klein noted that the main sequence could be broken down into sub-swarms, highly localized in space and time, which behaved individually like swarms. These sub-swarms were distributed along the seismic trend, were activated progressively with migration rates of between 1 and 2 km/day, and themselves defined linear trends at an angle to the overall seismic distribution. Moreover, the development of activity on these seocndary structures is initiated near the center of the seismic zone, with subsequent extension toward its margins. These structures, generally striking north-northeast, appear to align perpendicular to the least principal stress axis (Hill, 1977).

This is precisely the spatio-temporal arrangement of swarms and swarm sequences that we have discussed above for the Imperial Valley. One must realize, however, that Klein's "swarm" is what we have been referring to as a "swarm sequence" and our "swarm" is his "subswarm". This difference in nomenclature appears to stem from a fairly subtle difference in seismotectonic style. For the Reykjanes Ridge, "subswarms" are sufficiently closely spaced in

time as to be obviously related. In the Imperial Valley, the greater temporal spacing between bursts of activity forestalled the conclusion that they were coherently related as part of a more general swarm sequence.

Both the Reykjanes Ridge swarms and those in the Imperial Valley appear to be modulated by the solid earth tides (Klein, 1976). The triggering of seismicity by tidal forces is a rather rare phenomenon and thus, itself, bespeaks considerable seismotectonic similarity. Klein concluded that Icelandic swarms are driven by tectonic stresses rather than those arising from magmatic intrusion. Further, he concluded that the temporal patterns, particularly migration rate and duration of activity, suggested an underlying mechanism involving fault creep and fluid flow. These results are fully compatible with the model of Imperial Valley seismicity presented below.

A Mechanical Model for Imperial Valley Earthquake Swarms

From our observations it appears that a mechanical model of Imperial Valley seismicity must consist of three elements. The first element is a means of communicating information along the trend of the major transforms so that isolated swarms can behave as part of a swarm sequence. We have previously suggested that this mechanism is episodic fault creep. The second element of the seismicity model concerns the failure mode of the transverse structures giving rise to the bursts of seismicity identified as swarms. The model proposed by Hill (1977) and refined by Weaver and Hill (1978) seems well-adapted to this purpose. This model relates seismicity on oblique

strike-slip structures to differential fluid pressure between adjacent members of a dyke swarm. The only significant modification to this model is that we assume the fluid to be ground water rather than magma as proposed by Hill. The third aspect of the Imperial Valley seismicity model provides a means of connecting creep on the transform faults with activation of the transverse structures. We suggest that this interaction occurs as a result of fluctuations in pore pressure and tectonic stress associated with the propagation of an edge dislocation on the associated transform.

(1) Earthquake Swarms and Episodic Fault Creep

There are several reasons for proposing fault creep as the mechanism controlling migration and activation of component swarms along the two principle trends discussed above. There are numerous observations of fault creep both on the Imperial fault and the Brawley fault. At the north end of the Brawley fault Savage and others (1974) has found evidence for localized shear amounting to nearly 9 mm/yr. from a consideration of triangulation data. The only direct evidence relating fault creep and earthquake swarms comes from the January 1975 swarm and the 10 km extent of apparently aseismic surface cracks mapped by Sharp (1976). As mentioned above, we were extremely fortunate that the formation of the scarp at the north end of the fracture zone could be accurately correlated in time with the well-defined migration of seismicity along the same trend at depth.

On the Imperial trend the only direct relation between fault creep and earthquake swarms comes from the observation of 10 km of surface

breakage, along the trace of the 1940 earthquake, that occurred near the time of a small swarm reported by Brune and Allen (1967). This same section was reactivated in 1968 with 1.4 cm of offset apparently triggered by the Borrego Mountain earthquake. There are, however, abundant additional reports of episodic fault creep along the Imperial fault. Between 1940 and 1966, offset on the Imperial fault where it crosses Highway 80 increased about 36 cm (Brune and Allen, 1967) beyond the 46 cm observed by Buwalda (unpublished field notes) following the 1940 shock. It is not known whether this continued afterslip occurred continuously or episodically. Goulty and others (1978a) list five subsequent creep episodes recorded by an alignment array traversing the Imperial fault at Highway 80. This array was surveyed about every six months and clearly demonstrates that offset was not accumulating continuously. The most complete observations of the episodic nature of Imperial Valley creep come from an array of continuously recording creepmeters installed across the Imperial Fault by Goulty and others (1978a) in September 1975. An event, shown in Figure 70, was subsequently recorded on two or the three creepmeters 7 km apart. Despite the fact that intervening roads showed no obvious disturbance or cracking, the similarity of the two records, their coincidence in time, and the fact that no other events were recorded within 1.5 years before and after the event strongly suggest that a single propagating event was observed. If so, the apparent propagation velocity lies between 1.5 and 2 km/day. This rate compares well with the range of 1 to 10 km/day reported by King and others (1973) for the central San Andreas Fault. The absence of

intervening cracks does not necessarily constitute a severe problem. A creep event occurred on the Imperial Fault sometime between 15 June 1978 and 27 November 1978 and was preserved by a nail array (3 m spacing) installed on Worthington Road (Ralph Gilman and Stephen Cohn, personal communication, 1979). Although there was clear evidence of block motion amounting to about 1 cm, no obvious fresh road cracking or center-line offset were found. Apparently the deformation zone was sufficiently broad that the asphalt road surface was able to deform plastically. With the exception of the 1966 event, no earthquake swarms can be directly correlated with surface creep episodes along the Imperial Fault. However, it is possibly significant that both earthquake swarms and fault creep are largely confined to the same northernmost section of the 1940 surface trace.

The observation that episodic creep occurs at the surface does not prove that similar phenomena take place at depths of 6 to 10 km. Indeed, the results reported by Johnston and others (1977) indicate that at least for some central San Andreas creep events episodic deformation is confined to the near surface. Similar results were obtained by Goulty and others (1978b) for four creep events near Parkfield recorded on a creepmeter installed at Carr Ranch. An array of four strain meters spanning a distance range of .2 to 2.2 km from the Carr Ranch creepmeter failed to record concomitant strain changes. However, strain events did precede three of the observed creep episodes. A model of creep propagating diagonally from a depth of 480 to within 30 m of the surface was found to adequately explain the observations from the strainmeter array.

Eventually the creep event was able to penetrate the surface layer and was recorded at Carr Ranch as a creep event. The failure of the initial strain event to reach the surface was attributed to a water table effect. The implication here is that for episodic creep to propagate effectively a saturated condition was required. On the other hand, the geodetic results reported by Thatcher (1979) and discussed in Chapter 4, seem to require long-term average slip rates at depths along the Imperial Fault greatly exceeding those observed at the surface. Determining whether this deep creep is episodic is one of the most stringent tests of the proposed seismo-tectonic model.

This is hardly the first time that a direct relationship between fault creep and earthquakes has been proposed. In central California a correlation between creep slippage rates and seismicity was noted by Nason (1973). Wesson and others (1973) proposed a model where creep, viewed as migrating dislocation, loads patches of difficult slip until failure in moderate earthquakes can occur. Bufe and Tocher (1974) found an apparent relationship between fault creep, episodic strain, and moderate earthquakes. In particular, they concluded that a magnitude 4.6 earthquake on 4 September 1972 had induced a creep episode on a nearby section of the San Andreas, a situation not unlike our interpretation of the initiation of the November 1976 swarm sequence on the Brawley trend. Reichle and Reid (1977) interpreted the pulse-like nature of ridge swarms in the Gulf of California as evidence of an episodic source of strain arising either from magmatic pulses and/or slip along the Graben-

boundary fault. In the northern gulf, Thatcher and Brune (1971) found an apparent correlation of activity in the Delfin Basin with that in the Wagner Basin, about 150 km farther north. Three pairs of event sequences were coupled in this manner. If information is carried between these two basins by a connecting transform fault, then the apparent propagation rates of 1.9, 1.6, and 2.3 km/day fall well within the range of 1 to 10 km/day expected for episodic fault creep.

Further evidence for an intimate relationship between earthquake swarms and fault creep comes from the similarity of creep-time functions of the accumulated moment of swarms. This similarity was first noted from a graph of summed moment prepared by Thatcher and Brune (1971) for an earthquake swarm in the northern gulf. The comparison of this figure with typical continuously recorded creep episodes (e.g., King and others, 1973) is striking. Unlike similar plots for mainshock sequences, which are more angular and approximate step functions, summed moment for swarms are characterized by an initial rapid increase followed by an exponential decay of moment rate. The signatures of both creep events and swarms frequently are more complex, manifesting several "exponential" episodes of accelerated offset. This is illustrated in Figure 70, where we directly compare the summed moment of the November 1976 swarm in the upper frame to the Imperial Fault creep episodes reported by Goulty and others (1978a) in the two lower frames on the same time scale. The steep portions of the summed moment plot correspond to bursts of activity in the swarm sequence. Similar comparisons can be made for

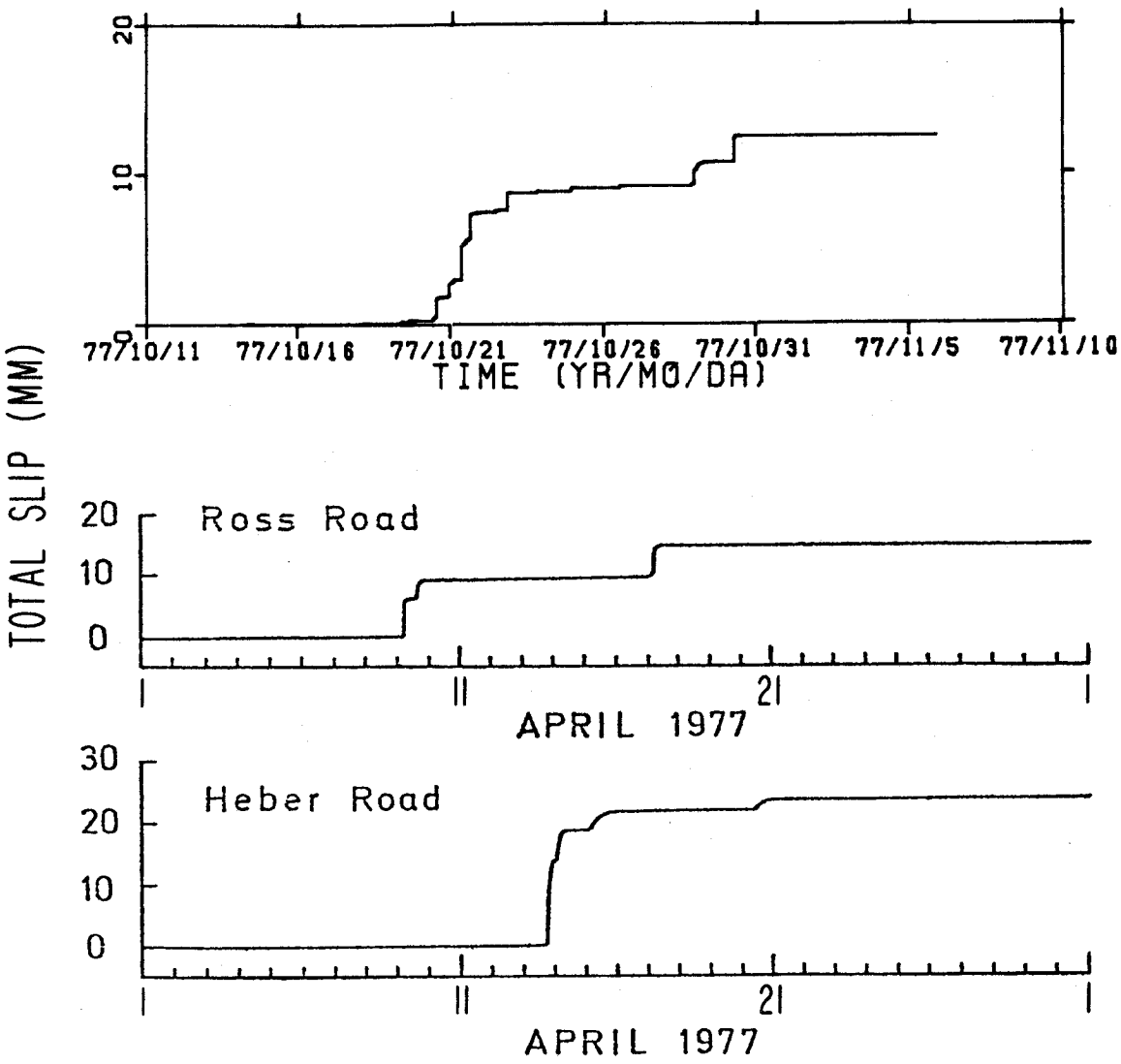

Figure 70. Comparison of equivalent slip calculated from summed moment for the 77 OCT swarm sequence (upper frame) with typical creepmeter records from the Imperial Fault (lower two frames). Creepmeter records are from Goulty and others (1978a).

other swarm sequences in Figures 9, 23, 36, 39, 42, and 45.

2. Swarms, Transverse Fractures, and Fluid Pressure

The second element of the proposed seismo-tectonic model concerns the relationship of earthquake swarms to structures transverse to the major transform faults. The trend of these structures varies from nearly due east for the one initiating the November 1976 swarm to due north as observed for the southernmost events of the October 1977 sequence. Particularly with regard to the latter, the agreement with the predictions of the geometrical model proposed by Hill (1977) is remarkable. Central to Hill's model is the idea that clusters of magma-filled dikes exist within brittle volumes of the earth's crust oriented perpendicular to the least principal stress. In the Imperial Valley this axis at seismogenic depths is thought to be essentially east-west and horizontal. The resulting dikes should then be vertical with a northerly strike, similar to the growing planar structures in the southern clusters of the October 1977 swarm sequence. This is also the same geometric arrangement one encounters with hydraulic fracturing (e.g., Hubbert and others, 1957) with opening fractures perpendicular to the least compressive stress. At shallow depths, horizontal fractures form at injection pressures at or exceeding lithostatic, while at greater depths vertical fractures form at hydraulic pressures well below lithostatic. This may account, in part, for the observation that focal mechanism in one part of the 1972 Reykjanes swarm varied from strike-slip to normal with increasing depth. From this Klein and others (1977) deduced that the overburden stress surpassed the northeast compressive

stress at depths of around 3 km. A similar explanation probably pertains to the variation in orientation of the transverse structures giving rise to swarms in the Imperial Valley. Unfortunately, in the Imperial Valley we have neither the focal mechanisms nor the absolute depth control to resolve these issues unambiguously. While the resolution in relative depth within a given swarm is adequate to reveal local planar distributions, the absolute depths and the relative depths of the swarms separated by as little as 10 km are poorly known. This problem stems from the fact that for all but one or two stations the first arrivals come from plunging rays. Consequently, inadequate knowledge of details of lateral variations in crustal structure results in an excessive number of inconsistent first motions. An extensive program of seismic profiling and time-term analysis currently being conducted in the Imperial Valley by the U. S. Geological Survey should serve to substantially mitigate this situation in the near future.

Whether the seismic activity illuminating the transverse structures represents reactivation of pre-existing fractures or the creation of new ones cannot be resolved from our observations. It seems likely that the 1940 earthquake left the southern portion of the Brawley seismic zone in a highly fractured state. Hartill (1978) suggested the possibility of such a highly fractured reservoir lying between the Imperial and Brawley faults south of Brawley in order to explain a coincident zone of low resistivity. On the other hand, contemporaneous metamorphism and mineral deposition from saturated brines may drastically shorten the lifetime of fractures at

seismogenic depths. It seems likely that activity close to the main trends represents reactivation, although new fracturing may become increasingly more important as seismicity develops. However, the possibility that all of the transverse faulting may be associated with the formation of new cracks cannot be ruled out based on our observations.

There are a number of instances in which intentional changes in pore pressure have been directly correlated with the inducement of seismicity, generally of a swarm-like character. Specific examples include the disposal of waste fluids at the Rocky Mountain Arsenal near Denver, Colorado (Healy and others, 1968), fluid pressure transients produced by a nuclear explosion (Healy and others, 1970), water flooding of an oil field at Rangely, Colorado (Raleigh and others, 1976), and the hydraulic mining of salt in western New York state (Fletcher and Sykes, 1977). In each case seismicity appears to have begun when bottom-hole pressures reached a critical value related to the lithostatic pressure and the least horizontal compressive stress by the effective stress hypothesis of Hubbert and Rubey (1959). In this vein, particularly well-controlled experiments were conducted at Rangely and also at Matsushiro (Ohtake, 1974) based solely on their research merit. Precise locations obtained at Rangely (Raleigh and others, 1976) revealed that hypocenters were largely confined to the vicinity of a pre-existing fracture. In addition, bottom-hole pressure contours manifested high pressure lobes following the fracture trend indicating preferential flow along its length. The rejuvenation

of pre-existing faults as a result of hydraulic pressurization seems to be generally observed when hypocentral control is adequate. When the onset of pressurization can be controlled, such experiments also tend to exhibit migratory behavior similar to that observed in the Imperial Valley. For example such was the case for the BENHAM nuclear test described by Healy and others (1970) where a delayed burst of seismicity was clearly associated with a linear extension of activity into a previously quiet region.

It might be argued that failure resulting from a local increase in fluid pressure should lead to a predominance of normal faulting. On the contrary, the strain energy that is radiated seismically appears to be extracted from the regional secular strain, and local perturbations, while the pressure increase acts more as a trigger for this release. This has been demonstrated recently in laboratory hydrofracture experiments conducted by Lockner and Byerlee (1977) using two samples of Weber sandstone. They found that faulting changed from tensile to shear with increasing injection rate and concluded that regions under tectonic shear stress, shear failure could be induced at much lower fluid pressures than would be required to produce tensional cracks in similar unstressed samples.

3. Episodic Fault Creep and Pore Pressure Variations

We still require in our development some kind of "pump" to generate the differential fluid pressures needed to drive seismicity. This is the third element in a seismotectonic model relating predominantly aseismic creep on the transforms with the seismic activation of the transverse structures.

Many faults, including the Imperial Fault, manifest two distinct time scales of deformation. A mechanism that can account for seismic rates (e.g., the 1940 shock) while also permitting the slow propagation rates (1 to 10 km/day) associated with fault creep is mandatory for models describing such faults. In this regard, the creep model proposed by Rice and Simons (1976) seems to be particularly appropriate. This model describes the advance of a shear fault in a fluid-infiltrated elastic porous material, a condition thought to persist to seismogenic depths along the Imperial Fault (Harthill, 1978). Slow propagation rates are governed by "drained" conditions, pore pressure is constant, and the elastic properties are essentially those of the matrix material. For more rapid deformations the response is elastically stiffer and deformation rates are controlled by "undrained" conditions. In the former case, an increase in propagation rate requires an increase in driving stress, permitting the quasi-static, episodic propagation of slip known as fault creep. Catastrophic (seismic) propagation can occur, but requires substantially higher load rates.

The relationship between swarms and creep-induced fluctuations in pore pressure proceeds along the same lines used to relate aftershocks to pore pressure changes caused by a mainshock. Such models have been proposed by Nur and Booker (1972), Booker (1973), Nur and Schultz (1973), Booker (1974), and Gupta (1974), for example. Unfortunately, the specific relationship between creep-induced changes in pore pressure and the activation of earthquake swarms is complex and depends upon a detailed knowledge of the physical environment

of active faults. For example, seismically active regions are likely to be highly fractured, substantially altering the flow paths induced by a given strain field (Weertman, 1974). Such a mechanism was used by Gupta (1974) to explain aftershock lineations that differed substantially in trend from the strike of the mainshock. It seems likely that similar phenomena are controlling the seismic activation of transverse structures in the Imperial Valley. To put this more succinctly, we believe that in a real sense Imperial Valley earthquake swarms can be viewed as aftershocks of aseismic fault creep.

Water-level changes in a shallow well near Hollister, California have been repeatedly correlated with episodic creep on adjacent sections of the San Andreas fault (e.g., Johnson, 1973, Johnson and others,1973; Johnson and Kovach, 1973; Johnson and others, 1974; Kovach and others, 1975; and Mortenson and others, 1977). Such changes can easily be ascribed to time-dependent fluctuation in pore pressure as predicted by the Rice and Simons (1976) creep model. By calibrating water level changes with atmospheric pressure fluctuations, Johnson and others (1973) were able to relate measured creep amplitudes with corresponding changes in pore pressure. For the central San Andreas Fault, their results suggest a change in pore pressure of between 3.5 and 5 mb for each 1 mm of fault creep. Assuming similar conditions on the Imperial Fault, creep amplitudes (from summed moment) ranging from 1 to 5 cm suggest reasonable fluctuations of pore-pressure of from 40 to 400 mb.

It seems somewhat enigmatic that pore pressure changes on the order of 100 mb could trigger earthquakes with stress drops of up to

3 orders of magnitude higher. For example, Hartzell and Brune (1977) and Hartzell (1978) report stress drops in the range 1 to 636 bars for the January 1975 swarm sequence on the Brawley trend. However, there is ancillary evidence that such a supposition may be reasonable. It is likely that hydrostatic stresses associated with the solid earth tides rarely exceed 100 bars (e.g., Heaton, 1975). Yet a strong correlation between swarm activity and earth tides is consistently observed (e.g., Nasu and others, 1931; Mauk and Kiener, 1973; Klein, 1976). Specific correlations between the semi-diurnal earth tide and swarms in the Imperial Valley have been demonstrated by Sauk (1975) for the January 1975 sequence, and by Klein (1976) based on swarms prior to 1973. Using the computer codes applied by Heaton (1976), we found a similar correlation for the October 1977 swarm sequence on the Imperial trend. Klein (1976) suggested one triggering mechanism related to pore-pressure variations in regions of anisotropic permeability, a mechanism quite similar to the one we have discussed above relating swarms to creep. That earth tides can induce differential pore pressure, and hence fluid flow, is supported by a number of observations correlating flow at the surface with tides. Mauk and Johnston (1973) and Hamilton (1973) have correlated volcanic eruptions with the fortnightly tide. Geyser activity has been found by Rinehart (1972) to vary with earth tidal forces, barometric pressure, and tectonic stresses. Tidal modulation of spring flows is also observed, as illustrated in a study of the Steamboat Springs thermal system in Nevada by White (1968).

One further example of the triggering of tectonic activity

in the Imperial Valley by relatively insubstantial stresses occurred in 1968, when approximately 1.5 cm of creep appeared on the Imperial Fault, among others in the area. This offset was ascribed to shaking at the time of the magnitude 6.4 Borrego Mountain earthquake by Allen and others (1972). The BENHAM nuclear event with an m_b of about 6.4 was comparable in magnitude to the 1968 Borrego Mountain earthquake. Dynamic strains for BENHAM on the order of 2×10^{-7} have been reported by Smith and others (1969) at a distance of 29 km. Assuming an R^{-3} dependence for near-field bodywaves, it appears that dynamic strains near Brawley ($d \sim 40$ km) should have been comparable with solid earth tidal strains of about 10^{-7}. BENHAM produced tectonic surface fault displacement to distances slightly in excess of 10 km (Hamilton and Healy, 1969).

Although it is not specifically required in the proposed model, it is possible that super-hydrostatic fluid pressures at seismogenic depths may be necessary for it to be viable. Berry (1973) has found that creeping sections of the San Andreas in Central California appear to be coincident with regions of high fluid potential at depths of several km. Along some sections fluid pressures approaching lithostatic were discovered. Referring to the laboratory results of Byerlee and Brace (1972), Berry suggested that the high pressures facilitated stable sliding rather than strike-slip motion (earthquakes) in lower pore pressure regimes. The mechanism proposed for achieving high fluid potentials was tectonic compression at rates precluding a return to hydrostatic pressures by fluid diffusion. Clearly the efficacy of such a mechanism would be greatly enhanced by a positive

permeability gradient with depth. Similarly, a layered permeability model was invoked by Healy and others (1970) in order to confine the pressure pulse generated by the BENHAM nuclear event and explain the restriction of induced aftershocks to a narrow depth range.

In the Imperial Valley, we lack evidence regarding shut-in pressures at depths greater than a few kilometers. However, a general coarsening of sediments from clays and mudstones near the surface to shale interbedded with thickening, fractured sandstone beds at depths of around 4 km (Muffler and White, 1969; Harthill, 1978) appears conducive to the local tectonic generating of high fluid pressures. Permeability in the uppermost few kilometers may be further reduced by mineral deposition from geothermal brines cooling as they rise. The possibility also exists for the formation of confined reservoirs by local crack formation in the immediate vicinity of active faults. Such a situation would provide a ready explanation for both the small stress perturbations thought to trigger Imperial Valley swarms as well as the 10 year hiatus in swarm activity following the 1940 quake. The idea here is that tectonic strains slowly increase pore pressure with time. The site of an incipient swarm is "ripe" when the pore pressure approaches within a few hundred millibars of the least compressive stress. Unlike dry models, excessive stresses are avoided by fluid diffusion contributing to the observed spatial homogeneity of required triggering stresses. Such a mechanism also explains why smaller terminal swarms tend to be more separated than larger ones. The correspondingly smaller creep events would generally have to travel farther before encountering a swarm site

sufficiently close to failure. We have also observed in Chapter 4 that swarms in the Imperial Valley do not tend to repeat in the same spot over the past 5 years. Since earthquakes in swarms have stress drops on the order of tens of bars and the proposed triggering stresses are fractions of a bar, it would be surprising if reactivation of a transverse structure were to occur over the five years of detailed study.

Suggestions for Instrumentation

No model can be considered complete without the suggestion of further means by which its implications can be tested. Some additional constraints can undoubtedly be obtained by extending the procedures described here for future swarms. Additional instrumentation would be required in order to provide enhanced refinement of focal mechanisms and depth of focus. However, more stringent tests should be directed at investigating the inference that individual swarms are but one aspect of a more pervasive process related to the aseismic propagation of a deformation along the major transforms. Likely experiments would provide for the real-time measurement of the resulting time-dependent strains. The best place to measure these strains would be at depth near the major faults. Such possibilities include the implacement of dilatometers or the direct measurement of pore pressures at depths exceeding 3 km after Bodvarsson (1970). Another possibility would be the continuous monitoring of strains at the free surface over distances of tens of kilometers. An instrument suitable for such a study with a required precision of

about 1 part in 10^7 is the multiwavelength laser strainmeter as described by Slater and Huggett (1976) and applied to the measurement of buried fault creep on the San Andreas Fault near Hollister by Huggett and others (1977). In either case, sampling intervals of an hour or less appear necessary. There also exists the possibility for an active experiment in the Imperial Valley. If the proposed model is correct, it should not be difficult to induce swarm activity by water injection at depths of a few kilometers. The attendant risks probably preclude the possibility for such an experiment.

Implications with Respect to Long Term Changes in Seismicity

The hiatus in seismicity from 1940 to 1950 can thus be directly related to the drop in pore pressure in the northeast dilational quadrant of the 1940 El Centro earthquake. This observation also permits a crude numerical test of our model. According to Booker (1974) the change in pore pressure at a distance, r, due to an infinite edge dislocation can be expressed as

$$\Delta p = \frac{\mu b \left(1 - e^{-r^2/4ct}\right) \sin \theta}{2\pi (1 - \gamma) r} \qquad (1)$$

where μ is the rigidity (10^5 bars), γ is Poisson's ratio (.25), b is the displacement, c is the hydraulic diffusivity, and theta is the angle measured from the fault extension. Assuming a fault displacement for the 1940 quake of 400 cm due east of El Centro, we calculate an initial drop in pore pressure at the site of the 1950 swarm ($\theta = 10°$, $r = 6 \times 10^6$ cm) of 241 mb. If recovery to a tidal amplitude of 60 mb occurs by diffusion alone in a period of 10 years (3×10^8s), then

the resulting value for the hydraulic diffusivity, c, is 10^5 cm^2/s. Although this value seems somewhat high, it does fall within the range of 10^4 to 10^5 cm^2/s reported by Anderson and Whitcomb (1975). In this light the seismic hiatus, the initiation of activity at the northern end of the Brawley seismic zone, with subsequent activity taking place progressively farther south (as discussed in Chapter 4) suggests a cycle of seismicity beginning at the time of the 1940 quake. Although the pattern of swarm sequences along the Imperial Fault may represent the "steady state", the fact that this trend has apparently been fully covered by local swarms suggests the possibility that the next stage in Imperial Valley seismicity may be different.

Earthquake Swarms and Rapid, Local Stress Perturbations

It is tempting to generalize our results to swarms and tectonic environments elsewhere in the world. In the proposed model we have attempted to relate the occurrence of earthquake swarms directly to a rapidly varying driving stress (pore pressure changes associated with episodic fault creep) superimposed on a slowly accumulating secular strain. While the physical origin of this perturbational stress may vary, it seems likely that the time pattern of swarms may be diagnostic of its existence. Specifically, we have discussed several examples where induced seismicity responds to injection rates. The affinity of swarms for extensional offsets of strike-slip faults demonstrated by Weaver and Hill (1978) can be explained directly by the proposed model. Swarms in volcanic regions and along mid-oceanic rifts may well be evidence for an intrusive episode superimposed on the stresses associated

with the inflation of a magma chamber as suggested by Hill (1977). More rarely, fluids other than water and magma may be the vehicle of rapidly varying stresses. For example, earthquake swarms in the Santa Barbara Channel may well be a response to the pressurization of higher strata resulting from the vertical flow of hydrocarbons. Presumably when fluids are involved we are dealing with fluctuations in effective stress. A more direct connection between earthquake swarms and the tectonic stresses associated with great earthquakes elsewhere along the boundary of the Philippine Sea plate has been suggested by Kanamori (1972). In this regard, the activation of the Wakayama swarm area prior to the 1923 Kanto earthquake was attributed to the stresses associated with precursory creep-like slow deformation at depth together with local structural weakening in the swarm area. The postulated post-1940 recovery of pore pressure should lead to a similar structural weakening in an area dominated by swarm seismicity. Consequently, the Imperial Valley may be one of the most sensitive instruments available for possible small stress fluctuations preceding a major earthquake on the southern San Andreas Fault. When fluids are involved one would expect to find swarms preferentially in areas of extensional tectonics, especially where super-hydrostatic fluid potentials are present to reduce the required amplitude of triggering stresses. The more rarely observed swarms of thrust events in areas of compressional tectonics, such as the Palmdale swarms described by McNally and others (1978), would then require substantial perturbational stresses. The progressive rotation of the Palmdale focal mechanisms with time might then be explained in

terms of a superimposed driving stress approaching a significant fraction of the regional tectonic stress.

The notion of a perturbational stress driving swarm seismicity is actually quite deeply rooted in the seismological literature. For example, Terada (1932) discussed a similar model after relating the time pattern of swarm earthquakes with that of the fall of camellia blossoms. In the latter case the driving stress was a change in stem turgidity responding to diurnal temperature changes.

CONCLUSIONS

Earthquake swarm sequences in the Imperial Valley over the past ten years have generally consisted of from two to five spatially and temporally isolated clusters distributed along one of two trends. The Brawley trend corresponds to the inferred position of the Brawley Fault and extends from just southeast of Brawley to the southern shore of the Salton Sea. The Imperial trend is spatially coincident with the northern third of the surface fault trace associated with the 1940 El Centro earthquake. The activation of component swarms is progressive with time from which we infer the existence of an unobserved, underlying physical process. Individual clusters appear to illuminate structures transverse to the two major trends. Activation of these transverse structures progresses with unilateral migration away from the major trends.

The detailed observation of seven swarms over the past five years can be explained by a tripartite physical model. This model holds that

(1) Episodic creep propagating at depth along the major strike-slip faults

(2) induces swarm activity on transverse fractures by a process similar to hydrofracture as a result of

(3) differential fluid pressure gradients associated with the creep dislocation moving through a fluid-infiltrated, elastic matrix.

In a sense earthquake swarms are viewed as aftershocks of episodic creep. Tests of the proposed model might be directed at verifying, if possible, the existence of buried, episodic creep along the northern third of the 1940 surface trace.

The changes in Imperial Valley seismicity since the 1940 El Centro earthquake also appear to be consistent with a model in which the swarms are occurring in a slowly weakening volume related to a slow decrease in effective stress resulting from the recovery of pore pressure changes induced by the 1940 earthquake. In this light the ten year hiatus in swarm activity followed by a gradual encroachment of renewed activity from north to south can be viewed as part of the natural recovery cycle for moderate mainshocks on the major strike-slip faults.

An extension of these ideas suggests that swarm earthquakes may generally represent a response to a rapidly varying perturbational stress superimposed on that derived from the secular strain. However, the physical nature of this proposed perturbational stress may vary greatly from one tectonic regime to another.

REFERENCES

Allen, C. R., M. Wyss, J. N. Brune, and R. E. Wallace (1972). Displacements on the Imperial, Superstition Hills, and San Andreas Faults triggered by the Borrego Mountain earthquake, U. S. Geol. Surv. Prof. Paper 787, 87-104.

Anderson, D. L. and J. H. Whitcomb (1975). Time-dependent seismology, J. Geophys. Res., 80, 1497-1503.

Berry, F. A. F. (1973). High fluid potentials in California coast ranges and their tectonic significance, Am. Assoc. Petrol. Geol. Bull., 57, 1219-1249.

Biehler, S. R., L. Kovach and C. R. Allen (1964). Geophysical framework of the northern end of the Gulf of California structural province, in Marine Geology of the Gulf of California, T. Van Andel and G. Shor,(eds.), Am. Assoc. Petrol. Geol. Mem., 3, 126-156.

Bodvarsson, G. (1970). Confined fluids as strain meters, J. Geophys. Res., 75, 2711-2718.

Booker, J. R. (1973). Pore pressure and strain, Proceedings of the Conference on Tectonic Problems of the San Andreas Fault System: Stanford Univ. Publ., Geol. Sci., 13, 446-452.

Booker, J. R. (1974). Time dependent strain following faulting of a porous medium, J. Geophys. Res., 79, 2037-2044.

Brazee, R. J. and W. K. Cloud (1959). United States Earthquakes 1957, U. S. Government Printing Office, Washington, D.C. 108 pp.

Brune, J. N. and C. R. Allen (1967). A low stress-drop, low-magnitude earthquake with surface faulting: the Imperial, California earthquake of March 4, 1966, Bull. Seism. Soc. Am., 57, 501-514.

Bufe, C. G. and D. Tocher (1974). Central San Andreas Fault: strain episodes, fault creep, and earthquakes, Geology, 2, 205-207.

Byerlee, J. D. and W. F. Brace (1972). Fault stability and pore pressure, Bull. Seism. Soc. Am., 62, 657-660.

Fletcher, J. B. and L. R. Sykes (1977). Earthquakes related to hydraulic mining and natural seismic activity in western New York state, J. Geophys. Res., 82, 3767-3780.

Fuis, G. and M. Schnapp (1977). The November-December 1976 earthquake swarms in northern Imperial Valley, California: seismicity on the Brawley Fault and related structures, Trans. Am. Geophys. Un., 58, 1188.

Goulty, N. R., R. O. Burford, C. R. Allen, R. Gilman, C. E. Johnson, and R. P. Keller (1978a). Large creep events on the Imperial Fault, California, Bull. Seism. Soc. Am., 68, 517-521.

Goulty, N. R. and R. Gilman (1978b). Repeated creep events on the San Andreas Fault near Parkfield, California, recorded by a strainmeter array, J. Geophys. Res., 83, 5415-5419.

Gupta, I. N. (1974). Dilatancy and spatial distribution of aftershocks, Bull. Seism. Soc. Am., 64, 1707-1713.

Hamilton, W. L. (1973). Tidal cycles of volcanic eruptions: fortnightly to 19 yearly periods, J. Geophys. Res., 78, 3363-3375.

Hamilton, R. M. and J. H. Healy (1969). Aftershocks of the BENHAM nuclear explosion, Bull. Seism. Soc. Am., 59, 2271-2282.

Harthill, N. (1978). A quadripole resistivity survey in the Imperial Valley, California, Geophys., 43, 1485-1500.

Hartzell, S. H. (1978). Interpretation of earthquake strong ground motion and implications for earthquake mechanism, Ph.D. Thesis, University of California, San Diego.

Hartzell, S. H. and J. N. Brune (1977). Source parameters for the 1975 Brawley-Imperial Valley earthquake swarm, Pageoph., 115, 335-355.

Healy, J. M., R. M. Hamilton, and C. B. Raleigh (1970). Earthquakes induced by fluid injection and explosion, Tectonophysics, 9, 205-214.

Healy, J. H., W. W. Rubey, D. T. Griggs, and C. B. Raleigh (1968). The Denver earthquakes, Science, 161, 1301-1310.

Heaton, T. H. (1975). Tidal triggering of earthquakes, Geophys. J. R. astr. Soc., 43, 307-326.

Heaton, T. H. and D. V. Helmberger (1978). Predictability of strong ground motion in the Imperial Valley: modeling the M 4.9, November 4, 1976 Brawley earthquake, Bull. Seism. Soc. Am., 68, 31-48.

Hileman, J. A. (1978). Part I: A contribution to the study of the seismicity of Southern California, Part II: Inversion of phase times for hypocenters and shallow crustal velocities, Ph.D. Thesis, California Institute of Technology, Pasadena.

Hill, D. P. (1977). A model for earthquake swarms, J. Geophys. Res., 82, 1347-1352.

Hill, D. P., P. Mowinckel, and L. G. Peake (1975a). Earthquakes, active faults, and geothermal areas in the Imperial Valley, California, Science, 188, 1306-1308.

Hill, D. P., P. Mowinckel, and K. M. Lahr (1975b). Catalog of earthquakes in the Imperial Valley, California, U. S. Geol. Surv. Open-File Report, Washington, D.C., 29 pp.

Hubbert, M. K. and D. G. Willis (1957). Mechanics of hydrofracture, Bull. Amer. Assoc. Petrol. Geol., 41, 153-163.

Hubbert, M. K. and W. W. Rubey (1959). Role of fluid pressure in mechanics of overthrust faulting, Bull. Geol. Soc. Am., 70, 115-166.

Huggett, G. R., L. E. Slater, and J. Langbein (1977). Fault slip episodes near Hollister, California: initial results using a multiwavelength distance-measuring instrument, J. Geophys. Res., 82, 3361-3368.

Johnson, A. G. (1973). Pore pressure changes associated with creep events on the San Andreas Fault, Ph.D. Thesis, Stanford Univ., 177 pp.

Johnson, A. G. and R. L. Kovach (1973). Water level fluctuations on the San Andreas Fault system south of Hollister, California, in Proceedings of the Conference on Tectonic Problems of the San Andreas Fault System, R. L. Kovach and A. Nur (eds.), Stanford Univ. Press, Palo Alto, California, 489-494.

Johnson, A. G., R. L. Kovach and A. Nur (1974). Fluid-pressure variations and fault creep in Central California, Tectonophysics, 23, 257-266.

Johnson, A. G., R. L. Kovach, A. Nur and J. Booker (1973). Pore pressure changes during creep events on the San Andreas Fault, J. Geophys. Res., 78, 851-857.

Johnson, C. E.,(1977). Swarm tectonics of the Imperial and Brawley faults of Southern California (abstract), Trans. Am. Geophys. Un., 58, 1188.

Johnson, C. E. (1978). A deterministic model for earthquake swarm sequences in the Imperial Valley, California, Trans. Am. Geophys. Un., 58, 1205.

Johnson, C. E., and D. M. Hadley (1976). Tectonic implications of the Brawley earthquake swarm, Imperial Valley, California, January, 1975, Bull. Seism. Soc. Am., 66, 1133-1144.

Johnston, M. J. S., A. C. Jones, and W. Daul (1977). Continuous strain measurements during and preceding episodic creep on the San Andreas Fault, J. Geophys. Res., 82, 5683-5691.

Kanamori, H. (1972). Relation between tectonic stress, great earthquakes and earthquake swarms, Tectonophysics, 14, 1-12.

King, C. Y., R. D. Nason, and D. Tocher (1973). Kinematics of fault creep, Phil. Trans. Roy. Soc. London, Ser. A., 274, 355-360.

Klein, F. W. (1976). Earthquake swarms and the semi-diurnal solid earth tide, Geophys. J. Roy. astr. Soc., 45 245-295.

Klein, F. W. Pall Einarsson, and M. Wyss (1977). The Reykjanes Peninsula, Icealnd, earthquake swarm of September 1972 and its tectonic significance, J. Geophys. Res., 82, 865-888.

Kovach, R. L., A. Nur, R. L. Wesson, and R. Robinson (1975). Water-level fluctuations and earthquakes on the San Andreas Fault zone, Geology, 3, 437-440.

Lee, W. H. K. and J. C. Lahr (1975). HYPO71 (Revised): A computer program for determining hypocenter, magnitude, and first motion pattern of local earthquakes, U. S. Geol. Surv. Open-File Report, Washington, D.C., 113 pp.

Lockner, D. and J. D. Byerlee (1977). Hydrofracture in Weber sandstone at high confining pressure and differential stress, J. Geophys. Res., 82, 2018-2026.

Mauk, F. J. and M. J. S. Johnston (1973). On the triggering of volcanic eruptions by earth tides, J. Geophys. Res., 78, 3356-3362.

Mauk, F. K., and J. Kiener (1973). Microearthquakes at St. Augustine Volcano, Alaska, triggered by earth tides, Science, 182, 386-389.

McNally, K. C., H. Kanamori, J. C. Pechman, and G. Fuis (1978). Earthquake swarm along the San Andreas Fault near Palmdale Southern California 1976 to 1977, Science, 201, 814-817.

Mogi, K. (1963). Some discussions on aftershocks, foreshocks, and earthquake swarms -- the fracture of a semi-infinite body caused by an inner stress origin and its relation to the earthquake phenomena (3), Bull. Earthquake Res. Inst. Tokyo Univ., 41, 615-658.

Mortenson, C. E., R. C. Lee, R. O. Burford (1977). Simultaneous tilt, strain, creep, and water level observations at the Cienega Winery south of Hollister, California, Bull. Seism. Soc. Am., 67, 641-650.

Muffler, L. J. P., and D. E. White (1969). Active metamorphism of upper Cenozoic sediments in the Salton Sea geothermal field and Salton Trough, southeastern California, Bull. Geol. Soc. Am., 80, 157-182.

Murphy, L. M. and F. P. Ulrich,(1952). United States Earthquakes 1950, U. S. Gov. Printing Office, Washington, D.C., 47 pp.

Nason, R. D. (1973). Fault creep and earthquakes on the San Andreas Fault, in Proceedings of the Conference on Tectonic Problems of the San Andreas Fault System: Stanford Univ. Pubs. Geol. Sci., 13, 275.

Nasu, N., F. Kishinouye and T. Kodaira (1931). 2. Recent seismic activities in the Idu Peninsula (Part 1), Bull. Earthquake Res. Inst. Tokyo Univ., 9, 22-35.

Nur, A. and J. R. Booker (1972). Aftershocks caused by pore fluid flow? Science, 175, 885-887.

Nur, A. and P. Schultz (1973). Fluid flow and faulting, 2: A stiffness model for seismicity in Proceedings of the Conference on Tectonic Problems of the San Andreas Fault System: Stanford Univ. Publ., Geol. Sci. 13, 405-416.

Ohtake, M. (1974). Seismic activity induced by water injection at Matsushiro, Japan, J. Phys. Earth, 22, 163-176.

Raleigh, C. B., J. H. Healy, and J. D. Bredehoeft (1976). An experiment in earthquake control at Rangely, Colorado, Science, 191, 1230-1237.

Reichle, M. and I. Reid (1977). Detailed study of earthquake swarms from the Gulf of California, Bull. Seism. Soc. Am., 67, 159-171.

Rice, J. R. and D. A. Simons (1976). The stabilization of spreading shear faults by coupled deformation-diffusion effects in fluid-infiltrated porous materials, J. Geophys., 81, 5322-5334.

Rinehart, J. S. (1972). Fluctuations in geyser activity caused by variations in earth tidal forces, barometric pressure, and tectonic stresses, J. Geophys. Res., 77, 342-350.

Sauk, W. A.,(1975). The Brawley, California earthquake sequence of January 1975, and triggering by earth tides, Geophys. Res., Lett., 2, 506-509.

Savage, J. C., D. Goodreau, and W. H. Prescott (1974). Possible fault slip on the Brawley Fault, Imperial Valley, California, Bull. Seism. Soc. Am., 64, 713-715.

Sharp, R. V. (1976). Surface faulting in Imperial Valley during the earthquake swarm of January-February 1975, Bull. Seism. Soc. Am., 66, 1145-1154.

Slater, L. E. and G. R. Mugget (1976). A multiwavelength distance-measuring instrument for geophysical experiments, J. Geophys. Res., 81, 6299-6306.

Smith, S. W., C. B. Archambeau, and W. Gile (1969). Transient and residual strains from large underground explosions, Bull. Seism. Soc. Am., 59, 2185-2196.

Terada, T. (1932). On swarm earthquakes, Bull. Earthquake Res. Inst. Tokyo Univ., 10, 29-35.

Thatcher, W. (1979). Horizontal crustal deformation from historic geodetic measurements in Southern California, J. Geophys. Res., 84 (in press).

Thatcher, W. and J. N. Brune (1971). Seismic study of an oceanic ridge earthquake swarm in the Gulf of California, Geophys. J., 22, 473-489.

Thatcher, W. and T. C. Hanks (1973). Source parameters of Southern California earthquakes, J. Geophys. Res., 78, 8547-8576.

Tryggvason, E. (1973). Seismicity, earthquake swarms, and plate boundaries in the Iceland region, Bull. Seism. Soc. Am., 63, 1327-1348.

Ulrich, F. P. (1941). The Imperial Valley earthquake of 1940, Bull. Seism. Soc. Am., 31, 13-31.

Weaver, C. S. and D. P. Hill (1978). Earthquake swarms and local crustal spreading along major strike-slip faults in California, Pageoph., 117, 51-64.

Weertman, J. (1974). Water flow paths around a dislocation on an earthquake fault, J. Geophys. Res., 79, 3291-3293.

Wesson, R., R. O. Burford, and W. L. Ellsworth (1973). Relationship between seismicity, fault creep, and crustal loading along the central San Andreas Fault, in Proceedings of the Conference on Tectonic Problems of the San Andreas Fault System: Stanford University Publ., Geol. Sci. 13, 303-321.

White, D. E. (1968). Hydrology, activity, and heat flow of the Steamboat Springs thermal system, Washoe County, Nevada, U. S. Geol. Surv. Prof. Paper 458-C, 1-109.

Wiggins, R. A. (1972). The general linear inverse problem: implication of surface waves and free oscillations for earth structure, Rev. of Geophys. and Space Phys., 10, 251-285.